UNIVERSIDADE DE SÃO PAULO
Escola de Engenharia de São Carlos

Optimal seismic design using Performance-Based Engineering

Projeto ótimo de estruturas sob ações sísmicas com base na engenharia baseada em desempenho

Isabela Durci Rodrigues

Ph.D. Thesis – Programa de Pós-Graduação em Engenharia Civil (Engenharia de Estruturas) da Escola de Engenharia de São Carlos, Universidade de São Paulo

EESC · USP

Isabela Durci Rodrigues

Optimal seismic design using Performance-Based Engineering

Projeto ótimo de estruturas sob ações sísmicas com base na engenharia baseada em desempenho

Thesis presented to the São Carlos School of Engineering of the University of São Paulo in partial fulfillment of the requirements for the degree of Doctor of Science in Postgraduate Program in Civil Engineering (Structural Engineering).

Advisor: Prof. André Teófilo Beck.

CORRECTED VERSION

(The original version is available at São Carlos School of Engineering)

São Carlos

2025

R696o

Rodrigues, Isabela Durci

Optimal seismic design using Performance-Based Engineering / Isabela Durci Rodrigues ; advisor André Teófilo Beck. -- São Carlos, 2025.

235 p.

Doctoral Thesis - Graduate Program in Civil Engineering and Concentration Area in Structures -- São Carlos School of Engineering of University of São Paulo, 2025.

1. Performance-Based Earthquake Engineering. 2. Performance-Based Risk Optimization. 3. Metamodeling. 4. Uncertainty quantification. 5. Structural optimization. I. André Teófilo, Beck, advisor. II. Título.

Responsible for the cataloging structure of the publication according to AACR2: EESC Librarians

FOLHA DE JULGAMENTO

Candidata: Engenheira **ISABELA DURCI RODRIGUES**.

Título da tese: "Projeto Ótimo de Estruturas sob Ações Sísmicas com base na Engenharia Baseada em Desempenho".

Data da defesa: 08/12/2025.

Comissão Julgadora	Resultado
Prof. Associado André Teófilo Beck (Orientador) (Escola de Engenharia de São Carlos/EESC-USP)	APROVADO
Prof. Dr. Seymour Milton John Spence (University of Michigan/UMIch)	APROVADO
Profa. Dra. Rubia Mara Bosse (Universidade Tecnológica Federal do Paraná/UFTPR)	APROVADO
Prof. Dr. Ketson Roberto Maximiliano dos Santos (University of Minessota/U of M)	APROVADO
Prof. Dr. Eduardo Marques Vieira Pereira (Universidade Presbiteriana Mackenzie/UPM)	APROVADO

Coordenador do Programa de Pós-Graduação em Engenharia Civil (Engenharia de Estruturas):
Prof Associado **Ricardo Carrazedo**

Presidente da Comissão de Pós-Graduação:
Prof. Titular **Carlos De Marqui Junior**

ACKNOWLEDGEMENTS

While writing these acknowledgments, I can't help but think about everything that has happened over the past five years, and about all the people who have crossed my path during that time, each contributing in their own way to the completion of this work. A lot has changed too — I started my PhD during the COVID-19 pandemic, in a different city, attending remote classes. Looking back now, it feels like a different lifetime. Yet, this work carries within it traces of all those changes — and, above all, the kindness and friendship of many people who may not be mentioned here by name but whose presence I deeply cherish and wish to acknowledge.

Despite all the changes, what has remained constant — and always will — is the unconditional support of my family. I want to thank my parents, Eliane and Carlos, and my brother, Marcelo. Your love, encouragement, and the countless opportunities you have given me have been essential throughout my life, and especially in bringing this work to completion. I also want to thank my grandparents, who are always praying for me and wishing me well, even if they do not fully understand what I do for a living. I love you all so much.

I want to thank my husband, Eduardo. Over the course of this PhD, we went through many milestones together, from boyfriend, to fiancé, to husband. Yet the love and patience you have given me over the past six years have never changed. You genuinely gave your blood to this PhD, literally, by donating plasma while we were in the United States to help with our living expenses. You shaped your life around mine during important phases of this journey, and for that, I will always be grateful. Along with him, I want to thank his family, who embraced me from the very beginning of our relationship. A special thanks to my mother-in-law, Rosana Lopes, who has always supported me in both my personal and professional choices.

Still regarding changes, this PhD was developed at a different institution from where I completed my undergraduate and Master's degrees. Studying at the University of São Paulo (USP), more specifically at the São Carlos School of Engineering (EESC), had been a dream of mine since high school. Although I faced some frustrations with previous applications, I can now see that being admitted specifically for the PhD was the best timing I could have asked for. A person who had a significant impact on that journey is my advisor, Prof. André Beck. At first, I admired the excellence of his work and his commitment to research, but I soon came to admire the kind and welcoming person he is, and the genuine effort he made to make me feel at home in the Structural Engineering Department and in his research group from the very beginning. I often hear people talk about the importance of the opportunities that he offers to his students, and now it is my

turn to thank him. My own career has already been shaped in meaningful ways by the opportunities he has given me over the past five years, and I know it will continue to be. It was a pleasure to be your student, and I look forward to the next chapter of our work during my postdoctoral period.

I also want to acknowledge the kind and brilliant people I met during my time at EESC–USP. First, to the senior PhD colleagues who welcomed me when I arrived, especially Rúbia Bosse and Lucas da Rosa Ribeiro, whom I can now call friends and whom I admire for their commitment to their work and their courage to venture into the challenges of research in our field. I am also grateful to my current colleagues in our research group, particularly Felipe Macedo, Luis Gustavo Costa, Luiz Eduardo de Mattos, and José Caio Couto, for their outstanding work and for the many insightful discussions we shared. To Thássia Zanardo, Débora Maia, and Luís Philipe Almeida, the colleagues from my incoming class whose friendship extended far beyond USP and became a source of constant support in my personal life. And finally, to the great students I met in the Structural Engineering Department, particularly Gustavo Gidrão, Murilo Bento, Matheus Rocha, Chiara Teodoro, Vinicius de Barros Souza, Marina Naomi and Luiz Fernando Teodoro, thank you for the conversations, the coffees, our conference trips together, and the burgers we shared while standing by each other through the difficult moments of research life.

During my PhD, I had the opportunity to spend one year as a visiting scholar at the University of Michigan. I am truly grateful to Prof. Seymour Spence for hosting me and for all his contributions to this research. He inspired me with his dedication to his work and to his students, and he challenged me in ways that helped me grow. I hope that one day I can be as good a supervisor to my students as he has been to me. I also thank him for making me feel part of his amazing research group, and I am grateful to my colleagues Liuyun Xu, Jieling Jiang, Srinivasan Arunachalam, Bowei Li, Sejin Kim, Tanmay Vora, and Haimiti Atila for all the encouragement and support during my time in Ann Arbor.

I like to say that life placed some angels in my path during this year abroad. First, my family in the United States: my beloved cousins Josi and Jimmy Moore - I wish that one day I can be as kind and humble as you are - my dear cousins Bruna Placucci, Juliana and Natalia Rodrigues, and my uncles João Francisco and Claudia Rodrigues, Silvia Placucci, Fabiano Rodrigues and Grace Ziglio. You watched over me and Eduardo the entire time we were in the US, making sure we were safe. All my love to you. Then, the good friends I made in Ann Arbor, especially Laura and Salomon Constain-Montoya, Beatriz Sahadi, Leticia Lança, and Mariana Bitu. Laura is one of the most amazing people I have ever met, bringing a bit of the Latino warmth into my life and being kind enough to open her home to me. I will never forget what she did for me, and “thank you” will never

be enough. Bia was brave enough to say yes to several of my bad deals, and suddenly became one of the people I can rely on the most. Thank you for being such an incredible friend. Leticia and Mari, we practically arrived in Ann Arbor together, and we shared so many great moments that I will always remember. Thank you for making this year in the United States such an unforgettable experience.

Besides all the wonderful people that USP and Michigan brought into my life, I also need to acknowledge the amazing engineering friends I have made since the early stages of my career, whose friendship only grew stronger throughout this PhD. I want to thank Fernanda Beluca, Giovanna Oliveira, Gabriela Moraes, Marcel Rodrigues, and Rafael Dupim for more than ten years of friendship and for always cheering for me. I also had the pleasure of completing my Master's degree with outstanding people who now live abroad but remain a constant presence in my life: Natalia Manzo, Vanessa Saback and Anderson Pires. Thank you for inspiring both my professional and personal path. Still from the Master's team, it is a tremendous pleasure to thank Eduardo Pereira and Gustavo Henrique Cavalcante, the OpenSees team. The fact that you are among my closest friends brings me great joy and inspires my work every day. There is also someone I met during my undergraduate years who stayed with me through my Master's and PhD, especially during my time in the United States: Dani Paulino. Thank you for all the good moments (and the conferences) we shared. I also want to thank Andreia Alvares, Bruno Fernandes, Fábio Fleming, Rodrigo Bezerra, and João Gabriel Duarte for their friendship and for being amazing professionals, in Brazil and worldwide.

Finally, I want to acknowledge the friendships that have been with me for a lifetime — the ones I know will never change, no matter how far apart we may be. Thais Segantini, Bruna Ferrari, Camila Oliveira, Juliana Haddad, Nathalia Marcelino, Carol Bufelli, and Camila Rocha, you have been with me since childhood, and each of you has inspired me in your own way. Thank you. Whenever I think of a safe place amid all the changes in my life, I think of you. Also, I want to thank Maressa Leão, Cecíllia Teixeira and Elisa Santos, the good friends I made during my time in the UK and are still by my side.

This study was financed in part by the Coordenação de Aperfeiçoamento de Pessoal de Nível Superior - Brasil (CAPES) – Grant Finance Code 001.

This study was financed, in part, by the São Paulo Research Foundation (FAPESP), Brazil - Process Numbers 2020/14072-7 and 2023/02504-8.

The opinions, hypotheses, conclusions, or recommendations expressed in this material are the responsibility of the author and do not necessarily reflect the views of CAPES and FAPESP.

ABSTRACT

RODRIGUES, I. D. **Optimal seismic design using Performance-Based Engineering**. 2025. 235p. Thesis (Doctor) - São Carlos School of Engineering, University of São Paulo, São Carlos, 2025.

Performance-Based Earthquake Engineering (PBEE) enables rational structural design by explicitly accounting for seismic hazard uncertainty and balancing construction costs with expected consequences such as repair costs, replacement, injury, and death. Risk-based optimization can be naturally integrated into PBEE to pursue economically efficient designs, forming a framework referred to as Performance-Based Risk Optimization (PBRO). However, the application of PBRO remains limited due to the heavy computational burden imposed by the nonlinear time history analysis (NLTHA) to propagate uncertainty and characterize the joint probability distribution of the Engineering Demand Parameters (EDP) and parameters of the fragility functions. This dissertation proposes methodologies for estimating statistical parameters of the EDPs and fragility functions using metamodeling (or surrogate modeling) strategies to emulate both the deterministic and stochastic simulations to obtain the structural response. The adopted framework builds upon the assessment procedures defined in international standards for PBEE, and introduces Gaussian process–based metamodels to approximate computationally intensive simulations while incorporating the associated uncertainties of the problem. Case studies on reinforced concrete and steel structures are presented to demonstrate how metamodels and PBRO can be combined to optimize structural parameters under seismic demands. The results show that the proposed framework enables accurate representation of EDP uncertainties and supports the derivation of optimal designs with significantly reduced computational cost. By comparing different strategies for uncertainty representation, the research illustrates how metamodels can maintain the fidelity of PBEE-based risk assessments while making PBRO computationally tractable. Overall, this work contributes to advancing the integration of risk optimization into seismic design practice, offering evidence that balanced trade-offs between construction cost and expected seismic loss can be achieved within a metamodel-enhanced PBRO framework.

Keywords: Performance-Based Earthquake Engineering. Performance-Based Risk Optimization. Metamodeling. Uncertainty quantification. Structural optimization.

RESUMO

RODRIGUES, I. D. **Projeto ótimo de estruturas sob ações sísmicas com base na engenharia baseada em desempenho**. 2025. 235p. Tese (Doutorado) - Escola de Engenharia de São Carlos, Universidade de São Paulo, São Carlos, 2025.

A Engenharia Sísmica Baseada em Desempenho (ESBD) permite o desenvolvimento de projetos estruturais que consideram explicitamente as incertezas associadas à ameaça sísmica, promovendo um equilíbrio entre os custos de construção e as consequências esperadas de eventos sísmicos, como custos de reparo, substituição estrutural, ferimentos e perdas de vidas. A otimização baseada em risco pode ser naturalmente integrada à ESBD para a obtenção de projetos economicamente eficientes, formando uma metodologia denominada Otimização de Risco Baseada em Desempenho (PBRO). No entanto, as aplicações de ORBD ainda são limitadas devido ao elevado custo computacional imposto pelas análises dinâmicas não lineares necessárias para propagar incertezas e caracterizar a distribuição conjunta de probabilidades dos Parâmetros de Demanda (PD) e dos parâmetros estatísticos das curvas de fragilidade estruturais. Este trabalho propõe metodologias para estimar os parâmetros estatísticos dos PD e das curvas de fragilidade com base em estratégias de modelos substitutos (ou metamodelos), capazes de emular tanto as respostas determinísticas quanto as estocásticas das simulações necessárias para obtenção da resposta estrutural. A metodologia proposta fundamenta-se nos procedimentos de avaliação definidos em manuais internacionais consolidados para a ESBD e introduz metamodelos baseados em processos Gaussianos para aproximar simulações computacionalmente intensas, incorporando simultaneamente as incertezas associadas ao problema. Estudos de caso em estruturas de concreto armado e aço são apresentados para demonstrar como os metamodelos e a ORBD podem ser combinados para otimizar parâmetros estruturais sob demandas sísmicas. Os resultados indicam que o arcabouço proposto permite uma representação precisa das incertezas dos PD e possibilita a obtenção de projetos ótimos com custo computacional significativamente reduzido. Ao comparar diferentes estratégias de representação da incerteza, a pesquisa evidencia que os metamodelos conseguem preservar a fidelidade das avaliações de risco no contexto da ESBD, tornando a ORBD computacionalmente viável. De modo geral, este trabalho contribui para o avanço da integração entre otimização de risco e projeto sísmico, oferecendo evidências de que é possível alcançar balanços eficientes entre custo de construção e perdas sísmicas esperadas dentro de um arcabouço de ORBD aprimorado por metamodelos.

Palavras- chave: Engenharia sísmica baseada em desempenho. Otimização de risco baseada em desempenho. Metamodelagem. Quantificação de incertezas. Otimização estrutural.

LIST OF FIGURES

LIST OF TABLES

LIST OF ABBREVIATIONS AND ACRONYMS

ATC	Applied Technology Council
BRB	Buckling Restrained Brace
CDF	Cumulative Distribution Function
CCDF	Complementary Cumulative Distribution Function
CMS	Conditional Mean Spectrum
DDO	Deterministic Design Optimization
DoE	Design of Experiments
DV	Decision Variable
EDP	Engineering Demand Parameter
FE	Finite Element
FEMA	Federal Emergency Management Agency
GA	Genetic Algorithm
GEM	Global Earthquake Model
GMM	Ground Motion Model
GMPE	Ground-Motion Prediction Equation
GSHAP	Global Seismic Hazard Assessment Program
IDA	Incremental Dynamic Analysis
IM	Intensity Measure
LCCO	Life-Cycle Cost Optimization
LDM	Lumped Damage Model
LHS	Latin Hypercube Sampling
LPM	Lumped Plasticity Model
MAFE	Mean Annual Frequency of Exceedance
MC	Monte Carlo

MSA	Multiple-Stripe Analysis
NLTHA	Nonlinear Time History Analysis
PBD	Performance-Based Design
PBDO	Performance-Based Design Optimization
PBE	Performance-Based Engineering
PBEE	Performance-Based Earthquake Engineering
PBRO	Performance-Based Risk Optimization
PDF	Probability Density Function
PEER	Pacific Earthquake Engineering Research Center
PFA	Peak Floor Acceleration
PGA	Peak Ground Acceleration
PGV	Peak Ground Velocity
PSDM	Probabilistic Seismic Demand Model
PSHA	Probabilistic Seismic Hazard Analysis
RBDO	Reliability-Based Design Optimization
RC	Reinforced Concrete
RO	Risk Optimization
SCWB	Strong-Column Weak-Beam
SCBF	Special Concentrically-Braced Frame
SMF	Special Moment Frame
SPCE	Stochastic Polynomial Chaos Expansions
SS	Stratified Sampling
UHS	Uniform Hazard Spectrum
USGS	United States Geological Survey

LIST OF SYMBOLS

$A(f; M_w, r)$	Frequency-domain radiation spectrum of the Stochastic Ground Motion Model
A_{BRB}	Area of Buckling Restrained Brace (BRB)
a_t, b_t, c_t	Constants of the Stochastic Ground Motion Model
BRC	Building replacement cost
$\mathbf{C}$	Kriging covariance matrix incorporating process correlation and observation noise
$c_{\boldsymbol{\alpha}}$	Coefficients of PCE
C_{BRB}	Cost per unit weight of the BRB
C_{comp}	Cost of the composition for Reinforced Concrete (RC) elements - injection, densification and finishing of concrete
C_{cons}	Construction cost
CC_{concrete}	Cost of concrete for RC elements
CC_{form}	Cost of timber formwork
CC_{rein}	Cost of reinforcement bars
C_d	Structural and nonstructural repair cost calculated with Hazus (2022a) manual
CS_{ds}	Structural repair cost for damage state ds calculated with Hazus (2022a) manual
C_{exReCo}	Expected repair cost calculated with FEMA P-58 (2012) procedure
C_{mat}	Cost of material for RC elements - concrete input and pumping
CNS	Total drift-sensitive nonstructural repair cost calculated with Hazus (2022a) manual
c_Q	Seismic velocity for the Stochastic Ground Motion Model
CS	Total structural repair cost calculated with Hazus (2022a) manual
C_{steel}	Cost per unit weight of structural steel

C_t	Total cost (repair cost + construction cost) calculated with Hazus (2022a) manual
CV	Coefficient of variation
$c_{w,d}$	RC column cross section dimensions (width and depth)
D_S	Number of Monte Carlo realizations in the loss analysis with FEMA P-58 (2012) procedure
ds	Damage limit state
E	Young's Modulus
$e(f; M_w, r)$	Temporal envelope function of the Stochastic Ground Motion Model
$E(f; M_w)$	Source term of the Stochastic Ground Motion Model
EDP	Random vector of N_p engineering demand parameters (EDPs)
edp	EDP
$F(x\|y)$	Conditional Cumulative Distribution Function (CDF)
F_a	Site coefficient for short periods
F_{comp}	Cost of the composition for timber formwork - production
F_v	Site coefficient for long periods
F_y	Yield stress
$G(f)$	Site amplification of the Stochastic Ground Motion Model
$G(x\|y)$	Conditional Complementary Cumulative Distribution Function (CCDF)
$I(x)$	Indicator function
im	Intensity measure
L	Length of a RC structural element
L_{brace}	Length of the steel brace
L_{BRB}	Length of the BRB
M	Number of scalar metamodel input parameters
M_w	Earthquake magnitude
m	Nominal mass of steel reinforcement

N_e	Number of ground motions in a specific set
N_p	Number of Engineering Demand Parameters (EDPs) evaluated
N_s	Independent repetitions of an experiment
N_{rea}	Number of realizations in a Monte Carlo simulation
$\hat{n}$	Number of realizations of the strata-wise samples
n_c	Number of coefficients of the Kriging regression basis function
n_{DV}	Number of design variables
n_{ele}	Number of RC elements
n_{long}	Number of longitudinal steel reinforcement bars
n_{LS}	Number of limit state equations
n_{RV}	Number of random variables
$n_{\mathbb{S}_i}$	Number of strata to the Stratified Sampling method
n_{st}	Number of samples in each stratum in the Stratified Sampling method
n_{trans}	Number of transverse steel reinforcement bars
p	Probability constant for the Stratified Sampling method
$P(x\|y)$	Conditional Cumulative Distribution Function (CDF)
$P(f;r)$	Path effects of the Stochastic Ground Motion Model
$P_{ds}(t_D)$	Unconditional probability of failure for damage state ds as a function of the time period t_D
$P_{\text{struc},ds}$	Probability of structural damage for damage state ds
$P_{\text{Nstruc},ds}$	Probability of nonstructural drift-sensitive damage for damage state ds
p_f	Probability of failure
$Q(f)$	Elastic attenuation factor of the Stochastic Ground Motion Model
$\mathbf{R}$	Kriging correlation matrix
R	Source-to-site distance
r	Ground motion epicentral distance

R_{JB}	Joyner-Boore distance to the rupture plane
R_{Φ}	Radiation pattern of the Stochastic Ground Motion Model
RCD_{ds}	Drift-sensitive nonstructural repair cost ratio
RCS_{ds}	Structural repair cost ratio
S	Number of support points for metamodels (Design of Experiment)
S_{compo}	Cost of steel reinforcement composition - cutting, bending rebar labor and spacers
S_{input}	Cost of steel reinforcement bars
S_1	Mapped spectral acceleration for long periods
S_s	Mapped spectral acceleration for short periods
S_{D1}	Design spectral acceleration for long periods
S_{DS}	Design spectral acceleration for short periods
S_a	Spectral acceleration
S_C	Median value of structural capacity
S_D	Median value of structural demand
T or $\bar{T}$	Fundamental period of vibration
t_{brace}	Thickness of the steel brace
t_D	Time period in years
$\bar{V}_s$	Mean shear wave velocity
$Y_{\mathbf{x}}$	Distribution obtained with a stochastic emulator
$\hat{Y}$	Noisy Kriging prediction
$\widetilde{Y}$	Stochastic Polynomial Chaos Expansion (SPCE) prediction
$\mathbf{X} \in \mathbb{R}^{N_e \times N_p}$	Demand matrix for loss analysis
$\mathbf{X_d}$	Design variables
$\mathbf{X_h}$	Ground motion variability
$\mathbf{X_m}$	Modeling uncertainty

$\mathbf{X_r}$	Random variables
$\mathbf{X_w}$	White noise sequence for the Stochastic Ground Motion Model
$\mathbf{W} \in \mathbb{R}^{D_S \times N_p}$	Synthetic sample matrix for FEMA P-58 (2012) loss analysis
W_{beams}	Total weight of steel beams
W_{brace}	Total weight of steel braces
W_{BRB}	Total weight of BRBs
W_{columns}	Total weight of steel columns
$\mathbf{Z}(\omega)$	Latent random variable of a stochastic simulator
$Z_{\text{kr}}(\mathbf{x})$	Zero-mean Gaussian stochastic field for Kriging
$\boldsymbol{\alpha}$	Multi-index of Polynomial Chaos Expansion (PCE)
$\boldsymbol{\beta}$	Vector of coefficients of the Kriging trend
β_C	Logarithmic standard deviation of structural capacity
β_D	Logarithmic standard deviation of structural demand
β_{gm}	Ground motion variability
β_m	Modeling uncertainty
ϵ	Estimated error of a statistical inference
$\boldsymbol{\varepsilon}$	Kriging noise term
η_t	Envelope function parameters of the Stochastic Ground Motion Model
$\boldsymbol{\theta}$	Vector of Kriging hyperparameters
$\lambda(im)$	Mean annual frequency of exceedance of intensity measure (IM)
λ_{ds}	Mean annual conditional failure rate for each damage state ds
λ_t	Envelope function parameters of the Stochastic Ground Motion Model
$\hat{\mu}_X$	Empirical mean of random variable X
$\hat{\mu}_{\text{coll}}$	Inferred mean value of the collapse fragility function
ρ_{BRB}	Material density for the BRB
ρ_S	Rock density for the Stochastic Ground Motion Model

$\rho_{\mathbf{X}}$	Correlation terms derived from the covariance matrix $\Sigma_{\mathbf{X}}$ of a random vector X
$\Sigma_{\mathbf{X}}$	Covariance matrix of a random vector X
$\boldsymbol{\Sigma}_n$	Covariance matrix of the Kriging noisy term
$\hat{\sigma}_X^2$	Empirical variance of random variable X
$\hat{\sigma}_{\text{coll}}$	Logarithmic standard deviation of the collapse fragility function
$\boldsymbol{\tau}$	Vector of strata-wise samples for the Stratified Sampling method
Φ	Standard normal CDF
ϕ	Diameter of reinforcement steel bars
$\psi_{\boldsymbol{\alpha}}$	Multivariate orthonormal polynomial of PCE with respect to $f_{\mathbf{X}}$
$\phi_{\alpha_j}^{(j)}$	Univariate orthonormal polynomial of degree α_j
$\boldsymbol{\Omega}$	Probability space representing the internal stochasticity of the stochastic simulator
Ω_f	Failure domain
Ω_s	Safe domain
$\mathbb{E}(X)$	Population mean of random variable X
$\mathcal{A}^{p,M}$	Multi-index set of retained basis functions in PCE (total degree $\leq p$)
$\mathcal{D}$	Domain of definition
$\mathcal{M}$	Simulation process with a computational model
$\mathcal{M}_d$	Deterministic simulator
$\mathcal{M}_s$	Stochastic simulator
$\tilde{\mathcal{M}}_d$	Metamodel for the deterministic simulator
$\tilde{\mathcal{M}}_s$	Stochastic emulator
$\mathbb{S}$	Space of the input random variable to be stratified in the Stratified Sampling method
$\mathcal{V}$	Stratification variable in the Stratified Sampling method
$\mathcal{X}$	Inputs of the system in a simulation
$\mathcal{Y}$	Outputs of a simulation

CONTENTS

1 INTRODUCTION

This chapter presents the initial considerations of this PhD research. Section 1.1 discusses the motivation and scope of the study, along with a brief overview of the state of the art. Section 1.2 outlines the main and specific objectives of the research. Finally, Section 1.3 presents the organization of the remaining chapters of this document.

1.1 Motivation

Seismic events are among the most destructive natural hazards, capable of causing significant economic losses and widespread societal disruption. In Brazil, a mid-plate country located within the South American tectonic plate—which is considered more stable than the boundary regions of tectonic plates—concerns about seismic activity are relatively recent. For comparison, an earthquake of magnitude 5 occurs in Brazil on average once every five years, whereas in the Andean region, earthquakes of the same magnitude occur approximately twice a week (Assumpção *et al.*, 2014; Assumpção *et al.*, 2016).

However, despite its location, Brazil has a history of small to moderate seismic events, with moment magnitudes greater than 5, which can cause significant damage to structures that have not been properly designed for this type of load. Fig. 1.1 presents the uniform seismic catalog for Brazil, filtered with the following criteria: events with magnitudes greater than 6.0 since 1940, as earthquakes of this size would have been reliably recorded by the global seismographic network; magnitudes greater than 5.0 since 1962 for the same reason; magnitudes greater than 4.5 since 1968, when Brazilian seismic stations became capable of detecting such events; and magnitudes greater than 3.5 since 1980, when nationwide coverage by Brazilian stations allowed consistent recording of earthquakes of this magnitude (Assumpção *et al.*, 2016). The catalog was subsequently updated using the database of the Institute of Astronomy, Geophysics, and Atmospheric Sciences at the University of São Paulo (IAG - USP 2024).

In 2006, recognizing the need to align Brazil with international design requirements for seismic actions (Santos; Lima, 2005), the Brazilian standard ABNT NBR 15421 2006 was published and later updated in 2023. Nevertheless, a study conducted by Miranda (2021) and Miranda, Varum and Pouca (2019) indicates that seismic loads are still not considered by most structural designers during the design phase, for several reasons.

Figure 1.1 – Uniform seismic catalog.

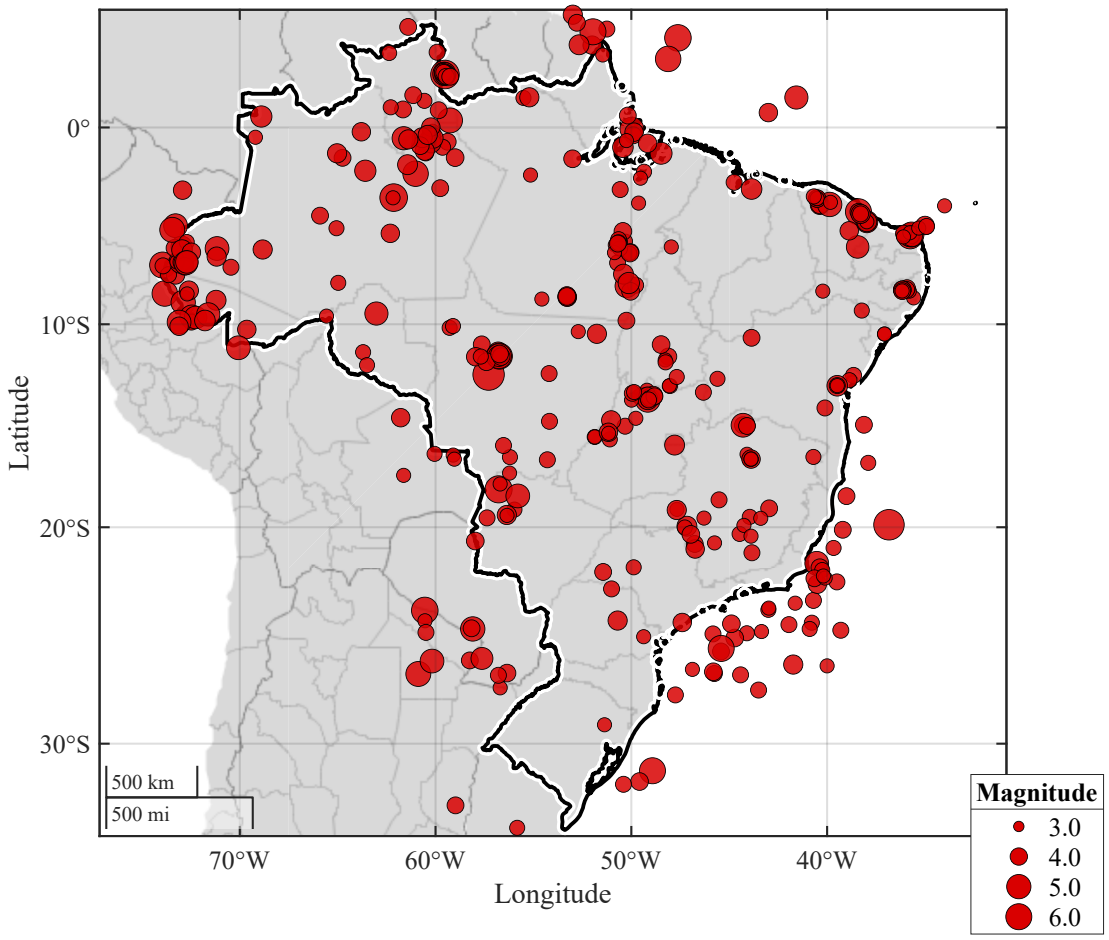

Source: Author.

The fact that most structures in Brazil are not designed to resist seismic loads raises concerns regarding the definition of seismic risk, which extends beyond the seismic hazard at a specific location. According to the United Nations Office for Disaster Risk Reduction, risk is defined as "the potential loss of life, injury, or destroyed or damaged assets that could occur to a system, society, or community within a specific period of time, determined probabilistically as a function of hazard, exposure, vulnerability, and capacity" (UNDRR, 2023). In this sense, seismic risk cannot be considered low solely because the seismic hazard is low, since exposure, vulnerability, and capacity must also be assessed.

From an economic standpoint, risk can be expressed as the product of the probability of failure and the cost associated with that failure (Beck; Gomes, 2012). Therefore, even in regions of low seismic hazard, exposure may be high due to population density, and vulnerability may increase because many structures lack the necessary capacity to withstand seismic actions, as they are not designed to account for earthquake loads.

To properly quantify this risk, it is necessary to perform a probabilistic evaluation of structural performance that explicitly incorporates hazard, exposure, and vulnerability.

This assessment can be achieved through the framework of Performance-Based Engineering (PBE), which provides a consistent framework for linking hazard to expected structural and economic losses. PBE is a structural engineering paradigm that seeks to achieve explicitly defined performance objectives for buildings and infrastructure, particularly under natural hazards such as earthquakes and strong winds (Moehle; Deierlein, 2004; Whittaker; Hamburger; Mahoney, 2003). The methodology assumes that structural performance can be predicted and evaluated with sufficient confidence to support decision-making based on expected losses. Unlike conventional prescriptive design methods, in which structural components are selected to satisfy generalized code provisions, PBE emphasizes the prediction and control of system behavior under specific hazard intensities. While prescriptive codes aim to ensure acceptable safety and functionality, their underlying performance expectations are often implicit or loosely defined, offering limited insight into how design choices affect actual reliability. By integrating nonlinear analysis, probabilistic modeling, and decision-oriented metrics—such as expected repair costs, casualties, and collapse probabilities—PBE enables a quantitative understanding of risk and supports informed, performance-based decision-making (Krawinkler, 1999; Ellingwood, 2001; Spence; Arunachalam, 2022).

When applied to seismic actions, the performance-based design approach is referred to as Performance-Based Earthquake Engineering (PBEE). PBEE quantifies the probability of different levels of loss associated with the range of earthquakes that may occur at a given site. The methodology is structured into four main stages: hazard analysis, structural analysis, damage analysis, and loss analysis—which will be detailed in the following chapters of this work (FEMA, 2018).

To further support decision-making that balances cost and performance, the PBEE framework can be extended to include optimization procedures aimed at improving structural design efficiency. Within this context, optimization under uncertainty offers significant advantages over traditional Deterministic Design Optimization (DDO). Deterministic approaches are typically formulated in terms of limit states and partial safety factors, accounting for uncertainties only in an indirect manner, and treating design constraints as indicators of structural failure. Such simplifications often lead to conservative designs and unnecessary increases in cost, as they provide limited insight into the expected performance of the structural system.

Reliability-Based Design Optimization (RBDO) emerged as an alternative approach to address safety and uncertainty quantification in structural design. It seeks to minimize an objective function, typically related to cost or material usage, subject to probabilistic constraints associated with each failure mode. However, from the perspective of achieving an optimum design, this approach presents certain limitations. It requires the specification of a target probability of failure for each failure mode, which can overly constrain the problem

and suppress the natural competition between different failure mechanisms (Beck, 2020). Also, despite the advantages of reliability-based design optimization over deterministic approaches, the literature indicates that the consequences of failure are often not explicitly considered in the analysis (Yi; Cheng; Jiang, 2008; Aoues; Chateauneuf, 2010; Valdebenito; Schuëller, 2010).

To incorporate the expected costs associated with failure into the objective function, Risk Optimization (RO) or Life-Cycle Cost Optimization (LCCO) can be employed (Beck; Gomes, 2012; Beck; Gomes; Bazán, 2012; Beck *et al.*, 2015; Beck, 2020). These formulations differ from traditional optimization methods by explicitly accounting for uncertainties in terms of both failure probability and associated costs, allowing a direct integration with the PBEE framework. In this context, the present work adopts the term Performance-Based Risk Optimization (PBRO) to refer to structural optimization conducted within the PBEE methods, in which structural damage and economic losses are evaluated according to their probability of occurrence.

The PBRO framework provides a natural extension of PBEE by identifying designs that minimize risk-related objectives—such as repair cost, downtime, or environmental impact—under prescribed seismic hazard conditions. However, the practical implementation of PBRO poses significant challenges, primarily due to the high computational cost of evaluating probabilistic performance metrics within the optimization loop. Each candidate design requires estimating the corresponding joint distribution of Engineering Demand Parameters (EDPs) through repeated Nonlinear Time History Analysis (NLTHA). The cost of these repeated evaluations can become prohibitive, especially for high-dimensional or complex structural systems (Spence; Kareem, 2014; Suksuwan; Spence, 2018; Suksuwan; Spence, 2019a; Joyner *et al.*, 2021; Subgranon; Spence, 2021; Rastegaran; Aval; Sangalaki, 2022; Movaghar *et al.*, 2025). To overcome these challenges, researchers have explored computationally efficient alternatives, including simplified nonlinear models (Basim; Estekanchi, 2015), artificial intelligence methods (Yazdani *et al.*, 2017), design of experiments (Möller *et al.*, 2015), and, in particular, metamodeling approaches (Gidaris; Taflanidis, 2015; Hassanzadeh; Moradi; Burton, 2024a).

Among the computational strategies proposed to reduce the cost of PBRO analyses, metamodels (or surrogate models) have shown significant promise due to their ability to emulate high-fidelity simulations at a fraction of the computational cost (Marelli; Sudret, 2018; Spence, 2018; Hao *et al.*, 2021; Miguel *et al.*, 2022; Miguel *et al.*, 2023; Miguel; Elias; Beck, 2024; Miguel; Beck, 2024; Giovanis; Taflanidis; Shields, 2025; Parisi; Nettis; Uva, 2025; Misra; Bocchini, 2025). Beyond computational efficiency, recent studies have expanded the application of metamodeling to seismic reliability and risk-optimization problems. Notable examples include the use of multi-fidelity cokriging for seismic reliability assessment and surrogate-based models for predicting structural seismic response (Skandalos; Chakraborty;

Tesfamariam, 2022; Zhong *et al.*, 2023; Samadian *et al.*, 2024). Within the Kriging family, recent research has focused on addressing noisy or statistically uncertain outputs, leading to the development of active-learning and stochastic (noisy) Kriging formulations for reliability analysis (Chun, 2024; Wan *et al.*, 2025; Pires *et al.*, 2025a).

Building upon these developments, recent research has introduced the concept of stochastic emulators within the PBE framework to approximate entire response distributions rather than single deterministic outcomes. These models extend the surrogate modeling paradigm by explicitly representing uncertainties, offering a more comprehensive characterization of the variability inherent in structural responses. Unlike deterministic metamodels, which predict mean or nominal responses, stochastic emulators aim to reproduce the probability distribution of structural demands for a given input, capturing the randomness introduced by factors such as ground motion variability, material heterogeneity, or modeling uncertainties. This capability is particularly valuable in the context of natural hazards, where structural performance is governed by highly uncertain, multidimensional inputs (Zhu; Broccardo; Sudret, 2023; Yi; Taflanidis, 2024; Yi; Taflanidis, 2025; Kim; Wang, 2025; Pires *et al.*, 2025b).

At the same time, optimization frameworks that explicitly propagate seismic hazard and structural response uncertainties through fragility and loss models have been developed under the general umbrella of PBRO, using probabilistic performance metrics such as expected repair costs, collapse probabilities, and downtime (Gidaris; Taflanidis, 2015; Shahnazaryan; O'Reilly, 2021; Suarez; Calvi; Gentile, 2024; Li; Guo; Kunnath, 2025). These developments represent an important step toward computationally tractable and risk-informed decision-making in structural design. However, across these approaches, the parameters used to train metamodels (e.g., EDP medians, dispersions, correlations, fragility parameters) are typically treated as exact. In practice, these quantities are often inferred from limited sets of ground motions and therefore carry finite-sample statistical uncertainty, which is rarely explicitly represented in the PBEE metamodeling frameworks. This limitation becomes even more pronounced in PBRO, where the joint EDP distribution evolves with the design. Each iteration of the optimization thus requires the estimation of a new joint EDP distribution corresponding to the current design, making the optimization landscape highly sensitive to uncertainty in these sample-based estimates. If this uncertainty is not properly addressed, it may bias convergence and lead to suboptimal designs when compared to those obtained under the true seismic variability.

Motivated by these challenges, this work proposes frameworks for PBRO aimed at identifying the optimum design of buildings subjected to seismic actions while explicitly accounting for the uncertainties inherent of the problem. The goal is to determine structural configurations that minimize expected repair costs and collapse probabilities under seismic loading within the PBEE framework, without incurring significant increases in construction

cost. To address the high computational demand associated with such probabilistic optimization, metamodeling techniques are incorporated to approximate the structural response efficiently and enable the practical implementation of the proposed framework.

1.2 Goals

The main objective of this research is to propose frameworks for RO within the PBEE approach, in order to identify the optimum design of buildings subjected to seismic actions while accounting for the inherent uncertainties of the problem. The specific objectives are as follows:

- To define and implement all four stages of the PBEE framework, including seismic hazard characterization, nonlinear finite element modeling of the structure, and subsequent damage and loss analyses associated with the considered hazard;
- To estimate structural construction and repair costs based on available databases and engineering references;
- To implement algorithms for the PBRO aimed at minimizing the total structural cost of a building subjected to seismic loads;
- To develop and apply metamodeling techniques to reduce the computational burden associated with evaluating the probability of structural failure within the PBEE framework embedded in the optimization loop;
- To incorporate the statistical uncertainties associated with the adopted metamodel framework, enhancing the robustness and efficiency of the proposed PBRO solution.

1.3 Outline

The remainder of this document is organized as follows:

Chapter 2 presents a literature review of the PBEE framework, addressing the different procedures proposed in existing guidelines and manuals.

Chapter 3 provides a literature review of optimization formulations applicable to the PBEE framework, along with algorithms for solving the associated problems and a discussion of their main challenges.

Chapter 4 introduces a literature review on deterministic and stochastic simulators, as well as techniques for system evaluation and emulation of responses. These approaches are referred to as metamodels for deterministic responses and emulators for stochastic responses.

Chapter 5 details the implementation of the adaptive Kriging metamodel for the computation of fragility functions. A Reinforced Concrete (RC) structural case study is analyzed, in which the seismic hazard is defined and real earthquake records are selected to perform a complete PBEE analysis. Results obtained using the original finite element model and the surrogate model are compared to verify the adequacy of the surrogate in representing the structural behavior. This chapter also presents the first structural optimization problem formulated under the PBRO framework, using the Firefly Algorithm and the adaptive Kriging surrogate for a three-story building.

Chapter 6 presents a noisy Kriging metamodeling framework developed to support PBRO within the FEMA P-58 (FEMA, 2018) methodology. The proposed approach explicitly incorporates statistical uncertainty arising from the limited number of ground motions used in training, allowing the metamodel to represent population-level behavior of structural responses. The framework is applied to a full-scale case study involving the optimization of buckling-restrained braces in a steel structure, formulated as a multi-objective problem balancing construction cost and seismic risk. Results demonstrate that the proposed method achieves performance estimates comparable to large-scale simulations, with substantial reductions in computational cost.

Chapter 7 introduces a framework that combines the Stratified Sampling (SS) technique with a Stochastic Polynomial Chaos Expansion (SPCE) to approximate the distribution of each component of the second-order random vector of Engineering Demand Parameters (EDPs) conditioned on non-collapse, without assuming a lognormal form for the data.

Finally, Chapter 8 summarizes the main conclusions of this research and provides recommendations for future developments.

2 STRUCTURAL SEISMIC PERFORMANCE

Performance-Based Earthquake Engineering (PBEE) gained traction in structural engineering during the 1990s as a response to the limitations of traditional prescriptive approaches. Historically, seismic design provisions have primarily relied on force-based procedures aimed at preventing collapse under a predefined "design earthquake" level. While effective in safeguarding life safety, these approaches provided little control over the actual performance of the structure in terms of damage, repair costs, downtime, or occupant safety in events of different intensities (Whittaker; Hamburger; Mahoney, 2003; Moehle; Deierlein, 2004).

A significant moment in this evolution was the 1994 Northridge earthquake, which resulted in substantial socioeconomic losses, despite the fact that the majority of the structures were built to contemporary code requirements. This event highlighted the need for methodologies capable of predicting and controlling performance across a range of seismic intensities, with explicit treatment of uncertainties from hazard to losses (Spence; Arunachalam, 2022; Hassanzadeh; Moradi; Burton, 2024a).

The "first generation" PBEE framework — such as ATC-40 (ATC, 1996), FEMA 350 (FEMA, 2000a), FEMA 356 (FEMA, 2000b), and ASCE/SEI 41 (ASCE, 2017a) — introduced discrete performance levels (operational, immediate occupancy, life safety, and collapse prevention) tied to Engineering Demand Parameters (EDPs) such as story drifts, plastic rotations, and floor accelerations. However, these early frameworks offered limited ability to integrate stakeholder-specific metrics such as repair cost, downtime, or casualty risk (Porter, 2003; Moehle; Deierlein, 2004).

Following these early efforts, the Federal Emergency Management Agency (FEMA), in collaboration with the Applied Technology Council (ATC) and the Pacific Earthquake Engineering Research Center (PEER), initiated a multi-phase research and development program to create a second-generation PBEE framework. This program aimed to incorporate fully probabilistic procedures, detailed fragility and consequence functions at the component level, and an explicit treatment of multiple sources of uncertainty. These coordinated efforts culminated in the publication of the FEMA P-58 ((FEMA, 2012)) methodology, which formalized a comprehensive framework for assessing the seismic performance of buildings (Spence; Arunachalam, 2022; Hassanzadeh; Moradi; Burton, 2024a).

The foundation of this procedure is the analytical framework developed by the PEER Center (Cornell; Krawinkler, 2000; Porter, 2003; Moehle; Deierlein, 2004; Yang *et al.*, 2009), which adopts a fully probabilistic approach. In this framework, the annual

rate of exceeding a given Decision Variable (DV) threshold is quantified by integrating conditional probability models across four main stages: hazard analysis, structural analysis, damage analysis, and loss analysis (Spence; Arunachalam, 2022). Fig. 2.1 presents the conceptual framework of PBEE, whose mathematical formulation can be expressed as:

$$\lambda\left(DV > dv\right) = \int_{im}\int_{dm}\int_{edp} G\left(dv|dm\right) dG\left(dm|edp\right) dG\left(edp|im\right) \left|d\lambda\left(im\right)\right| \tag{2.1}$$

where im is the seismic intensity measure; edp are the engineering demand parameters; dm is the damage measure; $\lambda(im)$ is the seismic hazard curve; and $G(x|y)$ denotes the conditional complementary Cumulative Distribution Function (CDF) of the random variable X given a particular outcome $Y = y$ of the random variable Y. The nested conditional distributions reflect the propagation of the uncertainty from seismic hazard to structural response, damage, and ultimately decision variables.

Figure 2.1 – Representation of PBEE framework.

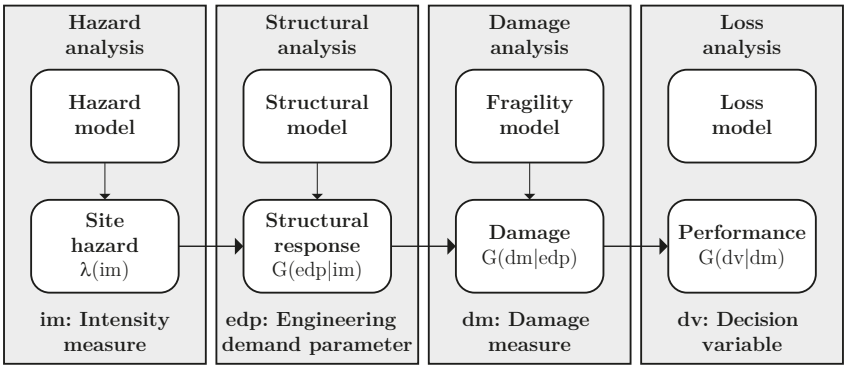

Source: Adapted from Cornell and Krawinkler (2000), Moehle and Deierlein (2004), Porter (2003), Yang *et al.* (2009).

The chapter proceeds along the PBEE stages—hazard characterization (Section 2.1), structural analysis and EDP estimation (Section 2.2), damage modeling (Section 2.3), and loss modeling with a repair cost DV (Section 2.4).

It is important to note that FEMA P-58 (2018) establishes a preliminary step concerning the assembly of the building performance model, defined as an organized collection of data that characterizes all building assets vulnerable to ground-motion effects. This dataset includes general building information, occupancy and population models, and descriptions of both structural and nonstructural components. The basic building information comprises the building dimensions, replacement cost and time, and data on embodied energy and carbon. Vulnerable structural and nonstructural components must be identified and described in sufficient detail to quantify their location within the building and the EDPs to which they are sensitive. Occupancy data define the spatial and temporal distribution of people within the building, including variability over time.

2.1 Hazard analysis

Earthquake hazards are characterized in terms of earthquake shaking, which has six components: three translational and three rotational (Beyer; Bommer, 2007). The rotational components are generally negligible, and the three translational components can be fully described by two orthogonal horizontal components and one vertical component. In most performance assessments, however, the vertical component is not a primary contributor to earthquake-induced damage and has limited influence on overall seismic performance. Therefore, only horizontal shaking is typically considered (FEMA, 2012).

The quantification of earthquake hazard involves describing the intensity of ground shaking and the probability that effects of a given intensity will occur at a site. This probabilistic representation is expressed through the hazard curve, which describes the mean annual frequency of exceedance (MAFE) of a seismic excitation represented by an Intensity Measure (IM). Formally, the hazard curve is defined by the function $\lambda(im)$, which denotes the MAFE with which the IM exceeds a specified level (Porter, 2003; Moehle; Deierlein, 2004). A representative hazard curve is shown in Fig. 2.2.

Figure 2.2 – Representation of a Hazard Curve.

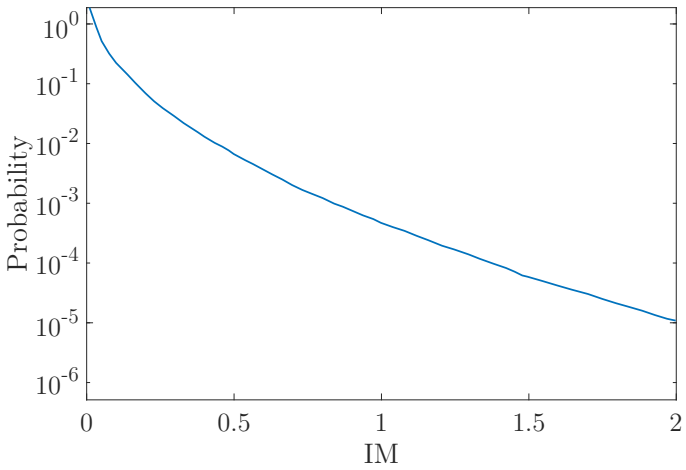

Source: Author.

In practice, the hazard curve is obtained through a Probabilistic Seismic Hazard Analysis (PSHA). While PSHA results can also be expressed in terms of the probability of exceedance over a specified time interval, the MAFE representation is more fundamental. Under the common assumption that earthquake occurrences follow a Poisson process, the probability of exceedance over a given period can be derived from $\lambda(im)$, and for sufficiently small values of $\lambda(im)$, the probability of exceedance is approximately equal to the MAFE. The main steps of a PSHA are: identification of earthquake sources; characterization of magnitude distributions and occurrence rates for each source; estimation of ground motion

at the site; and probabilistic integration of these components (McGuire, 2004).

IMs represent quantitative characteristics of ground motions that can be expressed as scalar values and are correlated with structural response parameters (McGuire, 2004; Andrade, 2021). Common examples include Peak Ground Acceleration (PGA), Peak Ground Velocity (PGV), spectral acceleration at a given vibration period ($S_a(T)$), and spectral acceleration with 5% damping ($\xi = 5\%$) corresponding to the first-mode vibration period of the structure ($S_a(T_1)$), among others. The hazard curve is parameterized by the selected IM, which may exhibit varying effectiveness in capturing the relationship between seismic intensity and structural consequences. Therefore, selecting an appropriate IM constitutes a critical step in the development of the methodology.

Two key concepts are associated with the choice of an IM: efficiency and sufficiency. Efficiency refers to an IM that yields low variability in structural demand, thereby reducing the number of Nonlinear Time History Analysis (NLTHA) and the number of ground-motion records required to estimate seismic demand. Sufficiency characterizes an IM that leads to a structural demand independent of earthquake magnitude and source-to-site distance. Sufficiency is desirable because it enables a more accurate estimation of the demand distribution without requiring detailed information about specific earthquake scenarios (Luco; Cornell, 2007; Padgett; Nielson; DesRoches, 2008).

The relationship between the expected value of an IM and the earthquake parameters—magnitude (M), distance to the epicenter (R), and site conditions—is described by attenuation relationships, also known as Ground-Motion Prediction Equation (GMPE) or Ground Motion Model (GMM). Combined with information on earthquake occurrence rates, GMPE form the foundation of seismic hazard analysis. Although these three variables are commonly used when discussing IM sufficiency, sufficiency can, in principle, be assessed with respect to any earthquake parameter (e.g., duration, fault orientation).

Specifically for Brazil, few studies have addressed seismic hazard, and most are concentrated in specific regions. Almeida *et al.* (2019) conducted a PSHA for Angra dos Reis, in the state of Rio de Janeiro, where Brazil's only nuclear power plant is located. Borges *et al.* (2020) carried out a probabilistic seismic hazard assessment for the offshore areas of the southern and southeastern regions of the country. Nóbrega, Souza and Nóbrega (2021) performed a PSHA focusing on the state of Rio Grande do Norte, in the Northeastern (NE) region of Brazil. More recently, Fonsêca, Nascimento and Lasocki (2025) and Pereira (2025) conducted PSHA for the NE region, with the latter addressing significant gaps in the treatment of epistemic uncertainties.

The main studies addressing seismic hazard for the entire Brazilian territory include: the Global Seismic Hazard Assessment Program (GSHAP) (Shedlock; Tanner, 1999); the Probabilistic Seismic Hazard Analysis for Brazil (PSHAB) Pirchiner *et al.* (2015), Assumpção *et al.* (2016); the study conducted by the United States Geological

Survey (USGS) (Petersen *et al.*, 2018); the study by Alves (2020), which also resulted in the publication by Alves and Santos (2021); and the Global Earthquake Model (GEM) (Pagani *et al.*, 2020), an international initiative for global earthquake risk assessment that was updated for South America in 2023 (Johnson *et al.*, 2023).

The GSHAP was an international program aimed at developing a global seismic hazard map. Among the several research groups that worked on specific regions, Shedlock and Tanner (1999) produced the hazard map for South America. This study was later used as the basis for the seismic hazard map adopted in the Brazilian standard ABNT NBR 15421 (ASSOCIAÇÃO BRASILEIRA DE NORMAS TÉCNICAS, 2006), corresponding to a return period of 475 years. Pirchiner *et al.* (2015) and Assumpção *et al.* (2016) subsequently published a preliminary version of the PSHAB study, presenting new hazard maps for the Brazilian territory with return periods of 475 and 2475 years. In 2018, the USGS completed and published the study by Petersen *et al.* (2018), which provided hazard maps for South America considering return periods of 72, 475, and 2475 years, and for PGA and $S_a(T)$ at both short and long periods. The most recent study for Brazil was conducted by Alves (2020) and supported the revised version of the Brazilian standard ABNT NBR 15421 (ASSOCIAÇÃO BRASILEIRA DE NORMAS TÉCNICAS, 2023).

Hazard analysis also involves the characterization of a suitable set of ground motion records for NLTHA (Porter, 2003). An essential step in this process is the selection of earthquake time histories used in nonlinear dynamic analyses, ensuring that the chosen records correspond to a specific level of seismic hazard—a concept known as hazard consistency (Miano *et al.*, 2018). Bommer, Scott and Sarma (2000) recommend three main approaches: (i) selecting and scaling records from real events; (ii) generating artificial ground motions compatible with the target design spectrum; or (iii) generating synthetic ground motions based on earthquake source models. Recent studies highlight that there is still no consensus within the engineering community regarding which type of ground motion should be used in time-history analyses (Manzo; Vassiliou, 2019). Nevertheless, regardless of the selected approach, the ground motions must be hazard-consistent with the site and representative of the expected seismic events (Baker, 2011).

Two main procedures for selecting hazard-consistent ground motions are described in Bommer and Acevedo (2004): (i) selection based directly on the results of the PSHA, or (ii) selection based on the elastic response spectra defined by design standards. Hazard consistency derived directly from PSHA can be established through seismic hazard disaggregation, which identifies the relative contribution of each earthquake scenario as a function of magnitude (M), distance (R), and IM, as well as in terms of epsilon, defined as the number of standard deviations by which a ground motion deviates from the mean prediction of the GMPE in logarithmic space (Bazzurro; Cornell, 1999). Based on this information, a hazard-consistent set of ground motions must represent the distributions of

these parameters corresponding to each intensity level of interest (Andrade, 2021).

An approach that incorporates the results of hazard disaggregation and GMPE into the selection of ground motion records is the Conditional Mean Spectrum (CMS) (Baker; Cornell, 2005; Baker; Cornell, 2006; Baker, 2011). The CMS represents a response spectrum conditioned on the occurrence of a target spectral acceleration value at a period of interest, such that the selected ground motions have mean and standard deviation close to those of the conditional spectrum. Although it provides a rational basis for ground motion selection, the information required to construct the CMS is often difficult to obtain, even in regions with extensive seismic hazard studies (Ay; Fox; Sullivan, 2017; Andrade, 2021). In the Brazilian context, disaggregation studies are scarce and typically restricted to specific locations, such as Petersen *et al.* (2018), which provides data only for the city of Natal, in the state of Rio Grande do Norte, limited to PGA and a single return period. More recently, Pereira (2025) generated disaggregation results for selected cities in the Northeast region of Brazil.

The methodologies discussed above provide the foundation for defining seismic hazard levels and selecting ground motions consistent with the target IMs. The next section presents the formal approach adopted in FEMA P-58 (2018) to define earthquake hazard according to the selected type of performance assessment.

2.1.1 Defining Earthquake Hazards

Within the FEMA P-58 (2018) framework, earthquake hazard can be represented in three complementary forms, depending on the type of performance assessment: (i) intensity-based assessments, which use a user-defined, 5%-damped horizontal acceleration response spectrum (e.g., a code design spectrum) (Rodrigues; Spence; Beck, 2026); (ii) scenario-based assessments, which use spectra derived for specific magnitude–distance pairsand/or other relevant scenario characteristics from appropriate GMPEs (Baird; Liel; Chase, 2020; Silva *et al.*, 2021); and (iii) time-based assessments, which use site-specific seismic hazard curves and spectra derived at selected annual frequencies of exceedance (Pereira *et al.*, 2024).

In intensity-based assessments, any spectrum consistent with the geologic characteristics of the site can be used as the target spectrum (e.g., a code design spectrum, a Uniform Hazard Spectrum (UHS), or a CMS).

In scenario-based assessments, analysts specify the earthquake magnitude and source-to-site distance for the scenario and then use a region and site appropriate GMPE to compute median spectral accelerations as the seismic input. If the GMPE's reference site condition differs from the project site, the spectra must be adjusted to reflect local site conditions. In contrast to intensity-based analyses, the target spectral shape for a

scenario should come directly from the selected GMPE for the chosen $[M, R]$ pair.

Time-based assessments employ a seismic hazard curve for $S_a(T)$ at the site and discretize the intensity range to integrate performance across all likely shaking levels within the period of interest. The recommended workflow is: (1) develop the $S_a(T)$ hazard curve; (2) determine $S_{a,\min}$ and $S_{a,\max}$; (3) split $[S_{a,\min}, S_{a,\max}]$ into n_{inter} intervals (with $n_{\text{inter}} \approx 8$ recommended); (4) compute, for each interval, the mean annual probability of occurrence as the difference between exceedance rates at the interval endpoints; and (5) for each interval, develop a target spectrum at the midpoint exceedance rate and extract $S_a(T_1)$ along each principal direction. The exceedance probabilities over a fixed time window T are obtained from a Poisson occurrence model combined with the hazard curve.

When a UHS at a specified annual frequency of exceedance is adopted as the target, the suite of ground motions should be selected and scaled to ensure consistency with that spectrum. FEMA P-58 (2018) outlines the general procedure for developing an appropriate target spectrum, selecting a representative set of recorded motions, and scaling them to match the target. These procedures are applicable to intensity-based, scenario-based, and time-based assessments. The following section describes the procedure established in the American standard ASCE 7-16 (ASCE, 2017b) for generating a code design spectrum, which can also be used as a target spectrum.

2.1.1.1 Design Response Spectrum

The design response spectrum presented in this section is based on the American standard ASCE 7-16 (ASCE, 2017b), using soil parameters representative of the region considered in this study. The adoption of the ASCE 7-16 design spectrum is justified by its broad international acceptance and frequent use as a reference in performance-based seismic assessments. Fig. 2.3 illustrates the shape of the spectrum.

Figure 2.3 – Shape of the Design Response Spectrum.

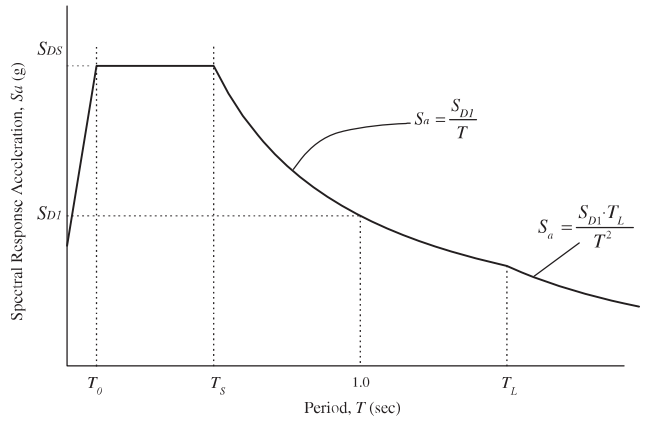

Source: ASCE (2017b).

The equation defining the design response spectrum is divided into four period ranges, determined by parameters specified for each soil type. The parameters S_{D1} and S_{DS} are computed as follows:

$$S_{D1} = \frac{2}{3} S_{M1} = \frac{2}{3} F_a S_s, \quad S_{DS} = \frac{2}{3} S_{MS} = \frac{2}{3} F_v S_1 \tag{2.2}$$

where S_s and S_1 correspond to the mapped spectral accelerations for short (0.2 seconds) and long (1.0 second) periods, respectively, and F_a and F_v are the site coefficients for short and long periods, defined in ASCE 7-16 (ASCE, 2017b) for each soil type. Some values for soils E and F are not provided, since ASCE (2017b) requires more detailed analyses for their determination. The resulting parameters represent the design spectral accelerations for short periods (S_{DS}) and long periods (S_{D1}).

Periods indicated in Fig. 2.3 as T_0 and T_S are calculated as $T_0 = 0.2\,(S_{D1}/S_{DS})$ and $T_S = S_{D1}/S_{DS}$, where T_L corresponds to the transition period for long-period behavior. For each interval represented in Fig. 2.3, the spectral acceleration is calculated as:

$$S_a(T) = \begin{cases} S_{DS}\left(0.4 + 0.6\frac{T}{T_0}\right), & 0 \leq T \leq T_0 \\ S_{DS}, & T_0 < T \leq T_S \\ \dfrac{S_{D1}}{T}, & T_S < T \leq T_L \\ \dfrac{S_{D1} T_L}{T^2}, & T \geq T_L \end{cases} \tag{2.3}$$

2.2 Structural analysis

Structural analysis is employed to evaluate building response to horizontal ground shaking and to estimate median values and dispersions of key EDPs that are predictive of structural and nonstructural damage, such as peak story drift ratios, peak floor accelerations, peak floor velocities, and residual story drift ratios. FEMA P-58 (2018) specifies two alternative procedures for predicting peak response values and their dispersion: nonlinear response-history analysis (referred to herein as NLTHA) and a simplified linear-static procedure.

The main idea of the NLTHA is to generate a suite of initial demand vectors of EDPs (one per record), which are assembled into a matrix whose entries are treated as a joint lognormal distribution to obtain median values, dispersions, and an EDP correlation matrix. The diagonal dispersions can also be augmented to account for modeling uncertainty and, in scenario-based assessments, for ground-motion attenuation uncertainty. The simplified procedure, on the other hand, employs linear models, static analyses, and an estimate of lateral yield strength to compute median values of the EDPs, assuming uncoupled response

and regularity constraints. In this case, a higher level of uncertainty is expected when compared with the results obtained from NLTHA.

This work adopts NLTHA to obtain the structural responses to the ground motions, and the following sections provide details of the structural modeling required to perform the analyses.

2.2.1 Structural modeling

A numerical model of the structure must be developed and evaluated through NLTHA to assess damage. This work employs Finite Element (FE) models implemented in *OpenSees* (McKenna; Fenves; Scott, 2006) to perform the analyses. The software is specifically developed for seismic structural analysis and provides an extensive library of elements and material models (Mazzoni *et al.*, 2006). One of its main advantages is the reduced computational time compared to other finite element platforms, which is particularly relevant for probabilistic analyses. An interaction between OpenSees and MATLAB (MATHWORKS, 2015) was established by Rodrigues (2021) and further enhanced in this work to automate the pre- and post-processing stages of the analyses. Fig. 2.4 illustrates the operation of the routine developed in this study.

FEMA P-58 (2018) recommends that building models should be developed as three-dimensional assemblies, explicitly incorporating all structural framing and any nonstructural components that provide measurable strength or stiffness, such as gravity-load systems, cladding, and partitions, as these elements can modify vibration periods and substantially influence loss estimates. Component models should capture nonlinear force–deformation behavior, including strengthening and stiffness degradation whenever relevant. The hysteretic response is expected to represent the primary mechanism of energy dissipation, while the equivalent viscous damping assigned to the analytical model is typically limited to 1% to 5% of critical damping (and not more than 3% for tall buildings).

For structural assessment, nonlinear models must be capable of simulating the progressive accumulation of damage and potential collapse under severe ground motions, identifying the key deterioration and collapse mechanisms (FEMA, 2009). They should also accurately capture structural behavior under both low-intensity, frequent earthquakes and rare, high-intensity events (Haselton; Deierlein, 2008). Two main approaches are commonly used to represent material behavior in nonlinear finite element analyses: distributed plasticity, typically modeled through fiber elements, and concentrated (or lumped) plasticity models (Bruschi; Calvi; Quaglini, 2021).

Figure 2.4 – Integration between OpenSees and MATLAB.

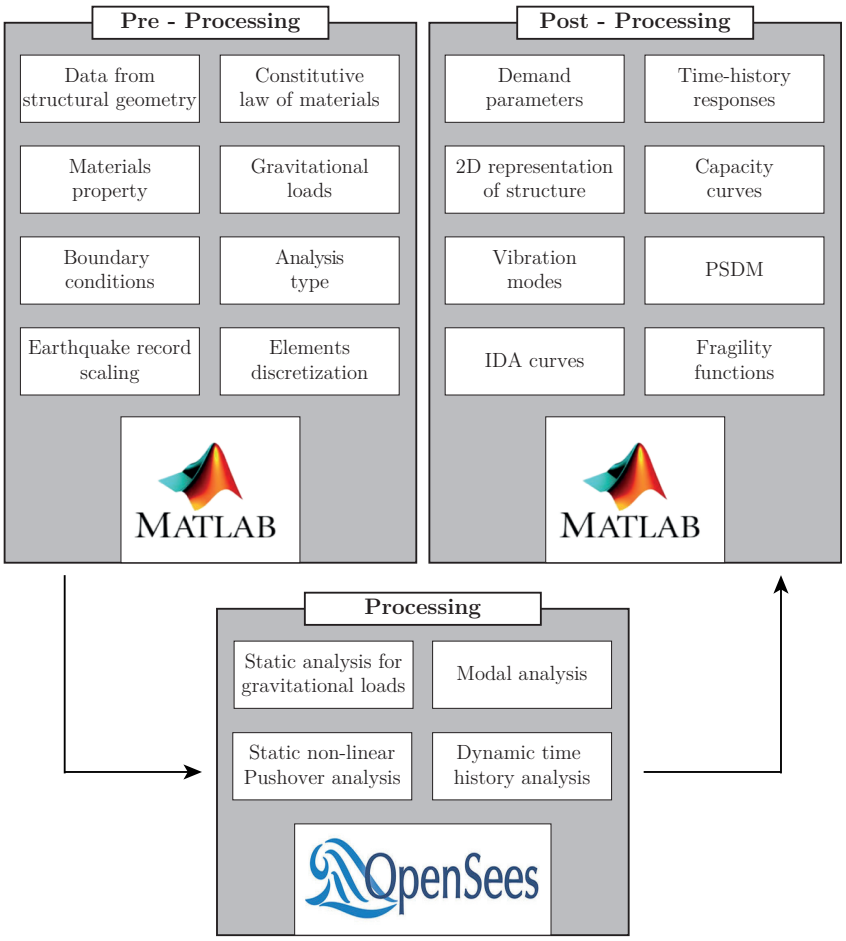

Source: Author (Rodrigues, 2021).

Fiber models have been widely employed to represent steel and Reinforced Concrete (RC) structures within the Performance-Based Engineering (PBE) framework (Cavalcante *et al.*, 2022; Arunachalam; Spence, 2022; Li; Spence, 2022; Li; Spence, 2024; Xu; Spence, 2024; Wakjira; Alam, 2024; Pereira *et al.*, 2024). For RC structures, they are capable of capturing cracking behavior and the spread of plasticity along the element length by discretizing the cross-section into fibers that account for confined and unconfined concrete, as well as different configurations of longitudinal reinforcement steel. However, an inherent limitation of their formulation is the difficulty in simulating the strain softening associated with rebar buckling (FEMA, 2009).

Lumped Plasticity Models (LPM) are also frequently adopted in structural analysis (Goulet *et al.*, 2007; Opabola; Elwood; Liel, 2021; Murray; Liel; Elwood, 2022; Andrade *et al.*, 2022) due to their simpler implementation (Wu; Pantelides, 2018). When properly calibrated, these models can capture the strength and stiffness degradation essential for collapse simulation. In addition, their parameters can be easily modified in sensitivity analyses to evaluate uncertainties in material properties. In such cases, the uncertain

parameters are commonly modeled as random variables with prescribed probability distributions, and their effects are assessed through repeated nonlinear analyses using sampled realizations of these distributions.

Salehi, Sideris and Liel (2020) emphasize that all damage mechanisms (concrete and steel degradation, bar buckling, and bar slipping) in concentrated plasticity elements are aggregated within the constitutive laws of zero-length springs. Consequently, these models cannot represent the spread of damage along the member length, since inelastic response is confined to predefined locations. Distributed plasticity models, on the other hand, require only the constitutive laws of the materials but demand a considerably higher computational cost, especially when force-based elements or fine member discretizations are employed. This increase is associated not only with internal element-level solution procedures, but also with the higher number of global structure-level iterations, i.e., iterative equilibrium solutions at the system level required to achieve convergence of the nonlinear structural response, due to the larger number of degrees of freedom.

Since both modeling strategies have advantages and limitations, the selection of an appropriate approach must consider the available modeling capabilities and be carefully evaluated for each structural system, as no single model is universally applicable (FEMA, 2009). A comparison between LPM and Fiber models was conducted by Rodrigues *et al.* (2023), whose results indicate that both approaches can adequately capture the maximum shear forces and collapse modes of the structure, with no conclusive evidence favoring one over the other. More recent studies have also explored the Lumped Damage Model (LDM), which combines fracture mechanics principles and classical damage theory with plastic hinges to assess collapse mechanisms and develop fragility curves for RC frames (Bosse *et al.*, 2024a) and steel structures (Bosse *et al.*, 2024b) subjected to earthquakes. Bosse *et al.* (2024a) compared the LDM with the fiber models available in OpenSees and with the Concrete Damage Plasticity (CDP) model implemented in Abaqus, reporting a strong agreement in top displacements and base shear forces among the three formulations. Consequently, the choice of model should depend on the primary objectives of the study.

In the following chapters, examples are presented using LPM for steel and RC structures, and Fiber models for steel structures.

2.3 Damage analysis

The third step of the PBEE framework corresponds to the development of a damage analysis that relates the EDPs to the Damage Measures (DM), which describe the physical damage to a structure (Moehle; Deierlein, 2004). The main objective is to characterize how structural and nonstructural components respond to seismic actions and to quantify the probability of different levels of physical damage, conditioned on the selected design

and the structural response. This objective is achieved through the calculation of fragility functions, which represent mathematical relationships modeling the conditional probability that a structure or structural component will exceed a specific Damage Limit State (DLS) as a function of an IM (Porter, 2019). Fig. 2.5 illustrates fragility functions for two Damage Limit States, and the expression based on conditional probability is presented as:

Figure 2.5 – Representation of fragility functions for different Damage Limit States.

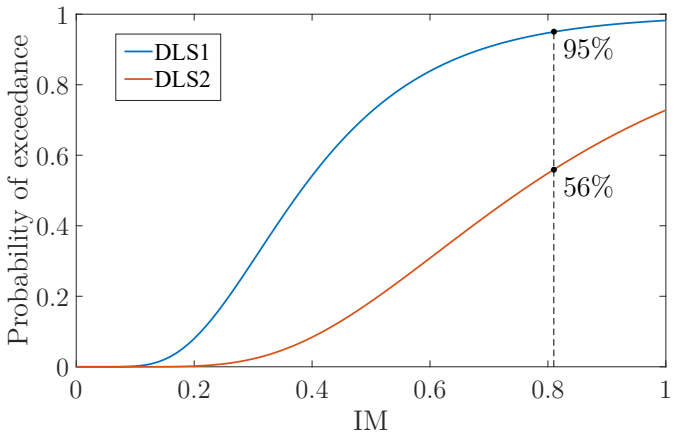

Source: Author.

$$Fragility\,(x) = P\,[LS|IM = x] \tag{2.4}$$

where LS denotes the Damage Limit State; IM is the intensity measure adopted to represent the earthquake excitation; and x represents a specific realization of the selected IM.

The concept of the fragility function dates back to Kennedy *et al.* (1980), who defined a fragility function for a component of a nuclear power plant considering peak ground acceleration as the intensity measure of an earthquake. In general, there are three main approaches to determine a fragility function: empirical, analytical, and expert judgment (Porter, 2019). Fragility functions developed through expert judgment rely on the experience of one or more specialists in the field but have inherent limitations due to subjectivity (Padgett, 2007). Empirical fragility functions, in turn, are derived from the statistical distribution of observed damage obtained from post-earthquake damage surveys or experimental data. This represents the most realistic type of assessment, as it directly incorporates the cumulative effects experienced by the structure during actual events (Elnashai; Sarno, 2008).

Analytical fragility functions are derived from representative numerical models of the structural system evaluated under seismic actions (Porter, 2019). Compared to those

developed through expert judgment, analytical functions generally provide results with higher confidence. However, their main limitation lies in the significant computational effort required for their estimation, and the numerical models often cannot capture all components and details of the actual structure, which can be a disadvantage when compared to empirical approaches (Elnashai; Sarno, 2008).

When developing analytical fragility functions for complex nonlinear systems through dynamic analysis, the structural model must be subjected to a set of ground motion records in order to evaluate the relationship between the EDPs and the IM. Among the procedures available in the literature, the Cloud Analysis, the Multiple-Stripe Analysis (MSA), and the Incremental Dynamic Analysis (IDA) are the most commonly used approaches (Miano *et al.*, 2018).

Cloud Analysis is the most straightforward approach to establish the relationship between EDPs and IMs. It relies on nonlinear analyses performed with unscaled ground motion records (Cornell *et al.*, 2002; Jalayer *et al.*, 2017). This method has recently been applied to evaluate the seismic risk, loss, and resilience of reinforced concrete buildings in Istanbul (Zhang *et al.*,); to perform seismic reliability assessments of non-seismic reinforced concrete structures designed according to ABNT NBR 6118:2014 in Brazil (Pereira *et al.*, 2021; Pereira *et al.*, 2024); and to develop methodologies for deriving fragility curves based on multi-fidelity nonlinear models (Sevieri; Gentile; Galasso, 2021).

An important aspect of the Cloud Analysis is the selection of ground motion records. Jalayer *et al.* (2017) highlighted several points to consider during this process: (i) the selected records should cover a wide range of spectral accelerations to reduce the standard error in subsequent regression analyses; (ii) a significant portion of the records should cause the EDP to exceed the considered Damage Limit State, thereby minimizing extrapolation during regression; (iii) when evaluating a two-dimensional structural model, both horizontal components of the same record should not be selected; and (iv) no more than 10% of the total number of records should originate from the same seismic event.

The MSA refers to a structural analysis performed with groups of ground motion records scaled to a common spectral acceleration level (Jalayer; Cornell, 2009). Each suite of ground motions used in a stripe should be representative of the seismic hazard corresponding to the spectral acceleration of interest. For this reason, MSA is often combined with the conditional spectrum approach to select records that are consistent with a specific site and IM level (Baker, 2015). According to Bradley (2013), MSA offers an advantage over IDA because scaling a single ground motion across a wide range of IM values does not account for the fact that ground-motion characteristics vary with IM. Consequently, IDA may produce an ensemble of ground motions that is not fully consistent with the seismic hazard associated with a given IM level.

The IDA, developed by Vamvatsikos and Cornell (2002) and later applied by

Vamvatsikos and Cornell (2004), is one of the most widely used procedures for nonlinear dynamic analysis. It consists of progressively scaling a ground motion record to evaluate the structural response under increasing intensity levels, until the IM associated with structural collapse is reached. In this method, each record is multiplied by a nonnegative scalar factor to uniformly increase or decrease its amplitude, and the corresponding nonlinear analyses produce curves of structural response versus IM. These parameterized curves allow a detailed assessment of the evolution of structural performance with increasing seismic demand. Fig. 2.6 illustrates the representation of a scaled ground-motion record.

Figure 2.6 – Scaling of a ground motion record.

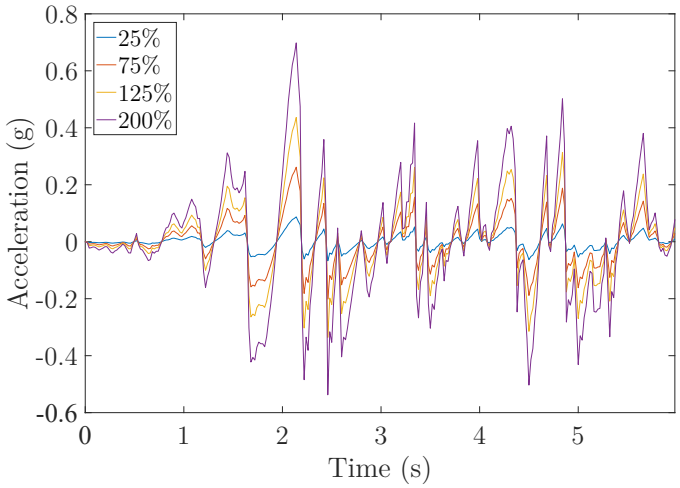

Source: Author.

The main objectives of the IDA include: (i) evaluating the variation of structural response across multiple intensity levels of a given ground motion; (ii) improving the understanding of structural behavior under increasingly severe seismic demands; and (iii) assessing the stability of structural response across different ground motion records. According to Vamvatsikos and Cornell (2004), a suite of approximately 10 to 20 ground motion records is typically sufficient to achieve accurate estimates of seismic demand.

The results of an IDA are typically expressed as a plot of the EDP versus the IM. The shape of the resulting curves depends on the structural characteristics and on the set of ground motion records used in the analysis. Four general behavioral patterns can be observed: softening, hardening, severe hardening, and weaving. Two distinctive features often identified in these curves are dynamic instability and structural resurrection. Dynamic instability is characterized by a nearly horizontal branch of the curve, indicating that the structure accumulates significant additional damage for small increments in IM. Structural resurrection refers to an apparent re-stiffening at large displacements, which may occur after dynamic instability and can indicate nonlinear numerical effects or transient stabilization of the response (Vamvatsikos; Cornell, 2002).

While the IDA provides a detailed representation of structural response, it also presents some limitations. The primary drawback is its high computational cost, since NLTHA must be repeatedly performed for each scaled ground motion record (Miano *et al.*, 2018). In addition, excessive scaling of ground motions may introduce bias in the estimation of fragility curves derived from IDA results (Luco; Bazzurro, 2007).

Recent studies demonstrate the continued use of IDA to assess the seismic vulnerability of reinforced concrete buildings with column discontinuities (Gwalani; Singh; Varum, 2023), to evaluate the seismic safety of informally built reinforced concrete houses in Puerto Rico (Murray *et al.*, 2023), to investigate the seismic fragility of steel frames equipped with dissipative devices (Giuliani *et al.*, 2022), to estimate seismic losses for wooden houses located in Canada (Goda; Zhang; Tesfamariam, 2021), and to evaluate the seismic fragility of nonstructural components in unreinforced clay brick masonry buildings (Derakhshan *et al.*, 2020).

In the developments carried out in this work, the IDA is employed to generate fragility functions for different structural Damage Limit States. It is common practice among researchers to assume a lognormal distribution for fragility functions, as well as for structural demand and capacity (Cornell *et al.*, 2002), and this assumption is adopted throughout the present study. Two main frameworks are considered for the derivation of fragility functions: (i) the methodology described in FEMA P-58 (2018), which defines collapse fragility based on IDA and provides procedures for developing fragility functions for individual structural and nonstructural components; and (ii) the closed-form solution proposed by Padgett (2007), which combines a probabilistic seismic demand model with the qualitative and quantitative Damage Limit States defined in the Hazus (FEMA, 2022a) manual to represent structural and nonstructural capacities.

2.3.1 Fragility Development from FEMA P-58 (2018)

The FEMA P-58 (2018) guidelines describe two procedures that can be employed to define the collapse fragility relationship: the IDA and the performance of a limited suite of NLTHA at selected intensity levels that lead to collapse predictions. As previously stated, this work adopts the IDA procedure to determine the collapse fragility function, from which the distribution parameters are statistically inferred. The collapse fragility function is expressed as (Baker, 2015):

$$P\left[C_{\text{oll}} \mid IM = x\right] = \Phi\left[\frac{\ln\left(x/\hat{\mu}_{\text{coll}}\right)}{\hat{\sigma}_{\text{coll}}}\right] \tag{2.5}$$

where $P\left[C_{\text{oll}} \mid IM = x\right]$ denotes the probability that a ground motion with intensity $IM = x$ will cause structural collapse; Φ is the standard normal CDF; $\hat{\mu}_{\text{coll}}$ is the median

value of the fragility function, corresponding to the IM level associated with a 50% probability of collapse; and $\hat{\sigma}_{\text{coll}}$ is the logarithmic standard deviation of IM.

The FEMA P-58 (2018) guidelines establish procedures for selecting ground-motion records consistent with a target spectrum, recommending the use of at least $N_e \geq 11$ record pairs. The NLTHA should be repeated with incremental increases in ground-motion intensity until structural collapse is reached, thereby identifying the IM level at which approximately 50% of the record pairs lead to collapse. The parameters of the collapse fragility function can then be statistically inferred as (Baker, 2015):

$$\ln \hat{\mu}_{\text{coll}} = \frac{1}{N_e} \sum_{i=1}^{N_{rec}} \ln(IM_i), \quad \hat{\sigma}_{\text{coll}} = \sqrt{\frac{1}{N_e - 1} \sum_{i=1}^{N_{rec}} \left(\frac{\ln(IM_i)}{\hat{\mu}_{\text{coll}}} \right)^2} \tag{2.6}$$

where IM_i denotes the IM associated with collapse for the i-th ground-motion record.

Within this framework, structural collapse is defined as the occurrence of any of the following: lateral sidesway instability, including P-Δ effects; loss of vertical load-carrying capacity in gravity or lateral-force-resisting elements due to excessive earthquake-induced drifts; or exceedance of non-simulated failure criteria, that is, deformation or strength limits beyond which components can no longer reliably carry load. In practice, collapse in analytical models is often indicated by numerical instability or by drifts so large that the model response is no longer physically meaningful.

The FEMA P-58 (2018) framework specifies fragility relationships determined at the component level. These component fragilities are defined as lognormal functions that describe the conditional probability of reaching or exceeding each damage state as a function of a component-specific demand parameter. Components are organized into fragility groups, with subcategories that capture differences in vulnerability (e.g., ductile detailing, bracing, or anchorage) and in repair consequences. Complete specifications—including damage states, fragilities, and associated consequences—are presented in Appendix D and implemented in the PACT Fragility Database (ATC, 2018). Appendix H of FEMA P-58 (2018) provides quantitative procedures for deriving median values and logarithmic standard deviations under different data conditions, ranging from measured demand data to expert judgment. It also details the required documentation and quality-control steps (such as goodness-of-fit tests) and includes equations for computing fragilities corresponding to strength-, ductility-, displacement-, and code-based limit states.

2.3.2 Closed-Form Solution for Different Limit States

Under the lognormal assumption, a closed-form expression for the fragility function considering the structural demand and capacity for the considered Limit States is introduced by Padgett (2007):

$$P\left[D \geq C \mid IM\right] = \Phi\left[\frac{\ln\left(S_D/S_C\right)}{\sqrt{\beta_D^2 + \beta_C^2}}\right] \tag{2.7}$$

where Φ denotes the cumulative standard normal distribution; S_C and β_C are the median value and the logarithmic standard deviation of structural capacity; and S_D and β_D are the median value and the logarithmic standard deviation of structural seismic demand.

An additional β_m can be incorporated in Eq. 2.7 to model uncertainty. The evaluation of structural demand and capacity is presented and discussed in the following sections.

2.3.2.1 Structural Demand

To evaluate the structural demand required in Eq. 2.7, the Probabilistic Seismic Demand Model (PSDM) can be employed to establish the relationship between the IM and the structural response. This approach is commonly adopted to represent seismic demand in fragility and risk analyses (Padgett, 2007). As proposed by Cornell *et al.* (2002), the median seismic demand can be estimated as:

$$S_D = a\left(IM\right)^b \tag{2.8}$$

where S_D represents the median value of the seismic demand, and a and b are regression coefficients to be determined.

As previously mentioned, seismic demands are typically assumed to follow a lognormal distribution about their median value (Cornell *et al.*, 2002). Accordingly, transforming Eq. 2.8 into logarithmic space simplifies the estimation of the parameters a and b, which can then be obtained through linear regression:

$$\ln\left(S_D\right) = \ln\left(a\right) + b\ln\left(IM\right) \tag{2.9}$$

The most direct way to estimate the parameters a and b is to perform NLTHA prior to regression, although IDA can also be employed for this purpose. The transformation to logarithmic space favors satisfaction of two key assumptions: (i) the model standard deviation is independent of the adopted IM (i.e., variance homoscedasticity); and (ii) the residuals are normally distributed about the mean. The assumption of a lognormal distribution for the seismic demand reinforces the latter, ensuring that the natural logarithms of the demand values follow a normal distribution (Ramamoorthy; Gardoni; Bracci, 2006; Luco; Cornell, 2007; Nowak; Collins, 2012). A representation of the PSDM in logarithmic space is shown in Fig. 2.7.

Figure 2.7 – Representation of PSDM in lognormal space.

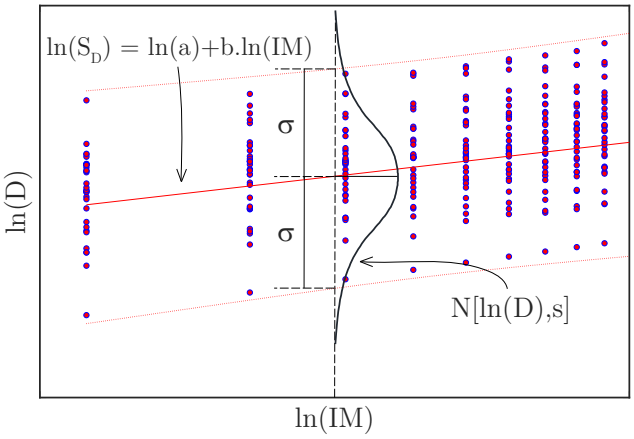

Source: Author (Rodrigues, 2021).

The dispersion of the demand model (β_D) is directly obtained from the linear regression and is equivalent to the root-mean-square error (RMSE) or residual standard deviation of the model (Siqueira *et al.*, 2014), as expressed by:

$$\beta_D \simeq \sqrt{\frac{\sum \left(\ln\left(d_i\right) - \ln\left(a \times IM^b\right)\right)^2}{N-2}} \tag{2.10}$$

where N is the number of simulations, and d_i is the peak demand of the component of interest.

Using the parameters a and b obtained from the PSDM analysis, the fragility function presented in Eq. 2.7 can be reformulated as:

$$P\left[D \geq C \mid IM\right] = P\left[LS \mid IM\right] = \Phi\left[\frac{\ln\left(IM\right) - \theta}{\beta}\right] \tag{2.11}$$

The median value (θ) and the logarithmic standard deviation (β) of the fragility function for each Damage Limit State are then calculated as:

$$\theta = \frac{\ln\left(S_C\right) - \ln\left(a\right)}{b}, \quad \beta = \frac{\sqrt{\beta_D^2 + \beta_C^2}}{b} \tag{2.12}$$

2.3.2.2 Structural Capacity

Structural capacity is defined as the maximum level of demand that a structure can sustain without exceeding a specified limit state (Wen; Ellingwood; Bracci, 2004). Damage Limit States (DLS) are established based on the performance objectives defined for structures subjected to seismic actions. In this context, structural performance is described in terms of the maximum acceptable damage states corresponding to a given seismic hazard

level (ASCE, 2017a). Performance levels are defined for both structural and nonstructural systems; however, this work focuses exclusively on the structural components.

Damage Limit States are qualitatively described in the literature for different building types, such as reinforced concrete, steel, and masonry structures. The classification criteria and performance levels follow the definitions provided in the Hazus (FEMA, 2022a) manual developed by FEMA and the performance objectives established by ASCE 41-17 (ASCE, 2017a). As a reference, Hazus (FEMA, 2022a) defines the reinforced concrete moment-resisting frame class (C1) as "reinforced concrete frames with a variety of old and new structural systems, in which the older ones may exhibit brittle failure leading to partial or complete collapse of the building" (FEMA, 2022a). The classification also accounts for building height, dividing structures into three categories: low-rise (1 to 3 stories, C1L), mid-rise (4 to 7 stories, C1M), and high-rise (more than 8 stories, C1H). The C1 class has the following qualitative descriptions of the Damage Limit States, as defined in Hazus (FEMA, 2022a):

A) *Slight Structural Damage (SSD)*: Flexural or shear-type hairline cracks may appear in some beams and columns, typically near or within beam–column joints.

B) *Moderate Structural Damage (MSD)*: Most beams and columns exhibit hairline cracks. In ductile frames, some members may reach their yield capacity, indicated by wider flexural cracks and localized concrete spalling. Nonductile frames may present larger shear cracks and spalling.

C) *Extensive Structural Damage (ESD)*: Several frame elements reach their ultimate capacity. In ductile frames, this condition is indicated by large flexural cracks, spalled concrete, and buckled longitudinal reinforcement. Nonductile frames may experience shear or bond failures at reinforcement splices, broken ties, or buckled column reinforcement, potentially leading to partial collapse.

D) *Complete Structural Damage (CSD)*: The structure has collapsed or is in imminent danger of collapse due to brittle failure of nonductile frame elements or loss of frame stability. Approximately 13% of the total floor area of C1 buildings with complete damage is expected to collapse.

Hazus (FEMA, 2022a) also provides detailed quantitative definitions of Damage Limit States, including numerical thresholds for interstory drift, plastic rotation, and other deformation measures associated with each performance level. These definitions, although not reproduced here, serve as reference parameters for the calibration of analytical fragility functions and for the evaluation of structural performance in this work.

Furthermore, ASCE 41-17 (ASCE, 2017a) defines qualitative performance levels for structural elements, describing the expected condition and usability of the structure

after a seismic event. Each performance level is associated with a corresponding Damage Limit State, as follows:

A) *Immediate Occupancy (IO)*: Structural elements exhibit limited damage, and the structure substantially retains its original strength and stiffness. The risk of injury or threat to life is minimal.

B) *Life Safety (LS)*: The structure experiences significant damage but maintains a safety margin between partial and total collapse. Some residual strength and stiffness remain in all stories, and gravity-load-resisting elements continue to function. However, the building may not be economical to repair, and continued occupancy is typically not permitted until repairs are completed.

C) *Collapse Prevention (CP)*: The structure is on the verge of collapse and cannot remain occupied. Residual stiffness and strength to resist lateral loads are minimal, permanent drifts are large, and nonstructural components sustain extensive damage.

Similar to structural demand, structural capacity is also assumed to follow a lognormal distribution, characterized by a median value S_C and a logarithmic standard deviation β_C (Cornell; Krawinkler, 2000). The capacity parameters can be obtained in two ways: (i) by adopting quantitative values available in the literature, or (ii) by performing a numerical static simulation, commonly referred to as Pushover analysis. In the latter case, a correspondence must be established between the qualitative descriptions of the Damage Limit States and the actual structural damage observed during the analysis for each frame model.

The Pushover analysis is a nonlinear static procedure conducted under constant gravitational loads and incrementally increasing horizontal loads. Its main objectives are to evaluate structural performance through capacity curves and to estimate the expected plastic mechanism and the distribution of damage along the structure (Krawinkler; Seneviratna, 1998). Fig. 2.8 illustrates the Pushover procedure, showing the applied lateral loads on a two-dimensional frame and the corresponding capacity curve.

International standards define criteria for selecting the load patterns used in Pushover analysis. Both FEMA 356 (FEMA, 2000b) and Eurocode 8 2004 establish that at least two lateral load distributions must be considered in all analyses. The first corresponds to a uniform load pattern, with lateral forces proportional to the story masses. The second is based on the natural vibration mode of the structure. While Eurocode 8 2004 does not specify which vibration mode should be used, FEMA 356 (FEMA, 2000b) recommends that the selected mode be associated with the percentage of mobilized effective mass. Specifically, if the first vibration mode mobilizes more than 75% of the effective mass, the load pattern may be taken as proportional to the shape of that mode.

Figure 2.8 – Representation of the Pushover Analysis and the Capacity Curve.

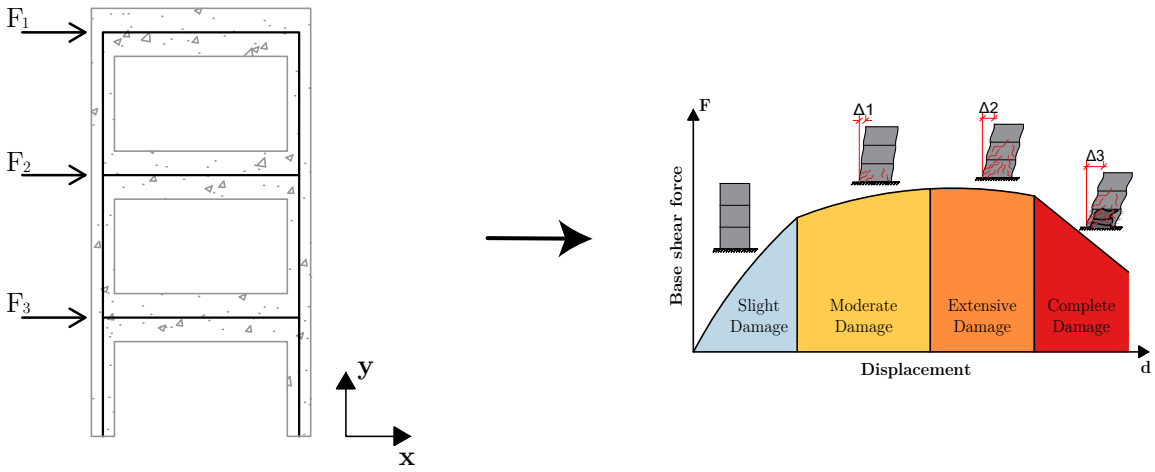

Source: Author (Rodrigues *et al.*, 2023).

Displacements are typically measured at the control point of the analysis, defined at the center of mass of the roof level. From the resulting force–displacement relationship, the capacity curve of the structure is obtained, relating the base shear force to the displacement of the control node.

Once the correspondence between the qualitative descriptions of the Damage Limit States and the actual structural damage observed during the analysis is established—based on measures such as global displacement, story drift, member ductility, or curvature—it becomes possible to determine the median value and standard deviation of the structural capacity. To capture the variability in the results, several frame models must be analyzed and the capacity parameters can then be calculated as illustrated in Fig. 2.9.

Figure 2.9 – Probabilistic Pushover analysis.

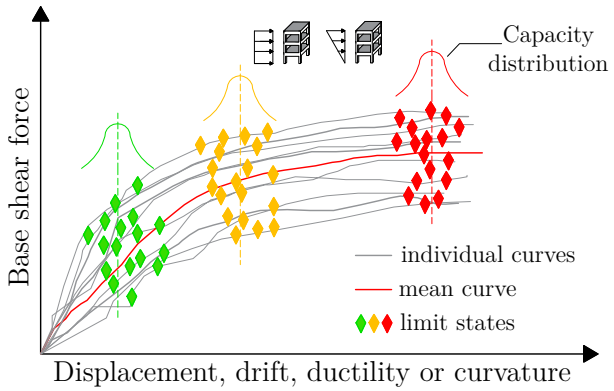

Source: Author.

When quantitative values from the literature are adopted, the median capacities S_C are typically taken as the limit values associated with each Damage Limit State. Based

on the qualitative definitions provided in the Hazus (FEMA, 2022a), representative median values for different structural types and performance levels are available in the tables presented in that document. Similarly, Ramamoorthy, Gardoni and Bracci (2006) suggest values of S_C corresponding to the qualitative performance levels defined in ASCE 41-17 (ASCE, 2017a). Since the adopted S_C values are derived from deterministic analyses, the logarithmic standard deviation β_C may also be taken from literature sources. The specific definitions adopted in this work are discussed in the following chapters.

Damage Limit States are also qualitatively described in Hazus (FEMA, 2022a) for each nonstructural damage category. Four limit states are defined—Slight, Moderate, Extensive, and Complete—following the same classification used for structural components. As with structural capacity, when quantitative values from the literature are adopted, the median capacities S_C are assumed to represent the limit values for each Damage Limit State. The manual also provides suggested values for the logarithmic standard deviation β_C.

The Hazus (FEMA, 2022a) also defines nonstructural components, encompassing "a large variety of different architectural, mechanical, and electrical components." These components are categorized into two groups according to the type of seismic demand that primarily affects them: drift-sensitive and acceleration-sensitive (FEMA, 2022a).

2.4 Loss analysis

The final stage of the PBEE framework corresponds to the loss analysis, which provides a probabilistic estimation of performance through DV conditioned on damage and structural design, expressed as $G\left(dv \mid dm\right)$ (Porter, 2003). This stage converts damage quantities into DVs that can be interpreted by building owners, engineers, or other stakeholders to support risk management decisions. The evaluation relies on parameters such as repair material quantities, labor and equipment costs, expected repair durations, and potential casualties associated with each damage state. The resulting metrics may include, for instance, the mean annual frequency of exceeding a given repair-cost threshold, the cumulative expected financial loss over a defined period, or the total repair cost associated with a specific hazard level (Yang *et al.*, 2009).

This work focuses on the estimation of the expected repair cost as the selected DV, considering two alternative approaches: (i) the framework proposed in FEMA P-58 (2018), which employs a Monte Carlo simulation procedure; and (ii) the methodology for estimating structural and nonstructural repair costs resulting from building damage defined in the Hazus (FEMA, 2022a) manual. Each approach is applied independently and is described in the following sections.

2.4.1 Monte Carlo Procedure

This step corresponds to the calculation of the building performance, which involves: (i) generating an expanded synthetic set of simulated demands (**W**); (ii) assessing collapse; (iii) determining damage; and (iv) computing losses in terms of repair costs. According to FEMA P-58 (2018), the ideal implementation would require performing a large number of NLTHA using an extensive suite of input ground motions to properly quantify uncertainty and capture variability in building performance. Each individual analysis represents a possible realization of the system response, and the ensemble of results forms a smooth probabilistic distribution that can be used to evaluate the seismic consequences.

In this context, each sample corresponds to a structural analysis performed under a specific ground-motion record, generating a realization of the EDPs, such as interstory drift or floor acceleration for that particular event. Considering N_p EDPs, these are typically arranged in the following random vector:

$$\mathbf{EDP} = \left\{ \begin{array}{c} EDP_1 \\ EDP_2 \\ \vdots \\ EDP_{N_p} \end{array} \right\} \in \mathbb{R}^{N_p} \tag{2.13}$$

Due to the cost of NLTHA, a limited set of N_e ground motions is typically used to characterize **EDP**, resulting in a demand matrix $\mathbf{X} \in \mathbb{R}^{N_e \times N_p}$, where each row is a realization of **EDP**. A fundamental assumption is that the ground motions sufficiently capture aleatory uncertainty (record-to-record variability) (FEMA, 2018). The random vector, **EDP**, is often modeled as a joint lognormal distribution, with parameters inferred from **X**. These include the mean vector, $\hat{\mu}_{\mathbf{EDP}}$, and covariance matrix, $\hat{\Sigma}_{\mathbf{EDP}}$, of the log-transformed demands. The inferred distribution is then used to generate a large synthetic sample matrix $\mathbf{W} \in \mathbb{R}^{D_s \times N_p}$, enabling efficient loss assessment through the FEMA P-58 procedure (Yang *et al.*, 2009; FEMA, 2018). An overview of this process is illustrated in Fig. 2.10.

The complete procedure to generate the large synthetic sample matrix **W** is described by Yang *et al.* (2009) and in Appendix G of the FEMA P-58 (2018) manual. It is important to note that the effects of model uncertainty, β_m, and ground motion uncertainty, β_{gm}, can be incorporated into the generation of **W** by inflating the variance matrix obtained from $\hat{\Sigma}_{EDP}$ using β_m and β_{gm}.

Once **W** is defined, Monte Carlo simulation is employed to propagate uncertainty across all realizations. For each realization D_s, the building performance is evaluated sequentially through the following steps: assessment of collapse, verification of repairability, estimation of component-level damage, and calculation of the corresponding losses.

Figure 2.10 – Generation of the synthetic demand set.

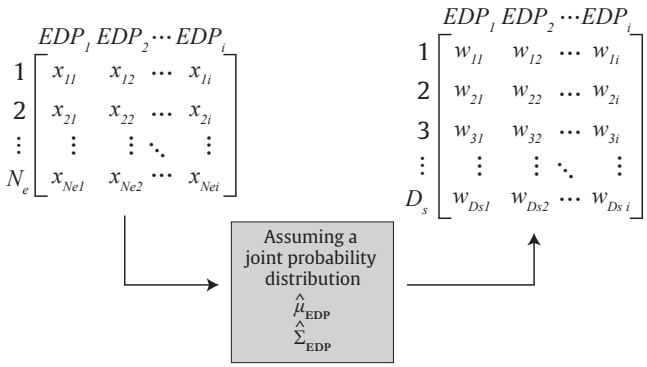

Source: Author.

Collapse is first assessed probabilistically using the collapse fragility function defined in Section 2.3.1. A random number between 0 and 1 is generated and compared with the conditional probability of collapse at the corresponding ground-motion intensity level. If the random number is less than or equal to this probability, collapse is assumed to occur; otherwise, the realization is classified as non-collapsed. When collapse is assumed to occur, the associated repair cost is taken as equal to the building replacement cost.

For non-collapsed realizations, the next step is to evaluate repairability based on residual-drift criteria, which are represented by a lognormal repair fragility function. This evaluation considers the maximum residual drift ratio obtained for each realization and the corresponding repair fragility function, which depends on the structural system under consideration and defines the probability that a building will be deemed irreparable as a function of residual drift.The same probabilistic procedure used for collapse is applied here: a random number between 0 and 1 is generated, and if it is less than or equal to the probability of irreparability, the building is deemed irreparable; otherwise, it is considered repairable. When the building is deemed irreparable, demolition is assumed to occur, and the associated repair cost is taken as equal to the building replacement cost.

If the structure does not collapse and is classified as repairable, component-level damage is then determined. The fragility functions associated with each performance group are used to identify the damage state of each component, and the repair costs are computed through the corresponding consequence models. The total repair cost for a given realization corresponds to the sum of the repair costs associated with all damaged components.

Finally, the expected repair cost, $C_{\text{exReCo}}(\mathbf{x})$, is obtained as the sample mean of the loss values across all D_s realizations. This quantity depends on the statistically inferred parameters of the random vector **EDP**, as well as on the collapse fragility function. In addition to the mean value, other statistical measures, such as the standard deviation and selected percentiles, can also be obtained from the analysis. A flowchart summarizing the

overall performance-evaluation process is presented in Fig. 2.11.

Figure 2.11 – Flowchart for performance evaluation and expected repair cost calculation.

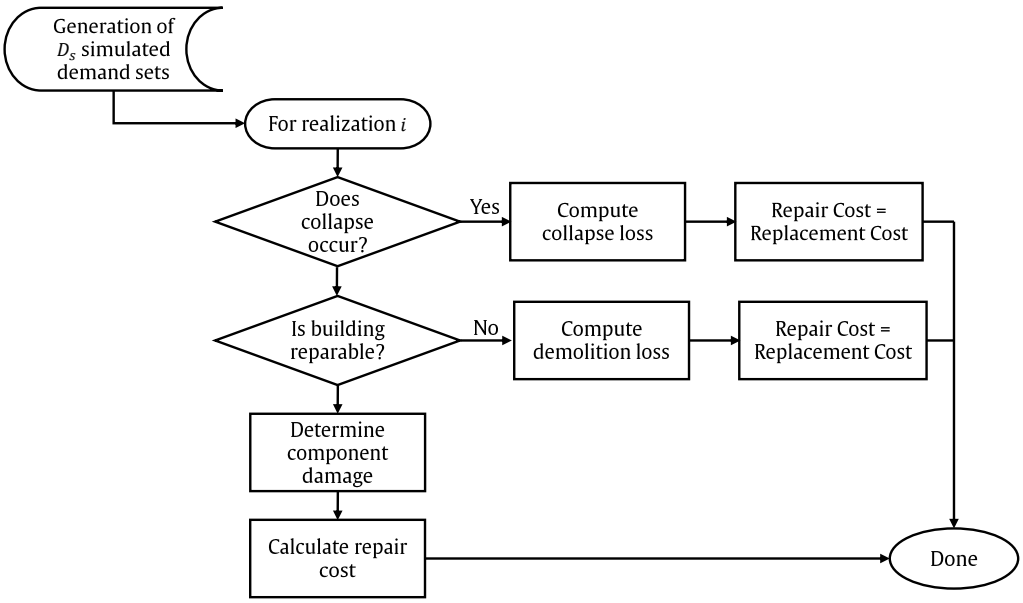

Source: Author.

The described procedure corresponds to the intensity-based assessment defined in FEMA P-58 (2018). In a time-based assessment, multiple intensity-based evaluations are performed across a range of ground-motion intensities and weighted by their respective frequencies of occurrence. This process yields a loss exceedance curve, which represents the total expected loss as a function of the annual rate of exceeding that loss level.

2.4.2 Hazus (2022a) Procedure

The methodology described in this section for estimating economic losses due to earthquake events is presented in the Hazus Earthquake Manual (FEMA, 2022a). It establishes a procedure to estimate monetary losses by converting the probabilities of building damage states into equivalent financial losses. In this work, losses are considered to result from both structural and nonstructural damage, with the nonstructural losses limited to components classified as drift-sensitive.

The occupancy classification of the building defined in the Hazus Inventory Manual (FEMA, 2022b, p. 4-1) aims to "group buildings with similar valuation, damage, and loss characteristics into a set of predefined categories for analysis." The manual defines 33 specific occupancy classes, including residential, commercial, industrial, agricultural, religious, governmental, and educational buildings. In addition, the Hazus Inventory Manual (FEMA, 2022b) provides estimates of building replacement costs, representing the average cost per occupancy type to reconstruct a structure in the United States.

The building repair cost for a given occupancy and damage state can be defined as "the product of the floor area of each building type within the given occupancy, the probability of the building type being in the given damage state, and the repair cost per square foot of the building type for that damage state, expressed relative to the replacement cost" (FEMA, 2022a, p. 11-5). For a specific building occupancy class, the structural repair cost can be expressed as:

$$CS_{ds} = BRC \times P_{\text{struc},ds} \times RCS_{ds} \tag{2.14}$$

where CS_{ds} is the mean structural repair cost for damage state ds, BRC is the building replacement cost, $P_{\text{struc},ds}$ is the probability that the building of the given occupancy class is in structural damage state ds (i.e., the probability of failure), and RCS_{ds} is the structural repair cost ratio (percentage of the building replacement cost) corresponding to damage state ds.

The total structural repair cost (CS) for a given occupancy class is obtained by summing the contributions of all damage states, as follows:

$$CS = \sum_{ds=2}^{5} CS_{ds} \tag{2.15}$$

Hazus (FEMA, 2022a) defines the structural repair cost ratio (RCS_{ds}) for each damage limit state and occupancy classification as a fraction of the building replacement cost. Table 2.1 presents the corresponding baseline values for residential buildings.

Table 2.1 – Structural repair cost ratios (in % of building replacement cost).

Occupancy	**Structural Damage Limit State**			
Label	**Slight**	**Moderate**	**Extensive**	**Complete**
RES1	0.5	2.3	11.7	23.4
RES2	0.4	2.4	7.3	24.4
RES3A-F	0.3	1.4	6.9	13.8
RES4	0.2	1.4	6.8	13.6
RES5	0.4	1.9	9.4	18.8
RES6	0.4	1.8	9.2	18.4

Source: Hazus Earthquake Manual (FEMA, 2022a).

It is important to mention that Hazus provides a deterministic (mean) value for the loss ratio. In addition to structural damage, Hazus (FEMA, 2022a) also defines the repair costs for drift-sensitive nonstructural components. For a specific building occupancy class, these costs can be expressed as

$$CNS_{ds} = BRC \times P_{\text{Nstruc},ds} \times RCD_{ds} \tag{2.16}$$

where CNS_{ds} is the repair cost associated with drift-sensitive nonstructural damage for damage state ds, BRC is the building replacement cost, $P_{\text{Nstruc},ds}$ is the probability that the building reaches nonstructural drift-sensitive damage state ds (corresponding to the probability of failure for each damage limit state), and RCD_{ds} is the drift-sensitive nonstructural repair cost ratio (percentage of the building replacement cost) for damage state ds.

The total repair cost associated with drift-sensitive nonstructural damage for a specific building occupancy class (CNS) is obtained as

$$CNS = \sum_{ds=2}^{5} CNS_{ds} \tag{2.17}$$

Hazus (FEMA, 2022a) defines the drift-sensitive nonstructural repair cost ratio ($RCD_{ds,i}$) for each damage limit state and building occupancy classification. Table 2.2 presents the corresponding baseline values for the residential occupancy class.

Table 2.2 – Drift-sensitive nonstructural repair cost ratios (in % of building replacement cost).

Occupancy	**Nonstructural Damage Limit State**			
Label	**Slight**	**Moderate**	**Extensive**	**Complete**
RES1	1.0	5.0	25.0	50.0
RES2	0.8	3.8	18.9	37.8
RES3A-F	0.9	4.3	21.3	42.5
RES4	0.9	4.3	21.6	43.2
RES5	0.8	4.0	20.0	40.0
RES6	0.8	4.1	20.4	40.8

Source: Hazus Earthquake manual (2022a).

The following section presents the procedure for calculating the probability of failure associated with each Damage Limit State.

2.4.2.1 Probability of Failure for each Damage Limit State

To compute the probability of failure associated with each damage limit state, it is necessary to estimate the mean annual failure rate, denoted by λ_{ds}. This parameter represents the expected frequency with which levels of the DV are exceeded within a given year. The calculation is based on the combination of the fragility functions, $P\left[LS \mid IM\right]$, and the mean annual frequency of exceedance of the IM that characterizes the seismic

hazard, $\lambda(im)$. As described by Fragiadakis *et al.* (2015) and Beck, Bosse and Rodrigues (2022), λ_{ds} is computed as:

$$\lambda_{ds} = \int_0^{\infty} P[LS \mid IM] \cdot |d\lambda(im)| \, dIM \tag{2.18}$$

Equation 2.18 is rarely solved in closed form because $\lambda(im)$ is typically available only at discrete intensity levels (Porter, 2019). For this reason, Porter (2019) proposed a numerical solution to Equation 2.18, considering $n+1$ discrete values of s at which both the fragility function $P(s)$ and the hazard curve $G(s)$ are defined. These values are denoted by s_i, F_i, and G_i, for $i = 0, 1, 2, \ldots, n$.

$$\lambda_{ds} = \sum_{i=1}^{n} (P_{i-1} a_i - \Delta P_i b_i) \tag{2.19}$$

where:

$$\begin{aligned}
\Delta P_i &= P_i - P_{i-1} \\
a_i &= G_{i-1}[1 - \exp(m_i \Delta s_i)] \\
b_i &= \frac{G_{i-1}}{\Delta s_i}\left[\exp(m_i \Delta s_i)\left(\Delta s_i - \frac{1}{m_i}\right) + \frac{1}{m_i}\right] \\
m_i &= \frac{\ln(G_i / G_{i-1})}{\Delta s_i} \\
\Delta s_i &= s_i - s_{i-1}
\end{aligned} \tag{2.20}$$

Assuming a Poisson occurrence model, the unconditional probability of failure, $P_{ds}(t_D)$, as a function of the time period in years t_D, for each damage limit state, can be expressed as:

$$P_{ds}(t_D) = 1 - \exp\left(-\int_0^{t_D} \lambda_{ds} dt\right) \tag{2.21}$$

It is important to emphasize the findings of Beck, Bosse and Rodrigues (2022) regarding the computation of the probability of failure, which demonstrate that non-ergodic system parameters can have a significant influence on annual collapse rates for buildings. As defined by Kiureghian (2005), system parameters are considered non-ergodic because they do not renew with each earthquake event. These parameters include uncertainties in mass, damping, stiffness, deformation capacity, and modeling of structural response. Conversely, all variables characterized by record-to-record variability are ergodic in nature. The consideration of non-ergodic system parameters may violate the Poisson assumption of independent crossings, and errors in estimating the lifetime failure probability can reach approximately 10–15% when such parameters are included.

2.5 Chapter Overview

In this chapter, the four steps of the PBEE framework are presented and discussed. Each section includes a literature review to provide context, highlight the current state of the art, and justify the methodological choices adopted in this work. The decisions made throughout this chapter are applied in the examples presented in the subsequent chapters.

The section on hazard analysis introduces the fundamentals of PSHA and provides an overview of studies related to seismic hazard assessment in Brazil. It also describes the procedures for selecting hazard-consistent ground motions for performance evaluations and discusses how seismic hazard can be represented depending on the type of performance assessment.

The section on structural analysis presents the types of analysis that can be used to obtain the EDPs, establishing that this study adopts NLTHA as the primary approach. It also summarizes key recommendations for the development of nonlinear FE models required for the analyses.

The section on damage analysis presented the frameworks used to construct fragility functions that relate EDPs to DM, which describe physical damage to the structure. It also introduced the methodology adopted for the development of collapse fragility functions, as well as a closed-form solution that combines structural demand and capacity to define multiple Damage Limit States.

The section on loss analysis presented the methodologies used to estimate building performance through DVs conditioned on damage and structural design. Two frameworks for calculating the expected repair cost of a building were described, based on an intensity-based assessment and a time-based assessment.

3 STRUCTURAL OPTIMIZATION

Design of engineering systems is inherently a complex process involving numerous possibilities and factors that must be considered during its formulation. It typically begins with the analysis of multiple alternatives, leading to a set of drawings, reports, and calculations that define the preliminary design stage. This stage involves the evaluation of several trial designs and corresponding analyses until an acceptable solution is obtained, characterizing an iterative process. In the context of structural optimization, each trial design is systematically assessed to determine whether it represents the best possible configuration (Arora, 2012).

Structural optimization can be defined as the process of searching for the best structural design that satisfies a given objective function while complying with prescribed constraints, which may be conflicting. Although it is difficult to guarantee that a particular solution is globally optimal, it represents the best design among those evaluated (Beck, 2024). The optimization problem can be mathematically formulated as follows:

$$\begin{aligned} &\text{Find} \quad \mathbf{x}_\mathbf{d}^* = \{x_{d_1}, \ldots, x_{d_{n_{\mathrm{DV}}}}\}^T \\ &\text{to minimize} \quad f(\mathbf{x}_\mathbf{d}) \\ &\text{subjected to} \quad h_i(\mathbf{x}_\mathbf{d}) = 0,\ i = 1, ..., p \\ &\qquad\qquad\ \ g_j(\mathbf{x}_\mathbf{d}) \leq 0,\ j = 1, ..., q \\ &\qquad\qquad\ \ \mathbf{x}_\mathbf{d} \in \mathcal{D}_{\mathbf{x}_\mathbf{d}} \subset \mathbb{R}^{n_{\mathrm{DV}}} \end{aligned} \tag{3.1}$$

where n_{DV} denotes the number of design variables $\mathbf{x}_\mathbf{d}$, p and q are the numbers of equality and inequality constraints, respectively, and $\mathcal{D}_{\mathbf{x}_\mathbf{d}} = \{\mathbf{x}_{\mathbf{d}_{\min}}, \ldots, \mathbf{x}_{\mathbf{d}_{\max}}\}$ represents the feasible domain. The general optimization problem defined in Eq. (3.1) serves as the basis for more specific formulations addressed in the subsequent sections.

The optimization problem can also be expressed as a multi-objective optimization problem, which involves the simultaneous minimization of two or more objective functions. The general formulation is given by:

$$\begin{aligned} &\text{Find} \quad \mathbf{x}_\mathbf{d}^* = \{x_{d_1}, \ldots, x_{d_{n_{\mathrm{DV}}}}\}^T \\ &\text{to minimize} \quad f_1(\mathbf{x}_\mathbf{d}), f_2(\mathbf{x}_\mathbf{d}), \ldots, f_k(\mathbf{x}_\mathbf{d}) \\ &\text{subjected to} \quad h_i(\mathbf{x}_\mathbf{d}) = 0,\ i = 1, ..., p \\ &\qquad\qquad\ \ g_j(\mathbf{x}_\mathbf{d}) \leq 0,\ j = 1, ..., q \\ &\qquad\qquad\ \ \mathbf{x}_\mathbf{d} \in \mathcal{D}_{\mathbf{x}_\mathbf{d}} \subset \mathbb{R}^{n_{\mathrm{DV}}} \end{aligned} \tag{3.2}$$

where k denotes the number of objective functions to be minimized.

In general, a multi-objective optimization problem does not have a unique solution, meaning that no solution vector $\mathbf{x_d}$ can minimize all k objective functions simultaneously. Instead, a set of Pareto-optimal solutions is obtained. A feasible solution vector $\mathbf{x_d}$ is said to be Pareto optimal if no other feasible solution exists that can reduce one objective function without causing a simultaneous increase in at least one of the others (Arora, 2012; Rao, 2019).

Structural optimization problems can be divided in three types: size, shape, and topology optimization, as illustrated in Fig. 3.1 (Tsavdaridis; Kingman; Toropov, 2015). Size optimization involves modifying the dimensions of the element cross sections without changing the structural shape or removing elements. In shape optimization, the nodal coordinates that define the structural geometry are treated as design variables. Topology optimization seeks the best material distribution within the design domain by removing elements that do not significantly contribute to the structural performance.

Figure 3.1 – Classifications of structural optimization.

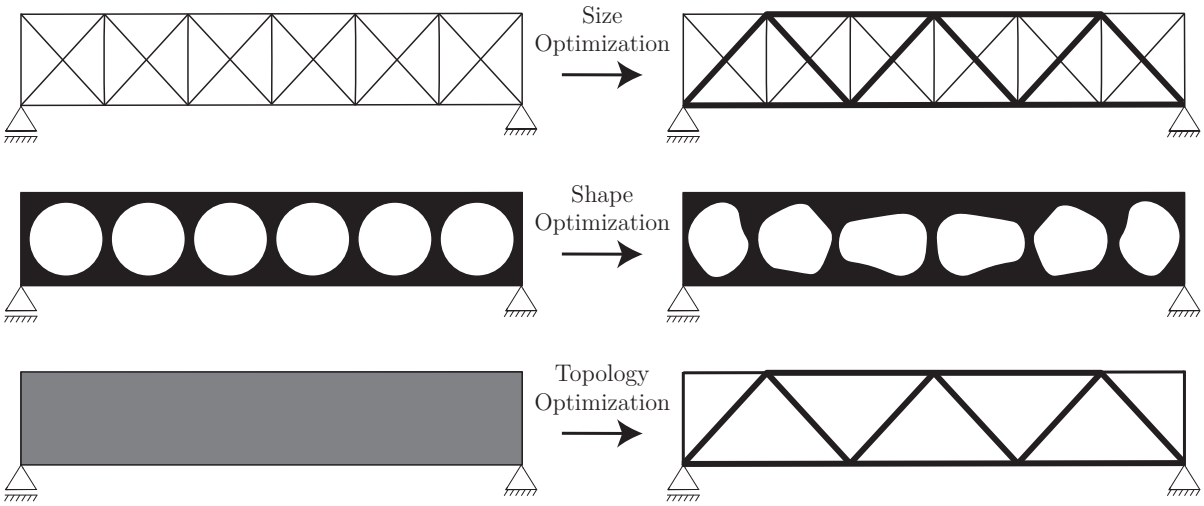

Source: Adapted from Tsavdaridis, Kingman and Toropov (2015).

According to Vanderplaats (1982), the concept of structural optimization dates back at least to the nineteenth century. Early studies in this field focused on simple examples and addressed the optimal design from a deterministic perspective. However, since uncertainties were not considered, the results obtained were not satisfactory. Seeking formulations that accounted for uncertainties, Hilton and Feigen (1960) investigated the minimization of structural weight considering the global failure probability of the system, using analytical expressions for normally distributed random loads. Kalaba (1962) included material cost in his study on the minimization of structural weight. Both replaced the deterministic constraints with probabilistic ones, incorporating failure probability—calculated through empirical relations—after the minimization of the objective function.

Size and topology structural optimization frameworks have been developed over the

last two decades, considering a deterministic perspective for Performance-Based Design (PBD) problems. These problems aim to identify optimal earthquake-resistant systems while minimizing the initial construction cost of a structure, herein denoted as C_{cons} and considered the objective function of the problem defined in Eq. 3.1. The problem may include several constraints, such as confidence intervals, Strong-Column Weak-Beam (SCWB) requirements, strength-related limits, and practical restrictions based on the dimensions of structural members, which can also be used to verify demand–capacity ratios of structural elements as required by seismic design standards (Hassanzadeh; Moradi; Burton, 2024a).

For reinforced concrete (RC) structures, the design variables may include the cross-sectional area of concrete elements, the area of steel reinforcement, or a combination of both. Other parameters can also be adopted as design variables, such as the relative flexural stiffness and strength of RC sections (Ganzerli; Pantelides; Reaveley, 2000; Chan; Zou, 2004; Mergos, 2017; Mergos, 2018; Zhang; Tian, 2019). For steel structures, the design variables may correspond to the dimensions of beam, column, or brace cross sections, characterizing a size optimization problem (Fragiadakis; Lagaros; Papadrakakis, 2006a; Gholizadeh *et al.*, 2022). Design variables can also refer to the position of braces in steel frames, which defines a topology optimization problem (Gholizadeh; Poorhoseini, 2016; Gholizadeh; Ebadijalal, 2018; Wang *et al.*, 2020). However, it is important to note that the composition and detailing of reinforced concrete structures involve a considerably larger number of design variables compared to steel frame structures (Mergos, 2017; Hassanzadeh; Moradi; Burton, 2024a).

While deterministic formulations provide valuable insights into cost-efficient structural configurations, they neglect the inherent uncertainties in loads, material properties, and structural response. To address these limitations, optimization methods incorporating reliability concepts were introduced. Frangopol (1985) reviewed and synthesized optimization techniques used in structural reliability through three main conceptual formulations. The first approach focuses on minimizing the total structural cost, which includes both the initial construction cost and the expected cost of failure, the latter being calculated as a function of the failure probability. The second formulation seeks to maximize the overall utility of the structure, balancing the benefits of its existence against the initial cost and the expected losses due to potential failure events.

Despite their conceptual clarity, these formulations presented practical limitations, particularly in assigning reliable monetary values to all possible failure consequences, especially those that involve human life. Consequently, a third and more tractable formulation emerged, focusing on minimizing the structural weight while constraining the probability of failure to remain below a prescribed threshold. This approach facilitated the integration of reliability concepts into structural optimization and motivated a significant body of

research devoted to improving the estimation of structural failure probabilities (Frangopol, 1985).

The following sections present the main reliability-based optimization approaches, discussing their conceptual similarities and differences, as well as their application in recent studies.

3.1 Reliability optimization approaches

3.1.1 Reliability-Based Design Optimization (RBDO)

A RBDO problem defines its constraints in terms of failure probability. Let us now separate $\mathbf{X_r}$ and $\mathbf{X_d}$ as vectors of the structural system. The vector $\mathbf{X_r} \in \mathbb{R}^{n_{\mathrm{RV}}}$ contains n_{RV} random variables that exhibit inherent uncertainties or cannot be deterministically defined, such as element dimensions, material strength, loads, or model errors. The vector $\mathbf{X_d} \in \mathbb{R}^{n_{\mathrm{DV}}}$, composed of n_{DV} design variables, represents quantities whose optimal values can be determined to achieve a specific objective, such as maximizing structural performance or minimizing structural weight (Beck, 2024).

Considering that the requirements for a structural design are represented by Limit States, the inclusion of uncertainties makes it possible for the structural system to exhibit unsatisfactory performance by reaching one or more Limit States. The Limit State equations $g_i(\mathbf{X_d}, \mathbf{X_r}) = 0$ divide the sample space into the failure domain $\Omega_{fi}(\mathbf{x_d})$ and the safe domain $\Omega_{si}(\mathbf{x_d})$ for $i = 1, ..., n_{LS}$, as follows:

$$\begin{aligned} \Omega_{fi}(\mathbf{x_d}) &= \{\mathbf{x_r} | g_i(\mathbf{x_d}, \mathbf{x_r}) \leq 0\} \\ \Omega_{si}(\mathbf{x_d}) &= \{\mathbf{x_r} | g_i(\mathbf{x_d}, \mathbf{x_r}) > 0\} \end{aligned} \tag{3.3}$$

where n_{LS} is the number of Limit State equations. Each Limit State equation describes a structural failure mode, with an associated probability of failure for each failure mode calculated as:

$$p_{fi}(\mathbf{x_d}) = P[\mathbf{X_r} \in \Omega_{fi}] = \int_{\Omega_{fi}} f_{\mathbf{X_r}}(\mathbf{x_r})\, d\mathbf{x_r} \tag{3.4}$$

where $f_{\mathbf{X_r}}(\mathbf{x_r})$ is the joint Probability Density Function (PDF) (Melchers; Beck, 2018).

Including the probability of failure as a constraint in the optimization problem defined in Eq. 3.1 transforms it into a RBDO problem, which can be expressed as follows:

$$\begin{aligned} &\text{Find} \quad \mathbf{x}_{\mathbf{d}}^{*} = \{x_{d_1}, \ldots, x_{d_{n_{\mathrm{DV}}}}\}^T \\ &\text{to minimize} \quad f(\mathbf{x}_{\mathbf{d}}) \\ &\text{subject to} \quad p_{f_i}(\mathbf{x}_{\mathbf{d}}) \leq p_{fT_i}, \\ &\qquad\qquad \mathbf{x}_{\mathbf{d}} \in \mathcal{D}_{\mathbf{x}_{\mathbf{d}}} \end{aligned} \tag{3.5}$$

where $p_{fi}\left(\mathbf{x}_{\mathbf{d}}\right)$ is the probability of failure associated with failure mode i, and p_{fTi} is the target probability of failure.

Constraints can also be replaced by a single constraint expressed in terms of the system probability of failure, $p_{f_{SYS}}$. In general, the objective function in RBDO problems involves the volume of structural elements or manufacturing costs. The results depend on the target probability of failure defined, and no balance between safety and economy is explicitly considered, since reliability is included in the constraints rather than in the objective function (Beck, 2024).

3.1.2 Risk Optimization (RO)

When the optimization problem is formulated to minimize the total cost over the service life of a structure, it becomes a RO problem. Also referred to as Life-Cycle Cost Optimization (LCCO), RO incorporates the economic balance between the initial construction cost and the expected failure costs associated with each limit state. In a deterministic approach, it is typically assumed that structures designed and constructed in accordance with code requirements will not fail. However, although such events are rare, structural collapses do occasionally occur. Indeed, the PBE framework discussed in the previous chapter is founded on the recognition that structural failure does not happen in a discrete manner, but rather as a gradual transition among multiple limit states (Beck, 2024).

Therefore, an inherent trade-off exists between structural performance and cost. When high-intensity loads with low probabilities of occurrence are considered, a structure may achieve excellent performance, but doing so typically requires a substantial initial investment. Conversely, reducing design and construction costs can compromise safety and serviceability. The goal of RO is to identify an economically efficient design that balances the initial construction cost with the expected failure costs over the structure's service life. This balance defines the optimal level of reliability from an economic standpoint, where additional investments in safety no longer lead to proportional reductions in expected losses. Fig. 3.2 illustrates the minimum total cost targeted in this formulation (Beck *et al.*, 2015).

Figure 3.2 – Expected total cost composition of a structural system.

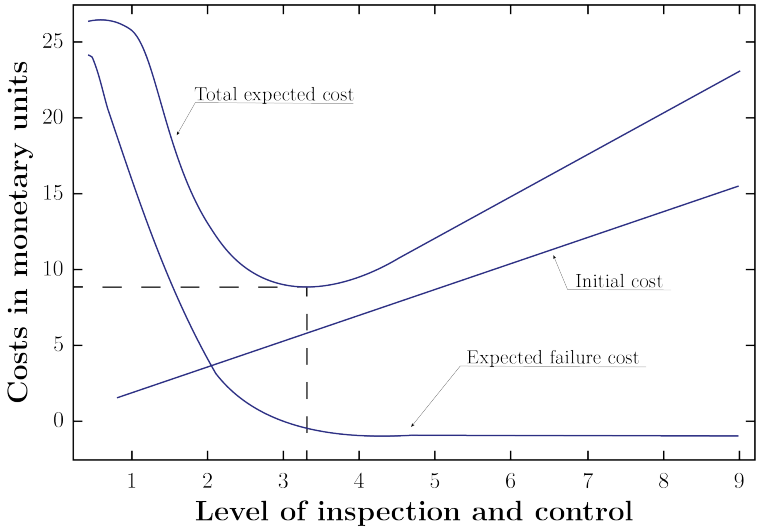

Source: Author.

If failure is recognized as an inevitable possibility, the expected cost of failure must be incorporated into the design phase. Extensive discussions exist regarding the various cost components that should be considered under the Ultimate Limit State, including structural replacement, relocation expenses, and loss of income, as described in the Hazus (FEMA, 2022b) manual. These discussions also encompass the costs associated with fatalities and environmental impacts (Beck, 2024), which are beyond the scope of this work. In general terms, the expected cost of failure for each failure mode can be expressed as $c_{ef_i}(\mathbf{x_d}) = c_{f_i}(\mathbf{x_d})\, p_{f_i}(\mathbf{x_d})$, where $c_{f_i}(\mathbf{x_d})$ denotes the cost of failure associated with failure mode i.

The total expected cost of a structural system over its life cycle can be calculated as:

$$c_{et}(\mathbf{x_d}) = C_{\text{cons}}(\mathbf{x_d}) + c_{op}(\mathbf{x_d}) + c_{in}(\mathbf{x_d}) + c_{dis}(\mathbf{x_d}) + \sum_{i=1}^{n_{LS}} c_{ef_i}(\mathbf{x_d}) \tag{3.6}$$

where $C_{\text{cons}}(\mathbf{x_d})$ is the construction cost, $c_{op}(\mathbf{x_d})$ is the operational cost, $c_{in}(\mathbf{x_d})$ is the inspection and maintenance cost, and $c_{dis}(\mathbf{x_d})$ is the disposal cost.

By incorporating all these costs into the objective function, the optimization problem becomes a RO problem, expressed as:

$$\begin{aligned} &\text{Find} \quad \mathbf{x_d^*} = \{x_{d_1}, \ldots, x_{d_{n_{\text{DV}}}}\}^T \\ &\text{to minimize} \quad c_{et}(\mathbf{x_d}) \\ &\text{subject to} \quad \mathbf{x_d} \in \mathcal{D}_{\mathbf{x_d}} \end{aligned} \tag{3.7}$$

Reliability constraints can also be incorporated into Eq. (3.7), still representing a RO problem. Fig. 3.3 illustrates the relationship among Deterministic Optimization, RBDO, and RO, synthesizing the concepts and techniques of reliability-based optimization presented in this section.

Figure 3.3 – Structural optimization formulations.

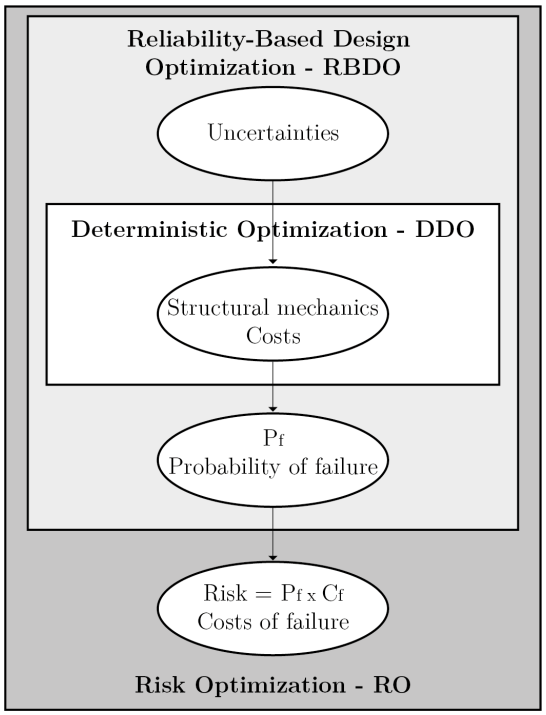

Source: Adapted from Beck and Gomes (2012).

RO problems can be formulated as single-objective or multi-objective problems, aiming to identify the optimal design among a set of feasible alternatives by accounting for the desired risk tolerance and the importance level of the structure (Hassanzadeh; Moradi; Burton, 2024a). For instance, Ghasemof, Mirtaheri and Mohammadi (2022) proposed a multi-objective structural optimization framework based on the FEMA P-58 (2018) methodology to address seismic performance objectives.

3.1.3 Performance-Based Risk Optimization (PBRO)

Within the PBE framework, optimization techniques are naturally integrated as part of the decision-making process. By incorporating optimization procedures, alternative structural configurations can be compared to identify designs that improve the Decision Variable (DV) while accounting for the expected performance of the system. The Performance-Based Risk Optimization (PBRO) approach extends the concepts of RBDO and RO by explicitly coupling the optimization process with the probabilistic performance assessment defined in the PBE methodology. The term Performance-Based Design Optimization (PBDO) can also be found in the literature to refer to PBRO. This

section presents a review of recent studies on PBRO formulations, their main applications in structural engineering, and the conventions adopted in this work.

The first studies on the optimization of seismically excited structures date back approximately two decades. Initially, however, only a small portion of these investigations focused on reinforced concrete and composite structures, for which numerous combinations of section dimensions and reinforcement can be considered. In contrast, because steel structures have standardized cross-sections available in commercial catalogs, structural optimization has been more frequently applied to their design, treating cross-sectional dimensions as design variables. Fragiadakis and Papadrakakis (2008) developed an optimization algorithm aimed at identifying cost- and performance-efficient designs for reinforced concrete structures, considering both deterministic and reliability-based formulations. Concrete sections were treated as discrete design variables based on predefined sets of available cross-sections. Examples of studies addressing steel structures and employing discrete sets of cross-sections as design variables include Fragiadakis and Lagaros (2011) and Saadat, Camp and Pezeshk (2014).

RBDO formulations have been applied to structures subjected to seismic (Fragiadakis; Lagaros; Papadrakakis, 2006a; Gholizadeh; Aligholizadeh, 2019; Gholizadeh; Mohammadi, 2017; Fattahi; Gholizadeh, 2019) and wind loads (Spence; Gioffrè, 2012; Spence; Kareem, 2014; Bobby *et al.*, 2014; Bobby; Spence; Kareem, 2016) within the PBE framework. Spence and Kareem (2014) highlighted the difficulty of solving RBDO problems due to the need to evaluate the probabilistic constraints involving the PBE integral defined in Eq. (2.18). Embedding this integral within an optimization process introduces several challenges: it complicates sensitivity analyses because the design variables are implicit in the integral, and it significantly increases the computational cost due to repeated probabilistic evaluations during the optimization. To address these issues, the authors proposed a framework that decouples the nested reliability analysis from the optimization loop by defining a sequence of high-quality approximate subproblems. Gholizadeh and Aligholizadeh (2019) also highlighted the computational burden associated with RBDO and suggested the use of surrogate models to accelerate convergence and reduce the overall cost of the optimization process.

In parallel, research considering RO or LCCO has gained increasing prominence since the early 2000s, with particular emphasis on studies addressing seismic actions. Wen and Kang (2001a) applied a cost optimization approach to a nine-story building subjected to combined seismic and wind loads, using the methodology previously proposed by Wen and Kang (2001b), which served as the basis for several subsequent studies (Fragiadakis; Lagaros; Papadrakakis, 2006b; Kaveh; Laknejadi; Alinejad, 2012). Several authors have also developed different techniques for RO within the context of PBE (Taflanidis; Beck, 2009; Ghasemof *et al.*, 2021; Mirfarhadi; Estekanchi; Sarcheshmehpour, 2021; Razavi; Gholizadeh,

2021; Varaee; Shishegaran; Ghasemi, 2021; Hassanzadeh; Moradi; Burton, 2024b; Lopez; Santos; Miguel, 2025; Li; Guo; Kunnath, 2025). Furthermore, Beck, Kougioumtzoglou and Santos (2014) extended the use of the LCCO framework to structures subjected to wind excitations, incorporating it into the optimal design of nonlinear dynamic systems and aiming to determine the optimal stiffness of a reinforced concrete structure.

Recent studies have expanded structural optimization approaches to account for multiple hazards acting on structures, aiming to achieve more resilient and cost-effective designs. Suksuwan and Spence (2018) proposed a multi-hazard optimization framework for structures subjected to both wind and seismic actions, formulating a topology optimization problem based on an approximate subproblem that decouples the simulation-based performance assessment from the optimization loop and transforms the dynamic and uncertain problem into a static and deterministic one. In addition, a gradient-based optimization framework was developed by Kleingesinds and Lavan (2022) for the design of multiple bi-tuned semi-active tuned mass dampers (BSTMDs) under combined seismic and wind actions, aiming to minimize the total added mass while considering the life-cycle cost as a performance constraint. Santos, Beck and Lopez (2024) proposed a PBDO framework to optimize the structural parameters of engineering systems modeled as hysteretic oscillators subjected to stationary (wind) and non-stationary (seismic) excitations. Despite these advances, Hassanzadeh, Moradi and Burton (2024a) emphasized that further research is still needed in the field of PBDO to develop more efficient and effective structural design methodologies.

Building upon these advances, several studies have adopted multi-objective frameworks to evaluate competing or conflicting performance goals within a PBE context. Saadat, Camp and Pezeshk (2014) conducted a multi-objective optimization study on steel structures, simultaneously considering direct economic and social losses. Taflanidis, Giaralis and Patsialis (2019) evaluated the compromise between the competing objectives of avoiding excessive forces in an inerter-based vibration absorber and reducing earthquake-induced vibrations in buildings. This framework was later extended by Patsialis, Taflanidis and Giaralis (2023) to account for the hysteretic behavior of structures. Suksuwan and Spence (2019b) proposed an efficient bi-objective optimization methodology for structural systems subjected to stochastic wind excitation, incorporating system-level probabilistic loss measures in a high-dimensional design space. Extensions of this framework were developed by Subgranon and Spence (2021) to explicitly account for correlations between component damages and losses. Multi-objective optimization formulations that jointly minimize the initial construction cost and the expected damage cost associated with seismic events have also been proposed for steel structures (Ghasemof *et al.*, 2021; Ghasemof; Mirtaheri; Mohammadi, 2022).

Despite the progress achieved, the practical implementation of these optimization

techniques remains challenging. Arroyo and Liel (2017) identified three key attributes as essential for ensuring that seismic design optimization effectively improves structural performance and can be adopted by practicing engineers: effectiveness, computational performance, and feasibility. This means that the optimization method must be capable of producing the intended seismic performance outcomes within an acceptable computational cost and through a procedure that is practical and easy to implement. Joyner *et al.* (2021) also discussed the influence of computational cost in multi-objective optimization problems, indicating that simplifying the analytical models and solution methods can help mitigate this issue. However, a trade-off between accuracy and efficiency must be carefully evaluated when such simplifications are introduced.

Beyond the simplification of analytical models, several researchers have also proposed approaches to reduce the computational cost required for PBRO and PBDO frameworks. Gidaris and Taflanidis (2015) reduced the optimization time through a Kriging-based metamodeling framework. Within an RBDO context, Miguel *et al.* (2023) proposed the use of a Kriging metamodeling approach to accelerate the optimization of damping systems in buildings subjected to stochastic excitations. Kriging has also been employed in frameworks that incorporate expected damage costs into the objective function to formulate PBDO problems, as presented by Miguel, Lopez and Ambrosini (2025) and Miguel, Lopez and Ambrosini (2026), introducing a methodology to optimize the parameters of dynamic absorbers in buildings subjected to ground motions while considering soil–structure interaction effects. Metamodeling approaches have also been adopted in several of the previously discussed studies (Suksuwan; Spence, 2019b; Santos; Beck; Lopez, 2024).

Model Order Reduction (MOR) techniques have likewise been used in PBDO frameworks to further decrease computational effort. Salles *et al.* (2023) applied MOR in the optimization of irregular buildings subjected to seismic excitation, enabling the evaluation of structures with thousands of degrees of freedom and multiple discrete design variables. Similarly, Salles *et al.* (2025) implemented an MOR-based framework for optimizing dampers in L-shaped buildings with shear cores.

It is important to note that most of the approaches developed to reduce computational cost have been limited to size optimization problems, highlighting the need for further research addressing performance-based topology optimization of structures (Hassanzadeh; Moradi; Burton, 2024a).

From the previous discussion on PBRO and PBDO, the following conclusions can be highlighted:

- PBRO is a relatively recent research field, with the earliest studies dating back approximately two decades;

- Most studies focus on the optimization of steel structures, since their cross-sections are standardized and available in commercial catalogs. When reinforced concrete structures are considered, the optimization is usually performed using a discrete set of predefined combinations of section dimensions and reinforcement ratios;

- One of the main challenges in solving RO problems within the PBEE framework is that the probabilistic constraints or objective function require the evaluation of the PBE integral inside the optimization loop, which significantly increases computational cost;

- Among the various strategies proposed to improve computational performance, a trade-off between accuracy and efficiency must always be considered. Finding an adequate balance between these aspects is essential to ensure solutions that are both computationally feasible and capable of producing well-performing, resilient structural designs.

Overall, the reviewed studies demonstrate the growing relevance of PBRO and PBDO as frameworks capable of integrating performance assessment, risk evaluation, and optimization in a unified manner. However, their application remains limited, particularly regarding computationally efficient formulations that can handle the nonlinearity and uncertainty inherent to these structures.

The investigation of optimization techniques for the design of structures within the PBEE framework is one of the main goals of this work. The strategies proposed to address the identified challenges—particularly those related to computational cost and model simplification—are presented and discussed in the following chapters.

In this work, the expected cost of failure (also referred to as expected damage cost or expected repair cost) is defined as described in the previous chapter: (1) $C_{\text{exReCo}}(\mathbf{x_d})$, estimated through the Monte Carlo procedure presented in FEMA P-58 (2018) and detailed in Section 2.4.1; and (2) $C_d(\mathbf{x_d}) = CS(\mathbf{x_d}) + CNS(\mathbf{x_d})$, corresponding to the structural and nonstructural repair costs of the building for each damage limit state, as described in Section 2.4.2 following the Hazus (2022a) manual. Frameworks for single- and multi-objective structural optimization are applied to reinforced concrete and steel structures, with different sources of uncertainty considered in each formulation.

3.2 Solution of RBDO, RO and PBRO problems

Several methodologies have been proposed in the literature to solve optimization problems. Classical approaches rely on information about the gradients of the objective and constraint functions to guide the iterative search toward an improved solution. These

gradient-based algorithms, also known as descent methods, make use of first- or second-order derivatives of the objective function and are generally more efficient than non-gradient techniques, as they incorporate more information about the function being minimized. However, their applicability is restricted to problems involving continuous and differentiable functions. In structural engineering, the evaluation of such derivatives often requires repeated Finite Element analyses, which can result in a high computational cost when a large number of design variables or constraints are involved (Rao, 2019; Luiz, 2020).

An alternative to the limitations of gradient-based algorithms is the use of heuristic or metaheuristic optimization methods, which do not require derivative information. These approaches perform a global search over the entire design space and are therefore classified as global optimization algorithms. Metaheuristic algorithms, in particular, have demonstrated superior performance in structural optimization by offering global search capabilities, derivative-free formulations, and an effective balance between exploration and exploitation (Hassanzadeh; Moradi; Burton, 2024b). Unlike traditional mathematical programming techniques, these modern or nontraditional methods are inspired by natural, biological, molecular, or swarm-based processes, and have emerged as powerful tools for solving complex engineering problems (Rao, 2019). The main drawback of these algorithms is their high computational cost, since a large population of candidate solutions is typically required, leading to repeated evaluations of the limit-state function (Beck, 2024). Nevertheless, heuristic and metaheuristic techniques offer significant advantages, including the ability to handle discontinuous functions, identify global minima, and operate effectively without gradient information (Luiz, 2020).

Heuristic optimization methods, such as Genetic Algorithm (GA) and Particle Swarm Optimization (PSO), have been widely used in structural engineering. In this work, the Firefly Algorithm, a type of heuristic algorithm developed by Yang (2010), is implemented and applied to solve single-objective optimization problems. This algorithm belongs to the class of nature-inspired methods, which simulate natural or biological phenomena through stochastic processes to explore the design space. The implementation procedure and computational steps adopted in this work are detailed in Annex B. The Firefly Algorithm has been successfully applied in several studies of structural optimization (Miguel; Miguel, 2012; Miguel; Lopez; Miguel, 2013; Lieu; Do; Lee, 2018; Luiz, 2020; Ribeiro, 2020).

Among the various nature-inspired methods, GA stands out as one of the most established and versatile approaches. As discussed by Arora (2012), it belongs to the class of stochastic, evolutionary optimization methods, in which the search process is guided by probabilistic rules rather than deterministic gradients. The algorithms rely solely on the evaluation of objective and constraint function values, which makes them applicable to discrete, continuous, or nondifferentiable problems. Their main advantage lies in their ability

to identify global optimum solutions, unlike derivative-based algorithms that typically converge to local minima. However, since the decisions made in each computational step are based on random number generation, the sequence of designs and the resulting solution may differ between runs, even when starting from the same initial conditions. Despite the absence of guaranteed global optimality, GAs and other nature-inspired algorithms are considered robust and flexible tools for solving complex engineering optimization problems.

The basic principle of a GA is to generate successive populations of candidate designs in such a way that the average fitness of the population progressively improves. Each population, known as a generation, consists of a fixed number of designs referred to as chromosomes, which encode the values of the design variables, or genes. The algorithm starts with an initial population randomly generated within the admissible ranges of the design variables. Each chromosome is evaluated using a fitness function, typically the objective function itself for unconstrained problems or a penalized objective function for constrained formulations. Based on these fitness values, new generations are created through three main stochastic operators: *reproduction* (or selection), *crossover*, and *mutation*.

The *reproduction* operator selects designs from the current population to form the next generation, giving preference to those with higher fitness values. Different strategies can be used for this step, such as roulette-wheel or tournament selection. The *crossover* operator allows selected pairs of designs, or mating strings, to exchange segments of their encoded variables, simulating genetic recombination and enhancing diversity in the population. Finally, the *mutation* operator introduces small random alterations in some chromosomes to prevent premature convergence and maintain genetic variability. This operation consists of randomly choosing a few chromosomes and flipping bits in their binary representation, changing a 0 to 1 or vice versa. These three operators are iteratively applied until a stopping criterion, such as the maximum number of generations or the stabilization of the fitness function, is satisfied, and the chromosome with the highest fitness value is considered the optimal design (Arora, 2012).

In this work, the GA is employed to solve both single- and multi-objective optimization problems. Its flexibility, robustness, and capability to handle nonlinear and nondifferentiable formulations make it a suitable tool for the class of problems addressed in this research. The algorithm's stochastic nature and population-based search enable the identification of globally efficient solutions without relying on gradient information, which is particularly advantageous in complex structural optimization applications.

3.3 Chapter Overview

This chapter presented the formulation of the structural optimization problem and discussed the three main categories of optimization: size, shape, and topology optimization.

The limitations of deterministic formulations were highlighted, emphasizing the need to incorporate uncertainties into the design process. Different approaches to account for such uncertainties were described, including Reliability-Based Design Optimization (RBDO), Risk Optimization (RO), and Performance-Based Risk Optimization (PBRO). It was shown that, since the 2000s, life-cycle cost optimization has gained increasing relevance, particularly in studies addressing seismic performance.

The chapter also introduced the main solution techniques for optimization problems. Classical gradient-based methods were described as efficient but limited to continuous and differentiable functions, while heuristic and metaheuristic algorithms were presented as flexible alternatives capable of performing global searches without requiring derivative information. Among these, two nature-inspired algorithms are considered in this research: the Firefly Algorithm, developed by Yang (2010) and implemented in this work for single-objective problems (details provided in Annex B), and the Genetic Algorithm (GA), which was used to solve both single- and multi-objective optimization problems.

Finally, the advantages and challenges of heuristic approaches were discussed, particularly regarding the high computational cost associated with the repeated evaluation of objective and constraint functions. The next chapter introduces the simulation procedures and the development of deterministic and stochastic surrogate models, which are used to improve the computational efficiency of the optimization process.

4 SIMULATION METHODS AND METAMODELS

In this chapter, the methods employed to address structural reliability problems are discussed. Among the various available approaches, emphasis is placed on simulation techniques and on the use of surrogate models as an effective strategy to mitigate the high computational cost typically associated with structural safety assessment within the Performance-Based Earthquake Engineering (PBEE) framework. These approaches enable the probabilistic evaluation of structural performance under seismic actions while maintaining computational feasibility.

Structural reliability quantifies the confidence that a structure or structural system will meet the prescribed design requirements throughout its intended lifetime, given the specified operating conditions. This concept can be expressed through the fundamental reliability problem, formulated in Eq. (3.4), presented in Section 3.1.1.

In general, Eq. (3.4) cannot be solved analytically. In most cases, the probability of failure is estimated using transformation techniques or simulation-based approaches (Melchers; Beck, 2018). This work focuses on simulation-based approaches, in which the simulator is regarded as a mapping that takes the system parameters as inputs $\mathcal{X}$ and provides the corresponding output quantities $\mathcal{Y}$ (Zhu, 2023). In addition, the Nonlinear Time History Analyses (NLTHA) required to evaluate the vector of Engineering Demand Parameters (EDPs) in the PBEE framework considers a computational model of the structure, which can also be seen as a mapping from the input parameter space to the output response space.

A discussion of deterministic and stochastic simulators is presented in the following sections, along with surrogate modeling techniques designed to alleviate the computational burden associated with repeatedly performing such analyses. In the subsequent discussions, the vector $\mathbf{X} \in \mathbb{R}^M$ refers to the set of random variables and design variables, where $M = (n_{\mathrm{RV}} + n_{\mathrm{DV}})$.

4.1 Deterministic Simulators

The simulation process can be understood as the numerical evaluation of an experiment that cannot be performed in practice, since it would require testing the structure under all possible combinations of uncertainties in resistance and load, which are represented as random variables (Beck, 2024). These evaluations are carried out using a computational model $\mathcal{M}$, which represents the behavior of a mechanical system governed by its fundamental equations. This model is often treated as a black box, meaning its internal behavior are not explicitly considered, and is generally expressed as:

$$y = \mathcal{M}(\mathbf{x}) \tag{4.1}$$

where $\mathbf{x}$ represents a realization of the vector $\mathbf{X}$ that parameterizes the variability of the input parameters and y denotes the corresponding model output, which is represented as the random variable Y.

Typically, the input parameters include structural geometry, material properties, boundary conditions, and, when dealing with time-dependent phenomena, initial conditions. The outputs correspond to quantities that characterize the behavior of the structural system, such as the EDPs (Zhu, 2023; Lüthen *et al.*, 2024b).

In engineering applications, simulators are usually deterministic. This means that, for a given set of input parameters, the simulator will always return the same output values. Mathematically, this can be expressed as:

$$\begin{aligned} \mathcal{M}_d : \mathcal{D}_{\mathbf{X}} &\rightarrow \mathcal{D}_{\mathbf{Y}} \\ \mathbf{x} &\rightarrow \mathcal{M}_d(\mathbf{x}) \end{aligned} \tag{4.2}$$

where the subscript $_d$ denotes a deterministic simulator, $\mathcal{D}_{\mathbf{X}}$ is the domain of the input parameters, and $\mathcal{D}_{\mathbf{Y}}$ is the corresponding output space.

The vector $\mathbf{x}$ is represented by a finite number M of scalar input parameters, with $\mathcal{D}_{\mathbf{X}} \subset \mathbb{R}^M$. The outputs correspond to a single scalar quantity, such that $\mathcal{D}_{\mathbf{Y}} \subset \mathbb{R}^1$.

The predictive capacity of a simulator is constrained by the accuracy of the system representation. Its performance is influenced by the assumptions and simplifications adopted in the modeling process, which introduce modeling errors, as well as by uncertainties in the model parameters. These uncertainties are generally classified into two categories:

- *Aleatory uncertainty*, associated with the irreducible intrinsic variability of the parameters;
- *Epistemic uncertainty*, arising from limited knowledge, modeling assumptions, or parameter estimation errors.

Although simulators are typically deterministic, it is not possible to avoid dealing with uncertainties in engineering applications. To address this, a general framework for uncertainty quantification was developed by Rocquigny (2006) and Sudret (2007), consisting of the following steps:

- **Step A**: definition of the computational model representing the engineering system;

- **Step B**: quantification of the sources of uncertainty by identifying and modeling the parameters whose exact values are uncertain or cannot be specified deterministically. This is commonly achieved using probability theory, where uncertainties are represented quantitatively (e.g., through probability distributions);

- **Step C**: propagation of uncertainties from the input parameters to the outputs by means of simulations with the computational model. In a probabilistic context, the output is a random variable characterized by a probability distribution. For reliability analysis and risk assessment, particular interest is given to distribution moments, quantiles, and the probability of failure.

A complementary aspect of Step C is sensitivity analysis, which evaluates the contribution of input uncertainties to the output. This step helps identify the parameters that most strongly influence the response, thereby guiding targeted investigations to efficiently reduce uncertainty (Zhu, 2023).

The following sections present a review and discussion of Monte Carlo (MC) simulation, a classical method for uncertainty propagation. As mentioned in Step C, when the uncertain input parameters of the simulator are modeled as a random vector, propagating these uncertainties through Eq. (4.2) results in the output being a random variable.

4.1.1 Monte Carlo (MC) Simulation

With the computational model available, MC simulation consists of generating random samples of the input variables according to their joint Probability Density Function (PDF) $f_{\mathbf{X}}(\mathbf{x})$. The idea is to produce a set of realizations (also referred to as simulations) of Y using the computational model as a sampler, and then analyze the sample statistics. Given a set of samples $\mathcal{X} = \{\mathbf{x}^{(1)}, \ldots, \mathbf{x}^{(N_{\text{rea}})}\}$ drawn from $f_{\mathbf{X}}(\mathbf{x})$, the computational model is evaluated as $y^{(i)} = \mathcal{M}_d(\mathbf{x}^{(i)})$ to obtain the output samples $\mathcal{Y} = \{y^{(1)}, \ldots, y^{(N_{\text{rea}})}\}$.

The samples of $\mathbf{X}$ are usually generated independently, so that $\mathcal{X}$ can be regarded as a single realization of the random vector sequence $\{\mathbf{X}^{(1)}, \ldots, \mathbf{X}^{(N_{\text{rea}})}\}$. Consequently, the realizations of Y are also independent, and $\mathcal{Y}$ can be regarded as a single realization of the random variable sequence $\{Y^{(1)}, \ldots, Y^{(N_{\text{rea}})}\}$ (Zhu, 2023). The empirical mean of the random variable Y is given by:

$$\hat{\mu}_Y = \frac{1}{N_{\text{rea}}} \sum_{i=1}^{N_{\text{rea}}} y_i \tag{4.3}$$

The estimator of the variance can be calculated as:

$$\hat{\sigma}_Y^2 = \frac{1}{N_{\text{rea}}} \sum_{i=1}^{N_{\text{rea}}} \left(y_i - \hat{\mu}_Y\right)^2 \tag{4.4}$$

The random variable $\hat{\mu}_Y$ converges almost surely to the deterministic value of the population mean $\mathbb{E}[Y]$ as N_{rea} increases, that is, $\hat{\mu}_Y \overset{a.s.}{\to} \mathbb{E}[Y]$. This property justifies the common use of $\hat{\mu}_Y$ as an estimator of $\mathbb{E}[Y]$. The Central Limit Theorem can then be applied to quantify the estimation uncertainty, which states that:

$$\sqrt{N_{\text{rea}}}\left(\hat{\mu}_Y - \mathbb{E}\left[Y\right]\right) \overset{d}{\to} \mathcal{N}\left(0, \text{Var}[Y]\right) \tag{4.5}$$

where $\mathcal{N}\left(0, \text{Var}[Y]\right)$ denotes the standard normal distribution with zero mean and variance $\text{Var}[Y]$.

From Eq. (4.4), it follows that the sample variance $\hat{\sigma}_Y^2$ converges almost surely to the distribution variance $\text{Var}[Y]$, as in $\hat{\sigma}_Y^2 \overset{a.s.}{\to} \text{Var}[Y]$.

To calculate the probability of failure associated with the N_{rea} realizations, each simulation outcome falls into one of the two domains defined by the limit state in Eq. (3.3). These domains can be identified by the indicator function $I(\mathbf{x})$, defined as:

$$\begin{aligned} I\left[\mathbf{x}\right] &= 1 \text{ if } \mathbf{x} \in \Omega_f \\ I\left[\mathbf{x}\right] &= 0 \text{ if } \mathbf{x} \in \Omega_s \end{aligned} \tag{4.6}$$

The probability of failure is then estimated as (Beck, 2024):

$$\hat{p}_f = \frac{1}{N_{\text{rea}}} \sum_{k=1}^{N_{\text{rea}}} I\left[\mathbf{x}_k\right] \tag{4.7}$$

MC simulation is widely applied to solve complex problems across different fields, providing satisfactory results for both linear and nonlinear problems in structural engineering. Moreover, there is no restriction on the complexity of the model, as long as the model can be solved and therefore used in the simulation (Beck, 2024). The estimator in Eq. (4.7) is based on a finite sample and is subject to a statistical error, which corresponds to the variance of $I(\mathbf{x})$. The coefficient of variation of the estimator is expressed as:

$$CV_{\hat{p}_f} = \frac{1}{\sqrt{N_{\text{rea}} \times p_f}} \tag{4.8}$$

In structural reliability applications, probabilities of failure p_f are typically very low (10^{-3}–10^{-6}, denoted as 10^{-r}). To achieve a coefficient of variation smaller than 10% ($CV_{\hat{p}_f} \leq 10\%$), approximately 10^{r+2} simulations are required. When a Finite Element (FE) computational model is employed to perform the simulations, the cost of each evaluation cannot be neglected, making such a number of simulations computationally prohibitive

(Sudret, 2012). To address this issue, several methods have been proposed to improve efficiency. Among them, the use of surrogate models, or metamodels, stands out as a promising alternative due to their low evaluation cost. This approach is detailed in the following section.

4.1.2 Metamodels or Surrogate Models

The use of MC simulation to assess structural performance is often prohibitive by its high computational cost, as it requires repeated evaluations of the FE model. A common strategy to mitigate this cost is to employ metamodels that replace the original simulator.

Metamodels replace the original high-fidelity computational model $\mathcal{M}$ with a simplified representation, typically analytical, that approximates the model outputs (Beck, 2024). This approximation is computationally inexpensive, providing a significant advantage over the original model. The replacement can be expressed mathematically for deterministic simulators as:

$$\tilde{y} = \tilde{\mathcal{M}}_d(\mathbf{x}) \approx \mathcal{M}_d(\mathbf{x}) \tag{4.9}$$

where $\tilde{\mathcal{M}}_d$ corresponds to the considered metamodel.

According to Sudret (2012), metamodels have the following properties: they belong to a specific class of functions characterized by a set of parameters once the class is selected; they are computationally inexpensive to evaluate; and they are fitted to the original model using a set of observations from the true model.

Metamodels can be classified into two groups, depending on how the function space is represented: (1) those defined by a countable set of parameters, and (2) those defined by a certain degree of regularity. In the first group, popular approaches include polynomial chaos expansions (Berveiller; Sudret; Lemaire, 2006), wavelet expansions (Mallat, 2009), and artificial neural networks (LeCun; Bengio; Hinton, 2015; Cartwright, 2015). In the second group, widely used methods include kernel regression (Schölkopf; Smola, 2002), Gaussian processes (Williams; Rasmussen, 2006; Lataniotis; Marelli; Sudret, 2018), and support vector regression (Moustapha *et al.*, 2018; Zhu, 2023).

For the metamodels considered in this work, the detailed structure of the computational model is treated as a black box, meaning that an input value produces the corresponding model response. The simulator is evaluated at a set of input values $\mathcal{X} = \{\mathbf{x}^{(1)}, \ldots, \mathbf{x}^{(S)}\}$ referred to as the Design of Experiment (DoE), with each input $\mathbf{x}^{(i)} \in \mathbb{R}^M$. The associated outputs are collected in $\mathcal{Y} = \{y^{(1)}, \ldots, y^{(S)}\}$, where $y^{(i)} = \mathcal{M}_d(\mathbf{x}^{(i)})$. Equivalently, the DoE can be represented as a matrix of inputs $\mathbf{X} \in \mathbb{R}^{S \times M}$ and a vector of outputs $\mathbf{Y} \in \mathbb{R}^S$. The metamodel is then constructed from the generated input–output pairs $(\mathbf{X}, \mathbf{Y})$ without

modifying the simulator. Methods for generating the DoE are discussed in the following sections.

The next section introduces the Kriging metamodel, also known as Gaussian processes.

4.1.2.1 Kriging

The Kriging methodology originated as a statistical approach for evaluating mineral resources and reserves, introduced by the South African engineer Krige (1951), which laid the foundation for the field of geostatistics later formalized by Matheron (1963). The technique was named after D. Krige in recognition of his contributions, and its core idea is to model a function known only at a finite number of sampling points as a Gaussian random field. In this context, the sampling space corresponds to a physical domain of dimension M (Sudret, 2012). The concepts that enabled its application in computational experiments were introduced by Sacks *et al.* (1989) in 1989, establishing the basis for Kriging-based metamodeling. They are:

- The data do not represent physical measurements but rather the outputs of a computer code;
- The points at which the data are collected do not correspond to physical coordinates in a 2D or 3D space but to parameters in an abstract input space.

Thus, the main objective of Kriging is to use the results of a complex model at a finite number of sampling points to construct a prediction model capable of estimating the response at any other point within the domain (Matheron, 1973). The mathematical formulation treats the function to be approximated as a realization of a Gaussian process, defined as:

$$\tilde{\mathcal{M}}_d\left(\mathbf{x}\right) \simeq \mathbf{f}\left(\mathbf{x}\right)^T \boldsymbol{\beta} + Z_{\mathrm{kr}}(\mathbf{x}) \tag{4.10}$$

where $\mathbf{f}(\mathbf{x})^T\boldsymbol{\beta}$ represents the mean value of the Gaussian process, i.e., the trend, with $\mathbf{f}(\mathbf{x})$ denoting the vector of basis functions evaluated at $\mathbf{x}$ and $\boldsymbol{\beta}$ the corresponding vector of coefficients (Sacks *et al.*, 1989; Matheron, 1973). The term $Z_{\mathrm{kr}}(\mathbf{x})$ is a zero-mean Gaussian stochastic field with variance $\sigma^2_{Z_{\mathrm{kr}}}$ and covariance function $\sigma^2_{Z_{\mathrm{kr}}} R(\mathbf{x}_j, \mathbf{x}_k; \boldsymbol{\theta})$, where $\boldsymbol{\theta}$ is the vector of hyperparameters defining the Kriging fit. The correlation function $R(\cdot)$ quantifies the similarity between sampling points and is calibrated by estimating the hyperparameters $\boldsymbol{\theta}$. The associated correlation matrix $\mathbf{R}$ is assembled by evaluating $R(\mathbf{x}_j, \mathbf{x}_k; \boldsymbol{\theta})$ for all pairs of design points.

Different variants of the Kriging metamodel are defined depending on the type of trend: *Simple Kriging*, where the coefficients $\boldsymbol{\beta}$ are fixed to one and the regression functions are arbitrary but fully specified; *Ordinary Kriging*, where the trend is constant with coefficient β_0 and, by convention, $\mathbf{f}(\mathbf{x}) = 1$; and *Universal Kriging*, where the trend is represented as a linear combination of prescribed arbitrary functions. Both Simple and Ordinary Kriging can be regarded as special cases of Universal Kriging (Dubourg, 2011; Lataniotis *et al.*, 2024). The linear combination of the trend is expressed as:

$$\mathbf{f}\left(\mathbf{x}\right)^T \boldsymbol{\beta} = \sum_{i=0}^{P} \beta_i f_i\left(\mathbf{x}\right) \tag{4.11}$$

where P corresponds to the polynomial order of the trend function.

In Universal Kriging, the trend is defined by a linearly independent vector of regression functions $\mathbf{f}(\mathbf{x})$. Several types of functions can be selected for this purpose, such as constants or polynomials (Lataniotis *et al.*, 2024). The coefficients of the weight vector $\boldsymbol{\beta}$ can be estimated using minimization or interpolation techniques, such as the Least Squares Method, which aims to minimize the difference between the exact response and its approximation. This process is expressed as:

$$\boldsymbol{\beta} = \left(\mathbf{F}^T\mathbf{R}^{-1}\mathbf{F}\right)^{-1}\mathbf{F}^T\mathbf{R}^{-1}\mathbf{Y} \tag{4.12}$$

where $\mathbf{F}$ is the regression matrix of size $S \times n_c$, containing the basis regression functions evaluated at all S support points, with n_c coefficients to be determined; $\mathbf{Y}$ is a vector of size $S \times 1$ containing the model outputs at the support points, i.e., $\mathbf{Y} = \mathcal{M}(\mathbf{x}_k)_{k=1,\ldots,S}^T$; and $\mathbf{R}$ is the $S \times S$ correlation matrix between pairs of support points (Beck, 2024).

The correlation matrix $\mathbf{R} = [R_{jk}]$ is constructed from a correlation function (also referred to as a kernel function), which quantifies the similarity between observations and new points. This function is a key component of Kriging prediction, since the correlation between two points depends only on their distance. Consequently, the choice of correlation function has a strong influence on the smoothness of the resulting metamodel (Milanez, 2022). A valid correlation function must satisfy two conditions: (1) the correlation matrix must be positive semi-definite for any number of support points S, and (2) the function must be symmetric (Lataniotis *et al.*, 2024). Among the correlation families described in the literature, two are considered in this work: the Exponential and Gaussian families.

- **Exponential**

$$R(\mathbf{x}_j, \mathbf{x}_k; \theta) = \exp\left(-\frac{\|\mathbf{x}_j - \mathbf{x}_k\|}{\theta}\right) \tag{4.13}$$

The resulting sample paths are continuous but non-differentiable.

- **Gaussian**

$$R(\mathbf{x}_j, \mathbf{x}_k; \theta) = \exp\left(-\frac{1}{2}\left(\frac{\|\mathbf{x}_j - \mathbf{x}_k\|}{\theta}\right)^2\right) \tag{4.14}$$

The resulting sample paths are infinitely differentiable.

The entries of the correlation matrix $\mathbf{R} = [R_{jk}]$, considering the Gaussian correlation family, are computed for support points in the i-th direction as:

$$R_{jk}(\mathbf{x}_j, \mathbf{x}_k; \boldsymbol{\theta}) = \prod_{i=1}^{M} \exp\left(-\frac{1}{2}\left(\frac{|\,(x_i)_j - (x_i)_k\,|}{\theta_i}\right)^2\right) \tag{4.15}$$

where M is the number of input variables (i.e., the input dimension), and θ_i are the hyperparameters controlling the correlation along each input direction.

The stochastic field represented by the second term in Eq. (4.10), $Z_{\text{kr}}(\mathbf{x})$, has a constant variance $\sigma^2_{Z_{\text{kr}}}$, calculated as:

$$\sigma^2_{Z_{\text{kr}}} = \frac{1}{S}\left(\mathbf{Y} - \mathbf{F}\boldsymbol{\beta}\right)^T \mathbf{R}^{-1}\left(\mathbf{Y} - \mathbf{F}\boldsymbol{\beta}\right), \tag{4.16}$$

As can be observed, the correlation matrix $\mathbf{R}$, the weight vector $\boldsymbol{\beta}$, and the variance of the stochastic field $\sigma^2_{Z_{\text{kr}}}$ all depend on the hyperparameter $\boldsymbol{\theta}$. Since the value of $\boldsymbol{\theta}$ is usually unknown, it must be estimated during the modeling process. One possibility is to adopt a trial-and-error approach based on values reported in similar problems in the literature. Although this strategy aims to minimize the error, it requires a reference solution for the problem under study, which may not always be available (Kroetz, 2015). Alternatively, several methods have been proposed to estimate a suitable set of parameters, the most common being maximum likelihood estimation and cross-validation (Dubourg, 2011). The maximum likelihood estimation can be formulated as an optimization problem expressed as:

$$\hat{\boldsymbol{\theta}} = \arg\min_{\boldsymbol{\theta} \in \mathcal{D}_\theta} \left[-\log \mathcal{L}(\boldsymbol{\theta}; \mathcal{Y})\right], \tag{4.17}$$

where $\mathcal{L}$ denotes the reduced likelihood function.

Several methods can be employed to solve the optimization problem in Eq. (4.17), including both local and global approaches. The choice between them involves trade-offs: local methods generally converge faster but may perform poorly when the objective function exhibits flat regions or multiple local minima (Lataniotis *et al.*, 2024). Once the hyperparameters $\boldsymbol{\theta}$, the coefficients $\boldsymbol{\beta}$, and the variance $\sigma^2_{Z_{\text{kr}}}$ are estimated, the second term of the stochastic field in Eq. (4.10) can be computed as:

$$Z_{\text{kr}}(\mathbf{x}) = \mathbf{r}(\mathbf{x})^T \mathbf{R}^{-1} (\mathbf{Y} - \mathbf{F}\boldsymbol{\beta}) \tag{4.18}$$

where $\mathbf{r}(\mathbf{x}) \in \mathbb{R}^S$ is the vector of correlations between the prediction point $\mathbf{x}$ and each support point $\mathbf{x}_k$, defined as $\mathbf{r}(\mathbf{x}) = \{R(\mathbf{x}, \mathbf{x}_k; \boldsymbol{\theta})\}_{k=1}^S$, and $\mathbf{R}$ is the correlation matrix (Beck, 2024).

Once all parameters are estimated and the model is defined, the prediction at any new point $\mathbf{x}$ is assumed to follow a normal distribution $\tilde{\mathcal{M}}_d \sim \mathcal{N}\left(\mu_{\tilde{\mathcal{M}}_d}(\mathbf{x}), \sigma^2_{\tilde{\mathcal{M}}_d}(\mathbf{x})\right)$, with mean $\mu_{\tilde{\mathcal{M}}d}(\mathbf{x})$ and variance $\sigma^2_{\tilde{\mathcal{M}}_d}(\mathbf{x})$ at any point, $\mathbf{x}$, of the design space, given as:

$$\begin{aligned} \mu_{\tilde{\mathcal{M}}_d}(\mathbf{x}) &= \mathbf{f}(\mathbf{x})^T \boldsymbol{\beta} + \mathbf{r}(\mathbf{x})^T \mathbf{R}^{-1} (\mathbf{Y} - \mathbf{F}\boldsymbol{\beta}) \\ \sigma^2_{\tilde{\mathcal{M}}_d}(\mathbf{x}) &= \sigma^2_{Z_{\text{kr}}} \left(1 - \mathbf{r}(\mathbf{x})^T \mathbf{R}^{-1} \mathbf{r}(\mathbf{x}) + \mathbf{u}(\mathbf{x})^T \left(\mathbf{F}^T \mathbf{R}^{-1} \mathbf{F}\right)^{-1} \mathbf{u}(\mathbf{x})\right) \end{aligned} \tag{4.19}$$

where $\mathbf{u}(\mathbf{x}) = \mathbf{F}^T \mathbf{R}^{-1} \mathbf{r}(\mathbf{x}) - \mathbf{f}(\mathbf{x})$.

Kriging can also account for observation noise, modeled as an additive Gaussian term $\boldsymbol{\varepsilon} \sim \mathcal{N}(0, \boldsymbol{\Sigma}_n)$ and referred to as noisy Kriging:

$$\mathcal{Y}_S = \left[\tilde{\mathcal{M}}_d\left(\mathbf{x}^{(1)}\right), \ldots, \tilde{\mathcal{M}}_d\left(\mathbf{x}^{(S)}\right)\right]^T + \boldsymbol{\varepsilon} \tag{4.20}$$

where $\mathcal{X}_S = [\mathbf{x}^{(1)}, \ldots, \mathbf{x}^{(S)}]$ is the matrix collecting the S support points within the design space with $\mathcal{Y}_S$ the vector of corresponding observed model outputs; and $\boldsymbol{\Sigma}_n$ is the noise covariance matrix.

In particular, $\boldsymbol{\Sigma}_n$ may be defined to represent homoscedastic, heteroscedastic, or correlated noise (Lataniotis *et al.*, 2024). In the homoscedastic case, the variance σ_n^2 is constant across all observed responses, and the covariance matrix is given by $\boldsymbol{\Sigma}_n = \sigma_n^2 \mathbf{I}$, where $\mathbf{I}$ is the identity matrix. In the heteroscedastic case, the variance differs for each observed response but remains uncorrelated, and the covariance matrix is given by $\boldsymbol{\Sigma}_n = \text{diag}(\sigma_n^2)$. In the correlated noise case, the variance may differ across responses, and correlations between observations are also possible. Examples of noise sources include inherent variability observed in measurements obtained from physical experiments; intrinsic variability associated with the model itself; and variability arising when combining physical experiments with numerical simulations, commonly referred to as hybrid simulators (Pires *et al.*, 2025a).

Once calibrated, noisy Kriging provides predictions of the mean $\mu_{\hat{Y}}(\mathbf{x})$ output and associated variance $\sigma^2_{\hat{Y}}(\mathbf{x})$ given as

$$\begin{aligned} \mu_{\hat{Y}}(\mathbf{x}) &= \mathbf{f}(\mathbf{x})^T \hat{\boldsymbol{\beta}} + \mathbf{c}(\mathbf{x})^T \mathbf{C}^{-1} \left(\mathcal{Y}_S - \mathbf{F}\hat{\boldsymbol{\beta}}\right) \\ \sigma_{\hat{Y}}(\mathbf{x}) &= \left(\sigma^2_{Z_{\text{kr}}} - \mathbf{c}^T(\mathbf{x}) \mathbf{C}^{-1} \mathbf{c}(\mathbf{x}) + \mathbf{u}_c^T(\mathbf{x}) \left(\mathbf{F}^T \mathbf{C}^{-1} \mathbf{F}\right)^{-1} \mathbf{u}_c(\mathbf{x})\right) \end{aligned} \tag{4.21}$$

where $\hat{\boldsymbol{\beta}} = \left(\mathbf{F}^T \mathbf{C}^{-1} \mathbf{F}\right)^{-1} \mathbf{F}^T \mathbf{C}^{-1} \mathcal{Y}$ is the generalized least squares estimate of the regression coefficients, $\mathbf{F}$ is the regression function matrix evaluated at the training points, $\mathbf{C} =$

$\sigma^2_{Z_{\text{kr}}}\mathbf{R}+\boldsymbol{\Sigma}_n$ is the covariance matrix that incorporates both the process correlation and the observation noise, $\mathbf{c}(\mathbf{x})=\sigma^2_{Z_{\text{kr}}}\mathbf{r}(\mathbf{x})$ is the cross-covariance vector between the prediction point and the training points, and $\mathbf{u}_c(\mathbf{x})=\mathbf{F}^T\mathbf{C}^{-1}\mathbf{c}(\mathbf{x})-\mathbf{f}(\mathbf{x})$.

4.1.2.2 Adaptive Kriging

The main idea of adaptive Kriging is to iteratively add new infill points to the DoE to improve the accuracy of the metamodel (Pires, 2021). This approach assumes that an initial Kriging model has already been constructed.

Several methodologies have been proposed for adaptive DoEs, all aiming to identify the next point $\mathbf{x}^{(S+1)}$ that improves the prediction by solving a global optimization subproblem. These approaches rely on the definition of a criterion, which depends on the input $\mathbf{x}$ and is maximized or minimized within a region of interest, such as a specific contour or the neighborhood of the global optimum of the model (Dubourg, 2011).

4.1.2.2.1 Efficient Global Optimization (EGO)

The technique discussed here was originally presented in Dubourg (2011) and is based on an efficient global optimization strategy that gained popularity in the 1990s following the work of Jones, Schonlau and Welch (1998). The main idea is to address a global optimization problem involving an objective function $\mathcal{M}$ that is expensive to evaluate. This problem can be formulated as:

$$\mathbf{x}^*=\arg\min_{\mathbf{x}\in\mathcal{D}_\mathbf{X}}\mathcal{M}(\mathbf{x}) \tag{4.22}$$

The innovation of the EGO algorithm lies in the fact that it selects the next evaluation point $\mathbf{x}^{(S+1)}$ by exploiting the probabilistic information provided by the Gaussian process predictor, which is constructed from a global experimental design that considers the entire input domain, rather than relying solely on the local information given by the partial derivatives of the function $\mathcal{M}$ with respect to $\mathbf{x}$.

Considering the initial dataset $\mathcal{D}=\{(\mathbf{x}^{(i)},y^{(i)})\}_{i=1}^S$ and an initial prediction of the Gaussian process $\hat{Y}(\mathbf{x})=\mu_{\hat{Y}}(\mathbf{x})$, Jones, Schonlau and Welch (1998) define the improvement function:

$$I(\mathbf{x})=\begin{cases}y_{\min}-\hat{Y}(\mathbf{x}), & \text{if } \hat{Y}(\mathbf{x})\le y_{\min},\\ 0, & \text{otherwise}\end{cases}=\max\{y_{\min}-\hat{Y}(\mathbf{x}),0\} \tag{4.23}$$

where $y_{\min}=\min\{y^{(i)},\ i=1,\dots,S\}$ is the minimum observed value of $\hat{Y}$ in the dataset $\mathcal{D}$.

The improvement at $\mathbf{x}$ is itself a Gaussian process, as it depends on the Gaussian prediction $\hat{Y}(\mathbf{x})$. Since negative improvements correspond to declines, the process is truncated to non-negative values. Consequently, it was proposed to use its expectation, leading to the expected improvement expressed as:

$$EI\left(\mathbf{x}\right) = \int_{-\infty}^{y_{min}} \left(y_{min} - \hat{y}\right) \varphi\left(\frac{\hat{y} - \mu_{\hat{Y}}\left(\mathbf{x}\right)}{\sigma_{\hat{Y}}\left(\mathbf{x}\right)}\right) \mathrm{d}\hat{y} \tag{4.24}$$

After integration by parts, the expression in Eq. 4.24 can be rewritten as:

$$EI\left(\mathbf{x}\right) = \left(y_{min} - \mu_{\hat{Y}}\right) \Phi\left(\frac{\hat{y} - \mu_{\hat{Y}}\left(\mathbf{x}\right)}{\sigma_{\hat{Y}}\left(\mathbf{x}\right)}\right) + \sigma_{\hat{Y}} \varphi\left(\frac{\hat{y} - \mu_{\hat{Y}}\left(\mathbf{x}\right)}{\sigma_{\hat{Y}}\left(\mathbf{x}\right)}\right) \tag{4.25}$$

where φ represents the standard Gaussian PDF and Φ represents the standard Gaussian Cumulative Distribution Function (CDF).

The next point to be added to the DoE is selected as the one that maximizes the expected improvement:

$$\mathbf{x}^{(S+1)} = \arg\max_{\mathbf{x}} EI\left(\mathbf{x}\right) \tag{4.26}$$

With the new infill point $\mathbf{x}^{(S+1)}$ added to the DoE, the metamodel is recalibrated.

4.2 Stochastic Simulators

In contrast to deterministic computational models, where uncertainties arise solely from the input variables, stochastic simulators are a class of models whose responses remain random even for a fixed set of input parameters, due to intrinsic stochasticity. Stochastic simulators can be represented as:

$$\begin{aligned} \mathcal{M}_s : \mathcal{D}_{\mathbf{X}} \times \Omega &\to \mathbb{R} \\ \left(\mathbf{x}, \omega\right) &\to \mathcal{M}_s\left(\mathbf{x}, \omega\right) \end{aligned} \tag{4.27}$$

where Ω denotes the probability space that represents the internal stochasticity.

The intrinsic stochasticity arises from the fact that the input variables $\mathbf{x}$ provide only partial information about the model response, while other relevant variables, referred to as latent random variables $\mathbf{Z}(\omega)$, are not explicitly considered as inputs and remain random. For a fixed vector of input parameters $\mathbf{x}_0$, each model evaluation corresponds to a particular realization of the latent variable, that is, a specific $\omega_0 \in \Omega$, which is usually determined by the random seed, producing one realization of the output random variable.

The stochastic simulator can be viewed as a deterministic mapping of the input vector $\mathbf{x}$ and the latent random variable $\mathbf{Z}$, expressed as $\mathcal{M}_s\left(\mathbf{x}, \omega\right) = \mathcal{M}_d\left(\mathbf{x}, \mathbf{Z}(\omega)\right)$. In

practice, only $\mathbf{x}$ can be controlled when evaluating the model, while $\mathbf{Z}$ is drawn from its underlying probability distribution. For a fixed input $\mathbf{x}_0$, each run of the simulator yields a different realization of $\mathbf{Z}$, denoted $z_0 = \mathbf{Z}(\omega_0)$, and consequently one realization of the output random variable $\mathcal{M}_d(\mathbf{x}_0, z_0)$. By performing R replications with the same input but different draws $\{z_1, \ldots, z_R\}$, the conditional distribution of $Y_{x_0} = \mathcal{M}_d(\mathbf{x}_0, \cdot)$ given $\mathbf{x}_0$ can be empirically characterized. The complete model, incorporating randomness from both the input and the latent variables, is then expressed as:

$$Y = \mathcal{M}_s\left(\mathbf{X}\left(\omega\right), \omega\right) = \mathcal{M}_d\left(\mathbf{X}\left(\omega\right), \mathbf{Z}(\omega)\right) \tag{4.28}$$

where $\mathbf{X}$ represents the random input vector (Zhu; Sudret, 2023; Zhu, 2023; Pires *et al.*, 2025a).

Common examples of stochastic simulators include epidemiological models, in which disease transmission and recovery are treated as random events with associated probabilities, and financial models, where stock prices are represented through stochastic processes. In addition, aero-servo-elastic simulations commonly used in wind turbine engineering exhibit significant latent stochasticity, as they rely on stochastic turbulent wind fields (Pires *et al.*, 2025a). Moreover, some sources of uncertainty may not be accessible or controllable, meaning that not all relevant variables affecting the model response can be identified. Such experiments can also be regarded as stochastic simulators (Zhu, 2023).

4.2.1 Stochastic Emulators

Similar to deterministic models, stochastic models can also be emulated to reduce the computational effort required for their evaluation. Referred to as stochastic emulators, they are represented in this work as follows:

$$Y_{\mathbf{x}} = \tilde{\mathcal{M}}_s\left(\mathbf{x}, \omega\right) \approx \mathcal{M}_s\left(\mathbf{x}, \omega\right) \tag{4.29}$$

Stochastic emulators are particularly relevant for representing structural responses influenced by multiple sources of uncertainty, and their key advantage lies in their ability to capture general response distributions beyond classical parametric assumptions (Kim; Wang, 2025; Zhu; Sudret, 2023; Lüthen *et al.*, 2024b).

Recent literature has proposed different methodologies for constructing stochastic emulators. Kim and Wang (2025) adopted a surrogate model based on dimensionality reduction (DR-SM) to represent the seismic response of structures. Yi and Taflanidis (2024) and Yi and Taflanidis (2025) proposed a Gaussian process-based stochastic emulator, which was evaluated using a structural example subjected to ground motions from stochastic ground motion models. Zhu (2023), in his doctoral research, introduced two stochastic

emulator techniques: the Generalized Lambda Models (GLaM) (Zhu; Sudret, 2021; Lüthen *et al.*, 2024a) and the Stochastic Polynomial Chaos Expansions (SPCE) (Zhu; Sudret, 2023; Lüthen *et al.*, 2024b).

The next section introduces the Stochastic Polynomial Chaos Expansions (SPCE).

4.2.1.1 Stochastic Polynomial Chaos Expansions (SPCE)

SPCE correspond to a stochastic emulator designed to reproduce the PDF of the random variable $Y_{\mathbf{x}} \equiv Y \mid \mathbf{X} = \mathbf{x}$. Introduced by (Zhu; Sudret, 2023), SPCE incorporates an artificial latent variable $\mathbf{Z}$ to capture the intrinsic stochasticity of the simulator within the framework of Polynomial Chaos Expansions (PCE).

PCE constitute a well-established and widely applied metamodeling technique for deterministic simulators. Considering the random vector with independent components $\mathbf{X} \in \mathbb{R}^M$ described by a joint PDF $f_{\mathbf{X}}$, PCE approximate the computational model output $\mathcal{M}_d(\mathbf{x})$ by a sum of orthonormal polynomials, defined as:

$$\tilde{\mathcal{M}}_d(\mathbf{x}) \approx \sum_{\boldsymbol{\alpha} \in \mathbb{N}^M} c_{\boldsymbol{\alpha}} \psi_{\boldsymbol{\alpha}}(\mathbf{x}) \tag{4.30}$$

where $\psi_{\boldsymbol{\alpha}}$ denotes multivariate orthonormal polynomials with respect to the input distribution $f_{\mathbf{X}}$, and $c_{\boldsymbol{\alpha}}$ are the corresponding coefficients to be estimated, associated with the basis function $\psi_{\boldsymbol{\alpha}}$ defined by the multi-index $\boldsymbol{\alpha}$.

Assuming that $\mathbf{X}$ has independent components, the basis function $\psi_{\boldsymbol{\alpha}}$ is obtained as the product of univariate orthogonal polynomials:

$$\psi_{\boldsymbol{\alpha}}(\mathbf{x}) = \prod_{j=1}^{M} \phi_{\alpha_j}^{(j)}(x_j) \tag{4.31}$$

where each $\phi_{\alpha_j}^{(j)}$ denotes a univariate orthonormal polynomial of degree α_j, associated with the marginal distribution of the j-th component of $\mathbf{X}$.

The spectral representation in Eq. (4.30) involves an infinite series of orthogonal polynomial terms, which must be truncated in practice. The standard truncation scheme selects all polynomials whose total degree does not exceed a prescribed value p, i.e., $\mathcal{A}^{p,M} = \{\boldsymbol{\alpha} \in \mathbb{N}^M, \sum_{j=1}^{M} \alpha_j \leq p\}$, where $\mathcal{A}^{p,M}$ denotes the multi-index set of retained basis functions. This approach, however, leads to a rapidly increasing number of terms as p and M grow (Zhu; Sudret, 2023). To mitigate this growth, Blatman and Sudret (2010) proposed the hyperbolic or q-norm truncation, a more flexible scheme defined as:

$$\mathcal{A}^{p,q,M} = \{\boldsymbol{\alpha} \in \mathbb{N}^M, \|\boldsymbol{\alpha}\|_q \leq p\} \tag{4.32}$$

where p is the maximum polynomial degree and $q \in (0, 1]$ defines the quasi-norm $\|\boldsymbol{\alpha}\|_q = \left(\sum_{j=1}^{M} |\alpha_j|^q\right)^{1/q}$ (Zhu; Sudret, 2023).

As a stochastic extension of PCE, the SPCE formulation is obtained by introducing the latent variable $\mathbf{Z}$ into the framework. Let $F_{Y\,|\,\mathbf{X}}(y\,|\,\mathbf{x})$ denotes the CDF associated with $Y_{\mathbf{x}}$. By applying the probability integral transform, any continuous random variable $\mathbf{Z}$ can be mapped to the target distribution, as shown in (Lüthen *et al.*, 2024b; Pires *et al.*, 2025b):

$$Y_{\mathbf{x}} \overset{d}{=} F^{-1}_{Y|\mathbf{X}}\left(F_{\mathbf{Z}}(\mathbf{Z}) \mid \mathbf{x}\right) \tag{4.33}$$

where F_Z denotes the CDF of $\mathbf{Z}$. The equality in Eq. (4.33) is to be understood *in distribution*, meaning that the random variables on both sides of the equation follow the same distribution.

In Eq. (4.33), the right-hand side is a deterministic function of the input $\mathbf{x}$ and the latent variable $\mathbf{Z}$. This equality can therefore be represented by employing the PCE in Eq. (4.30) within the augmented space $(\mathbf{X}, \mathbf{Z})$ of dimensionality $(M + 1)$:

$$F^{-1}_{Y|\mathbf{X}}\left(F_{\mathbf{Z}}(\mathbf{Z}) \mid \mathbf{X}\right) \overset{d}{=} \sum_{\boldsymbol{\alpha}\in\mathbb{N}^{M+1}} c_\alpha \psi_{\boldsymbol{\alpha}}(\mathbf{X}, \mathbf{Z}) \tag{4.34}$$

For a given $\mathbf{x}$, Eq. (4.34) is a function of the latent variable $\mathbf{Z}$, which makes the response $Y_{\mathbf{x}}$ a random variable. Considering a truncation set $\mathcal{A} \subset \mathbb{N}^{M+1}$, Eq. (4.34) may lead to singularity issues in the PDF. To enhance numerical stability, an additive noise term $\epsilon \sim \mathcal{N}(0, \sigma^2)$ is introduced. The resulting stochastic polynomial chaos expansion emulator, denoted as $\widetilde{Y}$, is written as:

$$\widetilde{Y}(\mathbf{x}, \mathbf{Z}) \approx \tilde{\mathcal{M}}_s(\mathbf{x}, \omega) = \sum_{\boldsymbol{\alpha}\in\mathcal{A}} c_\alpha \psi_{\boldsymbol{\alpha}}(\mathbf{x}, \mathbf{Z}) + \epsilon \tag{4.35}$$

To construct the SPCE defined in Eq. (4.35), the coefficients $c_{\boldsymbol{\alpha}}$ and the noise standard deviation σ must be estimated. The calibration of these parameters, along with the adaptive selection of the latent-variable distribution and the truncation scheme $\mathcal{A}$, follows the procedure described in (Zhu; Sudret, 2023), which is adopted in this work.

4.3 Sampling and Design of Experiments

To perform the MC simulation and construct the DoE, samples of $\mathbf{X}$ must be generated. This step is crucial, as the accuracy of the approximation depends on the appropriate selection of support points. Therefore, it is essential to employ a suitable sampling technique that adequately covers the entire sample space (Kalagnanam; Diwekar, 1997).

To obtain a random sample of a variable with a CDF of a random variable $F_{\mathbf{X}}(\mathbf{x})$, considering the Inverse transform method, the following procedure can be applied (Beck, 2024):

1. Generate a random number u_i from a uniform distribution in the interval [0, 1];
2. Compute the inverse of the CDF to obtain $x_i = F_{\mathbf{X}}^{-1}(u_i)$.

In addition, uniformly distributed random numbers can be generated in the interval [0, 1] using recursive algorithms, such as the congruential generator, which computes each new sample point as a function of the previous one (Beck, 2024).

Another category, known as stratified sampling, divides the space $[0, 1]^M$ into subdomains to generate samples that are more uniformly distributed. Among these techniques, the Latin Hypercube Sampling (LHS) is particularly noteworthy, as it reduces the number of required simulations while maintaining good coverage of the sampling domain. In LHS, the range of each random variable is partitioned into intervals, and one value is randomly selected within each interval, ensuring a well-distributed set of support points and a representative simulation (Nowak; Collins, 2012). Fig. 4.1 illustrates the sampling process using LHS.

Figure 4.1 – Sampling choice of the random variables with LHS.

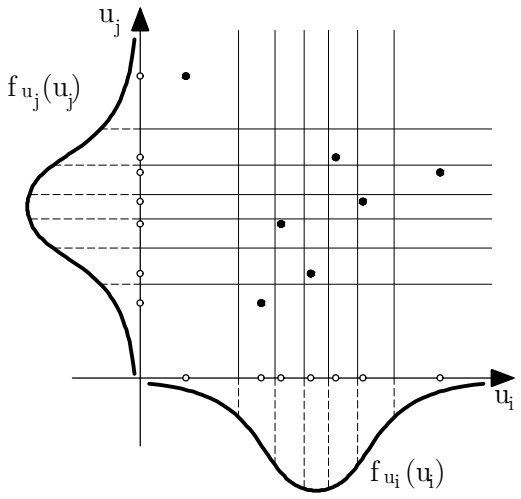

Source: Adapted from Hurtado and Barbat (1998).

Considering the number of sample points in the DoE S, and the number of random variables M, the sampling space has dimension M. For this analysis, two matrices are generated: $\mathbf{P}(S \times M)$, whose columns contain random permutations of the integers $1, \ldots, S$, and $\mathbf{R}(S \times M)$, whose entries are uniformly distributed random numbers in the interval $(0, 1)$. The sampling matrix $\mathbf{L}$ is then obtained as follows:

$$\mathbf{L} = \frac{1}{S}(\mathbf{P} - \mathbf{R}) \tag{4.36}$$

Each element of the sample is computed as follows (Olsson; Sandberg; Dahlblom, 2003):

$$\mathbf{x}_k = \{F_{\mathbf{x}_i}^{-1}(l_{ki})\}_{i=1,\ldots,M}^{t} \tag{4.37}$$

where $F_{\mathbf{x}_i}^{-1}$ denotes the inverse cumulative distribution function CDF of the variable $\mathbf{X}_i$ (Olsson; Sandberg; Dahlblom, 2003).

The steps of the LHS method are summarized by Choi, Grandhi and Canfield (2006) as follows:

1. Divide the support of each random variable into S intervals of equal probability;
2. Randomly select one value within each interval;
3. Repeat steps 1 and 2 until values are selected for all random variables;
4. Combine the S values obtained for each variable $\mathbf{X}_i$ with those obtained for the remaining variables $\mathbf{X}_j \neq \mathbf{X}_i$.

4.4 Chapter Overview

This chapter discussed the fundamental concepts associated with numerical simulation and uncertainty propagation. It began by introducing the notion of simulation and defining deterministic analyses, which provide a single response for a given input, enabling the direct evaluation of system performance under specific conditions. When uncertainties are present in the input variables, the MC method becomes essential to propagate such variability and to estimate statistical measures of the structural response.

Given the high computational cost of repeatedly evaluating complex numerical models within a MC framework, surrogate modeling techniques were introduced to improve efficiency. In particular, Kriging and Adaptive Kriging were presented as powerful metamodeling approaches capable of accurately reproducing nonlinear structural responses while significantly reducing the number of required simulations.

The chapter then extended the discussion to stochastic simulations, where the model outputs are inherently random even for fixed inputs. In this context, stochastic emulators were introduced as an extension of traditional surrogate models, designed to represent both the mean and the variability of stochastic simulators. The SPCE formulation was discussed as an efficient approach to emulate such systems by decomposing the stochastic response into orthogonal polynomial components.

Finally, sampling techniques used to build the DoE were presented, highlighting their importance in ensuring the representativeness of the surrogate or emulator. Methods such as random sampling, inverse transform sampling, and stratified approaches—particularly LHS—were described as efficient strategies for generating well-distributed support points across the input domain.

The concepts and methodologies introduced in this chapter establish the foundation for the development and application of surrogate and stochastic emulator frameworks in the subsequent chapters.

5 ADAPTIVE KRIGING FOR PBRO OF A RC STRUCTURE

This chapter presents the application of the Adaptive Kriging methodology to estimate fragility functions for RC structures by predicting the structural demand for individual ground motions using the metamodel. This approach is an essential tool for solving optimization problems within the PBEE framework, as it reduces the computational burden of the analyses. The metamodels are subsequently employed to compute the Damage Cost in an optimization problem formulated under the PBRO methodology, considering the Hazus (FEMA, 2022a) procedure defined in Section 2.4.2.

5.1 Problem setting

The optimization problem addressed in this chapter aims to determine the optimal cross-section dimensions of a structural element, denoted as $\mathbf{x_d}$, that minimize the total expected cost of the structure. This cost accounts for both construction costs and expected seismic damage losses under a specified hazard. The formulation can be expressed as the following single-objective optimization problem:

$$\begin{aligned} &\text{Find} \quad \mathbf{x}_\mathbf{d}^* = \{x_{d_1}, \ldots, x_{d_{n_{\mathrm{DV}}}}\}^T \\ &\text{To minimize} \quad C_t\left(\mathbf{x_d}, t_D\right) \\ &\text{Subjected to} \quad \mathbf{x_d} \in \mathcal{D}_{\mathbf{X_d}} \end{aligned} \tag{5.1}$$

where $\mathbf{x_d}$ indicates the design variables related to the element cross section, $C_t\left(\mathbf{x_d}\right)$ is the total cost of the structure for a design life t_D, and $\mathcal{D}_{\mathbf{X_d}} = \{\mathbf{x_d}_{\min}, \ldots, \mathbf{x_d}_{\max}\}$ represents the feasible domain.

As defined by Salles *et al.* (2023), the total cost of the structure evaluated for a design life t_D is given by:

$$C_t\left(\mathbf{x_d}, t_D\right) = C_{\mathrm{cons}}\left(\mathbf{x_d}\right) + C_d\left(\mathbf{x_d}, t_D\right) \tag{5.2}$$

where: $C_{\mathrm{cons}}\left(\mathbf{x_d}\right)$ is the building construction costs as a function of the design variables, and $C_d\left(\mathbf{x_d}, t_D\right)$ represents the Damage Costs for each Damage Limit State.

5.1.1 Damage Costs for each Damage Limit State

The Damage Cost is divided into structural cost CS and drift-sensitive nonstructural cost CNS, as defined in section 2.4.2 in Eq. 2.15 and Eq. 2.17. These equations define structural and nonstructural drift-sensitive costs as a function of the building replacement

cost of occupancy class BRC. However, since this example follows the cost calculation defined by Salles *et al.* (2023), the building's construction replaces the building replacement cost $C_{\text{cons}}(\mathbf{x_d})$. This means that the expected damage cost is given by:

$$\begin{aligned} C_d(\mathbf{x_d}, t_D) &= CS(\mathbf{x_d}, t_D) + CNS(\mathbf{x_d}, t_D) \\ C_d(\mathbf{x_d}, t_D) &= C_{\text{cons}}(\mathbf{x_d}) \sum_{ds=2}^{5} \left(P_{\text{struc},ds}(t_D) \times RCS_{ds} + P_{\text{Nstruc},ds}(t_D) \times RCD_{ds}\right) \end{aligned} \tag{5.3}$$

where $P_{\text{struc},ds}$ denotes the probability of the building being in structural damage state ds, corresponding to the probability of failure calculated from Eq. 2.21 for each Damage Limit State over a lifetime t_D; RCS_{ds} represents the structural repair cost ratio (expressed as a percentage of the initial building cost) for the building in damage state ds, as given in Tab. 2.1; $P_{\text{Nstruc},ds}$ is the probability of the building being in nonstructural drift-sensitive damage state ds, also corresponding to the probability of failure from Eq. 2.21 for each Damage Limit State over a lifetime t_D; and RCD_{ds} denotes the drift-sensitive nonstructural repair cost ratio (expressed as a percentage of the initial building cost), as given in Tab. 2.2.

As described in Chapter 3, a key challenge of the Risk Optimization problem proposed lies in the fact that $C_d(\mathbf{x_d}, t_D)$ must be re-evaluated for each design candidate, as the structural properties vary across the design space. Specifically, for each candidate $\mathbf{x_d}$, the following steps are required:

1. Compute the fundamental period $\bar{T}$ to scale ground motions;
2. Perform NLTHA to obtain the structural demand;
3. Estimate collapse fragility parameters from, for example, Incremental Dynamic Analysis (IDA);
4. Calculate Damage Costs for each Damage Limit State.

To address this challenge, the framework proposed in this chapter employs Adaptive Kriging to estimate the structural demand for individual ground motions. The purpose of the metamodel is to reduce the computational effort, enabling a more efficient exploration of the design space.

5.2 Proposed approach

As previously discussed, estimating collapse fragility parameters at each iteration of the optimization process substantially increases the computational cost. To mitigate this issue, metamodels can be incorporated into different stages of fragility function estimation. Andrade (2021) identified five stages that can be replaced by metamodels: time-history displacement responses, demand from a single record, demand trend line for unscaled ground motions, demand trend line and dispersion for scaled ground motions, and parameters of parametric fragility functions.

The methodology developed in this chapter focuses on predicting structural demand during IDA for each previously selected and scaled ground motion record. The core idea is to employ a metamodel to estimate the structural response to individual earthquake excitations as a function of the structural model parameters. A similar strategy was adopted by Mosleh *et al.* (2018), who used a generalized polynomial chaos expansion to predict the seismic response of concrete bridges while accounting for uncertainties in bearing and abutment stiffness. Fig. 5.1 illustrates the proposed approach, in which Kriging is applied to represent the structural drift as a function of the column cross-section for a given ground motion record, considering a specific scaling factor.

Figure 5.1 – Replacement of the FE model by Adaptive Kriging, column drift as a function of column cross-width.

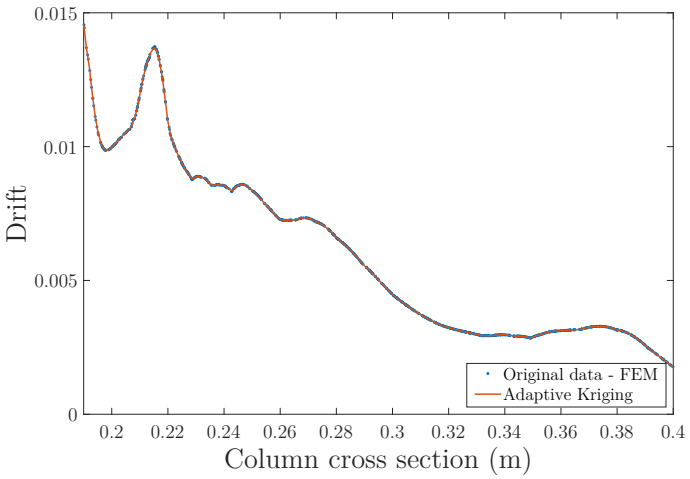

Source: Author.

The proposed methodology enables the estimation of the maximum structural response parameter—in this case study, the interstory drift—using Adaptive Kriging for any value of the structural variable within the interval in which the metamodel was trained, considering an IDA increment for a specific ground motion record. The drift values predicted by the metamodel are denoted as $\tilde{\mathcal{M}}_{\text{Drift}}(\mathbf{x_d})$. From these maximum drift values, a PSDM analysis can be performed and the corresponding fragility functions derived, substantially reducing the computational demand of the optimization process.

5.2.1 Adaptive Kriging algorithm

The algorithm developed for Adaptive Kriging with noise-free Kriging is represented in Fig. 5.2, based on the work of Dubourg (2011) and Pires (2021).

Figure 5.2 – Algorithm developed for the Adaptive Kriging.

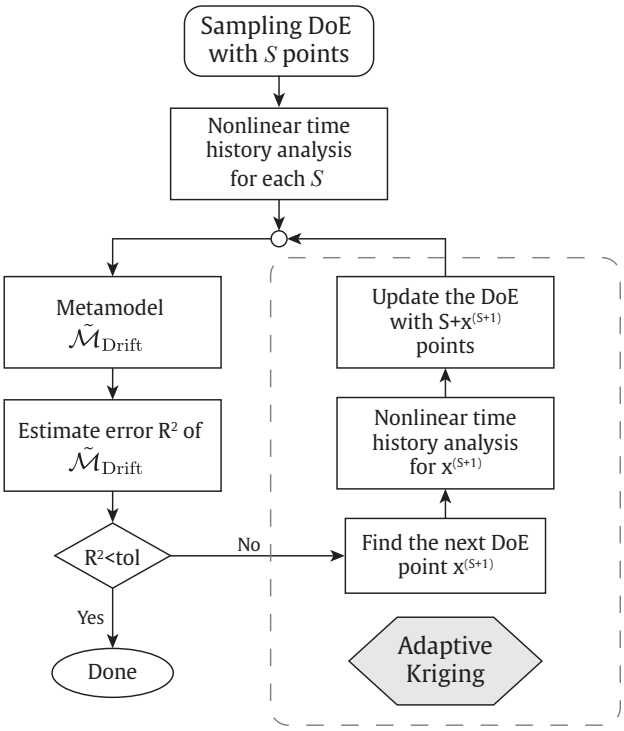

Source: Author.

The convergence criteria adopted in this work to stop the iterative process and to validate the metamodel are based on Wang and Shan (2007) and were also applied by Pires (2021). These criteria rely on estimating the error between the values obtained with the Kriging metamodel and those from the high-fidelity model. Three error measures are considered: the root mean square error (RMSE), given in Equation 5.4; the normalized root mean square error (NRMSE), shown in Equation 5.5; and the coefficient of determination (R^2), presented in Equation 5.6.

$$RMSE = \sqrt{\frac{\sum_{i=1}^{m} (y_i - \hat{y}_i)^2}{m}} \tag{5.4}$$

$$NRMSE = \frac{RMSE}{y_{max} - y_{min}} \tag{5.5}$$

$$R^2 = 1 - \frac{\sum_{i=1}^{m} (y_i - \hat{y}_i)^2}{\sum_{i=1}^{m} (y_i - \bar{y})^2} \tag{5.6}$$

where y_i is the exact value, $\hat{y}_i$ is the estimated value, m is the number of validation points, y_{max} is the maximum model output, y_{min} is the minimum model output, and $\bar{y}$ is the mean of the model output.

Appendix A presents three examples used to validate the proposed algorithm. For each case, all error metrics are reported; however, the coefficient of determination (R^2) was adopted as the algorithm's convergence criterion. The adaptive process continues adding infill points to the Design of Experiments (DoE) until R^2 exceeds 0.998. Under this criterion, the RMSE and the NRMSE are expected to progressively decrease throughout the iterations.

5.2.2 Algorithm for PBRO with Adaptive Kriging

After training the metamodel $\tilde{\mathcal{M}}_{\text{Drift}}(\mathbf{x_d})$, the PSDM analysis can be performed to derive fragility functions for each design candidate. It is important to note that the metamodel must be trained within the boundaries defined by the constraints of the optimization problem in Equation 5.1. Once trained, the metamodels can be incorporated into the optimization problem, replacing calls to the original FE model. The overall methodology proposed in this work to solve Performance-Based Risk Optimization problems is illustrated in Fig. 5.3.

Figure 5.3 – Algorithm for PBRO with Adaptive Kriging.

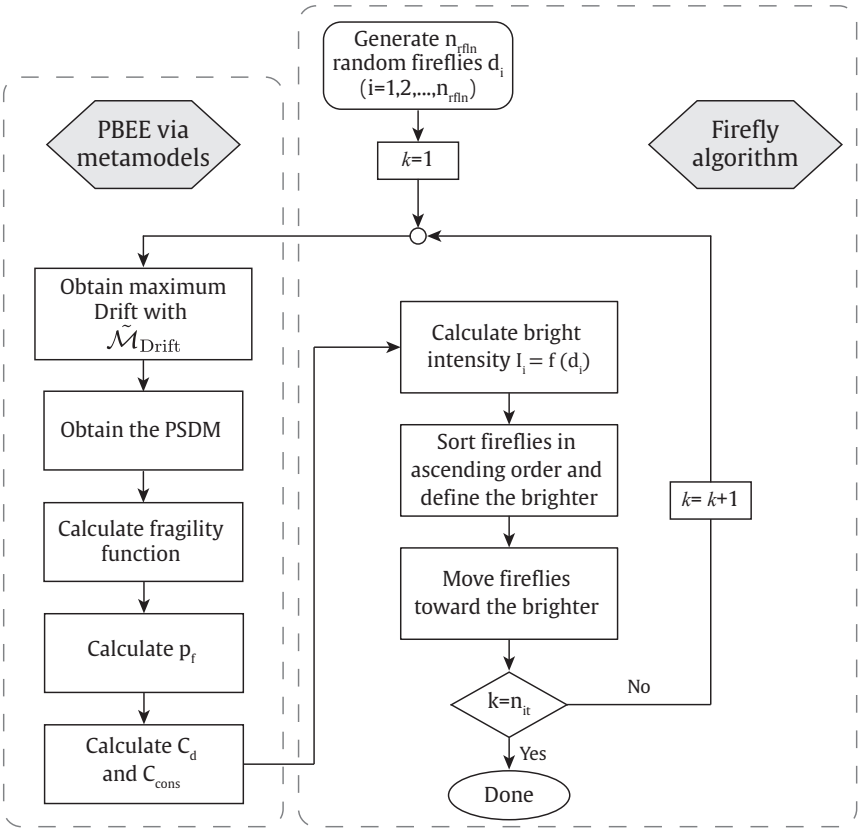

Source: Author.

The Firefly algorithm, described in Annex B, is used as the optimizer for this case study. The following steps of the proposed approach are implemented:

1. Define the design domain of the optimization problem.
2. Train the metamodel $\tilde{\mathcal{M}}_{\text{Drift}}(\mathbf{x_d})$ using the Adaptive Kriging approach to predict the maximum interstory drift for each IDA increment and ground motion record, within the boundaries of the design domain.
3. Initialize the optimization process by generating n_{frfl} random fireflies.
4. Calculate the light intensity of each firefly by using the metamodel to estimate the maximum drift for the selected ground motions, derive the fragility functions, and compute both the probability of failure and the damage cost of the structural system.
5. Move the fireflies toward the brighter ones.
6. Check the convergence of the algorithm.

5.3 Case Study

5.3.1 Overview

The proposed methodology is applied to an example of a residential archetype building with a moment-resisting frame structural system, which has been studied in Rodrigues *et al.* (2023). The frame was designed using TQS software (TQS Informática, 2019) according to ABNT NBR 6118:2014 with no seismic provisions. Fig. 5.4 illustrates the geometry of the building and the cross-sections of beams and columns. The 2D model considers a space frame system of the building, and the same reinforcement ratios are applied in structural elements in all floors. According to Liel (2008), the minimum number of bays necessary to capture the behavior of interior and exterior columns and joints of structure is two, which justifies consideration of a two-bay model in this example.

A space frame system is considered in the optimization problem, as illustrated in Fig. 5.5. For the calculation of the expected damage cost, the influence area inside the dashed line of Fig. 5.5b is considered for the space frame, corresponding to $50\,m^2$.

The design considers a compressive strength of concrete of $23\,MPa$ with Young's Modulus of $E = 22540\,MPa$, steel CA-50 with Young's Modulus of $E = 210000\,MPa$, and the concrete cover is 2.50 centimeters.

The objective of this case study is to determine the optimal column cross-section dimensions of a squared section column, width, and depth ($c_{w,d}$), that minimize the total expected cost of the structure, as defined in Section 5.1. The corresponding single-objective PBRO problem is formulated as:

$$\begin{aligned} &\text{Find} \quad x_d^* = \{c_{w,d}^*\} \\ &\text{To minimize} \quad C_t\left(x_d, t_D\right) = C_{\text{cons}}\left(x_d\right) + C_d\left(x_d, t_D\right) \\ &\text{Subjected to} \quad 25\,cm \leq c_{w,d} \leq 60\,cm \end{aligned} \tag{5.7}$$

Figure 5.4 – Representation of the 2D model (units in meters).

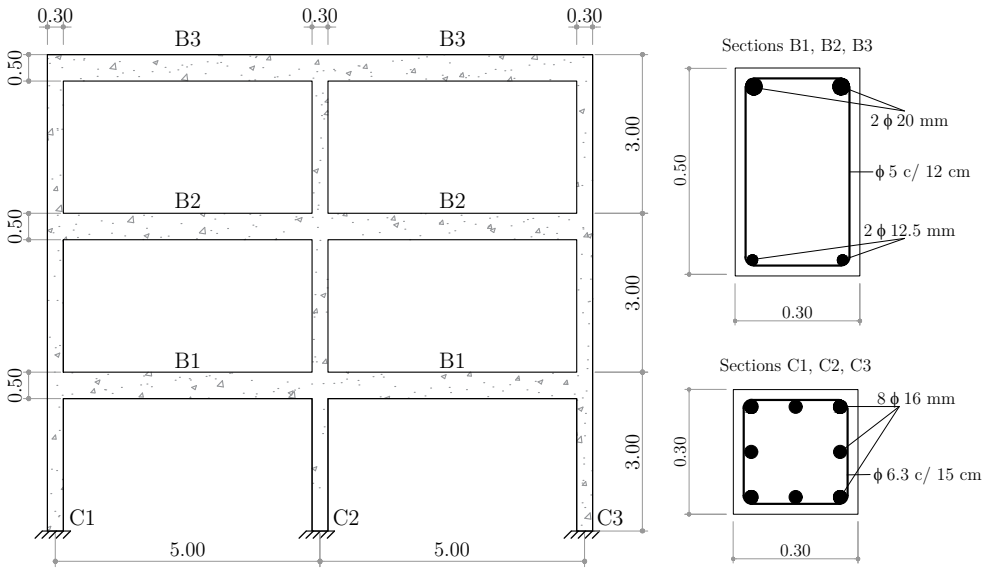

Source: Author.

Figure 5.5 – Ground plan of the structure (dimensions in centimeters).

(a) Ground plan. **(b)** Area of influence for the space frame.

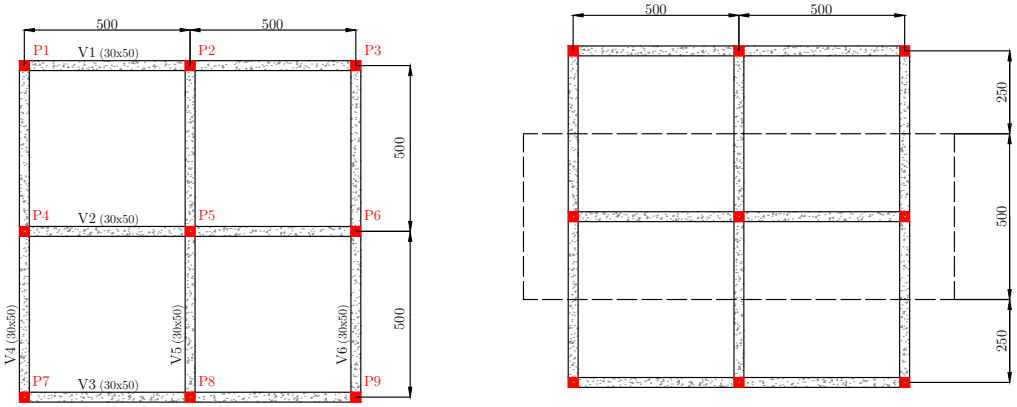

Source: Author.

It should be noted that the dimensions of the reinforcement rebars remain fixed throughout the optimization process. The following sections describe how the initial construction cost is determined in this example.

5.3.2 Construction costs

This work defines the construction cost as the cost associated with building the structural frame. It is important to note that the cost of structural materials can vary

significantly depending on geographical location. Accordingly, the Brazilian SINAPI database (INSTITUTO BRASILEIRO DE GEOGRAFIA E ESTATÍSTICA, 2023) was used to obtain the unit and composite costs for the structural frame. All costs were converted from Brazilian reais (R$) to U.S. dollars (US$) using an exchange rate of US$ 1.00 = R$ 5.02 (rate from 2023).

Since the majority of structures in Brazil are built in situ, the construction cost depends on the cost of concrete, steel for reinforcement, and the cost of formwork and steel forming. They are evaluated separately in the further sections for each beam and column of the frame, and the total construction cost is calculated as:

$$C_{\text{cons}}\left(x_d\right) = \sum_{i=1}^{n_{\text{ele}}} \left(CC_{\text{concrete},i}(x_d) + CC_{\text{rein},i}(x_d) + CC_{\text{form},i}(x_d)\right) \tag{5.8}$$

where CC_{concrete} corresponds to the cost of concrete, CC_{rein} corresponds to the cost of reinforcement, CC_{form} corresponds to the cost of the formwork and n_{ele} refers to the number of structural elements considered.

5.3.2.1 Cost of concrete

The concrete cost includes both the material cost (C_{mat})—comprising the concrete input and pumping—and the cost of the composition (C_{comp}), which covers injection, densification, and finishing. The SINAPI input codes for concrete are 1524, 1527, 1525, 11145, 34479, 34481, and 34483, corresponding to strength classes C20, C25, C30, C35, C40, C45, and C50, respectively. Composition 103673 refers to the structural concrete injection with densification and finishing. Since both costs are expressed per unit volume of concrete, the total concrete cost for each beam and column is calculated as:

$$CC_{\text{concrete}}(x_d) = (c_d \times c_w \times L) \times (C_{\text{mat}} + C_{\text{comp}}) \tag{5.9}$$

where c_d corresponds to the depth of the element, c_w corresponds to the width of the element, L corresponds to the length of the element.

5.3.2.2 Cost of reinforcement

The total reinforcement cost is defined as the sum of the steel input cost (S_{input}) and the reinforcement composition cost (S_{compo}), which includes steel cutting and bending, rebar placement labor, and spacers. The SINAPI input codes for steel reinforcement are 32, 33, 34, 43055, and 43056, corresponding to CA-50 steel with diameters ϕ of 6.3, 8, 10, 12.5 or 16, and 20 or 25 millimeters. Compositions 92760, 92761, 92762, 92763, 92764, 92765, and 92766 refer to the reinforcement of beams and columns using CA-50 steel in the same diameter range. The costs are expressed per kilogram of reinforcement, and the

reference weight for each bar diameter is obtained from Table B.1 of ABNT NBR 7480 (2022) for a nominal mass m in kg/m, as presented in Tab. 5.1.

Table 5.1 – Diameter and nominal mass of steel reinforcement.

ϕ **(mm)**	m **(kg/m)**
6.3	0.245
8.0	0.395
10.0	0.617
12.5	0.963
16.0	1.578
20.0	2.466
25.0	3.853

Source: ABNT NBR 7480 (2022).

Since the variation in the input and composition costs for the available bar diameters is small, a mean value is considered in this work for cost calculation, considering all input codes and all composition codes. The reinforcement mass of longitudinal and transverse bars is calculated according to the following equations:

$$\begin{aligned} m_{\text{long}} &= m \times n_{\text{long}} \times L \\ m_{\text{trans}}(x_d) &= [2\,(c_w - 2\text{cob}) + 2\,(c_d - 2\text{cob})] \times m \times n_{\text{trans}} \end{aligned} \tag{5.10}$$

where m corresponds to the nominal mass of the bar, n_{long} is the number of longitudinal bars in the element, L corresponds to the length of the element, c_d corresponds to the depth of the element, c_w corresponds to the width of the element, cob corresponds to the concrete cover and n_{trans} is the number of transverse bars in the element.

For each beam and column of the structure, the reinforcement cost is calculated as:

$$CC_{\text{rein}}(x_d) = (m_{\text{long}} + m_{\text{trans}}(x_d)) \times (S_{\text{input}} + S_{\text{compo}}) \tag{5.11}$$

5.3.2.3 Cost of formwork

In Brazil, formwork is typically made of timber. The SINAPI composition code adopted in this work is 92265, which corresponds to the production of formwork for beams and columns using resin-coated plywood. The cost is expressed per square meter of formwork and is calculated as follows:

$$CC_{\text{form}}(x_d) = (c_d + c_w) \times L \times F_{\text{comp}} \tag{5.12}$$

where c_d corresponds to the depth of the element, c_w corresponds to the width of the element, L corresponds to the length of the element and F_{comp} corresponds to the cost of the composition given by SINAPI.

Tab. 5.2 presents the construction costs obtained from the SINAPI database (INSTITUTO BRASILEIRO DE GEOGRAFIA E ESTATÍSTICA, 2023) for each element considered in the optimization problem, including the costs of concrete, reinforcement, and formwork for each element i.

Table 5.2 – Unitary construction cost of the building.

Material	**Cost**
Concrete ($CC_{\text{concrete},i}$)	$108.2\,\$/m^3$
Reinforcement ($CC_{\text{rein},i}$)	$4.34\,\$/kg$
Formwork ($CC_{\text{form},i}$)	$23.68\,\$/m^2$

Source: Author.

5.3.3 Finite Element Model of the Structural System

A two-dimensional nonlinear dynamic FE model of the three-story archetype RC building was developed using OpenSees (McKenna; Fenves; Scott, 2006). The floor slab was modeled with a rigid diaphragm assumption, while beams and columns were represented using the Lumped Plasticity Model, implemented through its own element library, as described in Annex A. A calibration example of a column using the LPM is provided in Appendix B.

Gravity loads were applied as uniformly distributed loads on the beams and were also used to define the seismic masses of the model. These loads include 1.05 times the dead load and a live load of $0.5\,kN/m^2$, following Liel (2008) and the recommendations of FEMA P695 (FEMA, 2009). The latter corresponds to 25% of the maximum live load of $2.0\,kN/m^2$ for residential buildings specified in ABNT NBR 6120 (ASSOCIAÇÃO BRASILEIRA DE NORMAS TÉCNICAS, 2019). P–Delta effects were included in the column modeling. Rayleigh damping was applied with a damping ratio of $\xi = 5\%$ for the first and third vibration modes. The fundamental period of the structure, obtained with OpenSees, is 0.553 seconds.

5.3.4 Seismic hazard and Ground Motion Selection

To introduce the methodology for deriving fragility functions based on a metamodel, a specific site must be defined to obtain the corresponding hazard curve and ground motion records. In this example, the selected site is the city of Natal, the state capital of Rio Grande do Norte, with a relatively large population in Brazil. This choice is justified

by the availability of detailed geotechnical data for the region (Rodrigues, 2021) and by its relatively high seismic hazard compared to other areas of the Brazilian territory, as illustrated in the hazard maps proposed by Petersen *et al.* (2018). The local soil is classified as Site Class D.

The seismic hazard data provided by Petersen *et al.* (2018) for Latin America include values of peak ground acceleration (PGA), spectral acceleration at a period of $T = 0.2\,\text{s}$ ($S_a(T = 0.2\,s)$), and spectral acceleration at a period of $T = 1.0\,\text{s}$ ($S_a(T = 1.0\,s)$). For this example, one intensity measure must be selected. Since the IM should be closely related to the expected structural response, the spectral acceleration $S_a(T)$ is adopted, as it is a widely used IM in fragility analyses of reinforced concrete (RC) buildings (Haselton *et al.*, 2011; Liel; Haselton; Deierlein, 2011; Andrade, 2021; Pereira *et al.*, 2021). Among the available periods, the spectral acceleration corresponding to $T = 1.0\,\text{s}$ is chosen.

The reference soil considered in the study by Petersen *et al.* (2018) corresponds to the boundary between Site Classes B and C ($V_{s30} = 760\,\text{m/s}$), which differs from the soil conditions adopted for the city of Natal. Therefore, the spectral accelerations must be amplified. The amplification factors used in this work are specified in ASCE 7-16 (ASCE, 2017b). The final values of $S_a(T = 1.0)$ are obtained by multiplying the amplification factors by the corresponding $S_a(T = 1.0)$ values provided in Petersen *et al.* (2018). The resulting hazard curve, derived from these considerations, is shown in Fig. 5.6.

Figure 5.6 – Hazard Curve for the city of Natal.

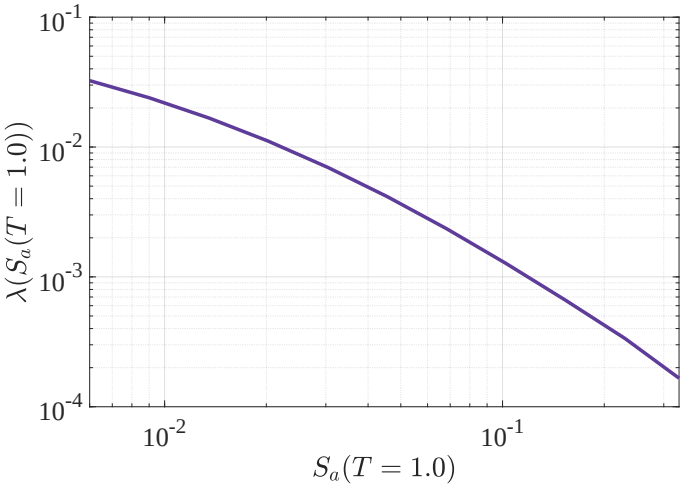

Source: Author.

In this example, the selection of the ground motion from real earthquake events is considered. The spectral accelerations of the selected signals are compared with the elastic response spectra for a return period of 475 years to check their correspondence. The selection of the earthquake records is a stage that requires studies in different areas to define the interval of parameters that are inserted into the database to obtain hazard-consistent

events. PEER NGA-West2 database for natural earthquakes (Ancheta *et al.*, 2014) is used, which considers two sources of earthquakes: NGA-East, with ground motions in Stable Continental Regions; NGA-West2, with shallow crustal earthquakes recorded worldwide in active tectonic regions.

In Rodrigues (2021), a discussion is made about considering the NGA-West2 database, since the scaling factors necessary for the NGA-East are higher than the ones recommended in the literature (Bommer; Scott; Sarma, 2000). The same decision is made in this example, since one of the main negative points of IDA, as discussed previously, is the excessive scaling of records, leading to bias in the IDA-based fragility curves. Using records from NGA-West2 database may avoid this issue, but it is important to define the interval of parameters that correctly suits the region of study. The chosen limits for the search for records are presented in Tab. 5.3.

Table 5.3 – Lower and upper limits for the earthquake record parameters.

Parameter	**Lower limit**	**Upper limit**
$R_{\mathbf{JB}}$ **(km)**	15	100
M_w	4	6.5
$\bar{V}_s$ **(m/s)**	180	370

Source: Author.

R_{JB} distance corresponds to the Joyner-Boore distance to the rupture plane. The limits chosen for the parameters consider the lack of knowledge about the exact hypocenter position of the event, as well as the different possibilities of the structure's position. The maximum value is defined as $100\,km$ to avoid the regional crustal structure becoming significant (Bommer; Stafford; Alarcón, 2009). The minimum value, defined as $15\,km$, aims to avoid selecting records too close to a fault (Krawinkler; Medina; Alavi, 2003).

The next factor considered is the magnitude M_w. Based on Nievas *et al.* (2020), the minimum magnitude value for causing structural damage is 4.0, which has been adopted as the lower limit. As the maximum magnitude, BUDNITZ, R. J. and APOSTOLAKIS, G. and BOORE, David M. (1997) suggests considering one order higher than the maximum earthquake that occurred in the studied region. Based on the João Câmara earthquake sequence that occurred in 1986 in the Rio Grande do Norte state in Brazil, the maximum registered magnitude was $M_w = 5.3$, so the adopted upper limit is 6.5.

The last parameter considered is the mean shear wave velocity, $\bar{V}_s$, which ensures that the selected earthquake records correspond to soil conditions compatible with those at the site. The adopted values correspond to the limits for soil type D, based on the soil classification proposed in ABNT NBR 15421:2006, and are also consistent with the values

specified in ASCE 7-16 (ASCE, 2017b).

The type of fault is not fixed in this study, following the recommendations of Beyer and Bommer (2007). Once the parameters are defined, the ground motion set is selected from the PEER NGA-West2 database. The records chosen for the analyses are presented in Tab. 5.4.

Table 5.4 – Selected earthquake records from PEER NGA-West 2 (Ancheta *et al.*, 2014).

Record Num.	**NGA Num.**	**Earthquake Name**	**Station Name**	M_w	**Year**
1	26	Hollister-01	Hollister City Hall	5.6	1961
2	152	Coyote Lake	SJB Overpass_ Bent 3 g.l.	5.74	1961
3	20	Northern Calif-03	Ferndale City Hall	6.5	1979
4	122	Friuli_ Italy-01	Codroipo	6.5	1976
5	103	Northern Calif-07	Petrolia_ General Store	5.2	1975
6	266	Victoria_ Mexico	Chihuahua	6.33	1980
7	421	Trinidad offshore	Rio Dell Overpass_E Ground	5.7	1983
8	314	Westmorland	Brawley Airport	5.9	1981
9	322	Coalinga-01	Cantua Creek School	6.36	1983
10	34	Northern Calif-05	Ferndale City Hall	5.6	1967
11	478	Lazio-Abruzzo_ Italy	Garigliano-Centrale Nucleare	5.8	1984

Source: Author.

Fig. 5.7a presents the mean response spectra for the selected ground motion set, obtained as the average of the 11 records. Fig. 5.7b compares this mean spectrum with the design response spectrum for Natal, developed according to the procedure described in Section 2.1.1.1 for soil class D and based on the spectral accelerations from the hazard

maps proposed in Petersen *et al.* (2018). The spectral acceleration values for short (S_S) and long periods (S_1) are: $S_S = 0.03\,g$ and $S_1 = 0.01\,g$ for $T = 72$ years; $S_S = 0.15\,g$ and $S_1 = 0.03\,g$ for $T = 475$ years; and $S_S = 0.675\,g$ and $S_1 = 0.15\,g$ for $T = 2475$ years.

Figure 5.7 – Mean Response Spectra for the selected ground motion set.

(a) Mean response spectra for all 11 records selected.

(b) Comparison with the design response spectra.

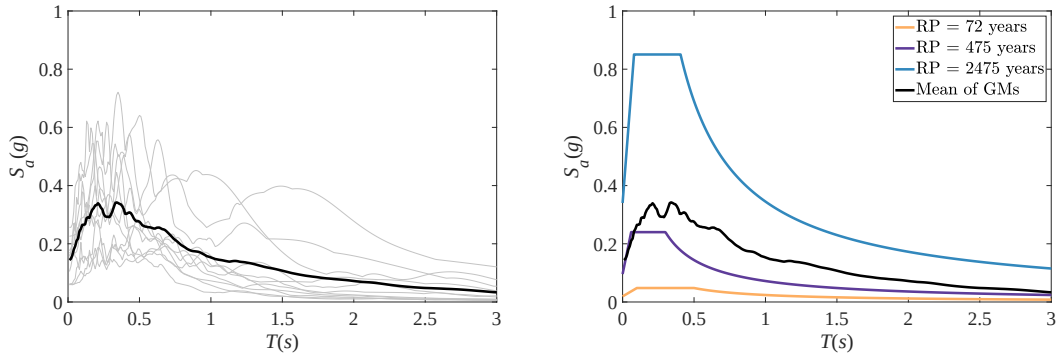

Source: Author.

5.3.5 Results

5.3.5.1 Preamble

This section presents the results of the case study in three parts: (1) application of the adaptive Kriging framework as a metamodel to predict structural demand, expressed in terms of $\tilde{\mathcal{M}}_{\text{Drift}}(x_d)$, for each selected ground motion and to compute fragility functions and Expected Damage Costs for each Damage State, (2) validation of the optimization problem boundaries, and (3) results of the optimization process using the proposed metamodels.

5.3.5.2 Adaptive Kriging metamodels

The Kriging metamodel for this case study is trained using the ground motion set listed in Tab. 5.4. The initial DoE consists of 17 support points, with samples randomly generated using LHS for column dimensions ranging from $l_b = 25\,cm$ to $u_b = 60\,cm$. An additional 12 samples are generated within this interval to serve as verification points, where the coefficient of determination (R^2) of the approximation is evaluated. The algorithm terminates when R^2 reaches 0.99 or when the adaptive DoE attains 50 infill points. At each support and verification point, a nonlinear time history analysis (NLTHA) is conducted with the original FE model to obtain the drift response of the building.

Fragility functions are then calculated for a given column cross-section, using both the NLTHA results from the FE model and $\tilde{\mathcal{M}}_{\text{Drift}}(x_d)$. The procedure follows the methodology described in Section 2.3.2, based on IDA and PSDM. As discussed in Section 2.3.2.2, quantitative values from the literature are adopted for the structural capacity. The values of S_C correspond to a low-rise structure (1 to 3 stories) with a pre-code classification, meaning that seismic actions are not explicitly considered in the design. The standard deviation β_C is defined according to Wen, Ellingwood and Bracci (2004), adopting a constant value of $\beta_C = 0.3$ for all Limit States. This represents a simplification, since higher limit states are subject to greater uncertainty due to the complexity of structural behavior near failure (Tavares; Padgett; Paultre, 2012).

To evaluate the trained metamodel $\tilde{\mathcal{M}}_{\text{Drift}}(x_d)$, a column cross-section of 30 cm is selected to compare its results with those of the original FE model. The PSDM results for the FE model are shown in Fig. 5.8a, while those obtained with the metamodel are presented in Fig. 5.8b. Drift values exceeding 10% were excluded from the PSDM evaluation, as this threshold is adopted herein to define global collapse and account for dynamic instability (Jalayer *et al.*, 2017; Baird; Liel; Chase, 2020).

Figure 5.8 – PSDM results.

(a) Original FE model with column cross-section of 30 centimeters.

(b) $\tilde{\mathcal{M}}_{\text{Drift}}$ for a column cross-section of 30 centimeters.

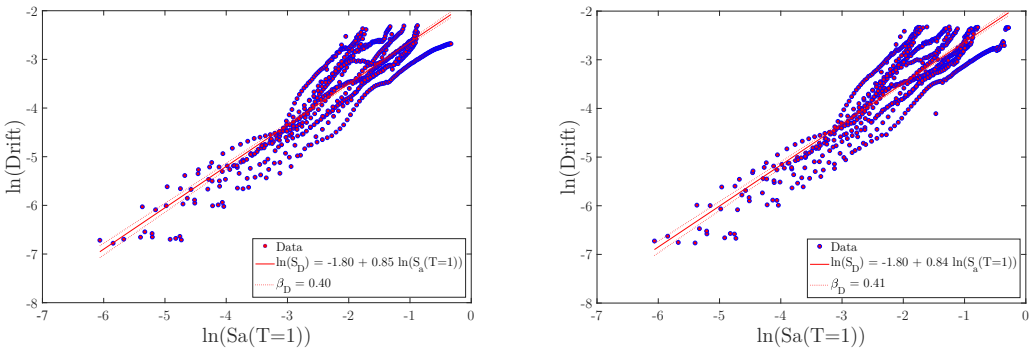

Source: Author.

A convention was adopted in the metamodel to avoid convergence issues in OpenSees. At high IDA levels, OpenSees often encounters convergence difficulties in the dynamic analysis due to global instability, which can lead to unrealistically large drift values, even with convergence algorithms implemented. This poses a challenge for the metamodel, as it becomes difficult to establish correlations between drift responses for different column cross-sections under such conditions. To address this, a constant drift value of 0.1 (corresponding to 10%) was assigned whenever the analysis produced drifts exceeding this threshold. This choice is consistent with the drift limit adopted herein to define global collapse.

Fig. 5.9 presents the fragility functions for structural damage obtained from the original FE model and from the adaptive Kriging metamodel. The corresponding median values and logarithmic dispersions for these fragility curves are summarized in Tab. 5.5.

Figure 5.9 – Fragility functions considering the structural damage for the original FE model and for the metamodel.

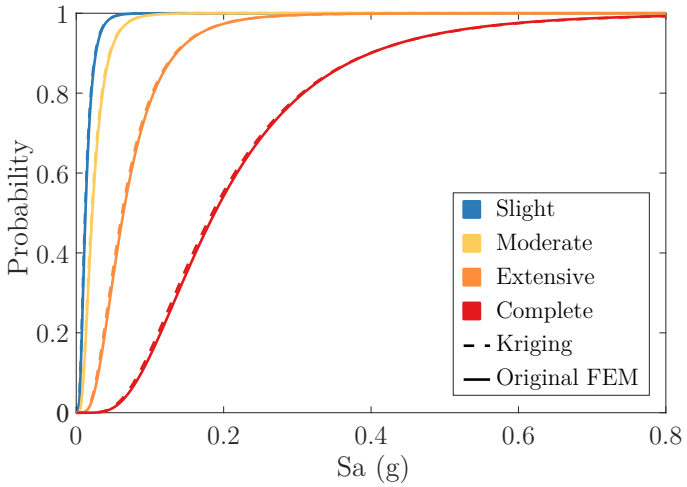

Source: Author.

Table 5.5 – Median and logarithmic dispersion for the Fragility Functions for $x_d = 30\,\text{cm}$.

Damage	**FE Model**		**Metamodel** ($\tilde{\mathcal{M}}_{\text{Drift}}(30)$)		**Relative**
Limit State	**Median**	**Dispersion**	**Median**	**Dispersion**	**error**(%)
Slight	0.0125	0.5883	0.0120	0.6100	4.4303
Moderate	0.0218	0.5883	0.0209	0.6100	3.8916
Extensive	0.0640	0.5883	0.0622	0.6100	2.8325
Complete	0.1879	0.5883	0.1847	0.6100	1.7617

Source: Author.

The results show a very good agreement between the fragility functions of all Damage Limit States obtained from the original FE model and the metamodel, with a maximum relative error of 4.43% for the median value in the Slight DLS. The smallest errors occur in the Complete DLS, suggesting that assigning a constant drift value of 10% in the metamodel, whenever the drift exceeded this threshold, was an appropriate choice.

The mean annual conditional failure rate for each Damage Limit State, for both the original FE model and the metamodel, is calculated using the hazard curve shown in Fig. 5.6 and Eq. 2.18. Since uncertainties from non-ergodic variables are not considered at this stage, the probability of failure is also computed using Eq. 2.21 for lifetimes of $t_D = 50$ and $t_D = 100$ years. The results are summarized in Tab. 5.6.

Table 5.6 – Mean annual conditional failure rate ($\lambda_{LS} \times 10^{-3}$) and probability of failure for FE and metamodel for $x_d = 30\,\text{cm}$.

Damage	**FE Model**				**Metamodel** ($\tilde{\mathcal{M}}_{\text{Drift}}(30)$)			
Limit State	λ_{LS}	$p_f\,(1)$	$p_f\,(50)$	$p_f\,(100)$	λ_{LS}	$p_f\,(1)$	$p_f\,(50)$	$p_f\,(100)$
Slight	19.56	1.93%	62.38%	85.85%	20.27	2.00%	63.71%	86.83%
Moderate	12.05	1.19%	45.26%	70.037%	12.58	1.25%	46.68%	71.57%
Extensive	3.54	0.35%	16.23%	29.82%	3.71	0.37%	16.94%	31.02%
Complete	0.75	0.07%	3.68%	7.22%	0.78	0.07%	3.84%	7.54%

Source: Author.

Once again, a good correspondence is observed between the failure probabilities obtained from the original FE model and the metamodel, with errors increasing for higher Damage Limit States and for longer lifetime probabilities.

The structure comprises four apartments of $70\,\text{m}^2$ per floor, including the ground level, totaling 16 apartments. According to the Hazus (FEMA, 2022b) manual, it can be classified under the specific occupancy class RES3D. The total building area is approximately $300\,\text{m}^2$. Based on this information, the mean annual damage cost for each damage state is calculated both per square meter and for the entire structure, considering only the structural cost $CS_{ds}(30)$, for both the FE model and the metamodel. The results are presented in Tab. 5.7.

Table 5.7 – Annual Structural Damage Cost (CS) calculated with FE model and metamodel for $x_d = 30\,\text{cm}$.

Damage	**FE Model**		**Metamodel** ($\tilde{\mathcal{M}}_{\text{Drift}}(30)$)	
Limit State	$CS_{ds}(\$/\mathbf{m}^2)$	$CS_{ds}(\$)$	$CS_{ds}(\$/\mathbf{m}^2)$	$CS_{ds}(\$)$
Slight	0.145	43.65	0.150	45.23
Moderate	0.420	126.02	0.438	131.50
Extensive	0.611	183.31	0.640	192.18
Complete	0.259	77.75	0.271	81.33
Total (CS)	1.436	430.75	1.501	450.24

Source: Author.

The evolution of the total repair cost over a lifetime ranging from 0 to 100 years is shown in Fig. 5.10 for both the FE model and the metamodel. Tab. 5.6 and Fig. 5.10 show the same trend: the error in the failure probability increases with lifetime. For a lifetime of 100 years, the total repair cost of the structure is $\$3.226 \times 10^6$ for the Finite Element model and $\$3.339 \times 10^6$ for the metamodel, corresponding to an error of 3.39%. These results demonstrate that the metamodel can be reliably applied in subsequent optimization problems to explore potential improvements in structural design aimed at

enhancing seismic performance.

Figure 5.10 – Evolution of Structural Expected Damage Cost ($CS\,(30, t_D)$) along 100 years lifetime.

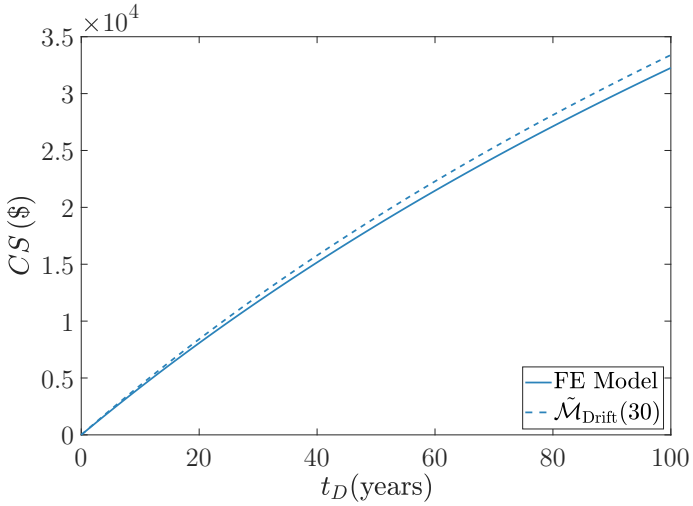

Source: Author.

5.3.5.3 Validation of optimization boundaries

To verify the lower and upper bounds of the design variables and to ensure that the cost calculations at these limits lead to an optimal total cost value, nine column cross-section dimensions were evaluated using the original FE model. The selected dimensions were 19, 25, 30, 35, 40, 45, 50, 55, and 60 cm. Based on these points, a third-order polynomial trend line was fitted to represent the expected failure cost of the structure within the 19 to 60 cm interval. Using this trend line, construction costs, expected damage costs, and total costs were estimated for 500 intermediate points within the defined interval. The results are presented in Fig. 5.11.

The results show that the total cost function has a well-defined minimum at approximately 35 cm, which validates the cost definition and calculation adopted for this example, as well as the boundaries defined previously for the column cross sections. This also confirms the suitability of using the trained metamodel presented in the previous chapter within the optimization problem.

The final step of the validation is to verify that the expected damage costs estimated with the metamodel have a small error when compared with the results from the original FE model. For this purpose, the expected costs were calculated using the metamodel for 700 column cross-sections within the trained range, from 25 to 60 cm. The results are shown in Fig. 5.12, while Tab. 5.8 reports the expected damage costs obtained from both the FE model and the metamodel for different column cross-sections, along with the relative errors.

Figure 5.11 – Verification of costs with original FE model points.

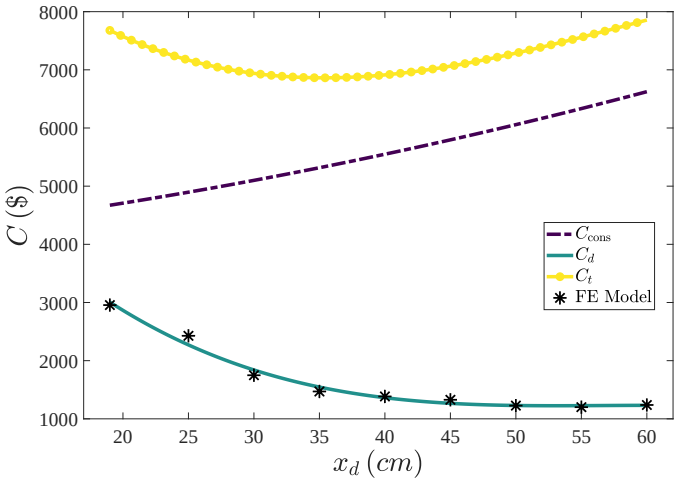

Source: Author.

Figure 5.12 – Verification of costs with original FE model points and Expected Damage Cost (C_d) via metamodel ($\tilde{\mathcal{M}}_{\text{Drift}}$).

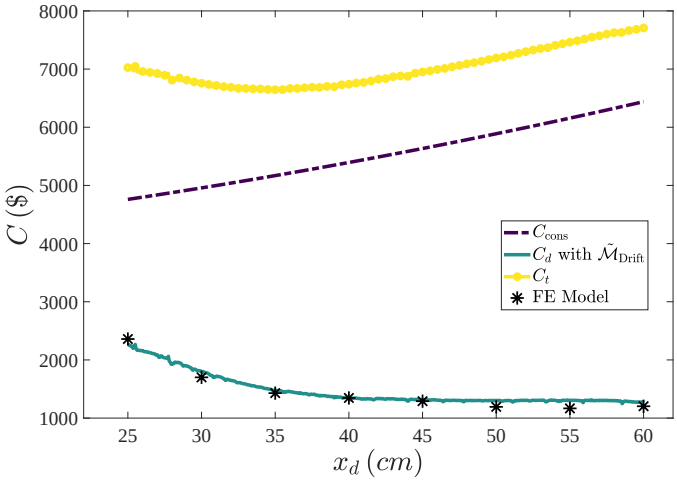

Source: Author.

A good agreement is observed between the expected damage costs estimated with the metamodel, trained for column cross-sections between 25 and 60 cm, and the eight points obtained from the original FE model. Tab. 5.8 shows relative errors ranging from 0.04% for a 40 cm cross-section to 11.9% for a 55 cm cross-section. The variation in errors across different cross-section values may be related to convergence issues in OpenSees caused by global dynamic instability, as discussed in the previous section. Although this issue is mitigated by adopting a constant drift value of 0.1 to define collapse, it can still influence the metamodel results as different DoE points are trained. In addition, Fig. 5.12 indicates a minimum total cost at a column cross-section of approximately 35 cm.

Table 5.8 – Damage Cost ($C_d\,(x_d)$) calculated with FE model and $\tilde{\mathcal{M}}_{\text{Drift}}$.

x_d	$C_d\,(x_d)$ **(\$)**		**Relative**
(cm)	**FE Model**	**Metamodel** ($\tilde{\mathcal{M}}_{\textbf{Drift}}$)	**error** (%)
25	2,359.7	2,266.1	3.96%
30	1,700.4	1,799.9	5.85%
35	1,429.3	1,476.9	3.32%
40	1,346.3	1,345.7	0.04%
45	1,290.5	1,316.6	2.01%
50	1,192.9	1,302.8	9.24%
55	1,167.0	1,305.9	11.90%
60	1,177.4	1,267.4	7.64%

Source: Author.

5.3.5.4 Optimization results

This section presents the results of the structural optimization problem using the PBRO approach, where the metamodel $\tilde{\mathcal{M}}_{\text{Drift}}(x_d)$ replaces the original FE model. As described previously, the heuristic Firefly algorithm is employed to solve the optimization problem.

At each iteration, 60 fireflies are randomly generated within the defined range of 25 to 60 cm. For each firefly, $\tilde{\mathcal{M}}_{\text{Drift}}(x_d)$ is used to calculate the fragility functions for each Damage Limit State and calculate the probability of failure. Fireflies are generated as values between 0.25 and 0.6, which are then scaled in the objective function to represent the column cross-section dimensions in centimeters. This approach is adopted because fireflies generated in a lower dimension (between 0 and 1) are more easily attracted to the brightest one. The parameters used in the algorithm are $\gamma = 1$, $\beta_0 = 0.2$, and $\alpha = 0.5$ at iteration 1, with α decreasing at each iteration.

To verify the robustness of the results, six simulations were performed, each with 100 iterations. Fig. 5.13 illustrates the convergence of the objective function across the iterations, while Tab. 5.9 reports the objective function values from all six simulations along with the design variable $c_{w,d}$ corresponding to the square column of the building.

All simulations converge to the same objective function value of \$ 6,632.5, with the column cross-section design variable $c_{w,d} = 34.86\,cm$. By approximately 60 iterations, convergence can be considered achieved in the six simulations. The minimum cost value obtained is consistent with the validation results shown in Fig. 5.12, which confirms that the Firefly algorithm converges to the true minimum of the objective function.

Figure 5.13 – Convergence of firefly throughout the simulations.

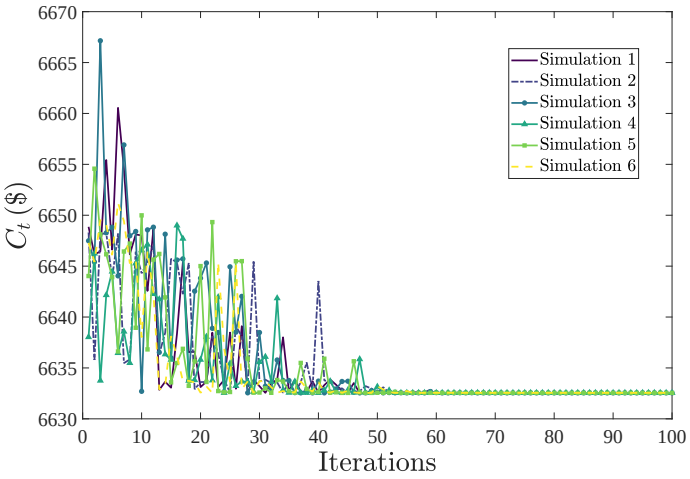

Source: Author.

Table 5.9 – Total Cost ($C_t(x_d)$) and design variable (x_d) values throughout the simulations.

Simulation	$C_t(x_d)$ **($)**	x_d **(cm)**
1	$6,632.5$	34.86
2	$6,632.5$	34.86
3	$6,632.5$	34.86
4	$6,632.5$	34.86
5	$6,632.5$	34.86
6	$6,632.5$	34.86

Source: Author.

The next step is to evaluate the attractiveness of the fireflies during the iterations of the algorithm. Fig. 5.14 illustrates the positions of all fireflies in six different iterations for one of the six simulations performed.

Fig. 5.14 confirms that the 60 fireflies generated for the problem converge toward the brightest one, corresponding to the optimal design variable $c_{w,d} = 34.86$ cm. At iteration 1, the fireflies are distributed across almost the entire design space, whereas by iteration 60 nearly all are concentrated around the optimal value, indicating that their movement is consistent with the algorithm's expected behavior.

Figure 5.14 – Representation of fireflies at different iterations of the algorithm.

(a) Iteration 1 **(b)** Iteration 20

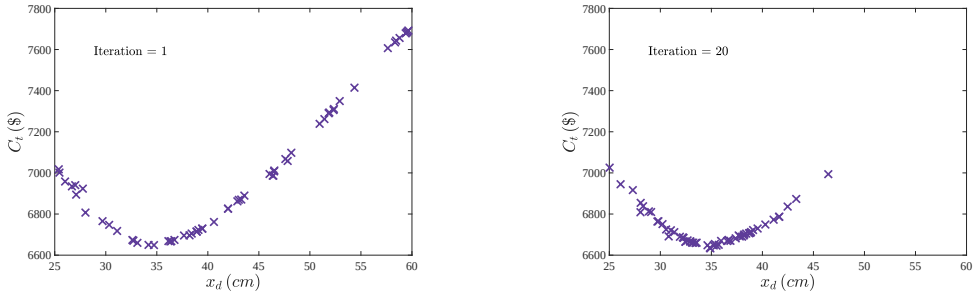

(c) Iteration 40 **(d)** Iteration 60

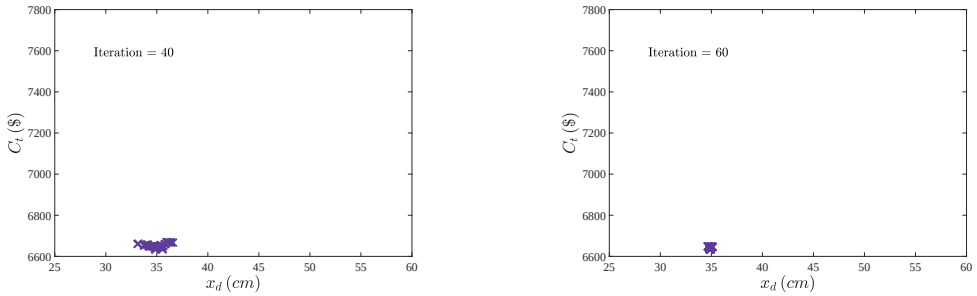

(e) Iteration 80 **(f)** Iteration 100

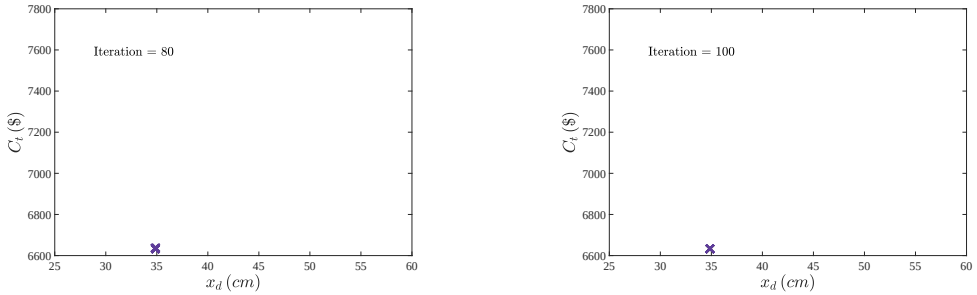

Source: Author.

5.4 Chapter overview

This chapter introduced a methodology that applies an Adaptive Kriging framework to build a metamodel capable of predicting the maximum structural demand response. For each IDA level and earthquake record, the metamodel estimates the maximum drift as a function of the column cross-section dimension. The complete PBEE framework was applied to the city of Natal, in the state of Rio Grande do Norte (Brazil), using a hazard curve and a ground motion set specific to the region. A three-story RC frame was analyzed, and fragility functions were derived from both the original FE model and the metamodel for a column cross-section of $30\,cm$.

The results showed relative errors up to 6.5% in the median values of the fragility

functions, with larger discrepancies for higher Damage Limit States, likely due to convergence issues in OpenSees at higher seismic intensities, indicating global instability. In the loss assessment, the maximum error in the total repair cost over a 100-year lifetime was 3.38%, confirming that the metamodel satisfactorily captures the mean annual conditional failure rate and the probability of failure. These results validate its use in optimization problems to explore structural design improvements under seismic actions.

The first optimization problem presented in this work was also discussed. The objective was to determine the optimal dimensions of a square column cross-section for the three-story building. The cost function was defined as the sum of initial construction costs, obtained from the Brazilian SINAPI database (INSTITUTO BRASILEIRO DE GEOGRAFIA E ESTATÍSTICA, 2023) and converted to US dollars, and expected damage costs estimated through the PBEE framework. Validation confirmed that the adopted cost definitions and design boundaries, with column dimensions ranging from 25 to 60 cm, lead to a consistent optimum solution. The Firefly algorithm, tested through six simulations, converged to the expected optimum column dimension after about 60 iterations. The analysis of firefly attractiveness further confirmed the proper functioning of the algorithm throughout the iterations.

Finally, it is important to note that, while the proposed framework effectively reduced computational time and accurately predicted the structural response, it is limited to the selected ground motion set and does not account for variability in seismic input. The next chapters address this limitation by incorporating ground motion uncertainties into the framework.

6 INCORPORATING STATISTICAL UNCERTAINTY INTO METAMODEL-DRIVEN PBRO

This chapter proposes a noisy Kriging metamodeling framework to support Performance -Based Risk Optimization (PBRO) under the FEMA P-58 (2018) methodology. The approach models Engineering Demand Parameters (EDPs) as a vector of joint lognormal random variables, with metamodels trained to predict the median, dispersion (standard deviation in natural log space), and correlation structure of the joint distribution as functions of the design variables. Crucially, statistical uncertainty in the estimated parameters—arising from the limited number of ground motions at each candidate design—is explicitly incorporated through the Kriging noise term (Rodrigues; Spence; Beck, 2026).

Moreover, the proposed framework addresses a limitation of the framework presented in Section 5 related to the selected ground motion set. The introduction of statistical variability in the estimation of the population parameters of the EDP distributions is adopted as a means to account for the hazard-related variability associated with the problem.

6.1 Preamble

Within the Performance-Based Earthquake Engineering (PBEE) framework defined in FEMA P-58, EDPs serve as the link between structural response, fragility, and loss models. They are typically obtained from NLTHA using a set of ground motions representing the seismic scenario of interest, with the resulting joint lognormal distribution capturing record-to-record variability—the dominant source of aleatory uncertainty in structural response. However, due to the high computational cost of Nonlinear Time History Analysis (NLTHA), the number of ground motions is often limited, and the distribution parameters (medians, dispersions, and correlations) must be statistically inferred from small samples. This introduces statistical uncertainty in the estimated parameters, which is rarely represented explicitly in PBEE analyses.

As previously discussed in this work, this limitation becomes even more pronounced in Performance-Based Risk Optimization (PBRO), where the joint EDP distribution evolves with design. The repeated estimation of distribution parameters during the optimization process amplifies the impact of statistical uncertainty, potentially affecting convergence and the quality of the obtained solution.

To address this issue, this chapter proposes a noisy Kriging metamodeling framework to support PBRO within the FEMA P-58 methodology. The approach models EDPs as a vector of joint lognormal random variables and trains metamodels to predict the median,

dispersion, and correlation structure of the joint distribution as functions of the design variables. Crucially, statistical uncertainty from the limited number of ground motions is explicitly incorporated through the Kriging noise term, allowing the metamodel to serve as a statistically grounded and computationally efficient representation of population-level behavior. The resulting PBRO problem is formulated as a multi-objective optimization balancing construction cost and seismic risk. A full-scale case study on the optimization of buckling-restrained braces in a steel seismic force-resisting system demonstrates that accurate performance metrics—comparable to those obtained with thousands of ground motions—can be achieved using as few as 50 records per metamodel training point, with orders-of-magnitude reductions in computational cost.

6.2 Problem Setting

In the PBEE formulation, closed-form evaluation of Eq. (2.1) is generally infeasible, especially for nonlinear systems. Monte Carlo simulation can be used (Yang *et al.*, 2009), with each sample involving a structural analysis under a ground motion, as described in Section 2.4.1.

The statistical inference required to estimate the parameters of $\mathbf{X} \in \mathbb{R}^{N_e \times N_p}$ introduces statistical uncertainty into the inferred joint distribution of **EDP**, particularly when only a limited number of ground motions are available. This inferred distribution is then employed to generate a large synthetic sample matrix, $\mathbf{W} \in \mathbb{R}^{D_s \times N_p}$, enabling an efficient loss assessment through the FEMA P-58 (2018) procedure (Yang *et al.*, 2009). As detailed in later sections, this work explicitly incorporates that statistical uncertainty into a metamodel-based framework to enhance the robustness of the loss estimation process.

6.2.1 Inference and Statistical Uncertainty

Let **EDP** of Eq. (2.13) represent a second-order random vector defined as $\mathbf{EDP}(S(t,\omega))$, where $S(t,\omega)$ is the seismic input parameterized by time t and a random realization ω drawn from the sample space Ω.

The population-level mean vector, $\mu_{\mathbf{EDP}}$, and covariance matrix, $\Sigma_{\mathbf{EDP}}$, of **EDP** are given by:

$$\mu_{\mathbf{EDP}} = \mathbb{E}[\mathbf{EDP}], \quad \Sigma_{\mathbf{EDP}} = \mathbb{E}\left[(\mathbf{EDP} - \mu_{\mathbf{EDP}})(\mathbf{EDP} - \mu_{\mathbf{EDP}})^T\right] \tag{6.1}$$

In practice, $\mu_{\mathbf{EDP}}$ and $\Sigma_{\mathbf{EDP}}$ are unknown and must be statistically inferred from a finite set of N_e NLTHAs. Given the demand matrix $\mathbf{X} \in \mathbb{R}^{N_e \times N_p}$ of N_p EDPs across N_e ground motion records, unbiased estimators of the mean and covariance are given by:

$$\hat{\mu}_{\mathbf{EDP}} = \frac{1}{N_e}\sum_{j=1}^{N_e} \mathbf{edp}_j, \quad \hat{\Sigma}_{\mathbf{EDP}} = \frac{1}{N_e - 1}\sum_{j=1}^{N_e} (\mathbf{edp}_j - \hat{\mu}_{\mathbf{EDP}})(\mathbf{edp}_j - \hat{\mu}_{\mathbf{EDP}})^T \tag{6.2}$$

These estimates inherently carry statistical uncertainty, as both $\hat{\mu}_{\mathbf{EDP}}$ and $\hat{\Sigma}_{\mathbf{EDP}}$ are random quantities dependent on the finite sample of ground motions. The accuracy of these estimates improves with increasing N_e, but expanding the ground motion set significantly increases computational cost.

To formally characterize this variability, the estimation process can be viewed as a repeated experiment. Let $\mathbf{X}_1, \mathbf{X}_2, \ldots, \mathbf{X}_{N_s}$ denote N_s independent realizations of the demand matrix, each obtained from an independent ground motion set. The sample mean across these experiments is:

$$\hat{\mu}_{\mathbf{X}} = \frac{1}{N_s} \sum_{j=1}^{N_s} \hat{\mu}_{\mathbf{EDP},j} \tag{6.3}$$

The variance of these mean estimates, denoted $\hat{\Sigma}_{\mathbf{X}}$, quantifies the statistical uncertainty due to limited data. For a component of **EDP**, the corresponding estimation error, ϵ, is a zero-mean random variable with variance inversely proportional to the number of experiments:

$$\sigma_\epsilon^2 = \frac{1}{N_s} \sigma_{EDP}^2 \tag{6.4}$$

where σ_{EDP}^2 is the population variance of EDP.

This relationship highlights the trade-off between reducing statistical uncertainty and increasing computational effort. Furthermore, by the Central Limit Theorem, for sufficiently large N_s, the sampling distribution of the mean can be approximated as:

$$\hat{\mu}_{EDP} \sim \mathcal{N}\left(\mu_{EDP}, \frac{\sigma_{EDP}^2}{N_s}\right) \tag{6.5}$$

In the context of this work, where the number of available NLTHAs is limited, explicitly accounting for this statistical uncertainty is critical to ensure reliable metamodel calibration and robust performance predictions.

6.2.2 Optimal Design Problem

In the context of PBEE, optimization techniques can be naturally integrated to identify structural configurations that balance construction cost and seismic risk. This study adopts a PBRO formulation aimed at minimizing the combined cost of construction and expected annual repair costs. The problem can be expressed as the following multi-objective optimization problem:

$$\begin{aligned} &\text{Find} \quad \mathbf{x}_\mathbf{d}^* = \{x_{d_1}, \ldots x_{d_{n_{\mathrm{DV}}}}\}^T \\ &\text{to minimize} \quad W(\mathbf{x}_\mathbf{d}) = \{C_{\mathrm{cons}}(\mathbf{x}_\mathbf{d}), C_{\mathrm{exReCo}}(\mathbf{x}_\mathbf{d})\}^T \\ &\text{subject to} \quad \mathbf{x}_\mathbf{d} \in \mathcal{X} \end{aligned} \tag{6.6}$$

where $\mathbf{x}_\mathbf{d}$ is a n_{DV}-dimensional vector of design variables belonging to design space $\mathcal{X} \in \mathbb{R}^N$; $C_{\mathrm{cons}}(\mathbf{x}_\mathbf{d})$ is the construction cost; and $C_{\mathrm{exReCo}}(\mathbf{x}_\mathbf{d})$ represents the expected

annual repair, demolition, and collapse costs, which in general depends on the mean annual rate $\lambda(DV > dv)$, as defined in Section 2.4.1.

A key challenge lies in the fact that $C_{\text{exReCo}}(\mathbf{x_d})$ must be re-evaluated for each design point (i.e., candidate value of $\mathbf{x_d}$), as structural properties and corresponding seismic response quantities vary across the design space. Specifically, for each candidate $\mathbf{x_d}$, the following steps are required:

1. Compute the fundamental period $\bar{T}$ to scale ground motions;
2. Perform NLTHA to generate the demand matrix $\mathbf{x_d}$;
3. Estimate collapse fragility parameters from, for example, Incremental Dynamic Analysis (IDA);
4. Generate synthetic demands, $\mathbf{W}$, based on an inferred joint distribution for **EDP**;
5. Evaluate expected repair costs using Monte Carlo simulation.

Consequently, key response quantities become explicit functions of $\mathbf{x_d}$, including: (i) the fundamental period $\bar{T}(\mathbf{x_d})$; (ii) the mean $\mu_{\mathbf{EDP}}(\mathbf{x_d})$ and covariance $\Sigma_{\mathbf{EDP}}(\mathbf{x_d})$ of **EDP**; and (iii) the median $\mu_{\text{coll}}(\mathbf{x_d})$ and dispersion $\sigma_{\text{coll}}(\mathbf{x_d})$ of the collapse fragility function. Among these, only $\bar{T}(\mathbf{x_d})$ is independent of the stochastic nature of seismic inputs, as it depends solely on the structural system. The remaining parameters depend on statistically inferred quantities derived from limited ground motion sets, and thus are affected by statistical uncertainty. In practice, solving the PBRO problem involves operating on these estimated quantities—$\hat{\mu}_{\mathbf{EDP}}(\mathbf{x_d})$, $\hat{\Sigma}_{\mathbf{EDP}}(\mathbf{x_d})$, $\hat{\mu}_{\text{coll}}(\mathbf{x_d})$, and $\hat{\sigma}_{\text{coll}}(\mathbf{x_d})$—rather than their true (population-level) values. This introduces variability in the objective function, complicating convergence and increasing bias towards the selected ground motion set. Conventional variance reduction techniques, such as Common Random Numbers (Kleinman; Spall; Naiman, 1999; Huan; Marzouk, 2013), only partially mitigate this issue and may introduce instability and/or bias in the optimization process.

To address these challenges, the proposed framework will employ a noisy Kriging metamodel to directly estimate the population values of the distribution parameters of **EDP** as well as the collapse fragility functions. This metamodeling approach will not only significantly reduce computational effort but also explicitly account for statistical uncertainty in the estimated distribution parameters, enabling more reliable and efficient exploration of the design space.

6.3 Proposed approach

6.3.1 Overview

As introduced in Section 6.2.2 and Eq. (6.6), the objective function considers both the structure's construction and expected repair costs. The design variables, collected in

the vector $\mathbf{x_d}$, correspond to structural parameters of the system.

The expected repair cost, $C_{\text{exReCo}}(\mathbf{x_d})$, is an implicit, nonlinear function of the structural system's first-mode period as well as the population values of the distribution parameters associated with both the collapse fragility function and the joint distribution of the random vector, **EDP**. Specifically, $C_{\text{exReCo}}(\mathbf{x_d})$ depends on:

- First-mode period, $\bar{T}(\mathbf{x_d})$.
- Collapse fragility parameters: median $\mu_{\text{coll}}(\mathbf{x_d})$ and dispersion $\sigma_{\text{coll}}(\mathbf{x_d})$.
- Parameters of the joint distribution of **EDP**: marginal means $\mu_{EDP_i}(\mathbf{x_d})$, standard deviations $\sigma_{EDP_i}(\mathbf{x_d})$, and correlation terms $\rho_{EDP_{ij}}(\mathbf{x_d})$, derived from the covariance matrix $\Sigma_{\mathbf{EDP}}(\mathbf{x_d})$.

In general, this nonlinear relationship g_{NL} can be expressed as:

$$C_{\text{exReCo}}(\mathbf{x_d}) = g_{\text{NL}}\left(\bar{T}(\mathbf{x_d}), \mu_{\text{coll}}(\mathbf{x_d}), \sigma_{\text{coll}}(\mathbf{x_d}), \mu_{EDP_i}(\mathbf{x_d}), \sigma_{EDP_i}(\mathbf{x_d}), \rho_{EDP_{ij}}(\mathbf{x_d})\right) \quad (6.7)$$

where $i, j = 1, 2, \ldots, N_p$, with N_p is the number of EDPs, i.e., components of **EDP**.

For systems without uncertainty in the parameters of the nonlinear dynamic FE model, the first-mode period is deterministic. However, as discussed earlier, the population values of $\mu_{\text{coll}}(\mathbf{x_d})$, $\sigma_{\text{coll}}(\mathbf{x_d})$, $\mu_{EDP_i}(\mathbf{x_d})$, $\sigma_{EDP_i}(\mathbf{x_d})$, and $\rho_{EDP_{ij}}(\mathbf{x_d})$ are generally unknown and must be estimated through statistical inference based on a limited set of data obtained from NLTHA and IDA. Even if statistical uncertainty is neglected during the optimization process—a common assumption that can complicate convergence and increase bias in the final solution—the computational burden of repeatedly performing NLTHA, which is also required for IDA, remains significant. This challenge is particularly pronounced during optimization, where the distribution parameters must be estimated for each candidate design.

To address both the computational burden of repeated nonlinear analyses and the treatment of statistical uncertainty, this work proposes replacing complex FE model evaluations with a Kriging metamodel that explicitly incorporates statistical uncertainty through an additive noise term. The treatment of this uncertainty and the proposed metamodel formulation are detailed in the following sections.

6.3.2 Statistical uncertainty in the distribution parameters

A key challenge addressed in this work is the estimation of the population values of the distribution parameters governing the EDPs. In practice, these parameters must

be inferred from a finite set of ground motion analyses at each support point in the design space. Consequently, only statistical estimates of the joint lognormal distribution parameters of the random vector **EDP**, denoted $\hat{\mu}_{\mathbf{EDP}}(\mathbf{x_d})$ and $\hat{\Sigma}_{\mathbf{EDP}}(\mathbf{x_d})$, as well as the lognormal collapse fragility parameters $\hat{\mu}_{\text{coll}}(\mathbf{x_d})$ and $\hat{\sigma}_{\text{coll}}(\mathbf{x_d})$, can be obtained. These quantities correspond to the unbiased estimators defined in Eq. (6.2) and represent the model outputs to be predicted by the Kriging metamodels of this work. However, due to the use of different, randomly selected ground motion sets at each support point, statistical uncertainty arises across the design space, as illustrated in Fig. 6.1.

Figure 6.1 – Variation in the mean of a generic EDP for different ground motion sets, as a function of a design variable.

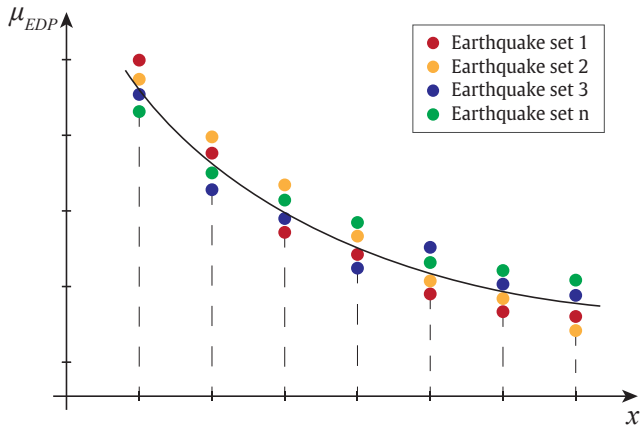

Source: Author.

The proposed framework seeks to model the underlying population trend, illustrated in Fig. 6.1 by the solid line, by appropriately defining the noise term, $\boldsymbol{\varepsilon}$, of Eq. (4.20). This noise term captures the estimation error resulting from the statistical uncertainty introduced by using a finite number of NLTHAs to obtain $\mathbf{x_d}$. Within this framework, the metamodels for the population values of the lognormal distribution parameters of the marginals of **EDP** are denoted as $\hat{Y}_{\mu_{EDP_i}}(\mathbf{x_d})$ and $\hat{Y}_{\sigma_{EDP_i}}(\mathbf{x_d})$. Similarly, the metamodels for the population values of the parameters of lognormal collapse fragility functions are denoted as $\hat{Y}_{\mu_{\text{coll}}}(\mathbf{x_d})$ and $\hat{Y}_{\sigma_{\text{coll}}}(\mathbf{x_d})$. Since the first-mode period $\bar{T}(\mathbf{x_d})$ is unaffected by the stochastic nature of the seismic inputs, it is approximated using a Kriging metamodel without an additive noise term, following Eq. (4.10), and is denoted by $\tilde{\mathcal{M}}_{\bar{T}}(\mathbf{x_d})$. Additionally, the terms of the correlation matrix, $\rho_{EDP_{ij}}$ are assumed to be weakly dependent on $\mathbf{x_d}$ and are approximated as constant across the design space. Under these assumptions, the expected repair cost can be expressed as:

$$C_{\text{exReCo}}(\mathbf{x_d}) = \tilde{g}_{\text{NL}}\left(\tilde{\mathcal{M}}_{\bar{T}}(\mathbf{x_d}), \hat{Y}_{\mu_{\text{coll}}}(\mathbf{x_d}), \hat{Y}_{\sigma_{\text{coll}}}(\mathbf{x_d}), \hat{Y}_{\mu_{EDP_i}}(\mathbf{x_d}), \hat{Y}_{\sigma_{EDP_i}}(\mathbf{x_d}), \rho_{EDP_{ij}}(\mathbf{x_{d0}})\right) \tag{6.8}$$

where $\mathbf{x_{d0}}$ is the point in the design space at which the correlation matrix is estimated.

Eq. (6.8) is an approximation that relies on the terms of the correlation matrix, $\rho_{EDP_{ij}}(\mathbf{x_{d0}})$, being treated as constant throughout the design space. However, the quality of this approximation depends on the choice of the point $\mathbf{x_{d0}}$ at which the terms $\rho_{EDP_{ij}}$ are estimated. Specifically, the terms of the correlation matrix, $\rho_{EDP_{ij}}(\mathbf{x_{d0}})$, best reflect the true correlation among the EDPs for designs close to $\mathbf{x_{d0}}$, while its accuracy may degrade for designs that differ significantly from this point. To provide a reasonable and broadly applicable approximation, this work assumes that $\mathbf{x_{d0}}$ corresponds to the mean of all support points considered. Under this assumption, $\rho_{EDP_{ij}}(\mathbf{x_{d0}})$ serves as an estimate of the average correlation structure across the design space, denoted by $\bar{\rho}_{EDP_{ij}}$. With this formulation, the objective function of the optimization problem can be computed without requiring additional evaluations of the nonlinear dynamic FE model, significantly reducing the computational burden of the optimization process.

Once the metamodels have been trained to estimate the population values of the distribution parameters required to compute the expected annual repair cost, $C_{\text{exReCo}}(\mathbf{x_d})$, a final Kriging metamodel, $\tilde{C}_{\text{exReCo}}(\mathbf{x_d})$, is constructed to further reduce the computational burden. This final surrogate encapsulates the effects of the intermediate metamodels by providing a direct approximation of the expected repair cost across the design space. As a result, the computationally intensive process of querying multiple intermediate metamodels, generating synthetic demand realizations, and performing Monte Carlo simulations for each candidate design is replaced by a single query to $\tilde{C}_{\text{exReCo}}(\mathbf{x_d})$. Under this formulation, Eq. (6.8) is rewritten as:

$$\tilde{C}_{\text{exReCo}}(\mathbf{x_d}) = \tilde{\mathcal{M}}_{\tilde{g}_{\text{NL}}}\left(\tilde{\mathcal{M}}_{\bar{T}}(\mathbf{x_d}), \hat{Y}_{\mu_{\text{coll}}}(\mathbf{x_d}), \hat{Y}_{\sigma_{\text{coll}}}(\mathbf{x_d}), \hat{Y}_{\mu_{EDP_i}}(\mathbf{x_d}), \hat{Y}_{\sigma_{EDP_i}}(\mathbf{x_d}), \bar{\rho}_{EDP_{ij}}\right) \tag{6.9}$$

The following section presents specific details on the proposed framework for modeling and propagating statistical uncertainty using noisy Kriging metamodels.

6.3.3 Proposed Approach for Incorporating Statistical Uncertainty in the Metamodels

6.3.3.1 Overview

To train the proposed metamodels, an initial DoE comprising S support points is generated. The selection of support points for calibrating Kriging is critical to controlling metamodel bias. This study employs LHS to efficiently distribute support points across the design space, ensuring space-filling properties (Morris; Mitchell, 1995; Nowak; Collins, 2012). An optimal LHS algorithm is used to further enhance the uniformity of point placement.

The number of support points, S, follows a standard heuristic for metamodeling of structural systems governed by smooth differential equations: $S = 10 \times (n_{\text{DV}})$, where n_{DV} is the number of design variables. This sampling plan has demonstrated robust performance

across similar engineering applications (Loeppky; Sacks; Welch, 2009). For each support point, a set of N_e ground motion records is randomly sampled from a stochastic ground motion model driven by a white noise sequence Z and scaled to match the target hazard spectrum at $S_a(\bar{T})$. While the developments presented here focus on synthetic ground motions, the approach can be extended to natural ground motion records. At each support point, the experiment yields the response matrix $\mathbf{X}$, which is used to infer the lognormal distribution parameters of the marginals of **EDP** based on Eq. (6.2). A similar procedure, employing N_e IDAs, is performed to estimate the lognormal parameters of the collapse fragility function. As discussed in Section 6.2.1, the inferred distribution parameters are subject to estimation error, ϵ, arising from the finite sample size. This error is modeled as a random variable with zero mean and variance $\hat{\sigma}_\epsilon^2$, as expressed for the sample mean in Eq. (6.4).

To estimate the population values of the lognormal distribution parameters, this work proposes performing N_s independent repetitions of the experiment described above, each using a different set of ground motions generated from the stochastic excitation model $S(t, \omega)$. This results in N_s estimates of the distribution parameters μ_{EDP_i} and σ_{EDP_i} for each component i of **EDP**. As discussed in Section 6.2.1, these estimates follow a normal distribution for sufficiently large N_s. The sample mean and variance of the estimated parameters are computed using Eq. (6.2). The variance of this distribution, $\hat{\sigma}_\epsilon^2$, quantifies the statistical uncertainty associated with the finite number of ground motions used in each experiment. This uncertainty is used to define the noise term in the Kriging formulation of Eq. (4.20).

Nevertheless, performing repeated experiments at every support point to directly estimate the population values of the distribution parameters would reintroduce substantial computational burden, rendering the approach impractical. To mitigate this, the proposed framework limits the N_s repetitions to the central point of the DoE. It is assumed that the variance of the estimation error, $\hat{\sigma}_\epsilon^2$, is approximately homogeneous across the design space. Consequently, the variance estimated at the central point is applied uniformly to all support points. Under this assumption, the noise term in the Kriging regression of Eq. (4.20) is modeled as homoscedastic. To support this assumption and validate limiting the N_s repetitions exclusively to the central point of the DoE, the parametric Bartlett's χ^2 test (Bartlett, 1937) is applied in Section 6.4.4.2 to evaluate the homogeneity of variances among all support points of the DoE.

Furthermore, the variance obtained from the evaluation of the statistical uncertainty of the EDPs is used to define the noise term for the metamodels estimating the distribution parameters of the collapse fragility functions. As collapse in this study is defined based on the lateral drift response, the variance associated with the drift EDP is specifically adopted as the noise term in the Kriging metamodels for the collapse fragility parameters.

6.3.3.2 Algorithm

The proposed approach is summarized in the flowchart shown in Fig. 6.2. Branch (a) illustrates the procedure for estimating the statistical uncertainty, $\hat{\sigma}_\epsilon^2$. Branch (b) presents the methodology for generating the distribution parameters of the marginals of **EDP**, incorporating the noise term obtained from the statistical uncertainty evaluation. Finally, branch (c) outlines the process for estimating the median and dispersion of the collapse fragility function, including the treatment of statistical uncertainty described in Sec. 6.3.3.1.

Figure 6.2 – Flowchart of the proposed methodology: (a) treatment of statistical uncertainty; (b) generation of **EDP** distribution parameters from NLTHA; (c) collapse fragility characterization based on IDA.

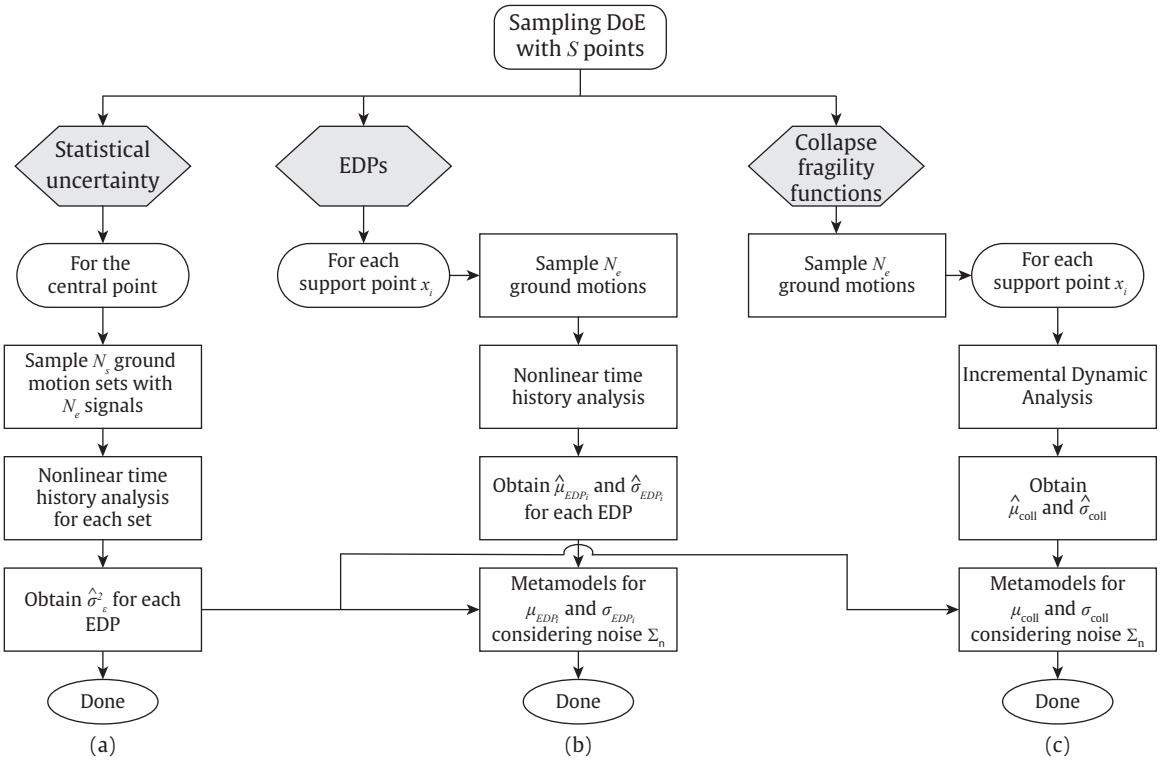

Source: Author.

To quantify the statistical uncertainty associated with the inference of the distribution parameters of the marginals of **EDP**, and incorporate this uncertainty as the noise term in the Kriging metamodels, the following steps are implemented:

1. Generate an optimal number of support points, S, based on the number of design variables (components of $\mathbf{x_d}$), ensuring that the central point of the design space is included.
2. Construct a sufficiently large parent set of ground motion records. The size of this set must be large enough to allow independent selection of N_s ground motion sets without repetition.

3. Randomly sample N_s ground motion sets, each containing N_e records, drawn without replacement from the parent set.
4. Scale each ground motion set to be consistent with the target response spectrum at the desired ground shaking intensity level.
5. Perform N_e NLTHAs at the central point for each of the N_s ground motion sets. For each set, compute $\mathbf{X}$ and infer the parameters of the marginals of **EDP**.
6. Fit a normal distribution to the N_s estimates of each marginal distribution parameter and compute the corresponding variance, $\hat{\sigma}_\epsilon^2$, which is used as the noise term in the Kriging metamodels.

With the statistical uncertainty characterized through $\hat{\sigma}_\epsilon^2$ for the parameters of the marginal distributions of **EDP**, the following steps are performed to generate the necessary nonlinear dynamic analysis data at each of the S support points:

1. Randomly sample N_e ground motions without replacement to create a ground motion set for each support point.
2. Scale the sampled ground motion set to match the target response spectrum at the desired ground shaking intensity level, consistent with standard engineering practice.
3. Perform NLTHAs using the scaled ground motion set.
4. Estimate the mean $\hat{\mu}_{EDP_i}(\mathbf{x_d})$ and standard deviation $\hat{\sigma}_{EDP_i}(\mathbf{x_d})$ for each marginal distribution of **EDP**.

With the results obtained for each support point, two Kriging metamodels are calibrated to estimate the population values of the parameters of each marginal distribution of **EDP**. The noise in these metamodels is incorporated through the term $\mathbf{\Sigma}_n = \mathbf{I}_S \hat{\sigma}_\epsilon^2$ with $\mathbf{I}_S$ the identity matrix of dimension S. Specifically, one Kriging metamodel is constructed to estimate $\mu_{EDP_i}(\mathbf{x_d})$, while a second metamodel is used to estimate $\sigma_{EDP_i}(\mathbf{x_d})$.

To obtain μ_{coll} and σ_{coll} for the collapse fragility function based on IDA, the following steps are performed at each of the S support points:

1. Sample N_e ground motions to create a set, without replacement, for all support points.
2. Perform IDA for each ground motion in the set until collapse is reached.
3. Estimate $\hat{\mu}_{\text{coll}}$ and $\hat{\sigma}_{\text{coll}}$ for the collapse fragility function based on the IDA results.

With the results obtained for each support point, two Kriging metamodels are calibrated: one for μ_{coll} and another for σ_{coll}. The effect of statistical uncertainty is incorporated into these metamodels through a noise term, based on the estimated variance of the drift EDP used to define collapse in the IDA procedure.

6.4 Case Study 1

6.4.1 Overview

The proposed framework is demonstrated through a case study involving a two-story archetype Special Moment Frame (SMF) building designed according to (ASCE, 2013; AISC, 2010). Plan and elevation views of the building are shown in Figs. 6.3a and 6.3b, respectively. Buckling Restrained Braces (BRBs) are incorporated into the design to enhance lateral stiffness and energy dissipation. These braces, shown in red in Fig. 6.3, are concentric structural elements that prevent local buckling and concentrate inelastic deformations within their core (Uang; Nakashima; Tsai, 2004), thereby improving the building's seismic performance by limiting structural damage.

Figure 6.3 – Case study 1 structure: (a) typical plan view of the building; (b) representation of the Special Steel Moment Frame (SMF).

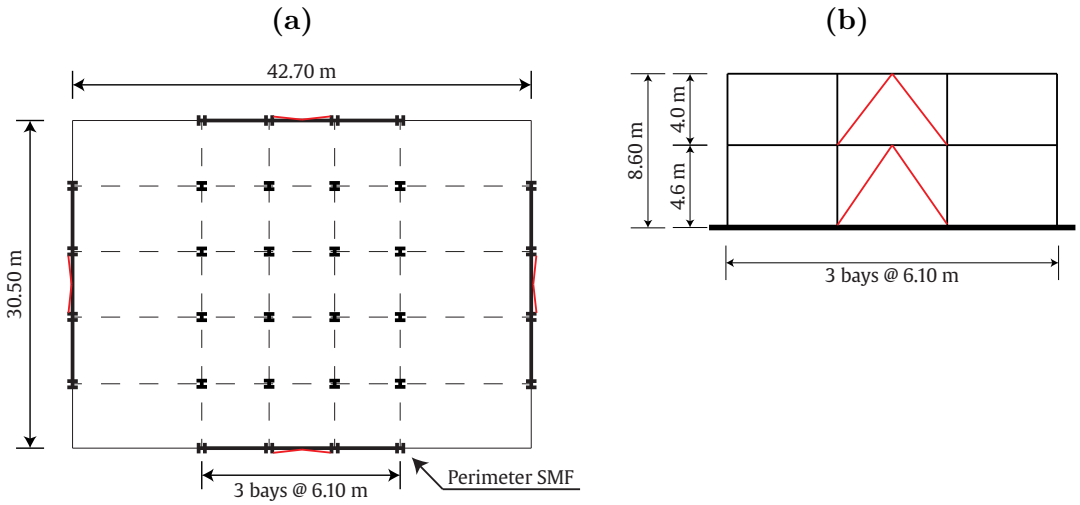

Source: Author.

The objective of this case study is to optimize the cross-sectional areas of the BRBs located on the first and second stories of the building. The design variables are defined as the BRB areas for the first story, $A_{\text{BRB},1}$, and for the second story, $A_{\text{BRB},2}$. The corresponding multi-objective PBRO is formulated as:

$$\begin{aligned} &\text{Find} \;\; \mathbf{x_d} = \{A_{\text{BRB},1}, A_{\text{BRB},2}\}^T \\ &\text{to minimize} \;\; W(\mathbf{x_d}) = \{C_{\text{cons}}(\mathbf{x_d}), \tilde{C}_{\text{exReCo}}(\mathbf{x_d})\}^T \\ &9.7 \leq A_{\text{BRB},1} \leq 64.5\,\text{cm}^2 \\ &9.7 \leq A_{\text{BRB},2} \leq 64.5\,\text{cm}^2 \end{aligned} \tag{6.10}$$

where $C_{\text{cons}}(\mathbf{x_d})$ represents the initial construction cost of the structural steel frame, including beams, columns, and BRBs, and $\tilde{C}_{\text{exReCo}}(\mathbf{x_d})$ is the expected annual repair cost,

computed following the FEMA P-58 methodology (FEMA, 2018), using the metamodeling framework outlined in Section 6.3.

Hypothetically situated in urban California (soil class C), the structure features a first-story height of 4.6 m and a second-story height of 4.0 m. The construction materials for beams and columns consist of ASTM A992 Gr. 50 steel. The geometric specifications of the structural elements are provided in Table 6.1, and additional details regarding the design can be found in (NIST, 2010; Zareian; Lignos; Krawinkler, 2010; Elkady; Lignos, 2014; Elkady; Lignos, 2015). The steel used for the BRB cores corresponds to ASTM A36.

Table 6.1 – Member Sizes for the Special SMF.

Story	Beam Size	Exterior Column Size	Interior Column Size
1	W30X132	W24X131	W24X162
2	W16X31	W24X131	W24X162

Source: Author.

The construction cost of the steel frame is estimated as:

$$C_{\text{cons}}(\mathbf{x_d}) = C_{\text{steel}}\left(W_{\text{beams}} + W_{\text{columns}}\right) + C_{\text{BRB}}W_{\text{BRB}} \tag{6.11}$$

where C_{steel} is the cost per unit weight of structural steel, C_{BRB} is the cost per unit weight of the BRBs, and W_{beams}, W_{columns}, and W_{BRB} are the total weights of the beams, columns, and BRBs, respectively. The unit costs adopted in this study are $C_{\text{steel}} = \$4.72/\text{kg}$ (Ghasemof; Mirtaheri; Mohammadi, 2022) and $C_{\text{BRB}} = \$8.99/\text{kg}$ (Guerrero *et al.*, 2017). The nominal weights of the beams and columns are obtained from the AISC database (v16.0) (AISC, 2022b). For the BRBs, the total weight is calculated as $W_{\text{BRB}} = A_{\text{BRB}}L_{\text{BRB}}\rho_{\text{BRB}}$, where A_{BRB} is the cross-sectional area, L_{BRB} is the element length, and ρ_{BRB} is the material density, assumed to be $7850\,\text{kg/m}^3$ for ASTM A36 steel.

The structure evaluated in this study is considered a commercial office building, with key performance information provided in Table 6.2.

Table 6.2 – Performance information for the studied building.

Number of stories	2
Floor area	$1300\,\text{m}^2$
Replacement Cost (RC)	\$5,443,760
Total loss threshold (% RC)	100

Source: Author.

The Replacement Cost of the building is estimated using the RSMeans Project Cost database. For a 2- to 4-story commercial office, the construction cost is taken as $\$2093.75/\text{m}^2$. The total loss threshold is assumed to be 100%, meaning that repair cost estimates are calculated regardless of whether they approach or exceed the Replacement

Cost. Environmental impacts are not considered in this assessment, although they could be incorporated in future extensions of this work. Consistent with FEMA P-58 (FEMA, 2018), the number of workers required for building repairs is set to 1 worker per 1000 ft^2 of floor area, which corresponds to approximately 1 worker per 100 m^2.

A summary of the building components is provided in Table 6.3. The fragility function database from the PACT tool (ATC, 2018) is used to define the building performance models, based on the listed contents. The corresponding EDPs associated with each fragility function are also shown in Table 6.3. Component categories are defined as follows: B for structural shell components; C for interior components; D for service components; and E for equipment and furnishing components. The quantity of each component is calculated using the Normative Quantity Estimation Tool provided in the FEMA P-58 support materials (FEMA, 2018).

Table 6.3 – Building component information and associated EDPs.

Cat.	Description	EDP	Floor	Quantity
B	Steel BRB, Chevron brace; weight $>$ 41 plf and $<$ 99 plf	SDR	All	4 units
B	Bolted shear tab gravity connections	SDR	All	44 units
B	Post-Northridge RBS connection, beam one side, dep. $\geq$ W30	SDR	1	12 units
B	Post-Northridge RBS connection, beam both sides, dep. $\leq$ W27	SDR	2	12 units
B	Concrete tile roof, tiles secured per UBC94	PFA	Roof	37.8 (100 ft^2)
C	Suspended ceiling, SDC D/E/F ($I_p = 1.5$), area $>$ 2500 ft^2	PFA	All	56.0 (2500 ft^2)
C	Gypsum wall partitions with wallpaper, fixed top and bottom	SDR	All	7.0 (100 ft^2)
C	Prefabricated steel stair with steel treads, no seismic joints	SDR	All	0.7 units
B	Midrise curtain wall with insulating glass units (dual pane)	SDR	All	70 (30 ft^2)
D	Hydraulic elevator, post-1998 installation	PFA	All	2 units
D	Fire sprinkler piping (horizontal), poorly braced, SDC D/E/F	PFA	All	2.8 (1000 ft)

Note: SDR = interstory drift ratio; PFA = peak floor acceleration.

Source: Author.

6.4.2 Seismic Hazard and Stochastic Ground Motion Model

The seismic hazard considered for this study corresponds to the 5% damped, 2% in 50 years (2/50) Target Hazard Spectrum, consistent with a site located in Los Angeles on soil type C. Seismic hazard curves are obtained from the U.S. Geological Survey (USGS) tool (U.S. Geological Survey, 2024) and used to derive the target spectrum following ASCE 7-16 provisions (ASCE, 2017b).

A stochastic ground motion model is used to generate synthetic ground motion records that are statistically consistent with the target spectrum. The model corresponds to a two-corner point-source formulation that captures both the physics of fault rupture and wave propagation (Vetter; Taflanidis, 2012; Arunachalam; Spence, 2023b; Atkinson; Silva, 2000). Non-stationarity in time is incorporated through a temporal envelope function, while the frequency content is controlled through a parametric radiation spectrum $A(f; M_w, r)$, both of which depend on earthquake magnitude M_w and epicentral distance r.

The frequency-domain radiation spectrum is expressed as:

$$A(f; M_w, r) = (2\pi f)^2 \, E(f; M_w) P(f; r) G(f) \tag{6.12}$$

where $E(f; M_w)$ represents the source term, $P(f; r)$ models path effects, and $G(f)$ accounts for site amplification.

The temporal envelope function, which governs the evolution of the ground motion over time, is given by (Boore, 2003):

$$e(t; M_w, r) = a_t \left(\frac{t}{t_n}\right)^{b_t} \exp\left(-c_t \frac{t}{t_n}\right) \tag{6.13}$$

where the constants a_t, b_t, and c_t are chosen to ensure that $e(t; M_w, r)$ peaks at $t = \lambda_t t_n$ with a normalized maximum of 1, and satisfies $e(t_n; M, r) = \eta_t$.

Synthetic ground motions are generated by modulating a white noise sequence $\mathbf{X_w} = [X_w(i\Delta t)]$ as follows:

1. Multiply $\mathbf{X_w}$ by the envelope function $e(t; M, r)$.
2. Transform to the frequency domain.
3. Normalize by the square root of the mean-square amplitude spectrum.
4. Multiply by the radiation spectrum $A(f; M, r)$.
5. Transform back to the time domain to obtain the acceleration time history.

The model parameters used for ground motion generation follow (Vetter; Taflanidis, 2012; Arunachalam; Spence, 2023b): radiation pattern $R_\Phi = 0.55$, shear-wave velocity $\bar{V}_s = 3.5$ km/s, rock density $\rho_s = 2.8$ g/cm^3, seismic velocity $c_Q = 3.5$ km/s, and elastic attenuation factor $Q(f) = 180 f^{0.45}$. Geometric spreading is modeled as $Z(R) = 1/R$ for $R < 70$ km, and $Z(R) = 1/70$ for $R \geq 70$ km, where R is the source-to-site distance. Site amplification follows the generic rock site model from Boore and Joyner (1997). The envelope function parameters are chosen as $\lambda_t = 0.2$ and $\eta_t = 0.05$ (Boore, 2003).

The earthquake magnitude M_w is modeled using a truncated Gutenberg-Richter distribution (Gutenberg; Richter, 1944):

$$p(M_w) = \frac{\beta \exp\left(-\beta(M_w - M_{w,\min})\right)}{1 - \exp\left(-\beta(M_{w,\max} - M_{w,\min})\right)} \tag{6.14}$$

where $M_{w,\min} = 6$, $M_{w,\max} = 8$, and $\beta = 0.9 \log_e(10)$.

The epicentral distance r is modeled as a lognormal random variable with a median of 2.5 km and a coefficient of variation of 0.4. The stochastic ground motion model is calibrated to produce accelerograms whose response spectra match the target spectrum. Fig. 6.4 shows the target spectrum, along with 1000 generated ground motion samples and their mean spectrum.

Figure 6.4 – Target Hazard Spectrum with 1000 generated ground motion (GM) samples.

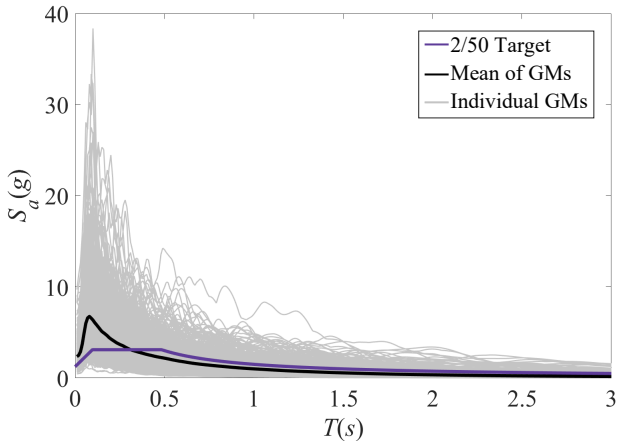

Source: Author.

6.4.3 Finite Element Model of the Structural System

A two-dimensional nonlinear dynamic FE model of the two-story archetype steel building was developed using OpenSees (McKenna; Fenves; Scott, 2006). The effect of the floor slab was represented using a rigid diaphragm assumption. Beams and columns were modeled with displacement-based beam-column elements incorporating distributed plasticity. Each element was discretized using five integration points, with six fibers along the depth of the web and breadth of the flange, and one fiber along the thickness of both the web and flange. The cyclic behavior of structural steel for the beams and columns was modeled using the Steel02 material model from the OpenSees library, originally proposed by FILIPPOU, POPOV and BERTERO (1983). A Young's modulus of 200 GPa and a yield strength of 345 MPa were adopted, with an isotropic strain hardening ratio of 1%. Rayleigh damping was applied with a damping ratio of 2% for the first and third vibration modes to simulate inherent damping. P-Δ effects were explicitly included in the column elements.

BRBs were modeled using corotational truss elements with elastoplastic material behavior represented by the SteelBRB model introduced by Zona and Dall'Asta (2012) and implemented within OpenSees by Gu *et al.* (2014). Experimental validation of the elastoplastic material can be found in Zona and Dall'Asta (2012). The material parameters adopted for the BRBs are summarized in Table 6.4, including the Young's modulus (E), core yield stress (F_y), and the maximum tension ($F^+_{y,\max}$) and compression ($F^-_{y,\max}$) yield stresses corresponding to fully saturated isotropic hardening conditions.

Table 6.4 – Material parameters for the steel BRBs.

E (GPa)	F_y (MPa)	$F^{+}_{y,\max}$ (MPa)	$F^{-}_{y,\max}$ (MPa)
200	370	492.10	580.68

Source: Author.

6.4.4 Results

6.4.4.1 Preamble

For the optimization problem in Eq. (6.10), and following the general rule for determining the number of support points outlined in Section 6.3.3.1, 20 support points were selected to construct the Kriging metamodels and define the DoE, as shown in Fig. 6.5. The points adequately cover the design domain, and the Kriging metamodels were not extrapolated beyond its bounds.

Figure 6.5 – Support points of the DoE.

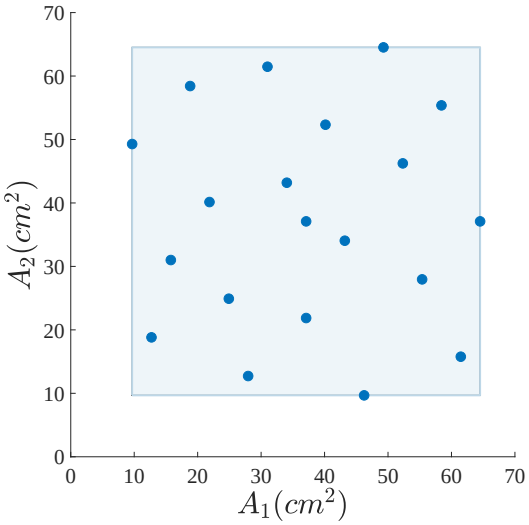

Source: Author.

A number of $N_e = 50$ ground motions was used to evaluate statistical uncertainty and to train the metamodels, in accordance with the minimum recommendation of FEMA P-58 (FEMA, 2018) and supported by recent studies (Baltzopoulos; Baraschino; Iervolino, 2019; Jalayer; Ebrahimian; Miano, 2021; Silva *et al.*, 2021; Patsialis; Taflanidis; Vamvatsikos, 2023; Wu; Burton, 2024).

This section presents the results in three parts: (1) evaluation of statistical uncertainty in the inferred distribution parameters, (2) Kriging metamodels developed to approximate the population values of the distribution parameters, and (3) outcomes of the multi-objective optimization process.

6.4.4.2 Statistical uncertainty

The evaluation of statistical uncertainty was initially performed at all support points, using $N_e = 50$ ground motions within each of the $N_s = 10$ ground motion sets. A parent set of 500 hazard-consistent ground motions was generated with the stochastic ground motion model. NLTHA were performed to estimate $\hat{\mu}_{EDP_i}(\mathbf{x_d})$ and $\hat{\sigma}_{EDP_i}(\mathbf{x_d})$ for each component of **EDP**. Figs. 6.6 and 6.7 present the results in terms of the means and standard deviations of the EDPs associated with drift at the first and second floors.

The results confirm noticeable variation in outcomes across different support points, highlighting the influence of the BRB area on the structural response. Additionally, variation is observed at individual support points depending on the specific ground motion set selected.

As discussed in Section 6.2.1, according to the Central Limit Theorem, if N_s is sufficiently large, the sample distribution of the estimated parameters tends toward a normal distribution. Furthermore, in Section 6.3.3, it is proposed to assume that the variance of the estimation error is homogeneous across the design space, allowing the variance estimated at the central point to be extended to all other support points. To evaluate whether $N_s = 10$ is a sufficiently large sample size and whether the assumption of homogeneous variance is reasonable, the Shapiro–Wilk (S–W) test (Shapiro; Wilk, 1965) is applied to assess the normality of the 10 observations at each support point. Additionally, Bartlett's χ^2 test (Bartlett, 1937) is used to evaluate the homogeneity of variances among the support points for all considered components of **EDP**.

For the S–W test, it was found that, with 99% confidence, the samples corresponding to the histograms of Figs. 6.6 and 6.7 at each support point are drawn from a normally distributed population. This confirms that using $N_s = 10$ ground motion groups is sufficient to assess the variance in the parameter estimates. The results from Bartlett's χ^2 test indicate that, at a 95% confidence level, the variances across the 20 support points are homogeneous. These findings suggest that, at least for this case study, the procedure outlined in Section 6.3.3 for modeling statistical uncertainty is valid.

6.4.4.3 The noisy Kriging metamodels

All metamodels developed in this study adopt the following configurations: ellipsoidal correlation type, anisotropic correlation, and the Maximum Likelihood Estimation method. The primary differences between the metamodels lie in the Kriging trend and the correlation families used.

Figure 6.6 – Histograms of the means of the underlying Gaussians of the drift EDP at the (a) 1st and (b) 2nd story for all support points.

(a) 1st story.

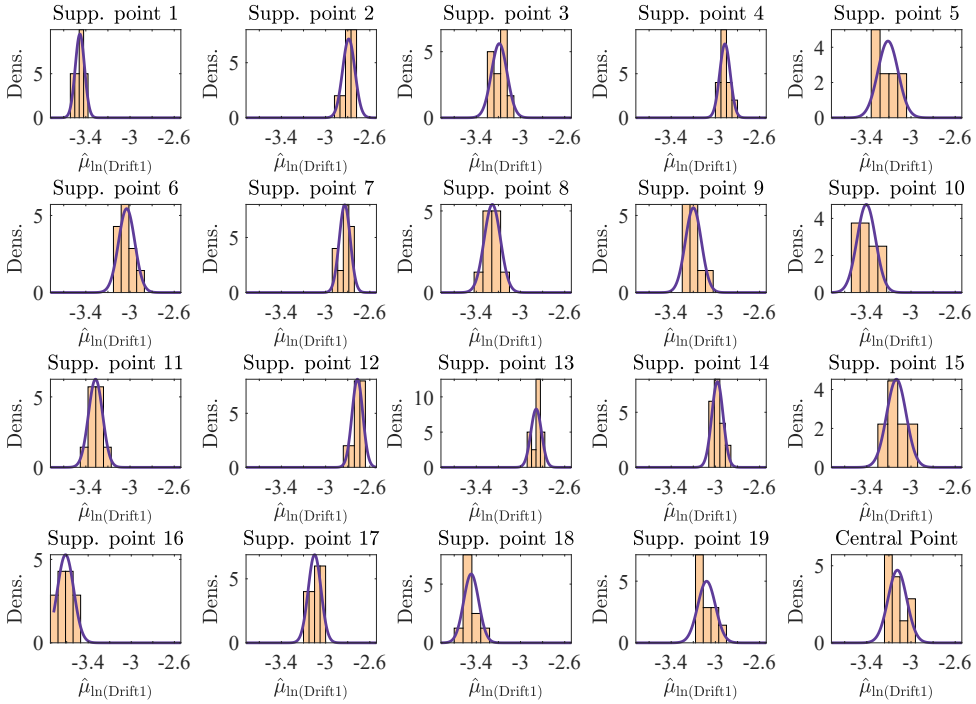

(b) 2nd story.

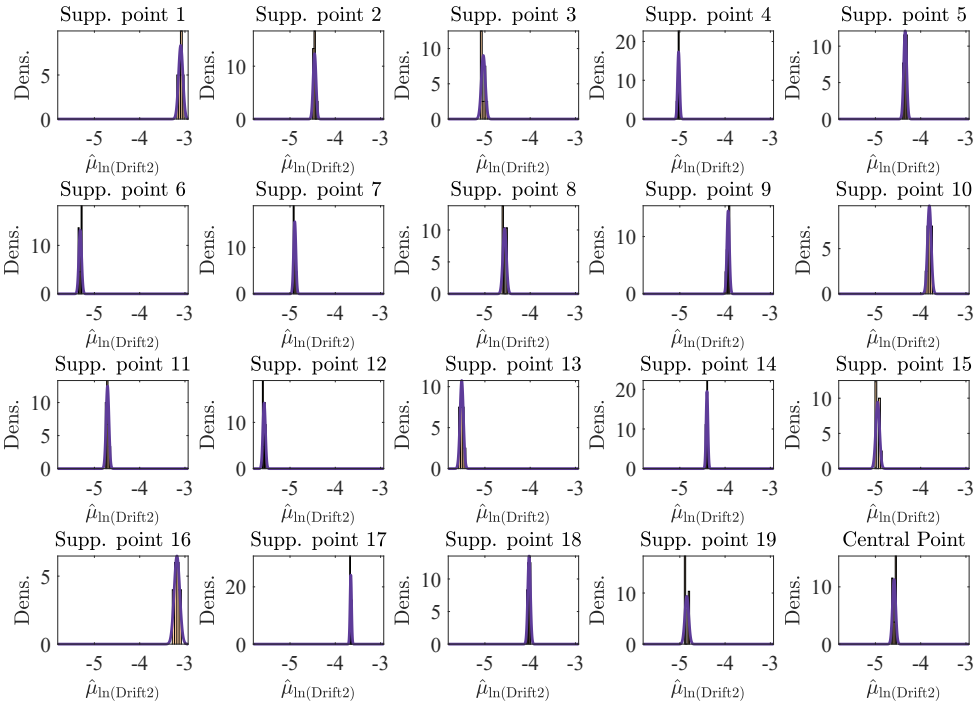

Source: Author.

Figure 6.7 – Histograms of the standard deviations of the underlying Gaussians of the drift EDP at the (a) 1st and (b) 2nd story for all support points.

(a) 1st story.

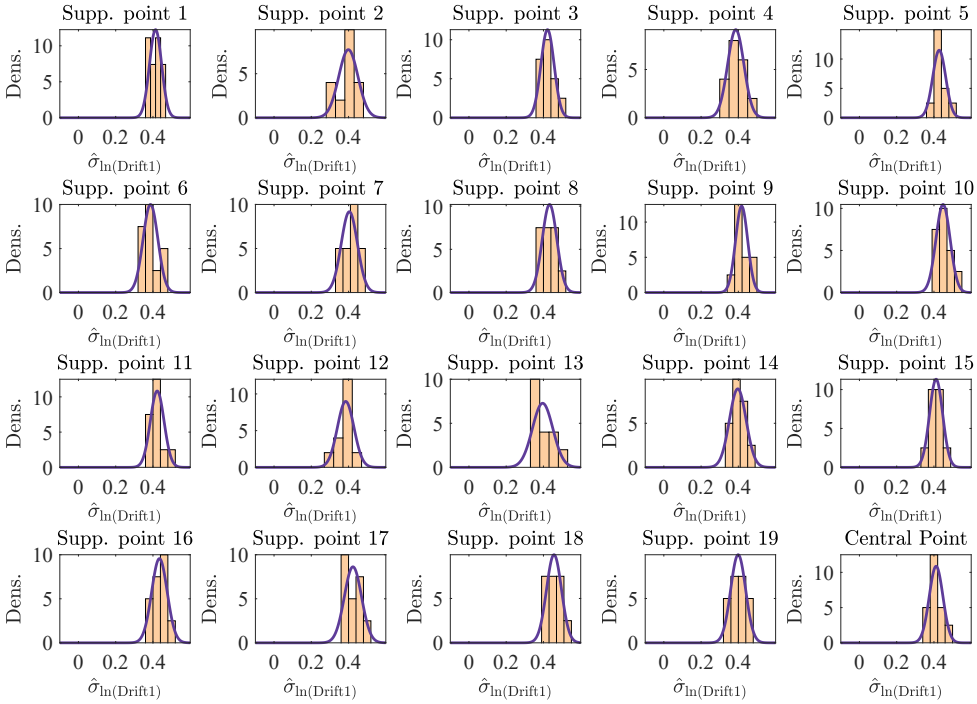

(b) 2nd story.

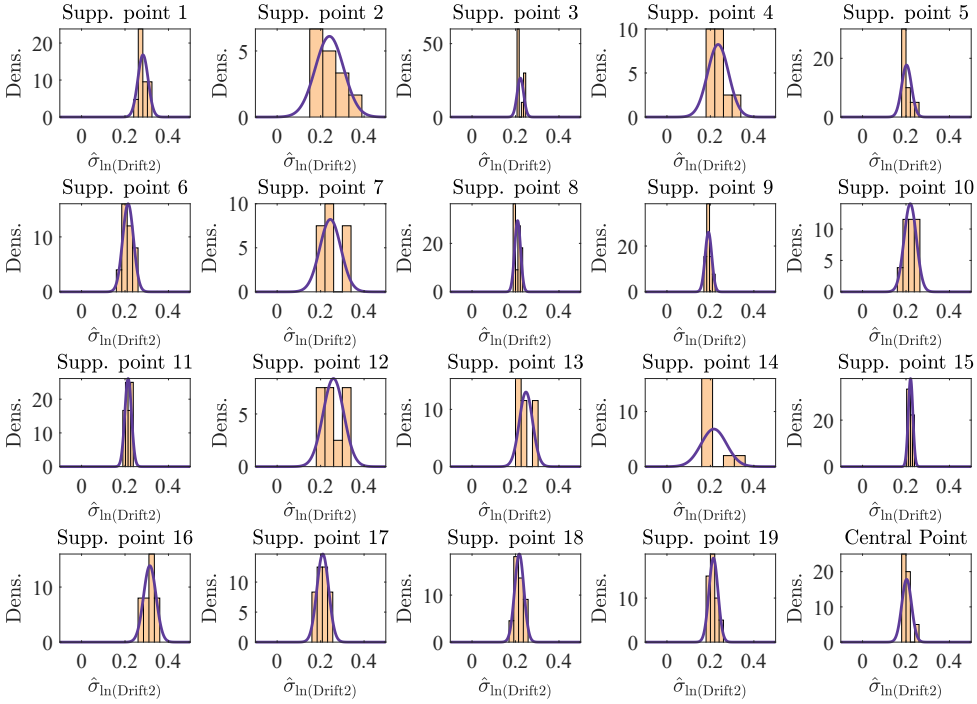

Source: Author.

Initially, all metamodels were created using a linear trend and an Exponential correlation family, as recommended in the literature for metamodels representing EDPs (Kyprioti; Taflanidis, 2021). However, the linear trend failed to adequately capture the variability of Residual Drift Ratio (RDR) across the design space. To reduce the leave-one-out cross-validation error in the metamodel, a quadratic trend was adopted for the metamodels of the population means and standard deviations of the RDR (Gidaris; Taflanidis; Mavroeidis, 2015). Similarly, the interpolation of the expected annual repair cost, $\tilde{C}_{exReCo}$, exhibited lower errors when employing a quadratic trend combined with a Gaussian correlation family.

Fig. 6.8 through Fig. 6.10 present the Kriging metamodels for estimating the population mean and standard deviation of the marginals of **EDP** associated with Interstory Drift Ratio (Drift), Peak Floor Acceleration (PFA), and RDR, respectively.

Figure 6.8 – Kriging metamodels for the population means and standard deviations of the underlying Gaussians of the marginals of **EDP** associated with drift.

(a) Metamodel of the population mean of the 1^{st} story drift EDP.

(b) Metamodel of the population standard deviation of the 1^{st} story drift EDP.

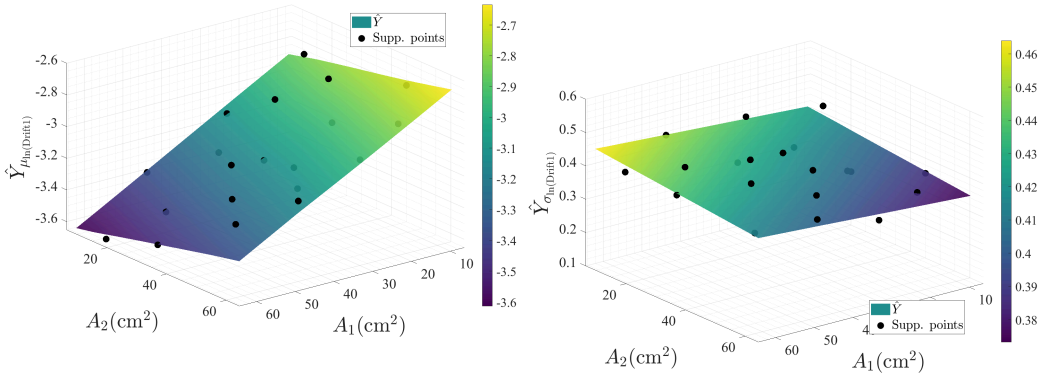

(c) Metamodel of the population mean of the 2^{nd} story drift EDP.

(d) Metamodel of the population standard deviation of the 2^{nd} story drift EDP.

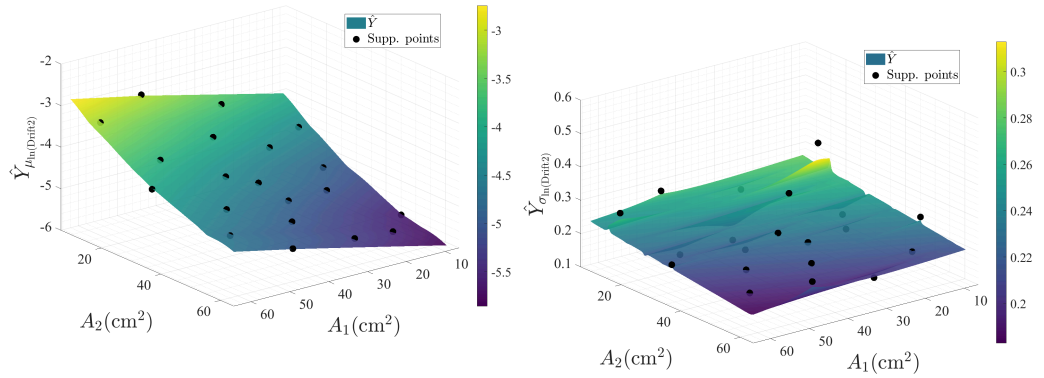

Source: Author.

Figure 6.9 – Kriging metamodels for the population means and standard deviations of the underlying Gaussians of the marginals of **EDP** associated with PFA.

(a) Metamodel of the population mean of the 1^{st} floor PFA EDP.

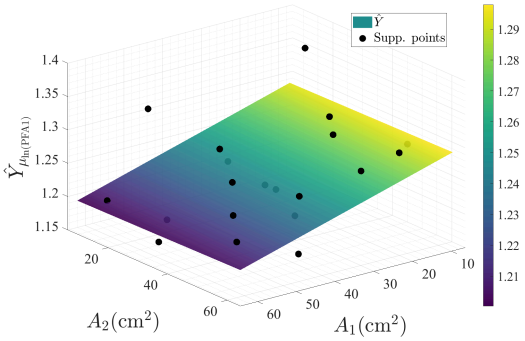

(b) Metamodel of the population standard deviation of the 1^{st} floor PFA EDP.

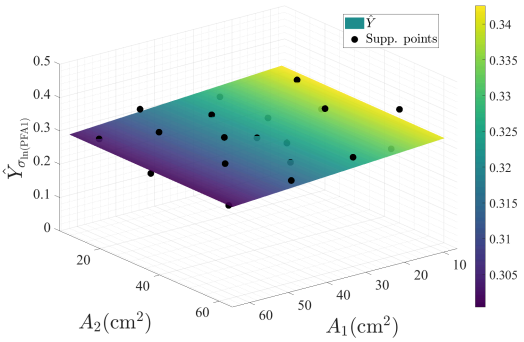

(c) Metamodel of the population mean of the 2^{nd} floor PFA EDP.

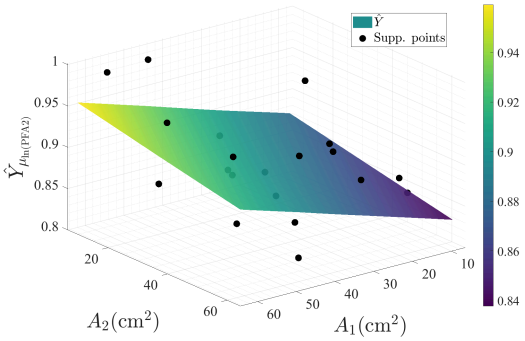

(d) Metamodel of the population standard deviation of the 2^{nd} floor PFA EDP.

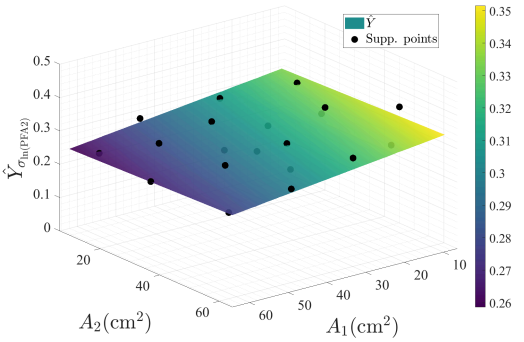

(e) Metamodel of the population mean of the 3^{rd} floor PFA EDP.

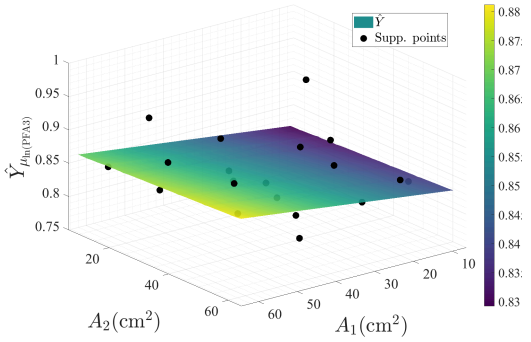

(f) Metamodel of the population standard deviation of the 3^{rd} floor PFA EDP.

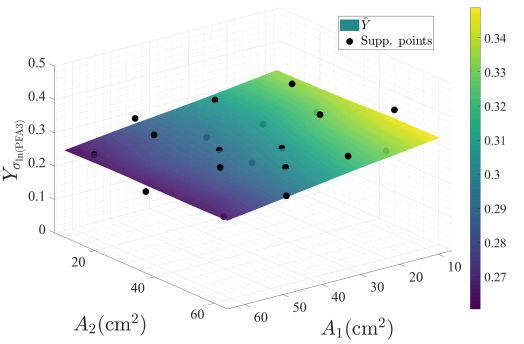

Source: Author.

Figure 6.10 – Kriging metamodels for the population means and standard deviations of the underlying Gaussians of the marginals of **EDP** associated with *RDR*.

(a) Metamodel of the population mean of the underlying Gaussian of the *RDR* EDP.

(b) Metamodel of the population standard deviation of the underlying Gaussian of the *RDR* EDP.

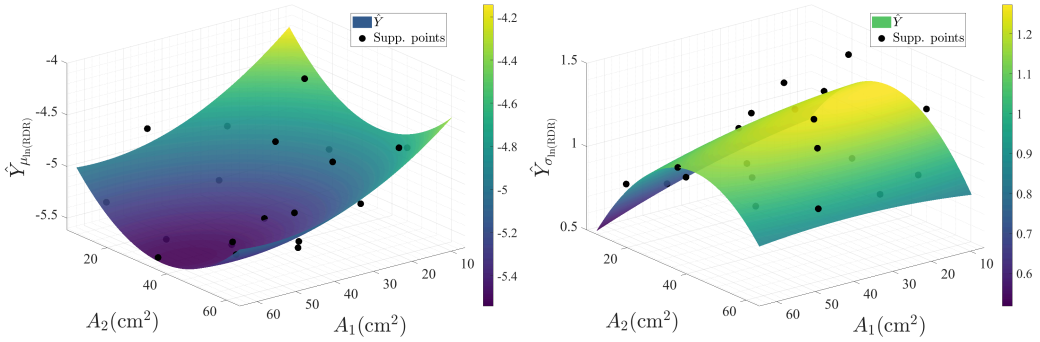

Source: Author.

These results demonstrate that the proposed Kriging metamodeling approach effectively estimates the underlying population values associated with the marginals of the **EDP** vector, as evidenced by the smooth trends of the metamodel surfaces, which successfully filter out the statistical uncertainty present in the support point estimates. Indeed, the scattered, seemingly random variation of the support point values around the metamodel surfaces reflects the inherent statistical uncertainty in the parameter inference process, whereas the metamodels capture the expected population trends across the design space. Interestingly, from Figs. 6.8 to 6.10, the metamodels for the population standard deviations of all components of **EDP** exhibit only minor variation, resulting in nearly flat surfaces. This suggests that the standard deviation values remain approximately constant across the design domain.

Fig. 6.11 shows the Kriging regressions for the population median $\hat{Y}_{\mu_{coll}}(\mathbf{x})$ and dispersion $\hat{Y}_{\sigma_{coll}}(\mathbf{x})$ of the collapse fragility function. The metamodel for the population median $\hat{Y}_{\mu_{\mathrm{coll}}}(\mathbf{x_d})$ exhibits limited scatter but accurately captures the expected trend across the design space. As anticipated, an increase in the BRB areas results in higher median values of $S_a(\bar{T})$ at collapse reflecting the enhanced lateral stiffness provided by the BRBs. The results also indicate that the first-story BRB area has a more pronounced influence on $S_a(\bar{T})$ at collapse compared to the second-story BRB area. For the population dispersion, $\hat{Y}_{\sigma_{\mathrm{coll}}}(\mathbf{x_d})$, the metamodel similarly demonstrates minimal variation across the support points. Consistent with the observations for the parameters of the marginals of **EDP**, these results demonstrate that the proposed Kriging metamodels effectively capture the underlying population values of the lognormal parameters of the collapse fragility function across the design domain by filtering out statistical uncertainty and revealing smooth,

physically meaningful trends.

Figure 6.11 – Kriging metamodels for the population median and dispersion of the collapse fragility functions.

(a) Metamodel of the population median, $\hat{Y}_{\mu_{\text{coll}}}(\mathbf{x_d})$, of $S_a(\bar{T})$ at collapse.

(b) Metamodel of the population dispersion, $\hat{Y}_{\sigma_{\text{coll}}}(\mathbf{x_d})$, of $S_a(\bar{T})$ at collapse.

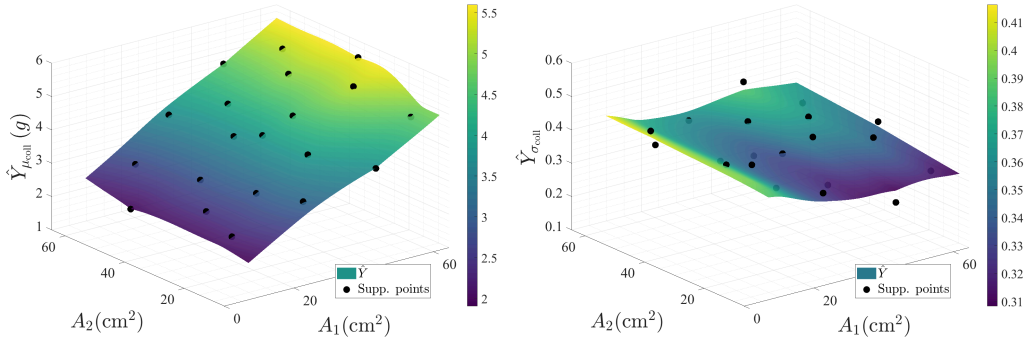

Source: Author.

The final set of Kriging metamodels discussed in this section are those used to estimate how $C_{\text{exReCo}}(\mathbf{x_d})$, expressed in dollars, varies across the design space based on the component inventory presented in Table 6.3. To compute $C_{\text{exReCo}}(\mathbf{x_d})$, $N_s = 5000$ synthetic demand realizations were generated for each design by sampling the calibrated joint lognormal random vector **EDP**. Given the relatively low computational cost of evaluating the expected repair cost once the intermediate metamodels for the population parameters of **EDP** and the collapse fragility function are established, the number of support points used to construct the final Kriging metamodel for $C_{\text{exReCo}}(\mathbf{x_d})$ was increased by 50%, resulting in a total of 30 support points.

Fig. 6.12a presents the resulting Kriging metamodel for $C_{\text{exReCo}}(\mathbf{x_d})$ across the design space. In addition, Fig. 6.12b illustrates the metamodel for the total cost, defined as the sum of construction cost and expected annual repair cost. The results indicate that increasing the BRB area on the first story has a more pronounced influence on reducing the expected annual repair cost compared to changes in the second story. The use of $N_s = 5000$ synthetic EDP realizations for each design ensures that statistical uncertainty in the estimated values of $C_{\text{exReCo}}(\mathbf{x_d})$ is minimal, as evidenced by the small variability of the support point results around the Kriging metamodel. This confirms the accuracy and robustness of the final metamodel in capturing the population trend across the design domain. By replacing repeated nonlinear dynamic FE model evaluations with this metamodel, the computational effort required for optimization is substantially reduced. Furthermore, the availability of an explicit, differentiable approximation for $C_{\text{exReCo}}(\mathbf{x_d})$ enables the potential application of gradient-based optimization methods—a direction

that warrants further investigation.

Figure 6.12 – Kriging metamodels of the Expected Repair Costs and Total Costs across the design domain.

(a) Kriging metamodel of the Expected Repair Cost ($).

(b) Kriging metamodel of the Total Cost ($C_{\text{cons}}(\mathbf{x}) + \tilde{C}_{\text{exReCo}}(\mathbf{x})$).

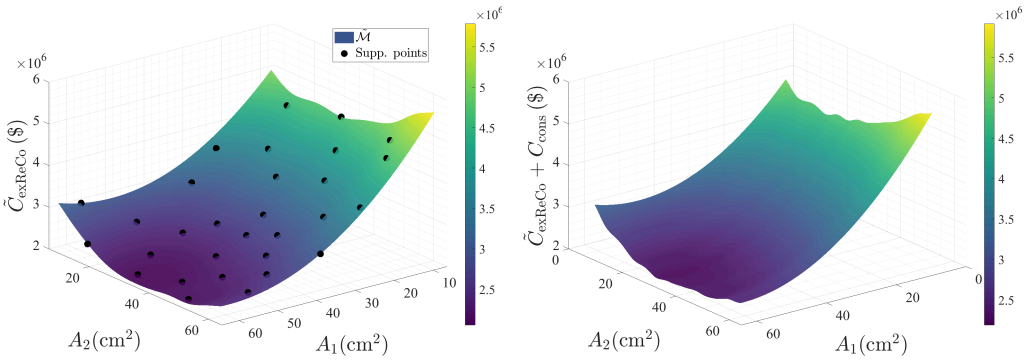

Source: Author.

6.4.4.4 Optimization Results

This section presents the results obtained by solving the optimization problem defined in Eq. (6.10) using the Kriging metamodels developed in Section 6.3. Given the multi-objective nature of the problem, which seeks to minimize both construction costs and expected repair costs, a Genetic Algorithm (GA) is adopted (Holland, 1992). The GA simulates natural evolutionary processes, employing reproduction, crossover, and mutation to explore the design space. A key advantage of GAs is their reduced susceptibility to entrapment in local minima, as they maintain a diverse population of candidate solutions and do not require gradient information (Rao, 2019).

Preliminary convergence tests were conducted for different population sizes, as shown in Fig. 6.13, considering the minimization of both objectives—Expected Repair Cost ($\tilde{C}_{\text{exReCo}}$) and Construction Cost (C_{cons}). All population sizes converged to the same minimum within the proposed number of generations, and a population size of 50 candidates was adopted for the optimization process.

For each candidate design, the Kriging metamodel for $C_{\text{exReCo}}(\mathbf{x_d})$, presented in Fig. 6.14, is queried to efficiently estimate the expected repair cost. The optimization results are summarized in Fig. 6.14, which presents the Pareto front depicting the trade-off between construction cost and expected annual repair cost.

Figure 6.13 – Convergence test for different population sizes.

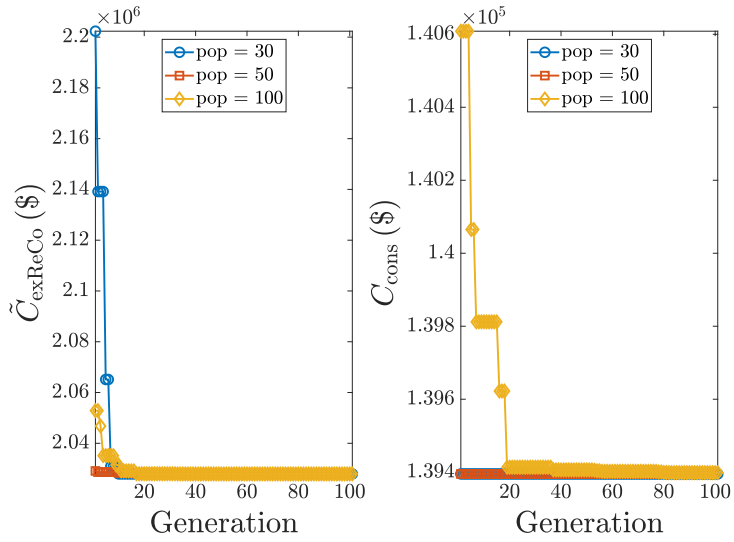

Source: Author.

Figure 6.14 – Pareto front for the multi-objective optimization problem.

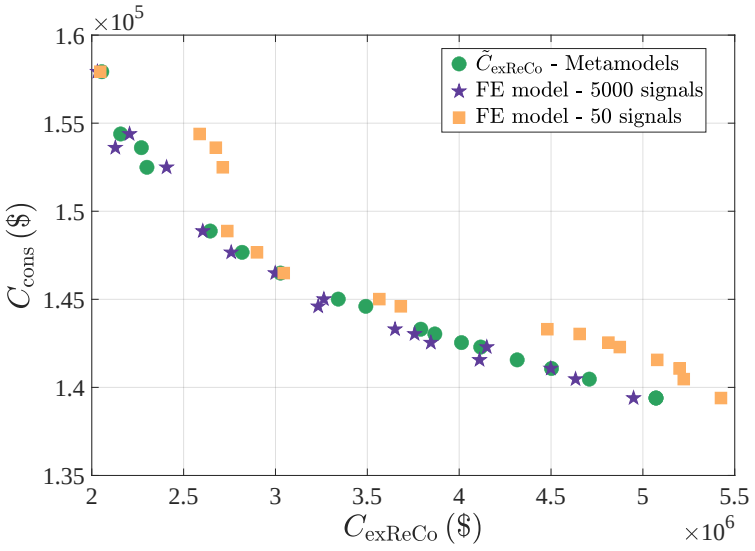

Source: Author.

In addition to the Pareto front obtained using the proposed metamodeling framework, Fig. 6.14 also presents the corresponding expected repair costs computed directly from the nonlinear dynamic FE model, without relying on metamodels. For this comparison, NLTHA and IDA were performed at each Pareto-optimal design identified through the metamodel-based optimization. Two sets of ground motions were considered for this verification: a large set containing 5000 records and a smaller set of 50 records. The larger set minimizes the influence of statistical uncertainty and serves as the benchmark for assessing the accuracy of the metamodel predictions. The smaller set, with $N_e = 50$ records,

matches the number of ground motions used to train the metamodels and reflects the level of statistical uncertainty present during the optimization process. It is important to note that construction costs are identical across both the metamodel-based and FE model-based evaluations, as they are computed directly from the analytical expression given in Eq. (6.11) using consistent input parameters.

The Pareto front in Fig. 6.14 illustrates the expected trade-off between construction costs and expected annual repair costs, providing a rational basis for comparing design alternatives for the BRB areas. This enables more informed decision-making by identifying design configurations that achieve an effective balance between initial investment and long-term performance. Furthermore, the results demonstrate the accuracy of the proposed metamodeling framework. Specifically, the differences in expected repair costs between the metamodel predictions and those obtained using the nonlinear dynamic FE model are minimal, with a maximum deviation of less than 10%. This agreement confirms that the metamodels successfully approximate the population values of the distribution parameters of **EDP**, with the incorporated noise term effectively capturing the statistical uncertainty arising from the finite ground motion set used during training. In contrast, expected repair costs computed using the nonlinear dynamic FE model with a smaller set of only 50 ground motions show significantly larger discrepancies, underscoring the critical role of statistical uncertainty in PBRO applications.

An important observation is that several points on the Pareto Front are positioned near the design domain boundaries, indicating that the metamodels remain accurate even near the limits of the design space. Additionally, to evaluate the impact of the lognormal assumption, $C_{\text{exReCo}}(\mathbf{x_d})$ was estimated from 5000 NLTHA using the FE model of the system. The resulting data were used to construct data-driven empirical distributions for the EDPs, treated as the synthetic demand set and employed in place of the lognormal distributions. Fig. 6.15 shows that, for this case study, the results obtained under the lognormal assumption are in close agreement with those derived from the empirical distributions.

It is also worth noting that the GA required 5100 evaluations of the objective function to obtain the Pareto front. Without metamodels, this would necessitate 5100 calls to the nonlinear dynamic FE model, resulting in a total of $5100 \times 500 = 2550000$ FE model evaluations for the considered parent earthquake set of 500 ground motions. In contrast, training the metamodels required only $50 \times 10 = 500$ model calls to evaluate statistical uncertainty at the central point, $20 \times 50 = 1000$ calls for NLTHA to estimate the distribution parameters of **EDP**, and $10 \times 20 \times 50 = 10000$ calls for IDA to characterize collapse fragility functions, for a total of 11500 FE model evaluations. This represents a reduction by a factor of approximately 220, clearly demonstrating the computational efficiency of the proposed methodology for optimizing structures within the PBRO framework.

Figure 6.15 – C_{exReCo} calculated using a data-driven empirical distribution for the Pareto Front points.

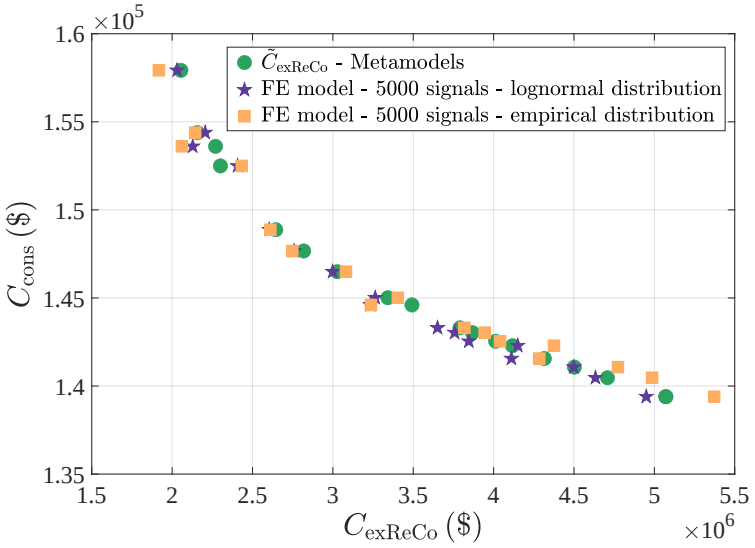

Source: Author.

Since Fig. 6.12b suggests the presence of a global minimum in the total cost of the structure, the following single-objective PBRO is evaluated:

$$\begin{aligned} &\text{Find } \mathbf{x_d} = \{A_{BRB,1}, A_{BRB,2}\}^T \\ &\text{to minimize } W(\mathbf{x_d}) = C_{cons}(\mathbf{x_d}) + \tilde{C}_{exReCo}(\mathbf{x_d}) \\ &9.7 \leq A_{BRB,1} \leq 64.5\,\text{cm}^2 \\ &9.7 \leq A_{BRB,2} \leq 64.5\,\text{cm}^2 \end{aligned} \tag{6.15}$$

where $C_{cons}(\mathbf{x_d})$ represents the initial construction cost of the structural steel frame and $\tilde{C}_{exReCo}(\mathbf{x_d})$ is the expected annual repair cost, as estimated by the Kriging metamodel. The GA is also applied to this single-objective PBRO using the same population size of 50 points as in the multi-objective case.

The optimization results are summarized in Table 6.5.

Table 6.5 – Results for the single-objective PBRO.

$A_{BRB,1}$ (cm^2)	$A_{BRB,2}$ (cm^2)	$W(\mathbf{x_d})$ ($) Metamodel	$\tilde{C}_{exReCo}(\mathbf{x_d})$ ($) Metamodel	$C_{exReCo}(\mathbf{x_d})$ ($) FE model	$\tilde{C}_{exReCo}(\mathbf{x_d})$ ($) Met. w/ cons. std.
58.5	33.2	2.2124×10^6	2.0547×10^6	2.0299×10^6	2.0649×10^6

Source: Author.

Table 6.5 summarizes the BRB areas for the first and second stories that minimize the total cost $W(\mathbf{x_d})$, along with the corresponding total cost value. For this design point, the Expected Repair Cost $C_{\text{exReCo}}(\mathbf{x_d})$ is evaluated under three scenarios: (i) using the proposed Kriging metamodels; (ii) using the nonlinear dynamic FE model with 5000 earthquake records for NLTHA and IDA; and (iii) using metamodels for the median

values of the **EDP** marginals while holding the dispersions constant at their mean values across all support points. This third scenario provides insight into the impact of assuming constant standard deviations, given the small variability observed in the standard deviation metamodels.

The optimal solution occurs near the upper bound of the first-story BRB area, a trend consistent with the results from the Pareto front in Fig. 6.14. This suggests that increasing the first-story BRB area significantly reduces repair costs, albeit with higher construction costs.

The Expected Repair Costs obtained from the three scenarios differ by less than 2%, confirming that the proposed metamodels effectively capture the loss behavior across the design space. Moreover, fixing the dispersion of the **EDP** marginals to their mean values has negligible influence on the results. Since these constant dispersions are derived from the same NLTHA results used to calibrate the metamodels, no additional nonlinear dynamic FE model evaluations are required. Thus, both approaches—using metamodel-derived dispersions or constant mean values—provide acceptable approximations for estimating $C_{\text{exReCo}}(\mathbf{x_d})$ within the proposed framework.

The methodology proposed in this work can be extended to a wide range of applications, provided that the **EDP** vectors do not deviate substantially from a joint lognormal distribution. Two additional case studies employing the same methodology are presented.

6.5 Case Study 2

6.5.1 Overview

The second case study evaluated in this work corresponds to a six-story Special Concentrically-Braced Frame (SCBF), presented in Hwang and Lignos (2017). The building is designed as a standard office building according to ASCE/SEI 7-05 (ASCE, 2005) and ANSI/AISC 341-05 (AISC, 2005), with occupancy category II. Situated in urban California, the building is designed for the lower bound of the seismic design category D, in the city of Sacramento.

Steel braces are designed in accordance with ANSI/AISC 341-05 (AISC, 2005) considering a round hollow structural section (HSSs). The braces are built with steel material ASTM A500 (ASTM, 2007) Grade B, with nominal yield stress $F_y = 315\,MPa$. Construction materials for beams and columns consist of steel ASTM A992 Gr. 50. Comprehensive information on the design and geometry is available in NIST (2010), Hwang and Lignos (2017). The typical plan view of the building is represented in Fig. 6.16a, and an elevation of the perimeter frame is represented in Fig. 6.16b.

Figure 6.16 – Case study structure: (a) typical plan view of the building; (b) representation of the Special Steel Moment Frame (SMF).

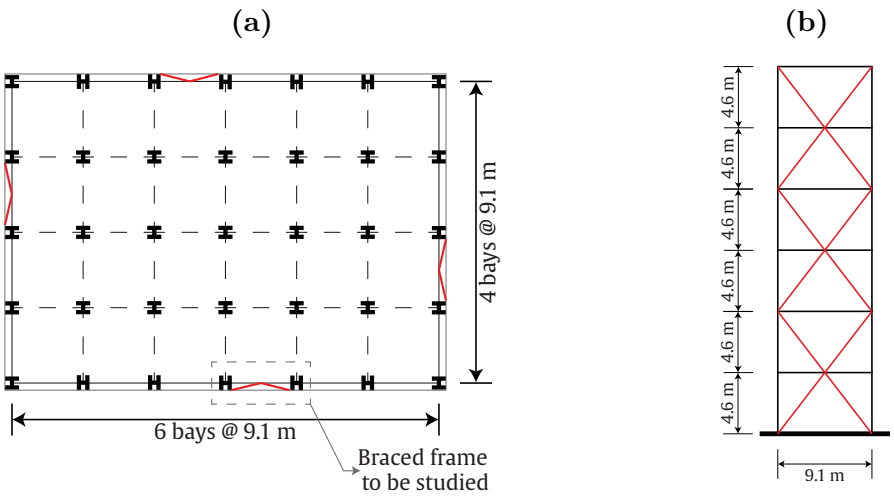

Source: Author.

The main goal of this case study is to optimize the diameter of the sections of the braces in each story of the building. In the proposed optimization problem, the design variables are the external diameter (or outside diameter) of the round hollow section of the brace in each story, and the optimization problem is represented by:

$$\begin{aligned} &\text{Find} \quad \mathbf{x_d} = \{d_{\text{ex},1}, d_{\text{ex},2}, d_{\text{ex},3}, d_{\text{ex},4}, d_{\text{ex},5}, d_{\text{ex},6}\}^T \\ &\text{to minimize} \quad W(\mathbf{x_d}) = \{C_{\text{cons}}(\mathbf{x_d}), \tilde{C}_{\text{exReCo}}(\mathbf{x_d})\}^T \\ &25.4 \leq \{d_{\text{ex},i}\}_{i=1}^{6} \leq 71.1\, cm \end{aligned} \tag{6.16}$$

where $C_{cons}\,(\mathbf{x})$ represents the initial construction cost of the structural steel frame (including beams, columns, and braces), and $\tilde{C}_{exReCo}\,(\mathbf{x})$ is the expected annual repair cost, calculated based on the FEMA P-58 methodology (FEMA, 2018), using the metamodeling framework outlined in Section 6.3.

The construction cost of the steel frame, indicated in Equation 6.16 as $C_{cons}\,(\mathbf{x})$, is estimated as follows:

$$C_{cons}\,(\mathbf{X}) = C_{steel}\,(W_{beams} + W_{columns} + W_{brace}) \tag{6.17}$$

where W_{brace} indicates the weight of the braces.

This case study adopts the same unit cost for steel as that used in Section 6.4, C_{steel} = \$4.72/kg (Ghasemof; Mirtaheri; Mohammadi, 2022). For beams and columns, the nominal weight is obtained from the AISC database (v16.0) (AISC, 2022b). For the braces, the weight is calculated as $W_{brace} = A_{brace} \times L_{brace} \times \rho$, where L_{brace} is the element length and ρ is the material density, which for ASTM A500 steel is $\rho = 7850\,\text{kg/m}^3$.

The thickness of the HSS section used for the braces is kept constant at $t_{brace} = 1.18\,\text{cm}$ ($t_{brace} = 0.465\,\text{in}$).

Similar to the previous case study, the structure is modeled as an office building, with its basic performance information summarized in Table 6.6. The same building replacement cost from Section 6.4 is adopted, and the total loss threshold is set to 100%. The number of workers and the population model are also the same as those used in Section 6.4.

Table 6.6 – Performance information for the studied building.

Number of stories	2
Floor area	$2,000\,m^2$
Replacement Cost, RC	$\$\,25,221,731.25$
Total loss threshold (% RC)	100

Source: Author.

A summary of the building components is presented in Table 6.7. The same fragility function database and component categories from Section 6.4 are used. The quantities of each component, also listed in Table 6.7, were calculated using the Normative Quantity Estimation Tool provided in the supporting materials of FEMA P-58 (FEMA, 2018).

Table 6.7 – Building component information and associated EDPs.

Category	Description	EDP	Floor	Quantity
B	Steel Column Base Plates	SDR	1	4 units
B	Welded column splices	SDR	3 and 5	4 units
B	Special Concentric Braced Frame HSS	SDR	All	4 units
B	Post-Northridge RBS connection	SDR	2	4 units
B	Bolted shear tab gravity connections	SDR	All	60 units
B	Curtain Walls	SDR	All	108 (30 ft^2)
C	Corrugated slab	SDR	All	2000 (10.76 ft^2)
C	Wall Partition	SDR	All	11 (100 ft)
C	Suspended Ceiling	PFA	All	86.4 (250 ft^2)
D	Fire Sprinkler Water Piping	PFA	All	4.32 (1000 ft)
D	Traction Elevator	PFA	All	3.02 units

Source: Author.

The 5%-damped, 2% in 50 years (2/50) Uniform Target Hazard Spectrum shown in Fig. 6.17 is used to define the seismic hazard. The building is assumed to be located in Sacramento, on the lower bound of soil type D. Seismic hazard curves are derived from Hwang and Lignos (2017), and the same stochastic ground motion model adopted in Case Study 1 (Section 6.4.2) is employed in this example.

6.5.2 Structural Finite Element Model

A two-dimensional model for the two-story archetype steel building is also formulated using OpenSees (McKenna; Fenves; Scott, 2006) software. The geometric specifications of the structural elements are indicated in Table 6.8.

Figure 6.17 – Target Uniform Hazard Spectrum.

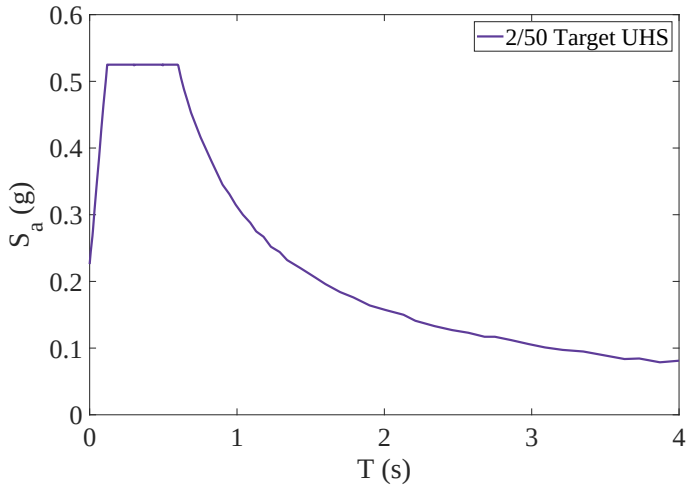

Source: Author (based on Hwang and Lignos (2017)).

Table 6.8 – Member Sizes for the Special SCBF.

Story	Beam Size	Column Size
1	W21X62	W14X342
2	W24X146	W14X342
3	W18X76	W14X176
4	W24X131	W14X176
5	W24X104	W14X68
6	W18X97	W14X68

Source: Author.

The model used in this example is developed by Hwang and Lignos (2017) and corresponds to "Model B", which represents the bare steel SCBF configuration. Steel beams and columns are modeled as elastic elements with zero-length springs at their ends to account for concentrated plasticity. These springs follow the Ibarra-Medina-Krawinkler (IMK) deterioration model (Ibarra; Medina; Krawinkler, 2005). The shear distortion of the panel zone is incorporated following the approach described in Gupta and Krawinkler (1999).

Steel braces in the frame are modeled using eight displacement-based fiber elements, enabling the representation of flexural buckling and fracture initiation due to low-cycle fatigue, as recommended by Karamanci and Lignos (2014). Additionally, a nonlinear out-of-plane rotational spring is assigned at each brace end to simulate the flexibility and flexural yielding of gusset plates caused by out-of-plane brace bending, following the recommendations of Hsiao, Lehman and Roeder (2013).

P-Delta effects are considered by coupling a leaning column and an equivalent gravity frame to the SCBF. The model also employs a corotational transformation to

accurately capture second-order effects. Further details regarding the Finite Element model can be found in Hwang and Lignos (2017).

6.5.3 Results

6.5.3.1 Preamble

To solve the problem defined in Equation 6.16, 60 sample points were generated using the optimal LHS, following the general rule for determining the number of support points in the DoE presented in Section 6.3.3.1. These support points were used to construct the Kriging surfaces that replace the high-fidelity nonlinear Finite Element model in the optimization process. The results are presented in two parts: (1) statistical variability analysis and (2) optimization results.

The Engineering Demand Parameters considered in this problem are: Interstory Drifts of stories 1 (Drift_1), 2 (Drift_2), 3 (Drift_3), 4 (Drift_4), 5 (Drift_5), 6 (Drift_6); Peak Floor Acceleration of floors 1 (PFA_1), 2 (PFA_2), 3 (PFA_3), 4 (PFA_4), 5 (PFA_5), 6 (PFA_6), 7 (PFA_7); Residual Drift (RDR).

This case study did not consider metamodels for the collapse fragility function, and the collapse evaluation was disregarded in the assessment of the Expected Repair Cost.

6.5.3.2 Statistical variability

The evaluation of statistical uncertainty was performed at the central point of the DoE, using $N_e = 24$ ground motions to ensure consistency with the number of records typically considered in practical design applications, within each of the $N_s = 10$ ground motion sets. A parent set of 500 hazard-consistent ground motions was generated using the stochastic ground motion model. NLTHA were performed to estimate $\hat{\mu}_{EDP_i}(\mathbf{x_d})$ and $\hat{\sigma}_{EDP_i}(\mathbf{x_d})$ for each component of **EDP**. Fig. 6.18 present the results in terms of the means and standard deviations of the EDPs associated with drift at all stories. Fig. 6.19 present the results in terms of the means and standard deviations of the EDPs associated with PFA at all floors. Fig. 6.20 present the results in terms of the means and standard deviations of the EDPs associated with RDR EDP.

The results indicate variations in the EDPs across different ground motion sets, confirming the presence of associated noise. As in Case Study 1, it is assumed that the results for each ground motion set follow a normal distribution. To verify this assumption, the Shapiro–Wilk (S–W) test for normality (Shapiro; Wilk, 1965) was applied, considering the 10 observations at the central point. Figs. 6.18 to 6.20 show that, at a 99% confidence level, the results of the 10 sets of random ground motions can be considered samples drawn from a population normally distributed for all analyzed EDPs.

Figure 6.18 – Histograms of the means and standard deviations of the underlying Gaussian of the drift EDP at all stories for the central point.

(a) Mean ($\hat{\mu}$). **(b)** Standard deviation ($\hat{\sigma}$).

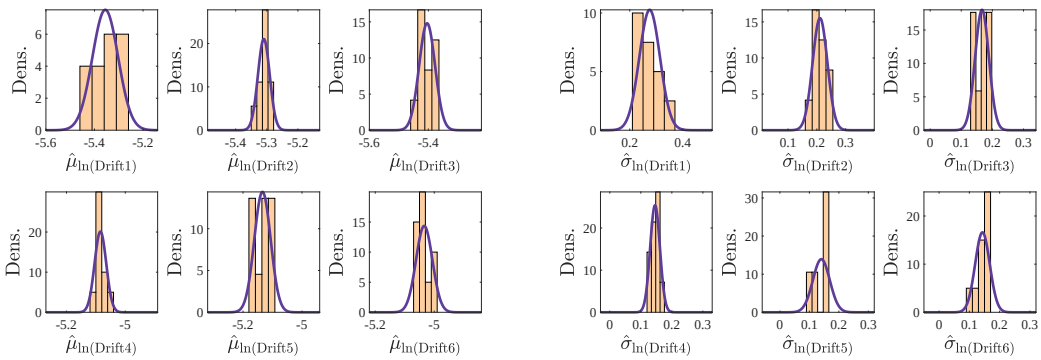

Source: Author.

Figure 6.19 – Histograms of the means and standard deviations of the underlying Gaussian of the PFA EDP at all floors for the central point.

(a) Mean ($\hat{\mu}$). **(b)** Standard deviation ($\hat{\sigma}$).

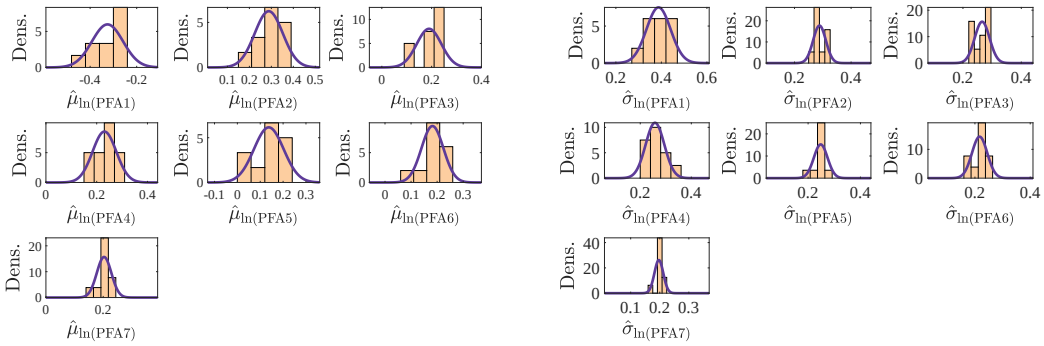

Source: Author.

6.5.3.3 Optimization results

The metamodels developed in this case study follow the same configuration defined in Section 6.4.4.4 for Case Study 1. The Genetic Algorithm (GA) (Holland, 1992) is also employed, with a population size of 50 candidates considered for the solution. For each candidate, the Kriging surface for the Expected Repair Cost ($\tilde{C}_{\text{exReCo}}$) is evaluated. The results are presented in Fig. 6.21, which shows the Pareto front of Construction Cost (C_{cons}) versus $\tilde{C}_{\text{exReCo}}$.

Figure 6.20 – Histograms of the means and standard deviations of the underlying Gaussian of the RDR EDP for the central point.

(a) Mean ($\hat{\mu}$). **(b)** Standard deviation ($\hat{\sigma}$).

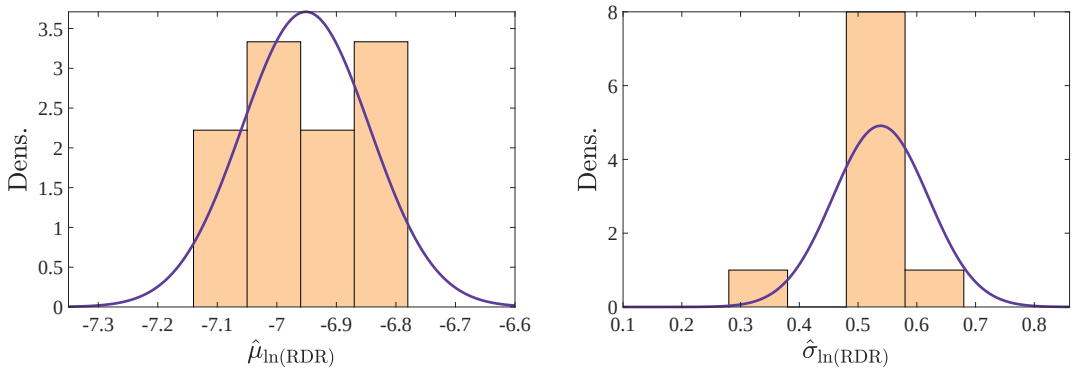

Source: Author.

Figure 6.21 – Pareto front for the multi-objective optimization problem.

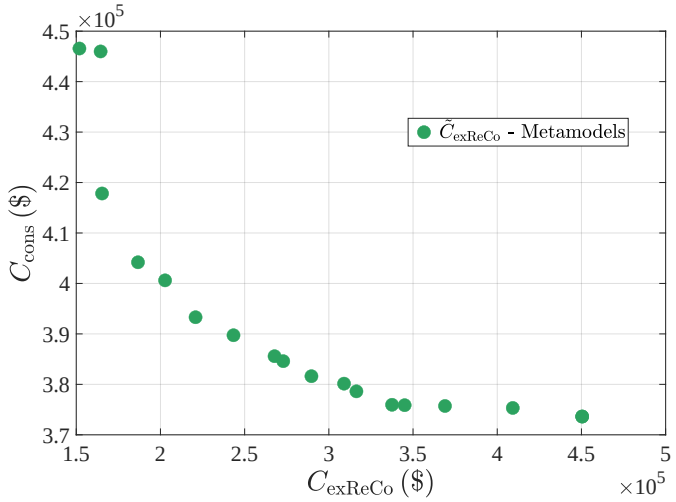

Source: Author.

Similar observations to those from Case Study 1, presented in Section 6.4.4.4, can be made here. The Pareto front illustrates the expected trade-off between construction cost and expected annual repair cost, providing a rational basis for comparing design alternatives for the brace diameter.

A second optimization problem is evaluated to find the global minimum in the Total Cost of the structure. The proposed single-objective PBRO is illustrated as follows:

$$\begin{gathered}\text{Find } \mathbf{x_d}^* = \{d_{\text{ex},1}, d_{\text{ex},2}, d_{\text{ex},3}, d_{\text{ex},4}, d_{\text{ex},5}, d_{\text{ex},6}\}^T \\ \text{to minimize } W(\mathbf{x_d}) = \left[C_{cons}(\mathbf{x_d}) + \tilde{C}_{exReCo}(\mathbf{x_d})\right] \\ 25.4 \leq \{d_{\text{ex},i}\}_{i=1}^{6} \leq 71.1\, cm\end{gathered} \tag{6.18}$$

The Genetic Algorithm (GA) is also applied in the single-objective PBRO with the same population size of 50 points, with results presented in Table 6.9.

Table 6.9 – Results for the single-objective PBRO.

$d_{ex,1}$ (cm)	$d_{ex,2}$ (cm)	$d_{ex,3}$ (cm)	$d_{ex,4}$ (cm)	$d_{ex,5}$ (cm)	$d_{ex,6}$ (cm)	$W(\mathbf{x})$ (\$) Surrogate	$\tilde{C}_{exReCo}(\mathbf{x})$ (\$) Surrogate
26.80	42.85	59.66	58.28	50.71	25.40	5.50×10^5	2.98×10^5

Source: Author.

Table 6.9 presents the external diameters of the braces for all stories of the building corresponding to the minimum total cost, along with the associated total cost value $W(\mathbf{x_d})$. The Expected Repair Cost, $C_{exReCo}(\mathbf{x_d})$, is also calculated for this specific point using the proposed surrogate models. The results indicate that the brace diameter can be minimized in the first and sixth stories, whereas the third and fourth stories require larger optimal diameters, suggesting that the observed drifts and accelerations at these levels govern the optimization problem.

6.6 Case Study 3 - Irregular building

6.6.1 Overview

The irregular building evaluated in this case study was presented by Saeedi et al. (2024) and corresponds to a five-story special moment-resisting frame with an irregularity of 26.67%. The building design follows AISC 360 (AISC, 2022b) and AISC 341 (AISC, 2022a). BRBs are incorporated into the building's design as a retrofit strategy. Beams and columns are constructed from Steel St 37, which has yield and ultimate stresses of 240 MPa and 370 MPa, respectively. The steel considered in the core of the BRB section corresponds to the ASTM A36 material. Fig. 6.22 illustrates the structure considered in this case study, with the typical plan view shown in Fig. 6.22a and the elevation of the perimeter frame depicted in Fig. 6.22b. The BRBs are represented in red in Fig. 6.22b.

The main goal of this case study is to optimize the areas of the BRBs in all stories of the building. In the proposed optimization problem, the design variables are the BRB areas for the first story ($A_{\text{BRB},1}$), second story ($A_{\text{BRB},2}$), third story ($A_{\text{BRB},3}$), fourth story ($A_{\text{BRB},4}$) and fifth story ($A_{\text{BRB},5}$), and the optimization problem is represented by:

Figure 6.22 – Case study structure: (a) typical plan view of the building; (b) representation of the irregular building.

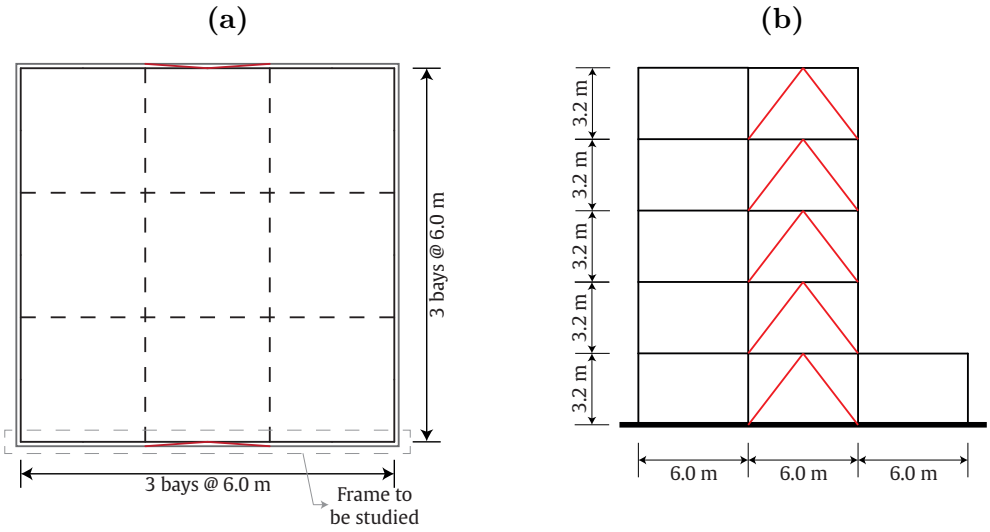

Source: Author.

$$\begin{aligned} &\text{Find} \;\; \mathbf{x_d} = \{A_{\text{BRB},1}, A_{\text{BRB},2}, A_{\text{BRB},3}, A_{\text{BRB},4}, A_{\text{BRB},5}\}^T \\ &\text{to minimize} \;\; W(\mathbf{x}) = \left[C_{cons}(\mathbf{x}), \tilde{C}_{exReCo}(\mathbf{x})\right]^T \\ &9.7 \leq \{A_{\text{BRB},i}\}_{i=1}^{5} \leq 64.5\, cm^2 \end{aligned} \tag{6.19}$$

where $C_{cons}(\mathbf{x})$ represents the initial construction cost of the structural steel frame (including beams, columns, and BRBs), and $\tilde{C}_{exReCo}(\mathbf{x})$ is the expected annual repair cost, calculated based on the FEMA P-58 methodology (FEMA, 2018), using the metamodel approximations.

In addition to the optimization, a static pushover analysis is performed in this example to evaluate the capacity of the irregular building both without and with BRBs, in order to assess whether they represent an effective retrofit strategy for this type of structure.

The construction cost of the steel is calculated following the same procedure adopted in Case Study 1, using Eq. (6.11). The unit costs of steel and BRBs, as well as the nominal weight of beams and columns and the weight of the BRBs, are also determined as described in Section 6.4.1. The same material density for the BRBs used in Case Study 1 is adopted here.

The performance information of the building is summarized in Table 6.10. The structure is modeled as a commercial office building, adopting the same replacement cost used in Case Study 1 (Section 6.4). The total loss threshold is also set to the same value, and environmental impacts are not considered in this assessment. The number of workers required for building repair is likewise consistent with that assumed in Case Study 1.

Table 6.10 – Performance information for the case study building.

Number of stories	5
Floor area - First floor	$324\,m^2$
Floor area - other floors	$216\,m^2$
Replacement Cost, RC	$\$\,2,485,900.00$
Total loss threshold (% RC)	100

Source: Author.

Table 6.11 presents a detailed list of the building contents. The fragility function database developed using the PACT tool (ATC, 2018) is employed in the building performance models, following the same procedure adopted in the previous case studies. The same component categories are also assumed for the irregular building.

Table 6.11 – Building component information and associated EDP.

Category	Description	EDP	Floor	Quantity
B	Steel Buckling Restrained Brace (BRB)	SDR	All	4 units
B	Bolted shear tab gravity connections	SDR	All	44 units
B	Post-Northridge RBS connection, beam one side of column	SDR	All	12 units
B	Concrete tile roof, tiles secured and compliant with UBC94	PFA	5	6.27 (100 ft^2)
C	Suspended Ceiling	PFA	All	0.84 (2500 ft^2)
C	Wall Partition, Type: Gypsum + Wallpaper	SDR	All	1.15 (100 ft)
C	Prefabricated steel stair - no seismic joints	SDR	All	0.7 units
B	Generic Midrise Stick-Built Curtain wall	SDR	All	11.60 (30 ft^2)
D	Hydraulic Elevator – postdate 1998	PFA	All	2 units
D	Fire Sprinkler Water Piping	PFA	All	0.46 (1000 ft)

Source: Author.

The hazard is defined based on the 5% damped Target Hazard Spectrum for a 2% probability of exceedance in 50 years (2/50). The building is assumed to be located in Los Angeles, on soil type C, resulting in the same Target Hazard Spectrum described in Section 6.4.2 for Case Study 1. The same stochastic ground motion model used to generate earthquake records in that case study is also adopted here.

A two-dimensional nonlinear dynamic FE model of the steel building was developed using OpenSees (McKenna; Fenves; Scott, 2006), with the same assumptions proposed for Case Study 1 in Section 6.4.3. The geometric properties of these structural components are provided in Table 6.12.

Table 6.12 – Member Sizes for the Irregular Frame

Story	Beam Size	Column Size
1	W18X71	HSS14X14X5/8
2	W18X86	HSS14X14X5/8
3	W18X86	HSS12X12X5/8
4	W16X50	HSS12X12X5/8
5	W16X50	HSS10X10X5/8

Source: Author.

6.6.2 Results

6.6.2.1 Preamble

To address the problem described in Equation 6.19, 50 sample points are selected as the DoE considering optimal LHS. The Engineering Demand Parameters considered in this problem are: Interstory Drifts of stories 1 (Drift_1), 2 (Drift_2), 3 (Drift_3), 4 (Drift_4) and 5 (Drift_5); Peak Floor Acceleration of floors 1 (PFA_1), 2 (PFA_2), 3 (PFA_3), 4 (PFA_4), 5 (PFA_5) and 6 (PFA_6); Residual Drift (RDR).

The results are presented in two parts: (1) static Pushover analysis and (2) optimization results. This case study did not consider metamodels for the collapse fragility function, and the collapse evaluation was disregarded in the assessment of the Expected Repair Cost.

6.6.2.2 Pushover Results

The first evaluation of the irregular building consists of a static pushover analysis, aimed at comparing the maximum lateral capacity of the structure with and without BRBs, as well as estimating the distribution of damage throughout the building. A rectangular load pattern was adopted, and the capacity curve was obtained by relating the displacement at the top of the structure to the total base shear recorded during the analysis. For the system with BRBs, a cross-sectional area of $A_{BRB} = 32.25\,cm^2$ was used for all stories of the building. The results of the Static Pushover analysis and the Capacity Curve for the buildings without and with the BRBs are represented in Fig. 6.23.

Figure 6.23 – Capacity Curve for the irregular building without and with the BRBs.

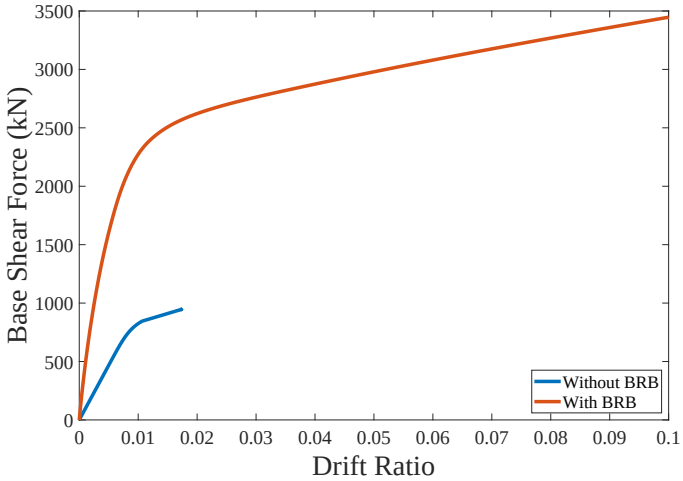

Source: Author.

It is important to note that the model without BRBs did not converge for displace-

ments beyond the point indicated in Fig. 6.23. Additionally, the improvement in structural capacity provided by the inclusion of BRBs is clearly observable. The fundamental period of the structure without BRBs is $T = 0.832\,s$, whereas the period of the structure with BRBs is reduced to $T = 0.374\,s$. This reduction reflects an increase in system stiffness and strength, which is also illustrated in Fig. 6.23.

In order to evaluate the distribution of damage throughout the structure, the deformed shape and the stress state of all elements were examined at a specific instant of the static analysis. The corresponding plots are presented in Fig. 6.24a, with the respective base shear value indicated for each case. Fig. 6.24a shows the yielded elements for the structure without BRBs, while Fig. 6.24b shows the yielded elements for the structure with BRBs.

Figure 6.24 – Deformed shape with partially and completely yielded components for a specific step of the Pushover analysis.

(a) Base Shear Force of $946.4\,kN$ **(b)** Base Shear Force of $1866.7\,kN$

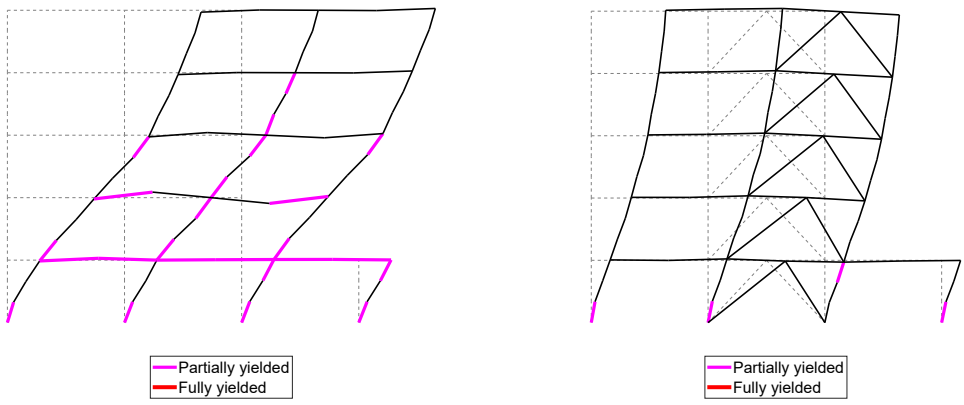

Source: Author.

It can be observed that the system with BRBs exhibits nearly twice the lateral capacity of the structure without BRBs, with significantly fewer elements reaching yielding. Moreover, in the structure with BRBs, yielding is primarily concentrated in the first story, indicating a more controlled and localized energy dissipation mechanism. In contrast, the structure without BRBs shows widespread yielding throughout its height, suggesting a less efficient and more dispersed plastic mechanism. This result validates the effectiveness of BRBs in enhancing the structural capacity under static loading. The following section presents an optimization of the BRB cross-sectional areas, adopting a Performance-Based Risk Optimization approach under seismic loading.

6.6.2.3 Optimization Results

The evaluation of statistical uncertainty was performed at the central point of the DoE, using $N_e = 24$ ground motions to ensure consistency with the number of records

typically considered in practical design applications, within each of the $N_s = 10$ ground motion sets. A parent set of 500 hazard-consistent ground motions was generated using the stochastic ground motion model. NLTHA were performed to estimate $\hat{\mu}_{EDP_i}(\mathbf{x_d})$ and $\hat{\sigma}_{EDP_i}(\mathbf{x_d})$ for each component of **EDP**.

The metamodels developed in this case study follow the same configuration defined in Section 6.4.4.4 for Case Studies 1 and 2. The Genetic Algorithm (GA) (Holland, 1992) is also employed, with a population size of 50 candidates considered for the solution. For each candidate, the Kriging surface for the Expected Repair Cost ($\tilde{C}_{\text{exReCo}}$) is evaluated. The results are presented in Fig. 6.25, which shows the Pareto front of Construction Cost (C_{cons}) versus $\tilde{C}_{\text{exReCo}}$.

Figure 6.25 – Pareto front for the multi-objective optimization problem.

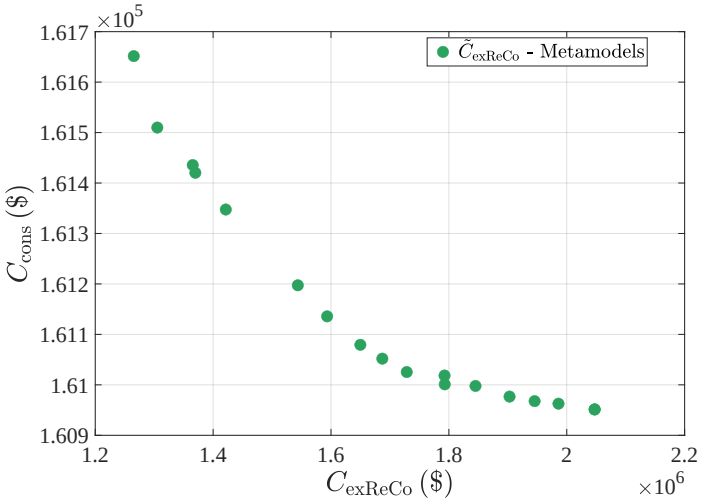

Source: Author.

The Pareto front illustrates an effective trade-off between construction costs and expected repair costs, facilitating the comparison of design alternatives for the diameter of the BRBs. It aids in choosing among different design options to enhance the building's resilience to seismic actions while evaluating the increase in initial construction costs.

A second optimization problem is evaluated to find the global minimum in the Total Cost of the structure. The proposed single-objective PBRO is illustrated as follows:

$$\begin{gathered} \text{Find } \mathbf{x_d}^* = \{A_{\text{BRB},1}, A_{\text{BRB},2}, A_{\text{BRB},3}, A_{\text{BRB},4}, A_{\text{BRB},5}\}^T \\ \text{to minimize } W(\mathbf{x_d}) = \left[C_{cons}(\mathbf{x_d}) + \tilde{C}_{exReCo}(\mathbf{x_d})\right] \\ 9.7 \leq \{A_{\text{BRB},i}\}_{i=1}^{5} \leq 64.5\, cm^2 \end{gathered} \tag{6.20}$$

The Genetic Algorithm (GA) is also applied in the single-objective PBRO with the same population size of 50 points, with results presented in Table 6.13.

Table 6.13 – Results for the single-objective PBRO.

$A_{\text{BRB},1}$ (cm^2)	$A_{\text{BRB},2}$ (cm^2)	$A_{\text{BRB},3}$ (cm^2)	$A_{\text{BRB},4}$ (cm^2)	$A_{\text{BRB},5}$ (cm^2)	$W(\mathbf{x})$ (\$) Surrogate	$\tilde{C}_{exReCo}(\mathbf{x})$ (\$) Surrogate
15.24	33.14	64.50	64.50	44.80	1.41×10^6	1.28×10^6

Source: Author.

The results of the Risk Optimization problem indicate that the BRB areas should be increased in all stories above the first floor, particularly in the third and fourth stories. In these levels, the BRB area reaches the upper limit of the design domain to effectively reduce the expected repair cost while maintaining a balance with the initial construction cost. In contrast, in the first story, the BRB area can remain close to the minimum, suggesting that damage is significantly greater in the stories where the building exhibits structural irregularities.

These findings demonstrate that the proposed framework can assist in prioritizing floors when a building retrofit is required, guiding decision-making to enhance seismic performance efficiently.

6.7 Chapter Overview

This Chapter presents a PBRO framework that incorporates metamodels capable of accounting for statistical uncertainty arising from limited ground motion data. Kriging metamodels are developed to replace the nonlinear dynamic FE model for estimating the first-mode period, the population values of the lognormal parameters of the marginals of the random vector of EDPs, and the lognormal collapse fragility parameters, following the FEMA P-58 methodology. The influence of statistical uncertainty in the estimation of distribution parameters is explicitly incorporated into the Kriging formulation through an additive noise term.

The proposed approach effectively filters statistical uncertainty from the noisy estimates obtained at each support point, providing smooth metamodels that directly approximate the population-level distribution parameters across the design domain. These metamodels are then used to compute the expected repair costs across different design alternatives. By replacing the repeated calls to the nonlinear dynamic FE model with these metamodels, the framework enables rapid and accurate evaluation of structural performance and risk within a PBRO process. The accuracy of the framework is demonstrated in Case Study 1 by validating the Pareto front solutions from the multi-objective PBRO using direct nonlinear dynamic FE simulations with 5000 ground motions per design, minimizing the influence of statistical uncertainty. Across all cases, differences in expected repair costs were within 8%, confirming that the metamodels provide reliable approximations of the true loss behavior.

The approach significantly reduces computational effort, requiring over 200 times fewer nonlinear dynamic FE model evaluations compared to a direct optimization approach. The availability of explicit, differentiable metamodels also introduces the potential for future application of gradient-based optimization methods. More broadly, the framework enables practical and computationally efficient optimization of structures under earthquake loading, while rigorously incorporating statistical uncertainty arising from limited ground motion datasets—a critical consideration in performance-based engineering practice.

Two additional case studies were evaluated with the proposed approach. In Case Study 2, a different Finite Element model was used, and the optimization problem aimed to determine the optimal external diameters of the building braces. Case Study 3 involved an irregular building, where BRBs were implemented as a retrofit solution to enhance its seismic performance.

7 A STRATIFIED STOCHASTIC EMULATION APPROACH FOR CONDITIONAL STRUCTURAL RESPONSE MODELING IN PBEE

This chapter introduces a framework that combines the Stratified Sampling (SS) technique with a Stochastic Polynomial Chaos Expansion (SPCE) to approximate the distribution of each component of the second-order random vector of Engineering Demand Parameters (EDPs) conditioned on non-collapse, without assuming a lognormal form for the data.

7.1 Preamble

PBEE frameworks require Nonlinear Time History Analysis (NLTHA) to propagate record-to-record variability and evaluate the probabilistic distribution of EDPs. In the FEMA P-58 (2018) methodology, a distinction is made between NLTHA conditioned on non-collapse, used to obtain response quantities (demands), and simulations that result in collapse, which are used to derive collapse fragility functions. Although this distinction is well established in FEMA P-58, it may lead to deviations from the lognormal assumptions commonly adopted in PBEE due to the lack of consideration of the probability-absorbing boundary associated with collapse.

This study proposes a stochastic emulation framework that integrates SS with SPCE to approximate the conditional distribution of EDPs given non-collapse, without imposing any predefined parametric form. The SS procedure partitions the input space according to seismic hazard intensity, ensuring balanced representation of rare but critical events, while separate SPCE emulators are trained for each stratum using only non-collapse responses. Record-to-record variability is represented through a latent random variable within the emulation process, making the emulator inherently stochastic.

Results demonstrate that the proposed framework accurately reproduces reference EDP distributions while reducing computational costs by more than one order of magnitude compared with full NLTHA-based Monte Carlo (MC) simulations. The stratified emulators effectively capture the heteroscedasticity of structural responses across hazard levels and yield smooth cumulative-distribution estimates consistent with the physical behavior of the system. Overall, the proposed approach provides a computationally efficient and non-parametric solution to PBEE, enabling scalable risk and reliability assessments under complex sources of uncertainty.

7.2 Problem Setting

7.2.1 Performance-Based Earthquake Engineering revisited

As discussed in Section 2.4.1, due to the high computational cost associated with NLTHA in nonlinear finite element (FE) models, the procedure outlined in FEMA P-58 (2018) establishes that a limited set of N_e ground motions can be used to characterize **EDP**, as represented in Eq. 2.13. The outcome is expressed as a demand matrix $\mathbf{X} \in \mathbb{R}^{N_e \times N_p}$, where each row represents one realization of **EDP**. In practice, the random vector **EDP** is typically modeled as a joint lognormal distribution, with its statistical parameters inferred from the sample matrix $\mathbf{X}$, as described below:

$$\ln(\mathbf{EDP}) \sim \mathcal{N}\left(\hat{\mu}_{\ln(\mathbf{EDP})}, \hat{\Sigma}_{\ln(\mathbf{EDP})}\right) \tag{7.1}$$

where $\hat{\mu}_{\ln(\mathbf{EDP})}$ denotes the mean vector and $\hat{\Sigma}_{\ln(\mathbf{EDP})}$ the covariance matrix inferred from the log-transformed demands.

The lognormal assumption has played a central role in PBEE models of seismic demand and fragility for more than two decades, providing a link between the hazard, represented by the Intensity Measure (IM), and the EDPs. Early analytical procedures proposed by Cornell *et al.* (2002), later consolidated in widely used guidelines, represented both demand and capacity as lognormally distributed variables. Accordingly, fragility curves were derived as lognormal cumulative distribution functions of the IM, with the logarithmic mean and standard deviation calibrated via regression (Ellingwood, 2001; Padgett; DesRoches, 2008) or maximum likelihood estimation (Baker, 2015). This formulation is attractive because it is mathematically simple, consistent with products of random effects, and easy to integrate into the PBEE convolution linking hazard, demand, damage, and loss. However, recent studies discussing this assumption have concluded that the lognormal hypothesis may be incompatible with statistical evidence (Karamlou; Bocchini, 2015; Lallemant; Kiremidjian; Burton, 2015; Mai; Konakli; Sudret, 2017; Cao; Feng; Beer, 2023).

7.2.2 Building Response Conditioned on Non-collapse

FEMA P-58 (2018) establishes that the NLTHA simulations performed to obtain $\mathbf{X}$ must be conditioned on the non-collapse state of the structure. In addition, it recommends excluding from $\mathbf{X}$ any simulations that result in structural collapse when evaluating repair and replacement costs. Additionally, the guideline suggests performing extra NLTHA runs if the number of collapse cases exceeds a predefined threshold. Based on these assumptions, $\mathbf{X}$ can be interpreted as the demand matrix of **EDP** conditioned on the non-collapse realizations.

Accordingly, the cumulative distribution function (CDF) for a component of **EDP** in Eq. 2.13 should be evaluated as "conditional on non-collapse". This can be written as:

$$\begin{aligned} F_{EDP}\left(e|im\right) = \left(1 - p_{\text{coll}}(e_{\text{crit}}|im)\right) F_{EDP}(e\,|\{im,\,\text{NC}\}) \\ + p_{\text{coll}}(e_{\text{crit}}|im) H(e - e_{\text{crit}}) \end{aligned} \tag{7.2}$$

where $p_{\text{coll}}(e_{\text{crit}}|im)$ is the probability of collapse, e_{crit} is the critical value of the EDP characterizing collapse, $H(\cdot)$ is the Heaviside step function, such that $H(e - e_{\text{crit}}) = 0$ for $e < e_{\text{crit}}$ and $H(e - e_{\text{crit}}) = 1$ for $e \geq e_{\text{crit}}$, NC refers to Non-Collapse and $F_{EDP}(e\,|\{im,\,\text{NC}\})$ is the conditional CDF from which expected costs of repair and replacement are computed. Equation 7.2 is not presented in FEMA P-58 (2018), but it is proposed herein, following the methodology of FEMA P-58, for handling the collapse / non-collapse condition in a more explicit way.

The sources of uncertainty in demand parameters, as defined by FEMA P-58 (2018), are: (1) modeling uncertainty, denoted as $\mathbf{X_m}$; (2) ground-motion variability, denoted as $\mathbf{X_h}$; and (3) record-to-record variability, denoted as $\mathbf{X_w}$. The random vector $\mathbf{X_r}$ representing the sources of uncertainty can be expressed as:

$$\mathbf{X_r} = \{\mathbf{X_m}, \mathbf{X_h}, \mathbf{X_w}\}^T \tag{7.3}$$

Building upon these discussions, this work proposes to combine the stochastic emulator framework with a Stratified Sampling technique to approximate the response distribution of the EDPs conditioned on the non-collapse state, as represented by $F_{EDP}(e\,|\{im,\,\text{NC}\})$ in Eq. 7.2. A key aspect of the proposed framework is that the selected stochastic emulator does not require any prior assumption regarding the shape of the response distribution, which enables a direct comparison with the traditional lognormal assumption. The Stratified Sampling technique is incorporated into the framework to define hazard-based strata in the random domain, allowing the training of independent emulators for each stratum. This approach aims to reduce the number of samples required for training while more accurately calibrating the noise effects of the emulator within each stratum, ultimately providing a more robust representation of the conditional response distribution.

7.3 Proposed Framework

7.3.1 Overview

Following the discussions presented in the previous section, the proposed framework employs a stochastic emulator to model the distribution of **EDP** conditioned on the non-collapse state of the structure, as represented in Eq. 7.2. In this formulation, the

uncertainty associated with record-to-record variability, $\mathbf{X_w}$, is incorporated directly into the emulator rather than treated as an external input variable. Specifically, for the stochastic emulator adopted in this work, the record-to-record variability is represented as a latent random variable $\mathbf{Z}(\omega)$ within the models. This representation makes the emulator output inherently stochastic, even for identical input conditions. Accordingly, the random vector $\mathbf{X_r}$ previously defined in Eq. 7.3 is now expressed as $\mathbf{X_r} = \{\mathbf{X_m}, \mathbf{X_h}\}^T$.

The concept of a Stochastic Simulation, introduced in Section 4.2, refers to a class of models whose responses remain random even for a fixed set of input parameters, due to intrinsic stochasticity. This intrinsic stochasticity arises because the input variables, represented here by the random vector $\mathbf{X_r}$, provide only partial information about the model response, while other relevant variables, referred to as latent random variables $\mathbf{Z}(\omega)$, are not explicitly included as inputs and therefore remain random.

Stochastic models can be emulated to reduce the computational effort required for their evaluation. These stochastic emulators are particularly relevant for representing structural responses influenced by multiple sources of uncertainty, and their main advantage lies in their ability to reproduce general response distributions beyond classical parametric assumptions. In this context, the SPCE introduced in Section 4.2.1.1 corresponds to a stochastic emulator designed to approximate the probability density function of the model output. The SPCE incorporates an artificial latent variable $\mathbf{Z}$ to capture the intrinsic stochasticity of the simulator within the framework of Polynomial Chaos Expansions (PCE).

An important advantage of the SPCE for the present problem is that it does not impose any predefined parametric form on the conditional model response. In addition, it does not require replications of the original simulator, allowing the computational budget to be fully allocated to a larger number of design points and thereby improving the coverage of the input random space. To further enhance this coverage, the Stratified Sampling (SS) technique is incorporated into the proposed framework.

7.3.2 Stratified Sampling (SS) scheme

The Stratified Sampling (SS) scheme adopted in this work follows the methodology proposed by (Arunachalam; Spence, 2023a; Arunachalam; Spence, 2023b) for risk assessment problems related to natural hazards, aimed at estimating multiple failure probabilities. In the present framework, the SS procedure is used to generate the support samples for the design of experiments (DoE) used to train the stochastic emulators defined in Section 4.2.1.1. The sampling is performed over the space of the input random variables represented by the vector $\mathbf{X_r} \in \mathbb{R}^{n_{\text{RV}}}$, denoted by $\mathbb{S} \subset \mathbb{R}^{n_{\text{RV}}}$. Accordingly, only Phase I of the generalized stratified sampling framework proposed by Arunachalam and Spence

(2023b) is considered in this study. The basic idea is to partition $\mathbb{S}$ into $n_{\mathbb{S}_i}$ disjoint strata,

$$\{\mathbb{S}_i : i = 1, \ldots, n_{\mathbb{S}_i}\}, \tag{7.4}$$

such that

$$\bigcup_{i=1}^{n_{\mathbb{S}_i}} \mathbb{S}_i = \mathbb{S} \quad \text{and} \quad \mathbb{S}_i \cap \mathbb{S}_j = \varnothing \ \text{ for } \ i \neq j. \tag{7.5}$$

To achieve the partitioning of the sample space described in Eq. 7.4, the stratification variables, represented by the vector $\boldsymbol{\mathcal{V}}$, must be defined together with the strata boundaries and the number of samples in each stratum, n_{st}. The resulting strata are required to satisfy the conditions given in Eq. 7.5.

When Monte Carlo (MC) is used to draw samples from each stratum, the procedure is referred to as stratified random sampling (Cochran, 2007). If the stratification is properly defined, meaning an appropriate choice of $\boldsymbol{\mathcal{V}}$, $\{\mathbb{S}_i\}_{1\leq i\leq n_{\mathbb{S}_i}}$ and $\{n_{\text{st},i}\}_{1\leq i\leq n_{\mathbb{S}_i}}$, the variance of the estimator of the performance evaluation associated with the considered limit state can be significantly smaller than that obtained using pure MC sampling with an identical sample size. To ensure proper stratification, the following steps are followed in this work (Arunachalam; Spence, 2023b):

1. **Choice of a stratification variable $\boldsymbol{\mathcal{V}}$:** for cases where $\boldsymbol{\mathcal{V}} \not\subseteq \mathbf{X_r}$, a computational model that depends on a subset of the input uncertainties is used to evaluate $\mathcal{V}$, as in $\boldsymbol{\mathcal{V}} = \mathcal{M}(\boldsymbol{\tau})$, where $\boldsymbol{\tau} = \{\mathbf{X_h}, \mathbf{X_w}\}$. When the cost of evaluating $\mathcal{M}$ is much lower compared to that of performing NLTHA to obtain **EDP**, MC simulation can be implemented to generate a large number $\hat{n}$ of independent and identically distributed (i.i.d.) samples $\boldsymbol{\tau}_k^{(i)}$ in each stratum, ensuring sufficient samples in every stratum $\{n_{\text{st},i}\}_{1\leq i\leq n_{\mathbb{S}_i}}$. A general rule can be applied here: if $P\left(\mathbb{S}_{n_{\mathbb{S}_i}}\right) \approx 10^{-k}$, it takes 10^{k+2} evaluations of $\mathcal{M}$ to generate 10^2 samples in the last stratum $\mathbb{S}_{n_{\mathbb{S}_i}}$.
2. **Definition of the number of strata and probability constant:** $n_{\mathbb{S}_i}$ and the probability constant $p \in [0.1, 0.3]$ must be chosen to define the stratification and to fix the probability estimates for each stratum.
3. **Populate strata-wise samples $\boldsymbol{\tau}_k^{(i)}$ to define the limits of each stratum $\mathcal{V}_i$ and $\mathbb{S}_i$ adaptively:** for each stratum, set $\mathcal{V}_i$ as the $(1-p^i)\,\hat{n}$th largest value of the stratum. Then, define $\mathbb{S}_i = \{\boldsymbol{\tau} : \mathcal{V} \in (\mathcal{V}_{i-1}, \mathcal{V}_i]\}$. Repeat this process for each stratum until the last stratum is defined by $\mathbb{S}_{n_{\mathbb{S}_i}} = \{\boldsymbol{\tau} : \mathcal{V} \in \left(\mathcal{V}_{n_{\mathbb{S}_i}-1}, \mathcal{V}_{n_{\mathbb{S}_i}}\right]\}$.
4. **Select samples from each defined stratum:** select n_{st} samples from each stratum. For this purpose, MC or LHS sampling can be used within each stratum.

7.3.3 Stratifed Stochastic Emulation

With the stratification of the space of the input random variables, support points for the DoE are drawn within each stratum according to the prescribed allocation rule.

Subsequently, a stochastic emulator is trained in each stratum $\mathbb{S}_i$ using the corresponding non-collapse responses. Each emulator provides a probabilistic representation of the conditional behavior of the EDP within its respective stratum. For inputs $\mathbf{X_r} \in \mathbb{S}_i$, this can be written as:

$$\widetilde{Y}^{(i)}(\mathbf{X_r}, \mathbf{Z}) \overset{d}{\approx} e \mid \text{NC}, \quad \mathbf{X_r} \in \mathbb{S}_i \tag{7.6}$$

where $\widetilde{Y}^{(i)}$ denotes the stochastic emulator associated with the i-th stratum and $\mathbf{Z}^{(i)}$ is a latent random variable representing the record-to-record variability.

Once the stochastic emulators are trained for all strata, the conditional distribution of the structural responses given the non-collapse condition $F_{EDP}(e\,|\{im,\,\text{NC}\})$, defined in Eq. 7.2, can be approximated by combining the contributions from each stratum. This combination follows the law of total probability, such that the global distribution of EDP conditioned on non-collapse is expressed as a mixture of the stratum-wise conditional distributions:

$$\widetilde{F}_{EDP}(e\,|\{im,\,\text{NC}\}) = \sum_{i=1}^{n_{\mathbb{S}_i}} P(\mathbb{S}_i \mid \text{NC})\, F^{(i)}_{EDP}(e \mid \{\text{NC},\,\mathbb{S}_i\}) \tag{7.7}$$

where $F^{(i)}_{EDP}(e \mid \text{NC},\,\mathbb{S}_i)$ is the stratum-wise conditional CDF, given by:

$$F^{(i)}_{EDP}(e \mid \{\text{NC},\,\mathbb{S}_i\}) := P(EDP \leq e\,|\,\text{NC},\ \mathbf{X_r} \in \mathbb{S}_i) \tag{7.8}$$

In practice, $F^{(i)}_{EDP}(e \mid \text{NC},\,\mathbb{S}_i)$ is approximated using the stochastic emulator $\widetilde{Y}^{(i)}(\mathbf{X_r}, \mathbf{Z}^{(i)})$, by propagating realizations of $\mathbf{X_r}$ restricted to $\mathbb{S}_i$ together with the latent variable $\mathbf{Z}^{(i)}$, as follows:

$$F^{(i)}_{EDP}(e \mid \{\text{NC},\,\mathbb{S}_i\}) \approx P\Big(\widetilde{Y}^{(i)}(\mathbf{X_r}, \mathbf{Z}) \leq e \,\Big|\, \text{NC},\ \mathbf{X_r} \in \mathbb{S}_i\Big) \tag{7.9}$$

This results in an approximation of $F_{EDP}(e\,|\{im,\,\text{NC}\})$, where each emulator contributes according to the relative importance of its corresponding stratum in the non-collapse domain.

7.3.4 Algorithm

The overall procedure of the proposed framework is summarized in the flowchart shown in Fig. 7.1.

Figure 7.1 – Flowchart of the proposed methodology.

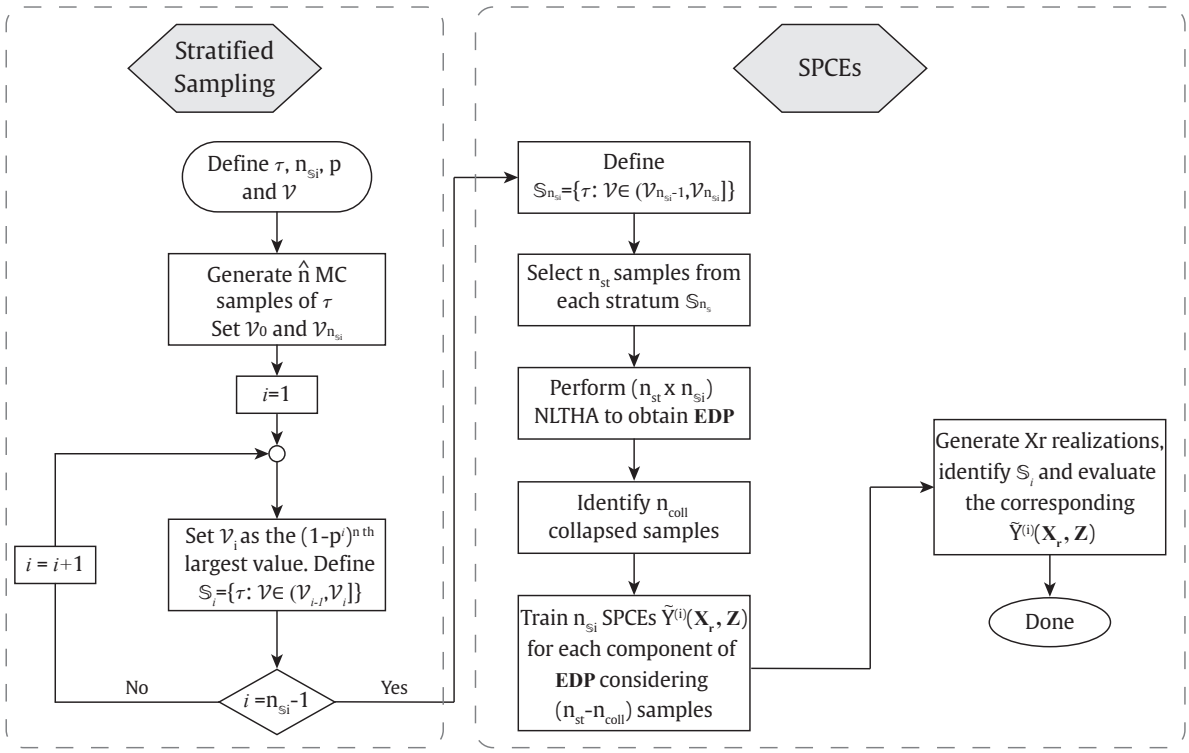

Source: Author.

To partition the sample space, select the number of samples in each stratum, train the SPCE emulators, and obtain the conditional distribution of **EDP** given the non-collapse condition, the following steps are implemented:

1. Define the vectors $\boldsymbol{\tau} = \{\mathbf{X_h}, \mathbf{X_w}\}$ and $\boldsymbol{\mathcal{V}} = \mathcal{M}(\boldsymbol{\tau})$, as well as the number of strata $n_{\mathbb{S}_i}$ and the probability constant $p \in [0.1, 0.3]$. Populate the strata-wise samples $\boldsymbol{\tau}_k^{(i)}$ with a sufficiently large number of realizations $\hat{n}$ to adaptively define the boundaries of each stratum, as described in Section 7.3.2. This procedure partitions the sample space $\mathbb{S}$ into $n_{\mathbb{S}_i}$ disjoint strata with enough samples in each region.
2. Randomly select n_{st} samples from each stratum $\mathbb{S}_i$ to serve as support points for training the SPCE emulators.
3. Perform $(n_{\mathbb{S}_i} \times n_{\text{st}})$ nonlinear time-history analysis (NLTHA) to obtain the response vector **EDP** for each realization of $\mathbf{X_r}$.
4. Check the collapse condition for each NLTHA and identify the number of collapsed samples, denoted by n_{coll}.
5. Train $n_{\mathbb{S}_i}$ SPCEs emulators for each component of the response vector **EDP**, as defined in Eq. 7.6. Each emulator $\widetilde{Y}^{(i)}(\mathbf{X_r}, \mathbf{Z})$ is calibrated using the $(n_{\text{st}} - n_{\text{coll}})$ non-collapse samples of $\mathbf{X_r}$ and the corresponding **EDP** values in the i-th stratum.
6. Generate a sufficiently large number of random realizations of $\mathbf{X_r}$, identify the

stratum $\mathbb{S}_i$ to which each sample belongs, and evaluate the corresponding SPCE emulator $\widetilde{Y}^{(i)}(\mathbf{x_r}, \mathbf{Z}) \mid \mathbf{x_r} \in \mathbb{S}_i$ for that stratum.

7. Empirically compute the cumulative distribution function $\widetilde{F}_{EDP}(e \,|\{im, \text{NC}\})$ by combining the stratum-wise contributions according to Eq. 7.7.

7.4 Case Study

7.4.1 Overview

The proposed framework is demonstrated through a case study involving a four-story archetype steel building with perimeter Special Moment Frames (SMFs), designed in accordance with (AISC, 2010; ASCE, 2013). The structure is assumed to be located in urban California. Plan and elevation views of the building are presented in Figs. 7.2a and 7.2b, respectively.

Figure 7.2 – Case study structure: (a) typical plan view of the building; (b) representation of the steel SMF.

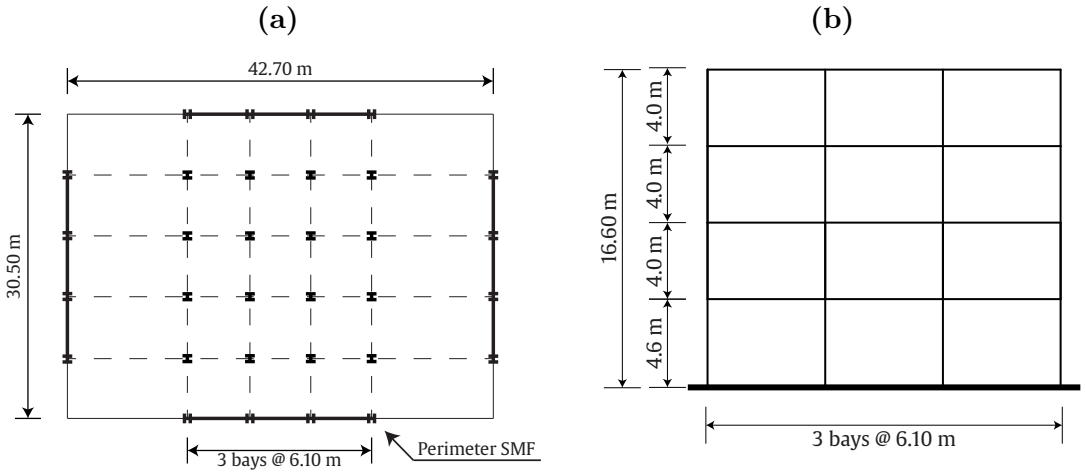

Source: Author.

The building has a first-story height of 4.6 m and a typical story height of 4.0 m. Steel columns are spliced at the mid-height of the odd-numbered stories, except for the first story. The beams and columns are made of ASTM A992 Grade 50 steel, and additional design details can be found in (NIST, 2010; Zareian; Lignos; Krawinkler, 2010; Elkady; Lignos, 2014; Elkady; Lignos, 2015). Table 7.1 summarizes the geometric specifications of the structural elements.

The objective of this case study is to emulate the conditional distribution of the following components of the vector **EDP**: Interstory Drifts of stories 1–4 (Drift_1, Drift_2, Drift_3, Drift_4); Peak Floor Accelerations of floors 1–5 (PFA_1, PFA_2, PFA_3, PFA_4, PFA_5); and Residual Drifts of stories 1–4 (RDR_1, RDR_2, RDR_3, RDR_4).

Table 7.1 – Member Sizes for the Special SMF.

Story	Beam Size	Exterior Column Size	Interior Column Size
1	W21X73	W24X103	W24X103
2	W21X73	W24X103	W24X103
3	W21X57	W24X62	W24X62
4	W21X57	W24X62	W24X62

Source: Author.

In this example, model uncertainties are not considered. Thus, the random input vector is reduced to the hazard-related variables, $\mathbf{X_r} = \mathbf{X_h}$, which only represent the variability of the ground-motion.

The stochastic ground-motion model described in Section 6.4.2 is adopted. In this model, the moment magnitude M_w and the epicentral distance r are treated as the random variables of the problem, such that $\mathbf{X_r} = \mathbf{X_h} = [M_w, r]$.The record-to-record variability, represented by the white-noise sequence $\mathbf{X_w}$, is incorporated into the SPCE as the latent variable $\mathbf{Z}$. M_w follows the truncated Gutenberg–Richter distribution presented in Eq. 6.14, with $M_{w,\min} = 6$, $M_{w,\max} = 8$, and $\beta = 0.9 \log_e(10)$. The epicentral distance r is modeled as a lognormal random variable with a median of 15 km and a coefficient of variation equal to 0.4.

The limit state associated with collapse is defined as the exceedance of a maximum peak interstory drift equal to 15%, following Elkady and Lignos (2019).

7.4.2 Finite Element Model of the Structural System

A two-dimensional nonlinear dynamic Finite Element (FE) model of the moment-resisting steel frame was developed in OpenSees (McKenna; Fenves; Scott, 2006) by Elkady (Elkady, 2016; Elkady; Lignos, 2019). The model represents the E–W loading direction, referred to as the B model in (Elkady; Lignos, 2014). It includes only the bare steel frame components of the SMF, neglecting the effects of the composite floor slabs and the gravity framing system.

The beams and columns are idealized as elastic elements with two flexural springs at their ends, representing the plastic hinge locations. The springs are modeled using the lumped plasticity modified IMK deterioration model, which captures the cyclic degradation of flexural strength and stiffness in steel components subjected to cyclic loading (Ibarra; Medina; Krawinkler, 2005; Lignos *et al.*, 2011; Lignos; Krawinkler, 2011; Lignos; Krawinkler, 2012). The panel zones are represented by the *parallelogram model* proposed by Gupta and Krawinkler (1999), with hysteretic behavior defined by a tri-linear backbone curve proposed by Krawinkler (1978). The input parameters for the panel zones are determined

according to PEER/ATC 72-1 (2010).

P–Delta effects are simulated using a fictitious column, referred to as a "leaning column", connected to the main SMF model through axially rigid truss elements. At each floor, the leaning column has zero rotational stiffness, and a vertical load equal to half of the seismic gravity load of the corresponding archetype building, minus the tributary load directly assigned to the SMF columns, is applied to it. Rayleigh damping is assigned with a damping ratio of 2% for the first and third vibration modes to represent inherent damping. The fundamental period of the structure is $\bar{T} = 1.43\,\text{s}$.

7.4.3 Results

7.4.3.1 Preamble

The results of this case study are presented in two parts: (i) the partitioning of the sample space into hazard strata, and (ii) the selection of samples within each stratum followed by the corresponding SPCE results for the considered components of **EDP**. The reference solutions are obtained using direct MC simulations, based on 25,000 NLTHAs performed with random realizations of M_w, r and $\mathbf{X_w}$ to generate ground-motion records through the stochastic ground-motion model.

Based on the adopted collapse criterion, 0.36% of the reference simulations resulted in collapse. These analyses are excluded from the reference dataset, ensuring that the comparison is performed only with responses conditioned on the non-collapse state.

7.4.3.2 Strata-wise samples

For this case study, the spectral acceleration at the first-mode period, $S_a(\bar{T})$, with 5% damping is selected as the stratification variable. This is the same variable adopted in (Arunachalam; Spence, 2023b), which demonstrated an increasing trend in drift ratio with increasing spectral acceleration, supporting this choice. Therefore, $\mathcal{V} = S_a(\bar{T})$, and the computational model $\mathcal{M}$ required to evaluate S_a corresponds to the ground motion model considering the random variables associated with the hazard, followed by the estimation of the linear oscillator response. Hence, $\mathcal{V} = S_a(\bar{T}) = \mathcal{M}(\boldsymbol{\tau})$, where $\boldsymbol{\tau} = [M_w, r, \mathbf{X_w}]$.

Following the rule described in Section 7.3.2, for $P\left(n_{\mathbb{S}_i}\right) \approx 10^{-3}$, at least 10^5 evaluations of $\mathcal{M}$ are required. Therefore, to ensure a sufficient number of samples in the last stratum, $\hat{n} = 10^6$ samples of $\boldsymbol{\tau}$ are generated using MC simulation. The remaining parameters are defined as $n_{\mathbb{S}_i} = 5$ and $p = 0.2$.

The stratum boundaries were adaptively determined as $\{\mathcal{V}_0, \mathcal{V}_1, \mathcal{V}_2, \mathcal{V}_3, \mathcal{V}_4, \mathcal{V}_5\} = \{0, 0.13, 0.30, 0.51, 0.74, \infty\}$, in units of g. The estimated empirical spectral acceleration hazard curve, along with the corresponding stratum thresholds, is shown in Fig. 7.3,

considering an exceedance rate of $\lambda_{M_w 6} = 0.6$ for the lower threshold magnitude. Fig. 7.4 presents the strata-wise scatter of the seismic hazard parameters M_w and r.

Figure 7.3 – Estimated empirical spectral acceleration hazard curve $\lambda(S_a)$, along with the strata thresholds.

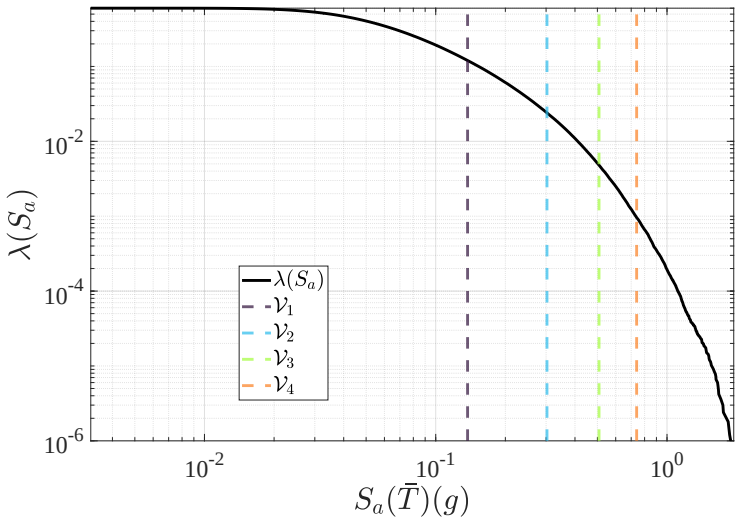

Source: Author.

Figure 7.4 – Strata-wise sample scatter of M_w and r.

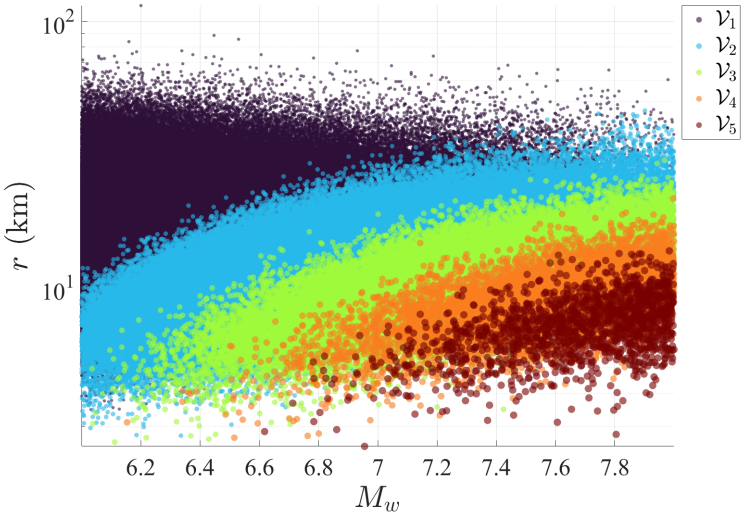

Source: Author.

Figure 7.5 presents the empirical PDFs of M_w and r for each stratum, based on the $\hat{n} = 10^6$ samples of $\boldsymbol{\tau}$. The results indicate that combinations of higher M_w and lower r tend to generate ground motion samples in the upper strata, whereas lower M_w and higher r predominantly lead to samples in the first strata.

Figure 7.5 – Empirical distribution of M_w and r for each strata.

(a) M_w **(b)** r (km)

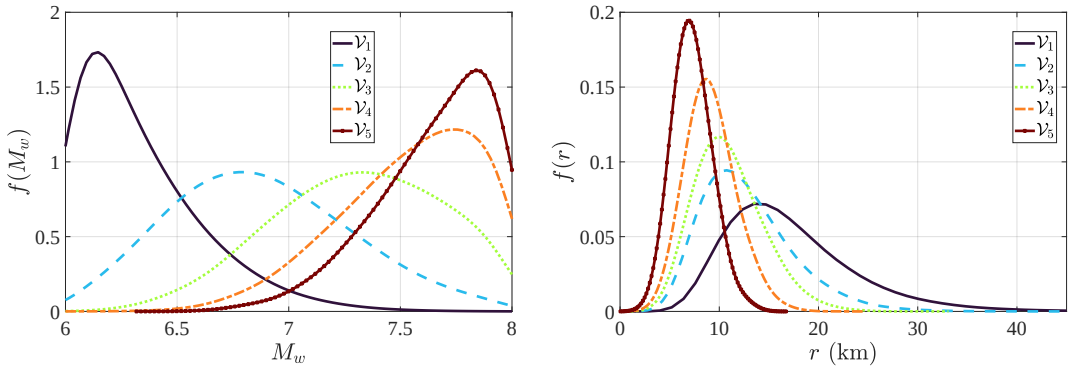

Source: Author.

7.4.3.3 SPCE results for each EDP

From the strata defined in Section 7.4.3.2, $n_{\text{st}} = 1000$ samples of M_w and r are randomly selected within each stratum to serve as support points for the construction of the SPCEs. The scatter of the selected samples for each stratum is shown in Figure 7.6.

Figure 7.6 – Scatter of $n_{\text{st}} = 1000$ samples per strata of M_w and r.

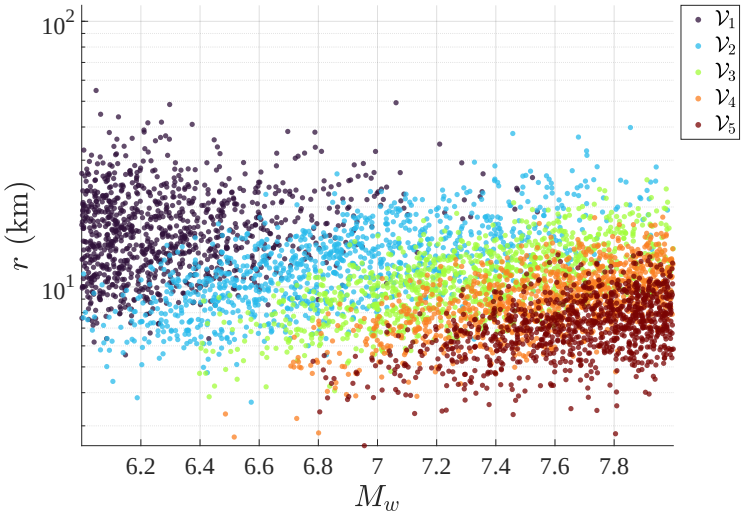

Source: Author.

Before using the $n_{\text{st}} = 1000$ samples to train the SPCEs, the collapse criterion was evaluated for the samples within each stratum to ensure that the emulators were trained exclusively on non-collapse data. The collapse probabilities $p_{\text{coll},n_{\mathbb{S}_i}}(e_{\text{crit}})$ obtained for each stratum are: $\{p_{\text{coll},1}p_{\text{coll},2}, p_{\text{coll},3}, p_{\text{coll},4}, p_{\text{coll},5}\} = \{0, 0, 3.2\%, 26.1\%, 61.9\%\}$, which shows the expected increase in the probability of collapse for the higher hazard strata.

The performance of the trained SPCE for each component and for each stratum of **EDP** (denoted $\widetilde{Y}_{\mathbf{EDP}}$) is evaluated by comparing its predictions with two models: (i) the empirical distribution obtained from the reference dataset, conditioned to non-collapse, estimated using a kernel density approach (indicated in the plots as Emp.), and (ii) a lognormal distribution fitted using 20 NLTHAs conditioned to non-collapse, following the recommendations of FEMA P-58 (2018) and employing Eq. 7.1 (indicated in the plots as LN). For this comparison, 25,000 samples of each **EDP** component are generated using $\widetilde{Y}_{\mathbf{EDP}}$, with random values of M_w and r that differ from those used to construct the reference dataset.

Figs. 7.7, 7.8 and 7.9 present the Probability Density Functions (PDFs) obtained with the three models for the Drift, PFA and RDR components, respectively.

Figure 7.7 – PDF plots for the Drift EDP in all stories.

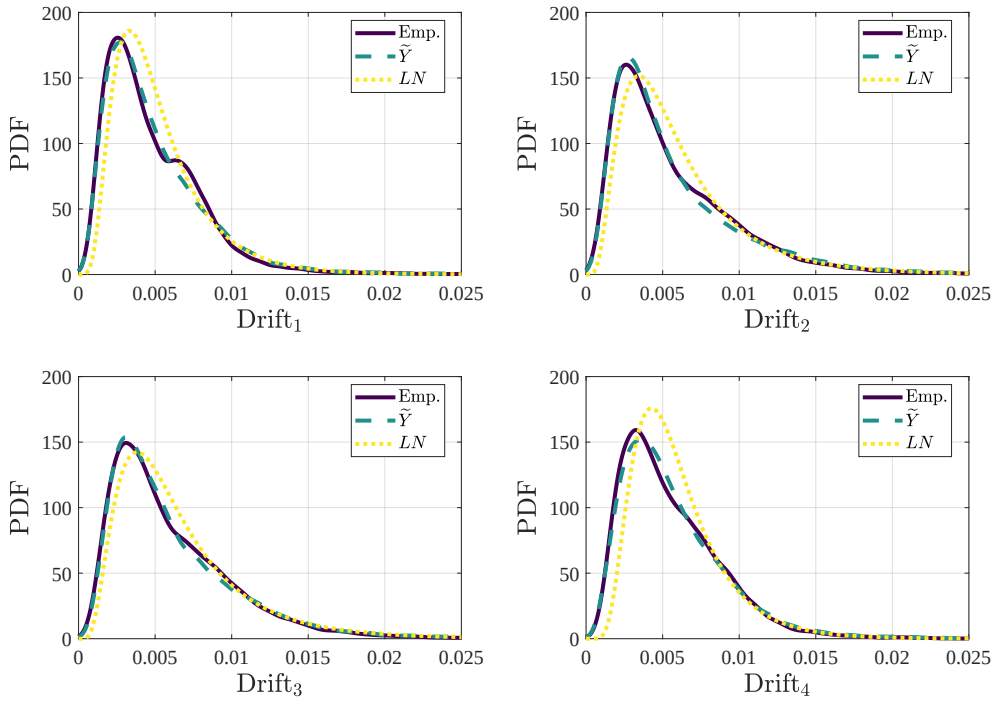

Source: Author.

The results show a close agreement between the empirical distribution derived from the 25,000 SPCE generated samples and the empirical distribution of the reference dataset conditioned on non-collapse. In contrast, the lognormal model fitted with a limited ground-motion set exhibits noticeable deviations from the reference, particularly in terms of the mean values, highlighting the limitations of relying on a reduced number of records for distribution fitting.

Figure 7.8 – PDF plots for the PFA EDP in all floors.

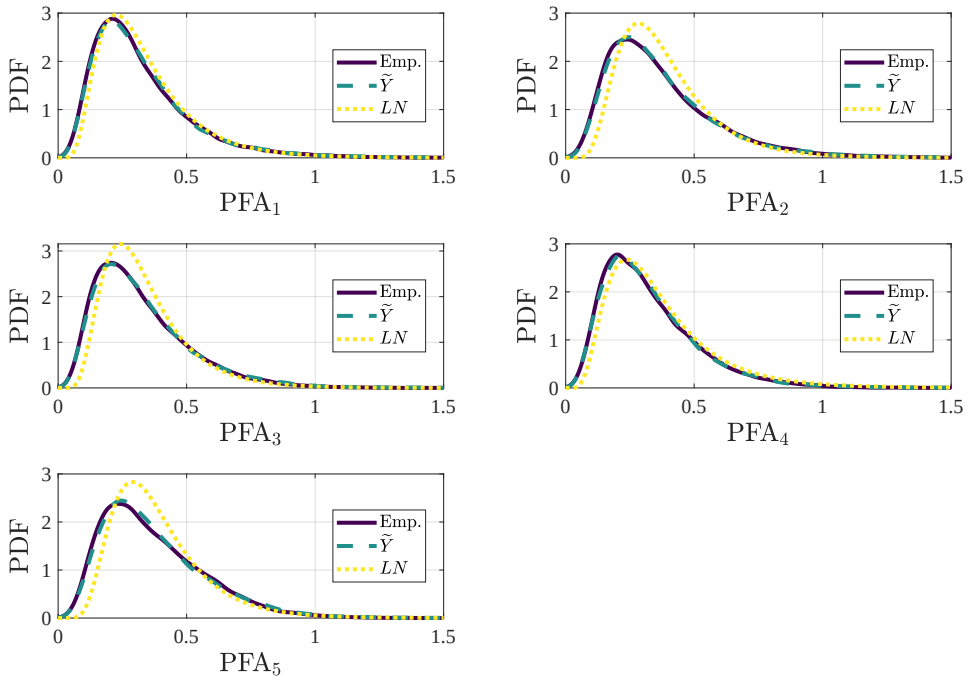

Source: Author.

Figure 7.9 – PDF plots for the RDR EDP in all stories.

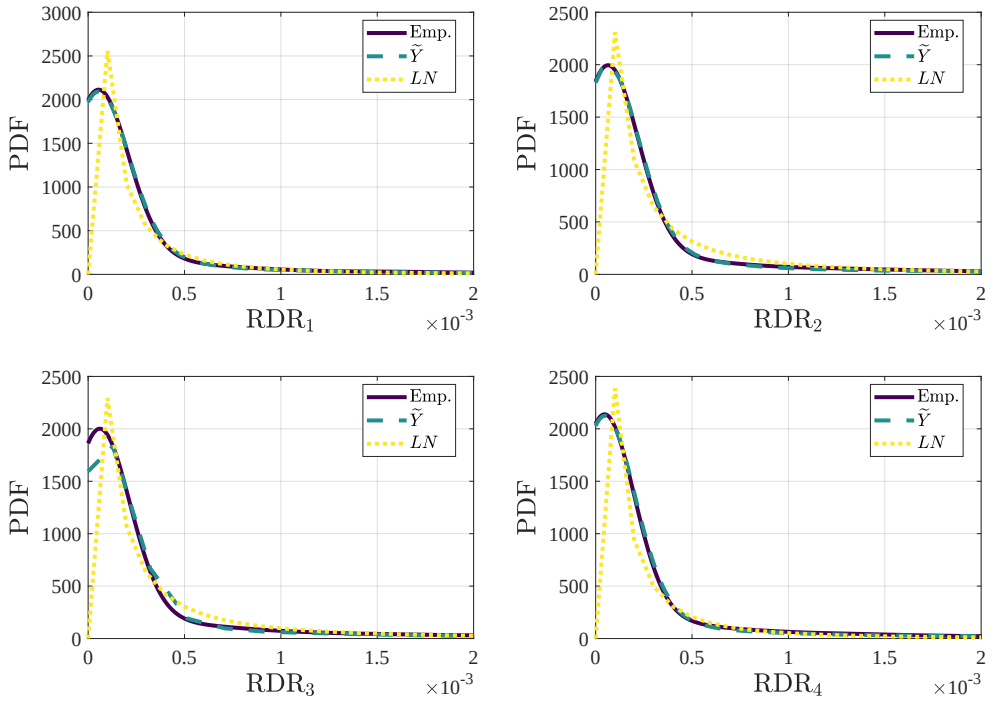

Source: Author.

For Drift and PFA EDPs, both the PDFs peak and the overall shape of the SPCE-based distributions are practically identical to those obtained from the empirical reference dataset, with only minor deviations in the upper tails. For RDR, an EDP characterized by a high concentration of probability near zero and a long right tail, the SPCE provides a realistic representation of the empirical variability.

For the Drift and PFA components, the lognormal PDFs are broader, with their modes shifted toward higher values compared to the empirical and SPCE based distributions, reflecting the larger dispersion obtained when fitting a lognormal model using a limited number of ground motions. For RDR, however, the behavior differs: the lognormal PDF is noticeably narrower and more sharply peaked, still with its mode slightly shifted toward higher values. This indicates that the parametric fitting procedure forces a concentrated distribution. This behavior indicates that the lognormal approximation does not adequately represent the true dispersion of the EDPs. This behavior indicates that the lognormal approximation does not accurately capture the true dispersion of the EDPs—either overestimating or underestimating it depending on the component—which leads to biased estimates of moderate-to-large demands and may affect risk predictions in PBEE applications.

Figs. 7.10, 7.11 and 7.12 present the CDFs obtained with the three models for the Drift, PFA and RDR components, respectively. The comparison of the CDFs further confirms the good performance of the SPCE in approximating the empirical distribution of the **EDP** components. The curves fitted to the SPCE-generated data exhibit a close match with the reference empirical distribution, particularly in the central region, where most of the probability mass is concentrated. This indicates that the SPCE successfully captures both the typical demand levels and the overall progression of cumulative probability.

In contrast, lognormal CDFs deviate more consistently from the empirical results. For the Drift and PFA components, the lognormal approximation tends to accumulate probability faster than the empirical curve, suggesting an underestimate of moderate-to-large responses. This behavior is consistent with the narrower shape of the lognormal PDFs. For RDR, the SPCE closely reproduces the empirical CDF across the entire range. In contrast, the lognormal distribution accumulates probability more slowly near zero and yields higher probabilities of moderate residual drifts compared to the empirical and SPCE curves.

Overall, the CDF results reinforce the limitations of fitting a parametric lognormal distribution using a small number of records, as recommended in FEMA P-58. Conversely, the SPCE provides a more flexible and accurate representation of the conditional EDP distributions, matching both the central trend and the cumulative behavior of the empirical reference.

Figure 7.10 – CDF plots for the Drift EDP in all stories.

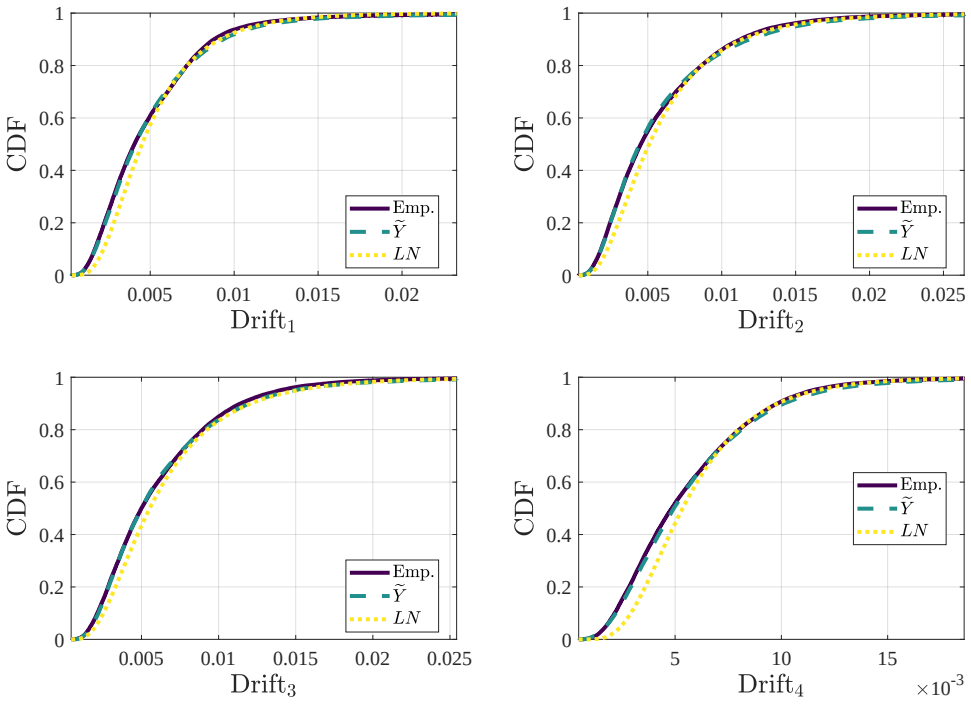

Source: Author.

Figure 7.11 – CDF plots for the PFA EDP in all floors.

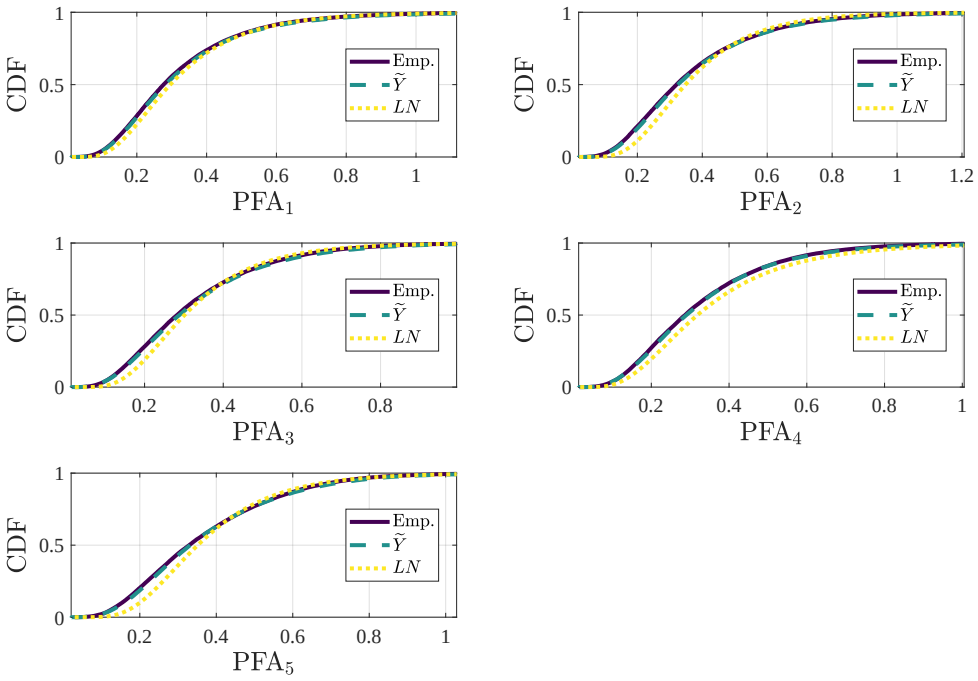

Source: Author.

Figure 7.12 – CDF plots for the RDR EDP in all stories.

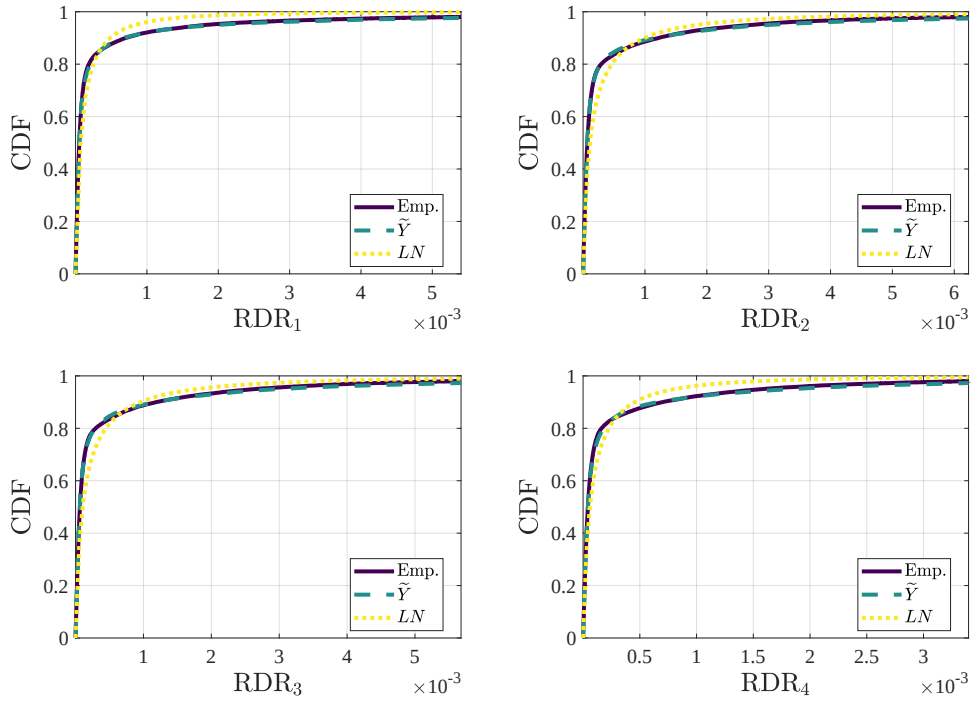

Source: Author.

Although PDFs and CDFs reveal that the SPCE provides a good match to the empirical distributions across the entire support, small differences are naturally harder to observe when probability densities are low. For this reason, the Complementary Cumulative Distribution Functions (CCDFs) presented in Figs. 7.13, 7.14, and 7.15 are included to explicitly examine the behavior in the upper tail. The CCDFs allow a more detailed assessment of the tail behavior of the conditional EDP distributions. For all components, the curves for the SPCE data remain close to the empirical CCDFs down to probabilities of the order of 10^{-2}, and the agreement is still reasonably good around 10^{-3}. In most cases, the SPCE produces slightly higher exceedance probabilities than the reference model in the upper tail, which leads to a mildly conservative representation of extreme demands. In contrast, the lognormal tails are substantially lighter for the Drift and RDR components, systematically underestimating the probability of large responses, whereas for the PFA components the lognormal model may either underestimate or overestimate the tail depending on the floor.

Figure 7.13 – CCDF plots for the Drift EDP in all stories.

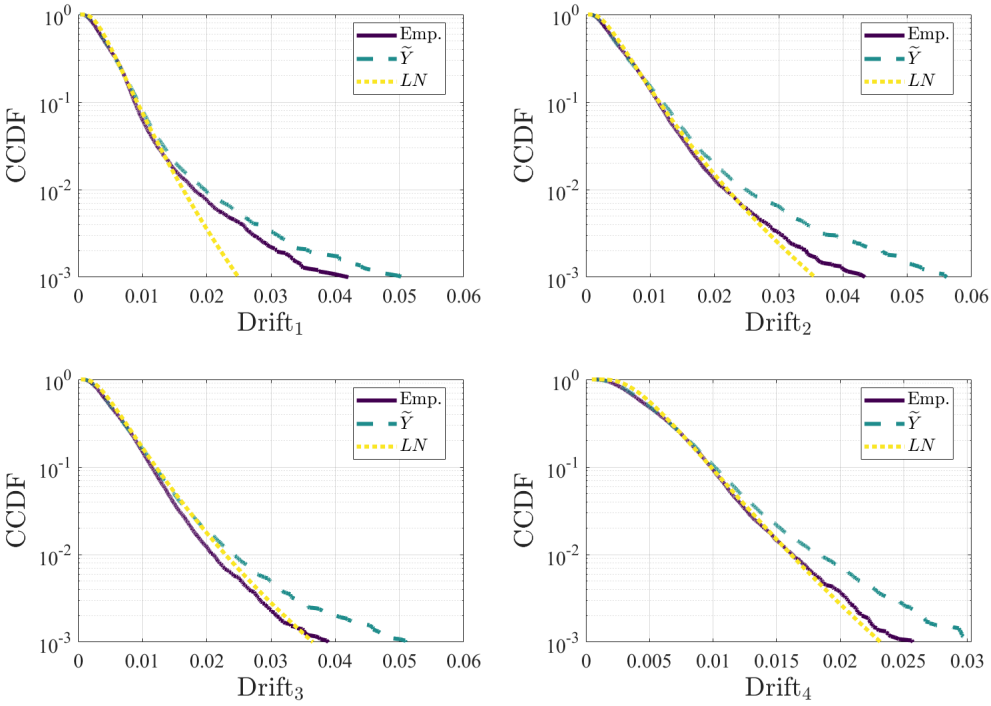

Source: Author.

Figure 7.14 – CCDF plots for the PFA EDP in all floors.

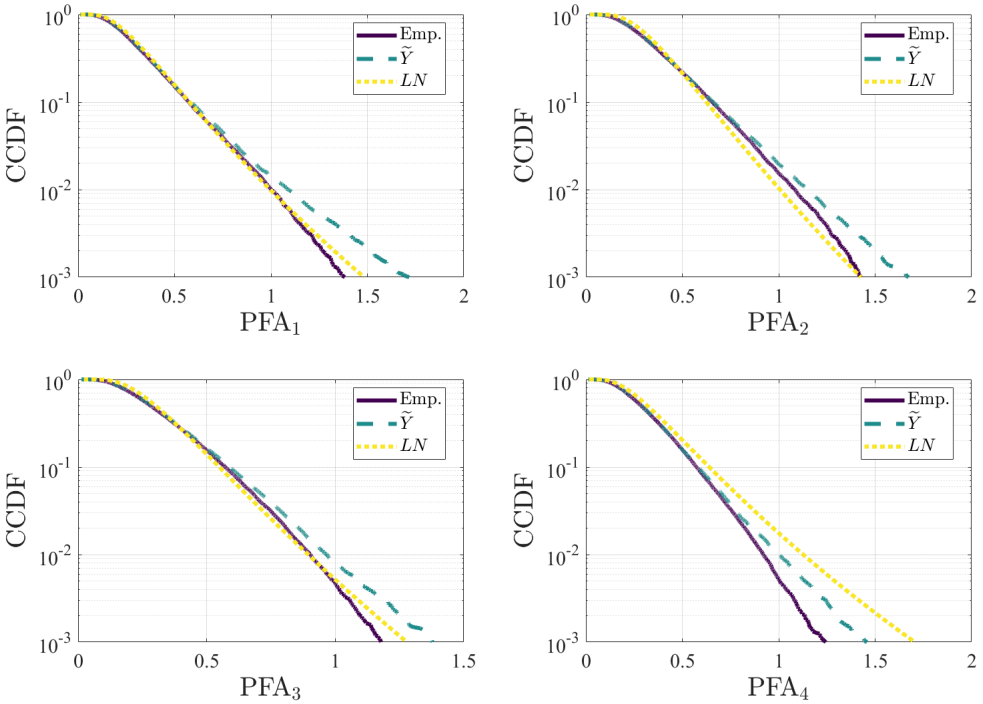

Source: Author.

Figure 7.15 – CCDF plots for the RDR EDP in all stories.

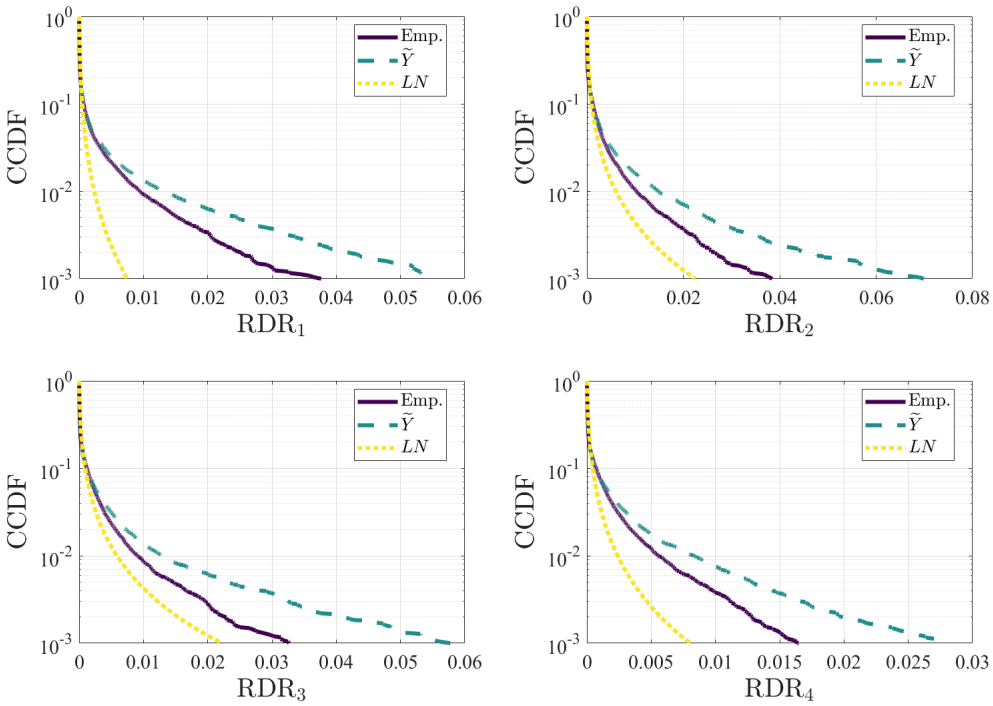

Source: Author.

These results also illustrate the effect of the Stratified Sampling scheme adopted for training the SPCEs. By allocating more samples to higher hazard strata, the emulator is exposed to a larger number of realizations associated with high EDP levels, which improves the stability of the tail estimates compared with a purely random sampling strategy. This targeted enrichment of the training set in the rare-event region is essential to obtain CCDFs that follow the empirical behavior over several orders of magnitude in probability.

Despite being trained exclusively on non-collapse data, the SPCE may still generate responses that fall within the collapse domain when propagated with new realizations of M_w, r and $\mathbf{Z}$. This behavior is consistent with the presence of the noise term in the SPCE formulation, which is introduced to account for the intrinsic stochasticity of the simulator and residual modeling errors. As a consequence, the predictive distribution is not strictly bounded by the training domain, and some realizations may exceed the collapse threshold. In practice, these samples must be discarded or censored when enforcing the non-collapse condition. This limitation suggests that future developments could incorporate explicit truncation better to control the emulator's behavior near the collapse limit.

7.5 Chapter Overview

This chapter presented the application of the proposed Stratified Stochastic Emulation framework to emulate the conditional distribution of structural demands under ground-motion uncertainty. The results demonstrated that the SPCE, trained using a SS scheme with 1000 samples in each stratum, accurately reproduces the empirical distributions of the considered **EDP** components. The emulator closely matches the reference PDFs, CDFs, and CCDFs obtained from 25,000 nonlinear dynamic analyses, successfully capturing both the central behavior and the tail characteristics of the conditional response. In contrast, the traditional lognormal approximation, fitted with a limited number of records following the FEMA P-58 (2018) guideline, exhibited significant discrepancies, particularly in the upper tails.

The adopted Stratified Sampling scheme played a central role in enabling the SPCE to represent rare-event behavior. By allocating more samples to higher hazard strata, the emulator is effectively exposed to a larger number of high-demand realizations, which improves the tail estimates and, consequently, the agreement with the empirical CCDFs. Notably, the SPCE with SS requires approximately five times fewer nonlinear dynamic analyses than the reference solution, while still achieving comparable accuracy across all EDP components. This demonstrates the substantial computational efficiency gained through the proposed framework.

Finally, the results suggest an opportunity to further reduce computational cost by investigating the evolution of the SPCE error as the number of training samples per stratum decreases. Evaluating how accuracy degrades with progressively smaller stratified training sets will allow the identification of an optimal allocation strategy and may reveal additional efficiency gains. This direction is particularly relevant for large-scale PBEE applications.

8 CONCLUSIONS

This work presented a methodology for the optimum design of structures subjected to seismic loads within the framework of Performance-Based Earthquake Engineering (PBEE). The proposed optimization problem aims to minimize the expected total cost, which accounts for the initial construction cost, the expected repair or damage costs, and the probability of structural collapse. Additionally, it investigated the trade-off between higher initial construction costs and lower expected damage costs within a multi-objective optimization framework.

Following the literature review on PBEE, this work provides a detailed discussion aimed at enhancing several stages of the framework. The reviewed chapter addressed the challenges associated with seismic hazard characterization in countries such as Brazil, where limited data on seismic actions are available. It also presents two different procedures for estimating the expected repair or damage cost of a structure, based on the Hazus (2022a) manual and the FEMA P-58 (2018) procedure.

In addition to the PBEE discussions, the structural optimization problem is formulated, and the different types of structural optimization are reviewed. A background on reliability-based optimization approaches was presented, followed by a state-of-the-art review of PBRO (also referred to as Performance-Based Design Optimization, PBDO), emphasizing the computational challenges involved in solving these problems. A concise discussion on the optimization methods applicable to this class of problems was also included.

The final part of the literature review introduced simulation methods and techniques to reduce the computational cost of numerical analyses through emulation. These approaches include deterministic metamodels (or surrogate models) and stochastic emulators. Such techniques are essential in the context of Performance-Based Risk Optimization (PBRO), as they significantly reduce the computational time associated with the Nonlinear Time History Analyses (NLTHA) required to estimate the Engineering Demand Parameters (EDPs) necessary for the loss analysis step in PBEE. Furthermore, these emulation techniques must be capable of capturing the uncertainties associated with both the seismic hazard and the structural parameters of the analysis.

For the first case study presented in this work, the seismic hazard was evaluated, and natural earthquake records consistent with the hazard at the specific location were selected. A Finite Element (FE) model with a lumped plasticity representation was developed and calibrated in OpenSees to represent a reinforced concrete (RC) structure, enabling NLTHA under the selected ground motions. A Probabilistic Seismic Demand Model (PSDM) was

constructed in conjunction with Incremental Dynamic Analysis (IDA) to establish the relationship between the earthquake Intensity Measure (IM) and the structural response, represented by the EDP, which defines the structural demand. Fragility functions were then derived from the PSDM results and deterministic capacity data, and were used to estimate the probability of structural failure and the corresponding expected loss.

Using the Adaptive Kriging methodology, a metamodel was developed to replace the original FE model in estimating the Drift EDP for different column cross-section sizes. The metamodel, whose validation is presented in Appendix A, was applied to the calculation of fragility functions and tested as a first attempt to reduce the computational burden associated with optimizing a structure within the PBEE framework during each iteration of the optimization process. The results included a comparison and validation of the fragility functions obtained from both the original FE model and the metamodel. The Firefly Algorithm was employed to solve this PBRO problem, with detailed descriptions of its formulation and implementation provided in Annex B.

The optimization problem for this case study consists of a single-objective optimization problem that aims to minimize the total cost of a building, considering the dimension of a square column cross-section as the design variable, with the metamodel replacing the original numerical model. The construction cost of the structure was defined based on representative construction prices in Brazil, while the expected failure costs were estimated as a percentage of the initial construction cost. Based on the results obtained from this analysis, the following specific conclusions are summarized:

- The structural fragility functions calculated using the metamodel, which was built and trained for column cross-section dimensions ranging from 25 cm to 60 cm and evaluated at 30 cm for the Slight, Moderate, Extensive, and Complete Damage Limit States, presented errors of less than 5% when compared with those obtained from the original FE model for the same cross-section dimensions. The probabilities of failure calculated along the selected hazard curve for design lives of 1, 50, and 100 years using both the FE model and the metamodel also present small discrepancies, confirming that the metamodel can reliably be used in an optimization framework.

- An initial step of the optimization process consisted of validating the problem constraints and cost formulation using points obtained from the original FE model for several column cross-section dimensions. A trend line was then fitted to these data within the range of 19 cm to 60 cm, indicating the presence of a minimum around 35 cm. This verification enabled the use of the metamodel developed in the first example to compute the expected damage cost for 700 intermediate cross-section values. The results show that the expected failure costs predicted by the metamodel are consistent with those from the FE model and also indicate a minimum column

cross-section close to 35 cm.

- The six simulations of the Firefly Algorithm converged to the same minimum value of the objective function, corresponding to a total cost of approximately $6,632.50 and an optimum column cross-section of 34.86 cm. This optimum value agrees with that observed during the validation stage, demonstrating that the optimization algorithm is effective in identifying the optimal design of structural elements when the metamodel is employed to evaluate fragility functions within the Performance-Based Earthquake Engineering framework. The movement of the fireflies was also verified, confirming that they consistently converged toward the brightest individual. After approximately 60 iterations, all simulations were nearly converged, with the fireflies concentrated around the optimum design solution.

It can be observed that the first case study, although relatively simple, was validated and successfully estimated the optimum column cross-section that minimizes both construction and damage costs. However, it is important to note that this analysis did not account for the uncertainties associated with the hazard description. The metamodels were trained using a specific set of 11 ground motion records, thus limiting the proposed framework to a predefined ground motion set.

Although several frameworks have addressed the uncertainties associated with seismic hazard through fragility and loss models, the distribution parameters that characterize the EDPs are often treated as exact. This implies that the optimization problem is solved based on inferred quantities rather than their true population values. In this context, the second case study proposed the use of a noisy Kriging metamodel framework that incorporates the statistical uncertainty arising from the inference of these parameters through the noise term in the Kriging formulation. Following the FEMA P-58 (2018) procedure, the approach models EDPs as a vector of jointly lognormal random variables, and the metamodels are trained to predict the median, dispersion, and correlation structure of the joint distribution as functions of the design variables. By doing so, the metamodel serves not only as a computationally efficient approximation but also as a statistically grounded representation of population-level behavior.

The trained metamodels were subsequently used to generate a large synthetic dataset of correlated EDPs, which served as inputs to the FEMA P-58 (2018) methodology for calculating the expected repair costs and collapse probabilities. The PBRO problem is formulated as a multi-objective optimization problem aimed at balancing construction cost and seismic risk, considering the areas of Buckling Restrained Braces (BRBs) as design variables. The case study involved a steel structure modeled as a FE model in OpenSees, using displacement-based beam–column elements with distributed plasticity. A stochastic ground motion model was adopted to generate the earthquake records used for training

the metamodels. A Genetic Algorithm (GA) was employed to solve the problem. The results obtained from this second approach lead to the following conclusions:

- The evaluation of statistical uncertainty, initially performed at the support points representing the Design of Experiments (DoE), confirmed noticeable variations in outcomes across different support points, highlighting the influence of the BRB area on the structural response. Additionally, variations were observed within individual support points depending on the specific ground motion set employed. The evaluation also indicated that the variances across the responses in the 20 support points considered were homogeneous.
- The results of the proposed Kriging surfaces demonstrated that the metamodeling approach effectively estimates the underlying population values associated with the marginals of the EDP vector. The smooth trends of the metamodel surfaces successfully filter out the statistical uncertainty present in the support point estimates. The scattered, seemingly random variation of the support point values around the metamodel surfaces reflects the inherent statistical uncertainty in the parameter inference process, whereas the metamodels capture the expected population trends across the design space. The results also demonstrated that the proposed Kriging metamodels effectively capture the population values of the lognormal parameters of the collapse fragility function across the design domain, filtering out statistical uncertainty and revealing smooth, physically meaningful trends.
- The Pareto front obtained illustrates the expected trade-off between construction cost and expected annual repair cost, providing a rational basis for comparing design alternatives for the BRB areas. This enables more informed decision-making by identifying design configurations that achieve an effective balance between initial investment and long-term performance.
- The accuracy of the framework was verified by validating the Pareto front solutions from the multi-objective PBRO using direct nonlinear dynamic FE simulations with 5,000 ground motions per design, minimizing the influence of statistical uncertainty. Across all cases, differences in expected repair costs were within 8%, confirming that the metamodels provide reliable approximations of the true loss behavior.
- The proposed methodology significantly reduces computational effort, requiring more than 200 times fewer nonlinear dynamic FE model evaluations compared to a direct optimization approach.

The proposed framework was also applied in two additional case studies by modifying the FE model in OpenSees to represent an irregular steel structure, indicating that BRBs also constitute an effective retrofit strategy for this type of structure.

Beyond the treatment of statistical uncertainty in the lognormal EDP parameters adopted in the second case study, a complementary analysis was conducted to explicitly represent the seismic uncertainty associated with record-to-record variability. To this end, the proposed Stratified Stochastic Emulator framework introduced the use of a stochastic emulator in which the structural responses are modeled as random variables conditioned on the non-collapse state of the structure. Instead of assuming a predefined distributional form for the EDPs, the stochastic emulator captures their full probability distribution by propagating both the input randomness and an artificial latent variable representing the intrinsic simulator noise. This approach enables a non-parametric characterization of the EDP distributions, avoiding restrictive assumptions and allowing the representation of complex behaviors that naturally arise in nonlinear dynamic analysis.

To improve the sampling efficiency under seismic excitation, a Stratified Sampling (SS) scheme was adopted to partition the hazard input space into strata. This strategy ensures an enhanced representation of the upper tail of the hazard space, which is particularly relevant for performance-based analysis. The stochastic emulator associated with each stratum was trained using responses obtained from NLTHA with samples associated with each stratum, significantly decreasing the computational cost.

The results obtained from this third framework lead to the following conclusions:

- The combination of stochastic emulators with stratified sampling successfully captured the probability distributions of the EDPs across the hazard strata, while requiring approximately five times fewer nonlinear dynamic analyses than a conventional Monte Carlo–based approach.
- The trained emulators presented good agreement with the reference distributions, accurately reproducing the mean trends and dispersion of the structural responses. The CCDFs and survival curves obtained from the SPCEs were consistent with the reference results, particularly in the non-collapse range, even when trained with a substantially reduced number of samples per stratum.
- The stochastic emulator occasionally produced response realizations outside the survival domain, despite being trained exclusively with non-collapse data. This result highlights the influence of the noise term incorporated in the emulator formulation.
- Overall, the combination of stratified sampling and stochastic emulation constitutes an efficient approach for approximating conditional response distributions.

Together, these contributions demonstrate that stochastic emulators offer a promising path toward further reducing the computational burden associated with PBEE, while retaining the ability to represent complex response distributions and providing a flexible basis for risk assessment and optimization.

8.1 Directions for Future Research

Future research should focus on the continued development of computational strategies capable of reducing the computational cost of optimization problems within the PBE framework for natural hazards. Such advances would enable the inclusion of a larger number of design variables and, consequently, a more comprehensive exploration of the design space. Another important direction involves incorporating practical design constraints, aligning the optimization problem more closely with conventional engineering practices. This would promote more economical and constructable solutions that can withstand natural hazards adequately while minimizing expected repair costs.

REFERENCES

AISC. ANSI/AISC 341-05: Seismic provisions for structural steel buildings. **American Institute of Steel Construction**, Chicago, IL, USA, 2005.

AISC. ANSI/AISC 341-10: Seismic provisions for structural steel buildings. **American Institute of Steel Construction**, Chicago, IL, USA, 2010.

AISC. ANSI/AISC 341-22: Seismic provisions for structural steel buildings. **American Institute of Steel Construction**, Chicago, IL, USA, 2022.

AISC. ANSI/AISC 360-22: Specification for structural steel buildings. **American Institute of Steel Construction**, Chicago, IL, USA, 2022.

ALMEIDA, A. A. D. *et al.* Probabilistic seismic hazard analysis for a nuclear power plant site in southeast brazil. **Journal of Seismology**, v. 23, p. 1–23, 2019.

ALVES, F. **Estudo de sismicidade do Brasil para revisão da ABNT NBR 15421**. 2020. Dissertação (Mestrado) — Universidade Federal do Rio de Janeiro, 2020.

ALVES, F. V.; SANTOS, S. H. C. Abalos mapeados. **Revista Estrutura**, v. 10, p. 29–33, 2021.

ANCHETA, T. D. *et al.* NGA-West2 database. **Earthquake Spectra**, v. 30, n. 3, p. 989–1005, 2014.

ANDRADE, R. B. **Análise de sensibilidade sobre a fragilidade sísmica de um edifício de concreto armado brasileiro**. 2021. Dissertação (Mestrado) — Universidade Estadual de Campinas, 2021.

ANDRADE, R. B. *et al.* Seismic fragility assessment for a rc building in seismically stable brazil: A sensitivity analysis. **Journal of Building Engineering**, v. 60, p. 105184, 2022.

AOUES, Y.; CHATEAUNEUF, A. Benchmark study of numerical methods for reliability-based design optimization. **Structural and multidisciplinary optimization**, v. 41, n. 2, p. 277–294, 2010.

ARORA, J. **Introduction to optimum design**. New York: Elsevier, 2012.

ARROYO, O.; LIEL, A. B. A call to refocus research goals for the development of seismic optimization methods. **Earthquake Spectra**, v. 33, n. 3, p. 1029–1031, 2017.

ARUNACHALAM, S.; SPENCE, S. M. J. Reliability-based collapse assessment of wind-excited steel structures within performance-based wind engineering. **Journal of Structural Engineering**, v. 148, n. 9, p. 04022132, 2022.

ARUNACHALAM, S.; SPENCE, S. M. J. An efficient stratified sampling scheme for the simultaneous estimation of small failure probabilities in wind engineering applications. **Structural Safety**, v. 101, p. 102310, 2023a.

ARUNACHALAM, S.; SPENCE, S. M. J. Generalized stratified sampling for efficient reliability assessment of structures against natural hazards. **Journal of Engineering Mechanics**, v. 149, n. 7, p. 04023042, 2023b.

ASCE. ASCE/SEI 7-05: Minimum design loads for buildings and other structures. **American Society of Civil Engineers**, Reston, VA, USA:, 2005.

ASCE. ASCE/SEI 7-10: Minimum design loads for buildings and other structures. **American Society of Civil Engineers**, Reston, VA, USA:, 2013.

ASCE. ASCE/SEI 41-17: Seismic evaluation and retrofit of existing buildings. **American Society of Civil Engineers**, Reston, VA, USA:, 2017a.

ASCE. ASCE/SEI 7-16: Minimum design loads for buildings and other structures. **American Society of Civil Engineers**, Reston, VA, USA:, 2017b.

ASSOCIAÇÃO BRASILEIRA DE NORMAS TÉCNICAS. **NBR 15421/2006: Projeto de estruturas resistentes a sismos - Procedimento**. Rio de Janeiro: ABNT, 2006.

ASSOCIAÇÃO BRASILEIRA DE NORMAS TÉCNICAS. **NBR 6118/2014: Projeto de estruturas de concreto - procedimento**. Rio de Janeiro: ABNT, 2014.

ASSOCIAÇÃO BRASILEIRA DE NORMAS TÉCNICAS. **NBR 6120/2019: Cargas para o cálculo de estruturas de edificações**. Rio de Janeiro: ABNT, 2019.

ASSOCIAÇÃO BRASILEIRA DE NORMAS TÉCNICAS. **NBR 7480/2022: Aço destinado às armaduras para estruturas de concreto armado - Requisitos**. Rio de Janeiro: ABNT, 2022.

ASSOCIAÇÃO BRASILEIRA DE NORMAS TÉCNICAS. **NBR 15421/2023: Projeto de estruturas resistentes a sismos - Procedimento**. Rio de Janeiro: ABNT, 2023.

ASSUMPÇÃO, M. *et al.* Intraplate seismicity in brazil. *In*: TALWANI, P. (ed.). **Intraplate Earthquakes**. Cambridge: Cambridge University Press, 2014. cap. 4, p. 50–71.

ASSUMPÇÃO, M. d. S. *et al.* Terremotos no brasil: preparando-se para eventos raros. **Boletim SBGf**, n. 96, p. 25–29, 2016.

ASTM. ASTM A500: Standard specification for cold-formed welded and seamless carbon steel structural tubing in rounds and shapes. **American Society for Testing and Materials**, West Conshohocken, PA, USA, 2007.

ATC. ATC 40: Seismic Evaluation and Retrofit of Concrete Buildings. **Applied Technology Council**, Redwood City, CA, USA:, 1996.

ATC. Performance assessment calculation tool (PACT). **Applied Technology Council**, Washington, DC, USA:, 2018.

ATKINSON, G. M.; SILVA, W. Stochastic modeling of california ground motions. **Bulletin of the Seismological Society of America**, v. 90, n. 2, p. 255–274, 2000.

AY, B. Ö.; FOX, M. J.; SULLIVAN, T. J. Practical challenges facing the selection of conditional spectrum-compatible accelerograms. **Journal of Earthquake Engineering**, v. 21, n. 1, p. 169–180, 2017.

BAIRD, B. W.; LIEL, A. B.; CHASE, R. E. Magnitude thresholds and spatial footprints of damage from induced earthquakes. **Earthquake Spectra**, v. 36, n. 4, p. 1995–2018, 2020.

BAKER, J. W. Conditional mean spectrum: Tool for ground-motion selection. **Journal of Structural Engineering**, v. 137, n. 3, p. 322–331, 2011.

BAKER, J. W. Efficient analytical fragility function fitting using dynamic structural analysis. **Earthquake Spectra**, v. 31, n. 1, p. 579–599, 2015.

BAKER, J. W.; CORNELL, C. A. A vector-valued ground motion intensity measure consisting of spectral acceleration and epsilon. **Earthquake Engineering & Structural Dynamics**, v. 34, n. 10, p. 1193–1217, 2005.

BAKER, J. W.; CORNELL, C. A. Spectral shape, epsilon and record selection. **Earthquake Engineering & Structural Dynamics**, v. 35, n. 9, p. 1077–1095, 2006.

BALTZOPOULOS, G.; BARASCHINO, R.; IERVOLINO, I. On the number of records for structural risk estimation in PBEE. **Earthquake Engineering & Structural Dynamics**, v. 48, n. 5, p. 489–506, 2019.

BARTLETT, M. S. Properties of sufficiency and statistical tests. **Proceedings of the Royal Society of London. Series A-Mathematical and Physical Sciences**, v. 160, n. 901, p. 268–282, 1937.

BASIM, M. C.; ESTEKANCHI, H. E. Application of endurance time method in performance-based optimum design of structures. **Structural safety**, v. 56, p. 52–67, 2015.

BAZZURRO, P.; CORNELL, C. A. Disaggregation of seismic hazard. **Bulletin of the Seismological Society of America**, v. 89, n. 2, p. 501–520, 1999.

BECK, A. T. Optimal design of redundant structural systems: fundamentals. **Engineering Structures**, v. 219, p. 110542, 2020.

BECK, A. T. **Confiabilidade e segurança das estruturas**. Florianópolis: Orsa Maggiore, 2024.

BECK, A. T.; BOSSE, R. M.; RODRIGUES, I. D. On the ergodicity assumption in performance-based engineering. **Structural Safety**, v. 97, p. 102218, 2022.

BECK, A. T.; GOMES, W. J.; BAZÁN, F. A. On the robustness of structural risk optimization with respect to epistemic uncertainties. **International Journal for Uncertainty Quantification**, v. 2, n. 1, 2012.

BECK, A. T. *et al.* A comparison between robust and risk-based optimization under uncertainty. **Structural and Multidisciplinary Optimization**, v. 52, p. 479–492, 2015.

BECK, A. T.; GOMES, W. J. de S. A comparison of deterministic, reliability-based and risk-based structural optimization under uncertainty. **Probabilistic Engineering Mechanics**, v. 28, p. 18–29, 2012.

BECK, A. T.; KOUGIOUMTZOGLOU, I. A.; SANTOS, K. R. D. Optimal performance-based design of non-linear stochastic dynamical rc structures subject to stationary wind excitation. **Engineering structures**, v. 78, p. 145–153, 2014.

BERVEILLER, M.; SUDRET, B.; LEMAIRE, M. Stochastic finite element: a non intrusive approach by regression. **European Journal of Computational Mechanics/Revue Européenne de Mécanique Numérique**, v. 15, n. 1-3, p. 81–92, 2006.

BEYER, K.; BOMMER, J. J. Selection and scaling of real accelerograms for bi-directional loading: a review of current practice and code provisions. **Journal of earthquake engineering**, v. 11, n. S1, p. 13–45, 2007.

BLATMAN, G.; SUDRET, B. An adaptive algorithm to build up sparse polynomial chaos expansions for stochastic finite element analysis. **Probabilistic Engineering Mechanics**, v. 25, n. 2, p. 183–197, 2010.

BOBBY, S. *et al.* Performance-based topology optimization for wind-excited tall buildings: A framework. **Engineering Structures**, v. 74, p. 242–255, 2014.

BOBBY, S.; SPENCE, S. M.; KAREEM, A. Data-driven performance-based topology optimization of uncertain wind-excited tall buildings. **Structural and Multidisciplinary Optimization**, v. 54, n. 6, p. 1379–1402, 2016.

BOMMER, J.; SCOTT, S.; SARMA, S. Hazard-consistent earthquake scenarios. **Soil Dynamics and Earthquake Engineering**, v. 19, n. 4, p. 219–231, 2000.

BOMMER, J. J.; ACEVEDO, A. B. The use of real earthquake accelerograms as input to dynamic analysis. **Journal of Earthquake Engineering**, v. 8, n. spec01, p. 43–91, 2004.

BOMMER, J. J.; STAFFORD, P. J.; ALARCÓN, J. E. Empirical equations for the prediction of the significant, bracketed, and uniform duration of earthquake ground motion. **Bulletin of the Seismological Society of America**, v. 99, n. 6, p. 3217–3233, 2009.

BOORE, D. M. Simulation of ground motion using the stochastic method. **Pure and applied geophysics**, v. 160, p. 635–676, 2003.

BOORE, D. M.; JOYNER, W. B. Site amplifications for generic rock sites. **Bulletin of the seismological society of America**, v. 87, n. 2, p. 327–341, 1997.

BORGES, R. G. *et al.* Seismicity and seismic hazard in the continental margin of southeastern brazil. **Journal of Seismology**, v. 24, p. 1205–1224, 2020.

BOSSE, R. M. *et al.* Seismic vulnerability of steel tubular structures based on local buckling driving variables. *In*: **Proceedings of XLV Ibero-Latin American Congress on Computational Methods in Engineering (CILAMCE)**. [*S.l.: s.n.*], 2024b.

BOSSE, R. M. *et al.* Collapse mechanisms and fragility curves based on lumped damage mechanics for RC frames subjected to earthquakes. **Engineering Structures**, v. 311, p. 118115, 2024a.

BRADLEY, B. A. A critical examination of seismic response uncertainty analysis in earthquake engineering. **Earthquake engineering & structural dynamics**, v. 42, n. 11, p. 1717–1729, 2013.

BRUSCHI, E.; CALVI, P. M.; QUAGLINI, V. Concentrated plasticity modelling of rc frames in time-history analyses. **Engineering Structures**, v. 243, p. 112716, 2021.

BUDNITZ, R. J. and APOSTOLAKIS, G. and BOORE, David M. **Recommendations for probabilistic seismic hazard analysis: guidance on uncertainty and use of experts**. Livermore: Lawrence Livermore National Laboratory, 1997. (NUREG-CR-6372 UCRL-ID-122160, v.2).

CAO, X.-Y.; FENG, D.-C.; BEER, M. Consistent seismic hazard and fragility analysis considering combined capacity-demand uncertainties via probability density evolution method. **Structural Safety**, v. 103, p. 102330, 2023.

CARTWRIGHT, H. (ed.). **Artificial neural networks**. New York: Springer, 2015. v. 1260.

CAVALCANTE, G. H. F. *et al.* Seismic fragility assessment of typical bridges in northeastern brazil. **Latin American Journal of Solids and Structures**, v. 19, n. 5, p. e457, 2022.

CHAN, C.-M.; ZOU, X.-K. Elastic and inelastic drift performance optimization for reinforced concrete buildings under earthquake loads. **Earthquake Engineering & Structural Dynamics**, v. 33, n. 8, p. 929–950, 2004.

CHOI, S.-K.; GRANDHI, R.; CANFIELD, R. A. **Reliability-based structural design**. London: Springer, 2006.

CHUN, J. Active learning-based kriging model with noise responses and its application to reliability analysis of structures. **Applied Sciences**, v. 14, n. 2, p. 882, 2024.

COCHRAN, W. G. **Sampling Techniques**. New York: John Wiley & Sons, 2007.

CORNELL, C. A. *et al.* Probabilistic basis for 2000 sac federal emergency management agency steel moment frame guidelines. **Journal of structural engineering**, v. 128, n. 4, p. 526–533, 2002.

CORNELL, C. A.; KRAWINKLER, H. Progress and challenges in seismic performance assessment. **PEER Center News 3, no. 2**, 2000.

DERAKHSHAN, H. *et al.* Seismic fragility assessment of nonstructural components in unreinforced clay brick masonry buildings. **Earthquake Engineering & Structural Dynamics**, v. 49, n. 3, p. 285–300, 2020.

DUBOURG, V. **Adaptive surrogate models for reliability analysis and reliability-based design optimization**. 2011. Tese (Doutorado) — Université Blaise Pascal-Clermont-Ferrand II, 2011.

ELKADY, A. **Collapse risk assessment of steel moment resisting frames designed with deep wide-flange columns in seismic regions**. 2016. Tese (Doutorado) — Dept. of Civil Engineering and Applied Mechanics, McGill University, 2016.

ELKADY, A.; LIGNOS, D. G. Modeling of the composite action in fully restrained beam-to-column connections: implications in the seismic design and collapse capacity of steel special moment frames. **Earthquake Engineering & Structural Dynamics**, v. 43, n. 13, p. 1935–1954, 2014.

ELKADY, A.; LIGNOS, D. G. Effect of gravity framing on the overstrength and collapse capacity of steel frame buildings with perimeter special moment frames. **Earthquake Engineering & Structural Dynamics**, v. 44, n. 8, p. 1289–1307, 2015.

ELKADY, A.; LIGNOS, D. G. Two-dimensional opensees numerical models for archetype steel buildings with special moment frames. **GitHub repository**, 2019.

ELLINGWOOD, B. R. Earthquake risk assessment of building structures. **Reliability Engineering & System Safety**, v. 74, n. 3, p. 251–262, 2001.

ELNASHAI, A. S.; SARNO, L. D. **Fundamentals of earthquake engineering**. Hoboken: Wiley Online Library, 2008.

EUROPEAN COMMITTEE FOR STANDARDIZATION. **EN 1998-1: Eurocode 8: Design of structures for earthquake resistance – Part 1: General rules, seismic actions and rules for buildings**. Brussels: European Committee for Standardisation, 2004.

FARDIS, M. N.; BISKINIS, D. E. Deformation capacity of RC members, as controlled by flexure or shear. *In*: **Otani Symposium**. [*S.l.: s.n.*], 2003. v. 511530.

FATTAHI, F.; GHOLIZADEH, S. Seismic fragility assessment of optimally designed steel moment frames. **Engineering Structures**, v. 179, p. 37–51, 2019.

FEMA. FEMA 350: Recommended Seismic Design Criteria for New Steel Moment-Frame Buildings. **Federal Emergency Management Agency**, Washington, DC, USA:, 2000.

FEMA. FEMA 356: Prestandard and Commentary for the Seismic Rehabilitation of Buildings. **Federal Emergency Management Agency**, Washington, DC, USA:, 2000.

FEMA. FEMA P695, Quantification of Building Seismic Performance Factors. **Federal Emergency Management Agency**, Washington, DC, USA:, 2009.

FEMA. FEMA P-58, seismic performance assessment of buildings - methodology. **Federal Emergency Management Agency**, Washington, DC, USA:, v. 1, 2012.

FEMA. FEMA P-58, seismic performance assessment of buildings - methodology. **Federal Emergency Management Agency**, Washington, DC, USA:, v. 1, 2018.

FEMA. Hazus 5.1 - earthquake model technical manual. **Federal Emergency Management Agency**, Washington, DC, USA:, 2022a.

FEMA. Hazus 6.0 - inventory technical manual. **Federal Emergency Management Agency**, Washington, DC, USA:, 2022b.

FILIPPOU, F. C.; POPOV, E. P.; BERTERO, V. V. **Effects of bond deterioration on hysteretic behavior of reinforced concrete joints**. Berkeley: Earthquake Engineering Research Center, University of California, College of Engineering, 1983. (Report nº UCB/EERC/19, August 1983).

FONSÊCA, J.; NASCIMENTO, A. F. do; LASOCKI, S. Probabilistic seismic hazard analysis for ne brazil. **Bulletin of Earthquake Engineering**, p. 1–21, 2025.

FRAGIADAKIS, M.; LAGAROS, N. D. An overview to structural seismic design optimisation frameworks. **Computers & Structures**, v. 89, n. 11-12, p. 1155–1165, 2011.

FRAGIADAKIS, M.; LAGAROS, N. D.; PAPADRAKAKIS, M. Performance-based earthquake engineering using structural optimisation tools. **International Journal of Reliability and Safety**, v. 1, n. 1-2, p. 59–76, 2006a.

FRAGIADAKIS, M.; LAGAROS, N. D.; PAPADRAKAKIS, M. Performance-based multiobjective optimum design of steel structures considering life-cycle cost. **Structural and Multidisciplinary Optimization**, v. 32, n. 1, p. 1–11, 2006b.

FRAGIADAKIS, M.; PAPADRAKAKIS, M. Performance-based optimum seismic design of reinforced concrete structures. **Earthquake Engineering & Structural Dynamics**, v. 37, n. 6, p. 825–844, 2008.

FRAGIADAKIS, M. *et al.* Seismic assessment of structures and lifelines. **Journal of Sound and Vibration**, v. 334, p. 29–56, 2015.

FRANGOPOL, D. M. Structural optimization using reliability concepts. **Journal of Structural Engineering**, v. 111, n. 11, p. 2288–2301, 1985.

GANZERLI, S.; PANTELIDES, C.; REAVELEY, L. Performance-based design using structural optimization. **Earthquake engineering & structural dynamics**, v. 29, n. 11, p. 1677–1690, 2000.

GHASEMOF, A.; MIRTAHERI, M.; MOHAMMADI, R. K. Multi-objective optimization for probabilistic performance-based design of buildings using fema p-58 methodology. **Engineering Structures**, v. 254, p. 113856, 2022.

GHASEMOF, A. *et al.* Multi-objective optimal design of steel mrf buildings based on life-cycle cost using a swift algorithm. **Structures**, v. 34, p. 4041–4059, 2021.

GHOLIZADEH, S.; ALIGHOLIZADEH, V. Reliability-based optimum seismic design of rc frames by a metamodel and metaheuristics. **The Structural Design of Tall and Special Buildings**, v. 28, n. 1, p. e1552, 2019.

GHOLIZADEH, S.; EBADIJALAL, M. Performance based discrete topology optimization of steel braced frames by a new metaheuristic. **Advances in Engineering Software**, v. 123, p. 77–92, 2018.

GHOLIZADEH, S. *et al.* On the seismic collapse capacity of optimally designed steel braced frames. **Engineering with Computers**, v. 38, n. 2, p. 985–997, 2022.

GHOLIZADEH, S.; MOHAMMADI, M. Reliability-based seismic optimization of steel frames by metaheuristics and neural networks. **ASCE-ASME Journal of Risk and Uncertainty in Engineering Systems, Part A: Civil Engineering**, v. 3, n. 1, p. 04016013, 2017.

GHOLIZADEH, S.; POORHOSEINI, H. Seismic layout optimization of steel braced frames by an improved dolphin echolocation algorithm. **Structural and Multidisciplinary Optimization**, v. 54, n. 4, p. 1011–1029, 2016.

GIDARIS, I.; TAFLANIDIS, A. A. Performance assessment and optimization of fluid viscous dampers through life-cycle cost criteria and comparison to alternative design approaches. **Bulletin of Earthquake Engineering**, v. 13, p. 1003–1028, 2015.

GIDARIS, I.; TAFLANIDIS, A. A.; MAVROEIDIS, G. P. Kriging metamodeling in seismic risk assessment based on stochastic ground motion models. **Earthquake Engineering & Structural Dynamics**, v. 44, n. 14, p. 2377–2399, 2015.

GIOVANIS, D. G.; TAFLANIDIS, A.; SHIELDS, M. D. Accelerating uncertainty quantification in incremental dynamic analysis using dimension reduction-based surrogate modeling. **Bulletin of Earthquake Engineering**, v. 23, n. 1, p. 391–410, 2025.

GIULIANI, G. *et al.* Seismic fragility curves of steel frames equipped with easily repairable dissipative devices. **ce/papers - Proceedings in Civil Engineering**, v. 5, n. 4, p. 720–728, 2022.

GODA, K.; ZHANG, L.; TESFAMARIAM, S. Portfolio seismic loss estimation and risk-based critical scenarios for residential wooden houses in victoria, british columbia, and canada. **Risk analysis**, v. 41, n. 6, p. 1019–1037, 2021.

GOULET, C. A. *et al.* Evaluation of the seismic performance of a code-conforming reinforced-concrete frame building—from seismic hazard to collapse safety and economic losses. **Earthquake Engineering & Structural Dynamics**, v. 36, n. 13, p. 1973–1997, 2007.

GU, Q. *et al.* Effect of buckling-restrained brace model parameters on seismic structural response. **Journal of Constructional Steel Research**, v. 98, p. 100–113, 2014.

GUERRERO, H. *et al.* Evaluation of the economic benefits of using buckling-restrained braces in hospital structures located in very soft soils. **Engineering Structures**, v. 136, p. 406–419, 2017.

GUPTA, A.; KRAWINKLER, H. **Seismic Demands for the Performance Evaluation of Steel Moment Resisting Frame Structures**. Stanford, CA, 1999.

GUTENBERG, B.; RICHTER, C. F. Frequency of earthquakes in california. **Bulletin of the Seismological society of America**, v. 34, n. 4, p. 185–188, 1944.

GWALANI, P.; SINGH, Y.; VARUM, H. Seismic vulnerability of reinforced concrete buildings with discontinuity in columns. **Earthquake Engineering & Structural Dynamics**, 2023.

HAO, P. *et al.* A novel nested stochastic kriging model for response noise quantification and reliability analysis. **Computer Methods in Applied Mechanics and Engineering**, v. 384, p. 113941, 2021.

HASELTON, C.; DEIERLEIN, G. G. Assessing Seismic Collapse Safety of Modern Reinforced Concrete Moment-Frame Buildings. **Pacific Earthquake Engineering Research Center**, v. 08, n. February, p. 295, 2008.

HASELTON, C. B. *et al.* Seismic collapse safety of reinforced concrete buildings. i: Assessment of ductile moment frames. **Journal of Structural Engineering**, v. 137, n. 4, p. 481–491, 2011.

HASELTON, C. B. *et al.* Calibration of model to simulate response of reinforced concrete beam-columns to collapse. **ACI Structural Journal**, v. 113, n. 6, p. 1141–1152, nov 2016.

HASSANZADEH, A.; MORADI, S.; BURTON, H. V. Performance-based design optimization of structures: State-of-the-art review. **Journal of Structural Engineering**, v. 150, n. 8, p. 03124001, 2024a.

HASSANZADEH, A.; MORADI, S.; BURTON, H. V. Performance-based optimum seismic design of self-centering steel moment frames with sma-based connections. **Earthquake Engineering & Structural Dynamics**, v. 53, n. 5, p. 1905–1929, 2024b.

HILTON, H. H.; FEIGEN, M. Minimum weight analysis based on structural reliability. **Journal of the Aerospace Sciences**, v. 27, n. 9, p. 641–652, 1960.

HOLLAND, J. H. **Adaptation in natural and artificial systems: an introductory analysis with applications to biology, control, and artificial intelligence**. Cambridge: MIT Press, 1992.

HSIAO, P.-C.; LEHMAN, D. E.; ROEDER, C. W. A model to simulate special concentrically braced frames beyond brace fracture. **Earthquake engineering & structural dynamics**, v. 42, n. 2, p. 183–200, 2013.

HUAN, X.; MARZOUK, Y. M. Simulation-based optimal bayesian experimental design for nonlinear systems. **Journal of Computational Physics**, v. 232, n. 1, p. 288–317, 2013.

HURTADO, J.; BARBAT, A. H. Monte carlo techniques in computational stochastic mechanics. **Archives of Computational Methods in Engineering**, v. 5, n. 1, p. 3, 1998.

HWANG, S.-H.; LIGNOS, D. G. Effect of modeling assumptions on the earthquake-induced losses and collapse risk of steel-frame buildings with special concentrically braced frames. **Journal of Structural Engineering**, v. 143, n. 9, p. 04017116, 2017.

IBARRA, L. F.; MEDINA, R. A.; KRAWINKLER, H. Hysteretic models that incorporate strength and stiffness deterioration. **Earthquake engineering & structural dynamics**, v. 34, n. 12, p. 1489–1511, 2005.

INSTITUTO BRASILEIRO DE GEOGRAFIA E ESTATÍSTICA. **SINAPI - Sistema nacional de pesquisa de custos e índices da construção civil**. [*S.l.: s.n.*]: Caixa Economica Federal, 2023.

INSTITUTO DE ASTRONOMIA, GEOFÍSICA E CIÊNCIAS ATMOSFÉRICAS - USP. **Seismological Database**. 2024. Accessed on: Oct. 13, 2025. Available at: https://moho.iag.usp.br/.

ISHIGAMI, T.; HOMMA, T. An importance quantification technique in uncertainty analysis for computer models. *In*: IEEE. **[1990] Proceedings. First international symposium on uncertainty modeling and analysis**. [*S.l.: s.n.*], 1990. p. 398–403.

JALAYER, F.; CORNELL, C. Alternative non-linear demand estimation methods for probability-based seismic assessments. **Earthquake Engineering & Structural Dynamics**, v. 38, n. 8, p. 951–972, 2009.

JALAYER, F.; EBRAHIMIAN, H.; MIANO, A. Record-to-record variability and code-compatible seismic safety-checking with limited number of records. **Bulletin of Earthquake Engineering**, v. 19, n. 15, p. 6361–6396, 2021.

JALAYER, F. *et al.* Analytical fragility assessment using unscaled ground motion records. **Earthquake Engineering & Structural Dynamics**, v. 46, n. 15, p. 2639–2663, 2017.

JOHNSON, K. *et al.* **Global Earthquake Model (GEM) Seismic Hazard Map (version 2023.1 - June 2023)**. 2023. Zenodo. Available at: https://doi.org/10.5281/zenodo.8409647. Accessed on: 01 October 2025.

JONES, D. R.; SCHONLAU, M.; WELCH, W. J. Efficient global optimization of expensive black-box functions. **Journal of Global optimization**, v. 13, n. 4, p. 455–492, 1998.

JOYNER, M. D. *et al.* Resilience-based seismic design of buildings through multiobjective optimization. **Engineering Structures**, v. 246, p. 113024, 2021.

KALABA, R. Design of minimal-weight structures for given reliability and cost. **Journal of the Aerospace Sciences**, v. 29, n. 3, p. 355–356, 1962.

KALAGNANAM, J. R.; DIWEKAR, U. M. An efficient sampling technique for off-line quality control. **Technometrics**, v. 39, n. 3, p. 308–319, 1997.

KARAMANCI, E.; LIGNOS, D. G. Computational approach for collapse assessment of concentrically braced frames in seismic regions. **Journal of Structural Engineering**, v. 140, n. 8, p. A4014019, 2014.

KARAMLOU, A.; BOCCHINI, P. Computation of bridge seismic fragility by large-scale simulation for probabilistic resilience analysis. **Earthquake Engineering & Structural Dynamics**, v. 44, n. 12, p. 1959–1978, 2015.

KAVEH, A.; LAKNEJADI, K.; ALINEJAD, B. Performance-based multi-objective optimization of large steel structures. **Acta Mechanica**, v. 223, n. 2, p. 355–369, 2012.

KENNEDY, R. P. *et al.* Probabilistic seismic safety study of an existing nuclear power plant. **Nuclear engineering and design**, v. 59, n. 2, p. 315–338, 1980.

KIM, J.; WANG, Z. Uncertainty quantification for seismic response using dimensionality reduction-based stochastic simulator. **Earthquake Engineering & Structural Dynamics**, v. 54, n. 2, p. 471–490, 2025.

KIUREGHIAN, A. D. Non-ergodicity and peer's framework formula. **Earthquake engineering & structural dynamics**, v. 34, n. 13, p. 1643–1652, 2005.

KLEINGESINDS, S.; LAVAN, O. Bi-tuned semi-active tmds: Multi-hazard design for tall buildings using gradient-based optimization. **Structural Control and Health Monitoring**, v. 29, n. 3, p. e2901, 2022.

KLEINMAN, N. L.; SPALL, J. C.; NAIMAN, D. Q. Simulation-based optimization with stochastic approximation using common random numbers. **Management Science**, v. 45, n. 11, p. 1570–1578, 1999.

KRAWINKLER, H. Shear in beam-column joints in seismic design of steel frames. **Engineering Journal**, v. 15, n. 3, p. 82–91, 1978.

KRAWINKLER, H. Challenges and progress in performance-based earthquake engineering. *In*: **International Seminar on Seismic Engineering for Tomorrow–In Honor of Professor Hiroshi Akiyama**. [*S.l.: s.n.*], 1999. v. 26.

KRAWINKLER, H.; MEDINA, R.; ALAVI, B. Seismic drift and ductility demands and their dependence on ground motions. **Engineering structures**, v. 25, n. 5, p. 637–653, 2003.

KRAWINKLER, H.; SENEVIRATNA, G. Pros and cons of a pushover analysis of seismic performance evaluation. **Engineering structures**, v. 20, n. 4-6, p. 452–464, 1998.

KRIGE, D. G. A statistical approach to some basic mine valuation problems on the witwatersrand. **Journal of the Southern African Institute of Mining and Metallurgy**, v. 52, n. 6, p. 119–139, 1951.

KROETZ, H. M. **Meta-modelagem em confiabilidade estrutural**. 2015. Dissertação (Mestrado) — Universidade de São Paulo, 2015.

KYPRIOTI, A. P.; TAFLANIDIS, A. A. Kriging metamodeling for seismic response distribution estimation. **Earthquake Engineering & Structural Dynamics**, v. 50, n. 13, p. 3550–3576, 2021.

LALLEMANT, D.; KIREMIDJIAN, A.; BURTON, H. Statistical procedures for developing earthquake damage fragility curves. **Earthquake Engineering & Structural Dynamics**, v. 44, n. 9, p. 1373–1389, 2015.

LATANIOTIS, C.; MARELLI, S.; SUDRET, B. The gaussian process modelling module in uqlab. **Journal of Soft Computing in Civil Engineering**, 2018.

LATANIOTIS, C. *et al.* **UQLab user manual – Kriging (Gaussian process modeling)**. Zurich: Chair of Risk, Safety and Uncertainty Quantification, ETH Zurich, Switzerland, 2024. Report UQLab-V2.1-105.

LECUN, Y.; BENGIO, Y.; HINTON, G. Deep learning. **Nature**, v. 521, n. 7553, p. 436–444, 2015.

LI, B.; SPENCE, S. M. Metamodeling through deep learning of high-dimensional dynamic nonlinear systems driven by general stochastic excitation. **Journal of Structural Engineering**, v. 148, n. 11, p. 04022186, 2022.

LI, B.; SPENCE, S. M. Deep learning enabled rapid nonlinear time history wind performance assessment. **Structures**, v. 66, p. 106810, 2024.

LI, C.; GUO, Y.; KUNNATH, S. Direct economic loss-based seismic design using genetic algorithm. **Earthquake Engineering & Structural Dynamics**, v. 54, n. 4, p. 1125–1140, 2025.

LIEL, A. B. **Assessing the collapse risk of California's existing reinforced concrete frame structures: Metrics for seismic safety decisions**. 2008. Tese (Doutorado) — Stanford University, 2008.

LIEL, A. B.; HASELTON, C. B.; DEIERLEIN, G. G. Seismic collapse safety of reinforced concrete buildings. ii: Comparative assessment of nonductile and ductile moment frames. **Journal of Structural Engineering**, v. 137, n. 4, p. 492–502, 2011.

LIEU, Q. X.; DO, D. T.; LEE, J. An adaptive hybrid evolutionary firefly algorithm for shape and size optimization of truss structures with frequency constraints. **Computers & Structures**, v. 195, p. 99–112, 2018.

LIGNOS, D. *et al.* Numerical and experimental evaluation of seismic capacity of high-rise steel buildings subjected to long duration earthquakes. **Computers & Structures**, v. 89, n. 11-12, p. 959–967, 2011.

LIGNOS, D. G.; KRAWINKLER, H. Deterioration modeling of steel components in support of collapse prediction of steel moment frames under earthquake loading. **Journal of Structural Engineering**, v. 137, n. 11, p. 1291–1302, 2011.

LIGNOS, D. G.; KRAWINKLER, H. **Sidesway Collapse of Deteriorating Structural Systems under Seismic Excitations**. Stanford, CA, 2012.

LOEPPKY, J. L.; SACKS, J.; WELCH, W. J. Choosing the sample size of a computer experiment: A practical guide. **Technometrics**, v. 51, n. 4, p. 366–376, 2009.

LOPEZ, R. H.; SANTOS, K. R. dos; MIGUEL, L. F. F. An efficient approach for taking into account uncertainties in structural parameters in performance-based design optimization. **Engineering Structures**, v. 336, p. 120382, 2025.

LUCO, N.; BAZZURRO, P. Does amplitude scaling of ground motion records result in biased nonlinear structural drift responses? **Earthquake Engineering & Structural Dynamics**, v. 36, n. 13, p. 1813–1835, 2007.

LUCO, N.; CORNELL, C. A. Structure-specific scalar intensity measures for near-source and ordinary earthquake ground motions. **Earthquake Spectra**, v. 23, n. 2, p. 357–392, 2007.

LUIZ, C. B. **Otimização topológica de treliças hiperestáticas considerando incertezas**. 2020. Dissertação (Mestrado) — Universidade de São Paulo, 2020.

LÜTHEN, N. *et al.* **UQLab user manual – Generalized Lambda Model**. Zurich: Chair of Risk, Safety and Uncertainty Quantification, ETH Zurich, Switzerland, 2024. Report UQLab-V2.1-120.

LÜTHEN, N. *et al.* **UQLab user manual – Stochastic polynomial chaos expansions (SPCE)**. Zurich: Chair of Risk, Safety and Uncertainty Quantification, ETH Zurich, Switzerland, 2024. Report UQLab-V2.1-121.

MAI, C.; KONAKLI, K.; SUDRET, B. Seismic fragility curves for structures using non-parametric representations. **Frontiers of Structural and Civil Engineering**, v. 11, n. 2, p. 169–186, 2017.

MALLAT, S. **A wavelet tour of signal processing**. New York: Elsevier, 2009.

MANZO, N. R.; VASSILIOU, M. F. Displacement-based analysis and design of rocking structures. **Earthquake Engineering & Structural Dynamics**, v. 48, n. 14, p. 1613–1629, 2019.

MARELLI, S.; SUDRET, B. An active-learning algorithm that combines sparse polynomial chaos expansions and bootstrap for structural reliability analysis. **Structural Safety**, v. 75, p. 67–74, 2018.

MATHERON, G. Principles of geostatistics. **Economic geology**, v. 58, n. 8, p. 1246–1266, 1963.

MATHERON, G. The intrinsic random functions and their applications. **Advances in applied probability**, v. 5, n. 3, p. 439–468, 1973.

MATHWORKS. MATLAB R2015a. **The MathWorks: Natick, MA, USA**, 2015.

MAZZONI, S. *et al.* Opensees command language manual. **Pacific Earthquake Engineering Research (PEER) Center**, Berkeley, California, United States, v. 264, n. 1, p. 137–158, 2006.

MCGUIRE, R. K. **Seismic hazard and risk analysis**. Oakland: Earthquake Engineering Research Institute, 2004.

MCKENNA, F.; FENVES, G.; SCOTT, M. **OpenSees: Open system for earthquake engineering simulation. Pacific Earthquake Engineering Research Center, UC Berkeley, CA**. 2006.

MELCHERS, R. E.; BECK, A. T. **Structural reliability analysis and prediction**. Hoboken: John Wiley & Sons, 2018.

MERGOS, P. E. Optimum seismic design of reinforced concrete frames according to eurocode 8 and fib model code 2010. **Earthquake Engineering & Structural Dynamics**, v. 46, n. 7, p. 1181–1201, 2017.

MERGOS, P. E. Efficient optimum seismic design of reinforced concrete frames with nonlinear structural analysis procedures. **Structural and Multidisciplinary Optimization**, v. 58, n. 6, p. 2565–2581, 2018.

MIANO, A. *et al.* Cloud to ida: Efficient fragility assessment with limited scaling. **Earthquake Engineering & Structural Dynamics**, v. 47, n. 5, p. 1124–1147, 2018.

MIGUEL, L. F. F.; BECK, A. T. Optimal path shape of friction-based track-nonlinear energy sinks to minimize lifecycle costs of buildings subjected to ground accelerations. **Reliability Engineering & System Safety**, v. 248, p. 110172, 2024.

MIGUEL, L. F. F.; ELIAS, S.; BECK, A. T. Reliability-based optimization of supported pendulum tmds' nonlinear track shape using padé approximants. **Engineering Structures**, v. 306, p. 117861, 2024.

MIGUEL, L. F. F.; LOPEZ, R. H.; AMBROSINI, D. Performance-based optimization of inerter-assisted t-ness considering ssi effects. **Mechanical Systems and Signal Processing**, v. 225, p. 112277, 2025.

MIGUEL, L. F. F.; LOPEZ, R. H.; AMBROSINI, D. Performance-based optimization of t-ness considering ssi effects on rectangular embedded foundations. **Soil Dynamics and Earthquake Engineering**, v. 200, p. 109797, 2026.

MIGUEL, L. F. F. *et al.* Performance-based optimization of nonlinear friction-folded ptmds of structures subjected to stochastic excitation. **Mechanical Systems and Signal Processing**, v. 195, p. 110291, 2023.

MIGUEL, L. F. F.; LOPEZ, R. H.; MIGUEL, L. F. F. Multimodal size, shape, and topology optimisation of truss structures using the firefly algorithm. **Advances in Engineering Software**, v. 56, p. 23–37, 2013.

MIGUEL, L. F. F. *et al.* Reliability-based optimization of multiple folded pendulum tmds through efficient global optimization. **Engineering Structures**, v. 266, p. 114524, 2022.

MIGUEL, L. F. F.; MIGUEL, L. F. F. Shape and size optimization of truss structures considering dynamic constraints through modern metaheuristic algorithms. **Expert Systems with Applications**, v. 39, n. 10, p. 9458–9467, 2012.

MILANEZ, M. O. **Análise de confiabilidade de estruturas sujeitas ao colapso progressivo considerando sua resposta estrutural global**. 2022. Tese (Doutorado) — Universidade Federal de Santa Catarina, 2022.

MIRANDA, P. S.; VARUM, H.; POUCA, N. V. Reflexões sobre o risco sísmico no brasil. *In*: **11º Congresso Nacional de Sismologia e Engenharia Sísmica**. [*S.l.: s.n.*], 2019.

MIRANDA, P. S. T. **A influência das ações sísmicas nas edificações brasileiras em concreto armado**. 2021. Tese (Doutorado) — Faculdade de Engenharia da Universidade do Porto (FEUP), 2021.

MIRFARHADI, S. A.; ESTEKANCHI, H. E.; SARCHESHMEHPOUR, M. On optimal proportions of structural member cross-sections to achieve best seismic performance using value based seismic design approach. **Engineering structures**, v. 231, p. 111751, 2021.

MISRA, S.; BOCCHINI, P. Metaimnet: A physics-informed neural network architecture for surrogate response and fragility modeling of structures subjected to time-varying hazard loads. **Structural Safety**, p. 102650, 2025.

MOEHLE, J.; DEIERLEIN, G. G. A framework methodology for performance-based earthquake engineering. **13th world conference on earthquake engineering**, v. 679, 2004.

MÖLLER, O. *et al.* Optimization for performance-based design under seismic demands, including social costs. **Earthquake Engineering and Engineering Vibration**, v. 14, p. 315–328, 2015.

MORRIS, M. D.; MITCHELL, T. J. Exploratory designs for computational experiments. **Journal of statistical planning and inference**, v. 43, n. 3, p. 381–402, 1995.

MOSLEH, A. *et al.* Stochastic collocation-based nonlinear analysis of concrete bridges with uncertain parameters. **Structure and Infrastructure Engineering**, v. 14, n. 10, p. 1324–1338, 2018.

MOUSTAPHA, M. *et al.* Comparative study of kriging and support vector regression for structural engineering applications. **ASCE-ASME Journal of Risk and Uncertainty in Engineering Systems, Part A: Civil Engineering**, v. 4, n. 2, p. 04018005, 2018.

MOVAGHAR, P. T. *et al.* Sustainability-driven risk-based design of inerter vibration absorbers for multistory hysteretic buildings under seismic hazard. **Journal of Engineering Mechanics**, v. 151, n. 11, p. 04025058, 2025.

MURRAY, P. B. *et al.* Seismic safety of informally constructed reinforced concrete houses in puerto rico. **Earthquake Spectra**, v. 39, n. 1, p. 5–33, 2023.

MURRAY, P. B.; LIEL, A. B.; ELWOOD, K. J. A framework for assessing impaired seismic performance as a trigger for repair. **Earthquake Engineering & Structural Dynamics**, v. 51, n. 2, p. 438–456, 2022.

NIEVAS, C. I. *et al.* A database of damaging small-to-medium magnitude earthquakes. **Journal of Seismology**, v. 24, n. 2, p. 263–292, 2020.

NIST. NIST GCR 10-917-8: Evaluation of the FEMA P695 methodology for quantification of building seismic performance factors. **National Institute of Standards and Technology**, Gaithersburg, MD, USA, 2010.

NÓBREGA, P. G. B. d.; SOUZA, B. R. S.; NÓBREGA, S. H. S. d. Towards improving the seismic hazard map and the response spectrum for the state of rn/brazil. **Revista IBRACON de Estruturas e Materiais**, v. 14, n. 3, p. e14302, 2021.

NOWAK, A. S.; COLLINS, K. R. **Reliability of structures**. London: CRC Press, 2012.

OLSSON, A.; SANDBERG, G.; DAHLBLOM, O. On latin hypercube sampling for structural reliability analysis. **Structural safety**, v. 25, n. 1, p. 47–68, 2003.

OPABOLA, E. A.; ELWOOD, K. J.; LIEL, A. B. Evaluation of seismic performance of as-built and retrofitted reinforced concrete frame structures with lap splice deficiencies. **Earthquake Engineering & Structural Dynamics**, v. 50, n. 12, p. 3138–3159, 2021.

PADGETT, J. E. **Seismic vulnerability assessment of retrofitted bridges using probabilistic methods**. 2007. Tese (Doutorado) — Georgia Institute of Technology, 2007.

PADGETT, J. E.; DESROCHES, R. Methodology for the development of analytical fragility curves for retrofitted bridges. **Earthquake Engineering & Structural Dynamics**, v. 37, n. 8, p. 1157–1174, 2008.

PADGETT, J. E.; NIELSON, B. G.; DESROCHES, R. Selection of optimal intensity measures in probabilistic seismic demand models of highway bridge portfolios. **Earthquake engineering & structural dynamics**, v. 37, n. 5, p. 711–725, 2008.

PAGANI, M. *et al.* The 2018 version of the global earthquake model: Hazard component. **Earthquake Spectra**, v. 36, n. 1_suppl, p. 226–251, 2020.

PANAGIOTAKOS, T. B.; FARDIS, M. N. Deformations of reinforced concrete members at yielding and ultimate. **Structural Journal**, v. 98, n. 2, p. 135–148, 2001.

PARISI, F.; NETTIS, A.; UVA, G. Machine learning-aided cloud analysis for seismic fragility assessment of multi-span bridges. **Engineering Structures**, v. 343, p. 121175, 2025.

PATSIALIS, D.; TAFLANIDIS, A.; GIARALIS, A. Tuned-mass-damper-inerter optimal design and performance assessment for multi-storey hysteretic buildings under seismic excitation. **Bulletin of Earthquake Engineering**, v. 21, n. 3, p. 1541–1576, 2023.

PATSIALIS, D.; TAFLANIDIS, A.; VAMVATSIKOS, D. Improving the computational efficiency of seismic building-performance assessment through reduced order modeling and multi-fidelity Monte Carlo techniques. **Bulletin of Earthquake Engineering**, v. 21, n. 2, p. 811–847, 2023.

PEER/ATC. PEER/ATC 72–1: Modeling and Acceptance Criteria for Seismic Design and Analysis of Tall Buildings. **Prepared for Pacific Earthquake Engineering Research Center (PEER) by Applied Technology Council (ATC)**, Redwood City, CA, USA, 2010.

PEREIRA, E. M. V. **Estudo da fragilidade sísmica de pórticos de concreto armado com irregularidades estruturais**. 2021. Dissertação (Mestrado) — State University of Campinas, 2021.

PEREIRA, E. M. V. **Probabilistic Seismic Hazard and Risk Analysis in Northeastern Brazil**. 2025. Tese (Doutorado) — State University of Campinas, 2025.

PEREIRA, E. M. V. *et al.* Seismic risk evaluation of non-ductile low-rise rc buildings in brazil: Time-based and intensity-based assessments considering different performance metrics. **Journal of Building Engineering**, v. 88, p. 109147, 2024.

PEREIRA, E. M. V. *et al.* Seismic reliability assessment of a non-seismic reinforced concrete framed structure designed according to abnt nbr 6118: 2014. **Revista IBRACON de Estruturas e Materiais**, v. 15, 2021.

PETERSEN, M. D. *et al.* Seismic hazard, risk, and design for south americaseismic hazard, risk, and design for south america. **Bulletin of the Seismological Society of America**, v. 108, n. 2, p. 781–800, 2018.

PIRCHINER, M. *et al.* PSHAB: probabilistic seismic hazard analysis for brazil, a national map building effort. **26th General Assembly of the International Union of Geodesy and Geophysics (IUGG 2015)**, Prague, Czech Republic, 2015.

PIRES, A. V. **Metamodelagem baseada em Kriging aplicada à dinâmica de geleiras**. 2021. Dissertação (Mestrado) — Universidade Estadual de Campinas, 2021.

PIRES, A. V. *et al.* Reliability analysis for data-driven noisy models using active learning. **Structural Safety**, v. 112, p. 102543, 2025a.

PIRES, A. V. *et al.* Reliability analysis for non-deterministic limit-states using stochastic emulators. **Structural Safety**, p. 102621, 2025b.

PORTER, K. **A Beginner's Guide to Fragility, Vulnerability, and Risk**. Boulder: University of Colorado Boulder, 2019. Available at: https://www.sparisk.com/pubs/Porter-beginners-guide.pdf.

PORTER, K. A. An overview of peer's performance-based earthquake engineering methodology. *In*: **Proceedings of ninth international conference on applications of statistics and probability in civil engineering**. [*S.l.: s.n.*], 2003.

RAMAMOORTHY, S. K.; GARDONI, P.; BRACCI, J. M. Probabilistic demand models and fragility curves for reinforced concrete frames. **Journal of structural Engineering**, v. 132, n. 10, p. 1563–1572, 2006.

RAO, S. S. **Engineering optimization: theory and practice**. Hoboken: John Wiley & Sons, 2019.

RASTEGARAN, M.; AVAL, S. B.; SANGALAKI, E. Multi-objective reliability-based seismic performance design optimization of SMRFs considering various sources of uncertainty. **Engineering Structures**, v. 261, p. 114219, 2022.

RAZAVI, N.; GHOLIZADEH, S. Seismic collapse safety analysis of performance-based optimally designed reinforced concrete frames considering life-cycle cost. **Journal of Building Engineering**, v. 44, p. 103430, 2021.

RIBEIRO, L. d. R. **Otimização de estruturas reticuladas em concreto armado considerando incertezas e riscos**. 2020. Dissertação (Mestrado) — Universidade de São Paulo, 2020.

ROCQUIGNY, É. de. La maîtrise des incertitudes dans un contexte industriel. 1re partie: une approche méthodologique globale basée sur des exemples. **Journal de la Société française de statistique**, v. 147, n. 3, p. 33–71, 2006.

RODRIGUES, I. D. **Avaliação da vulnerabilidade sísmica de edificações regulares em concreto armado no Brasil através da elaboração de curvas de fragilidade**. 2021. Dissertação (Mestrado) — Universidade Estadual de Campinas, 2021.

RODRIGUES, I. D. *et al.* Seismic fragility assessment of a rc frame considering concentrated and distributed plasticity modelling. **Revista IBRACON de Estruturas e Materiais**, v. 17, p. e17105, 2023.

RODRIGUES, I. D.; SPENCE, S. M.; BECK, A. T. Incorporating statistical uncertainty into metamodel-driven performance-based risk optimization for seismic design. **Engineering Structures**, v. 348, p. 121744, 2026. ISSN 0141-0296.

SAADAT, S.; CAMP, C. V.; PEZESHK, S. Seismic performance-based design optimization considering direct economic loss and direct social loss. **Engineering Structures**, v. 76, p. 193–201, 2014.

SACKS, J. *et al.* Design and analysis of computer experiments. **Statistical science**, v. 4, n. 4, p. 409–423, 1989.

SAEEDI, K.; TEHRANI, P.; BEHNAM, B. Investigating post-earthquake progressive collapse resistance of irregular steel structures. **Structures**, v. 67, p. 107010, 2024.

SALEHI, M.; SIDERIS, P.; LIEL, A. B. Assessing damage and collapse capacity of reinforced concrete structures using the gradient inelastic beam element formulation. **Engineering Structures**, v. 225, p. 111290, 2020.

SALLES, H. B. de *et al.* A fast frequency sweep approach for performance-based optimization of earthquake-resistant irregular large-scale buildings. **Engineering Structures**, v. 285, p. 116094, 2023.

SALLES, H. B. de *et al.* A model order reduction framework for performance-based seismic design optimization of friction-tuned mass dampers in large-scale l-shaped buildings with shear cores. *In*: **Structures**. [*S.l.: s.n.*], 2025. v. 77, p. 109073.

SAMADIAN, D. *et al.* Surrogate models for seismic and pushover response prediction of steel special moment resisting frames. **Engineering Structures**, v. 314, p. 118307, 2024.

SANTOS, K. R. dos; BECK, A. T.; LOPEZ, R. H. Sequential simulated annealing for life-cycle optimization of nonlinear stochastic systems via arbitrary polynomial chaos expansion. **Engineering Structures**, v. 304, p. 117675, 2024.

SANTOS, S.; LIMA, S. Elements for a future brazilian standard for seismic resistance of concrete structures of buildings. **IBRACON Structural Journal**, v. 1, p. 47–62, 2005.

SCHÖLKOPF, B.; SMOLA, A. J. **Learning with kernels: support vector machines, regularization, optimization, and beyond**. Cambridge: MIT Press, 2002.

SEVIERI, G.; GENTILE, R.; GALASSO, C. A multi-fidelity bayesian framework for robust seismic fragility analysis. **Earthquake Engineering & Structural Dynamics**, v. 50, n. 15, p. 4199–4219, 2021.

SHAHNAZARYAN, D.; O'REILLY, G. J. Integrating expected loss and collapse risk in performance-based seismic design of structures. **Bulletin of Earthquake Engineering**, v. 19, n. 2, p. 987–1025, 2021.

SHAPIRO, S. S.; WILK, M. B. An analysis of variance test for normality (complete samples). **Biometrika**, v. 52, n. 3-4, p. 591–611, 1965.

SHEDLOCK, K. M.; TANNER. Seismic hazard map of the western hemisphere. **Annals of Geophysics**, v. 42, 1999.

SILVA, A. H. da *et al.* Damage estimation in reinforced concrete buildings from induced earthquakes in Brazil. **Engineering Structures**, v. 234, p. 111904, 2021.

SIQUEIRA, G. H. *et al.* Fragility curves for isolated bridges in eastern canada using experimental results. **Engineering Structures**, v. 74, p. 311–324, 2014.

SKANDALOS, K.; CHAKRABORTY, S.; TESFAMARIAM, S. Seismic reliability analysis using a multi-fidelity surrogate model: Example of base-isolated buildings. **Structural Safety**, v. 97, p. 102222, 2022.

SPENCE, S. M.; ARUNACHALAM, S. Performance-based wind engineering: Background and state of the art. **Frontiers in Built Environment**, v. 8, p. 830207, 2022.

SPENCE, S. M.; GIOFFRÈ, M. Large scale reliability-based design optimization of wind excited tall buildings. **Probabilistic Engineering Mechanics**, v. 28, p. 206–215, 2012.

SPENCE, S. M.; KAREEM, A. Performance-based design and optimization of uncertain wind-excited dynamic building systems. **Engineering Structures**, v. 78, p. 133–144, 2014.

SPENCE, S. M. J. Optimization of uncertain and dynamic high-rise structures for occupant comfort: An adaptive kriging approach. **Structural Safety**, v. 75, p. 57–66, 2018.

SUAREZ, D.; CALVI, G. M.; GENTILE, R. Direct loss-based seismic design of low-rise base-isolated reinforced concrete buildings. **Earthquake Engineering & Structural Dynamics**, v. 53, n. 15, p. 4641–4669, 2024.

SUBGRANON, A.; SPENCE, S. M. Performance-based bi-objective optimization of structural systems subject to stochastic wind excitation. **Mechanical Systems and Signal Processing**, v. 160, p. 107893, 2021.

SUDRET, B. Uncertainty propagation and sensitivity analysis in mechanical models–contributions to structural reliability and stochastic spectral methods. **Habilitationa diriger des recherches, Université Blaise Pascal, Clermont-Ferrand, France**, v. 147, p. 53, 2007.

SUDRET, B. Meta-models for structural reliability and uncertainty quantification. **arXiv preprint arXiv:1203.2062**, 2012.

SUDRET, B. Polynomial chaos expansions and stochastic finite-element methods. *In*: PHOON, K.-K.; ZHANG, L. (ed.). **Risk and Reliability in Geotechnical Engineering**. Boca Raton: CRC Press, 2015. p. 265–300.

SUKSUWAN, A.; SPENCE, S. M. Performance-based multi-hazard topology optimization of wind and seismically excited structural systems. **Engineering Structures**, v. 172, p. 573–588, 2018.

SUKSUWAN, A.; SPENCE, S. M. Performance-based bi-objective design optimization of wind-excited building systems. **Journal of Wind Engineering and Industrial Aerodynamics**, v. 190, p. 40–52, 2019.

SUKSUWAN, A.; SPENCE, S. M. Performance-based design optimization of uncertain wind excited systems under system-level loss constraints. **Structural Safety**, v. 80, p. 13–31, 2019.

SUKSUWAN, A.; SPENCE, S. M. J. Optimization of uncertain structures subject to stochastic wind loads under system-level first excursion constraints: A data-driven approach. **Computers & Structures**, v. 210, p. 58–68, 2018.

TAFLANIDIS, A. A.; BECK, J. L. Life-cycle cost optimal design of passive dissipative devices. **Structural Safety**, v. 31, n. 6, p. 508–522, 2009.

TAFLANIDIS, A. A.; GIARALIS, A.; PATSIALIS, D. Multi-objective optimal design of inerter-based vibration absorbers for earthquake protection of multi-storey building structures. **Journal of the Franklin Institute**, v. 356, n. 14, p. 7754–7784, 2019.

TANAKA, H. **Effect of lateral confining reinforcement on the ductile behaviour of reinforced concrete columns**. 1990. Tese (Doutorado) — University of Canterbury, Christchurch, New Zealand, 1990.

TAVARES, D. H.; PADGETT, J. E.; PAULTRE, P. Fragility curves of typical as-built highway bridges in eastern canada. **Engineering Structures**, v. 40, p. 107–118, 2012.

TQS Informática. **TQS – Sistema Computacional para Projetos Estruturais**. São Paulo, Brazil, 2019. Software de projeto estrutural. Available at: http://www.tqs.com.br/conheca-os-sistemas-cadtqs/analise-estrutural/95-modelo-tqs.

TSAVDARIDIS, K. D.; KINGMAN, J. J.; TOROPOV, V. V. Application of structural topology optimisation to perforated steel beams. **Computers & structures**, v. 158, p. 108–123, 2015.

UANG, C.-M.; NAKASHIMA, M.; TSAI, K.-C. Research and application of buckling-restrained braced frames. **International Journal of Steel Structures**, v. 4, n. 4, p. 301–313, 2004.

UNDRR. **United Nations Office for Disaster Risk Reduction**. 2023. Available at: https://www.unisdr.org/. Accessed on: 01 August 2023.

U.S. Geological Survey. **Unified Hazard Tool**. 2024. Available online. Available at: https://earthquake.usgs.gov/hazards/interactive/.

VALDEBENITO, M. A.; SCHUËLLER, G. I. A survey on approaches for reliability-based optimization. **Structural and Multidisciplinary Optimization**, v. 42, p. 645–663, 2010.

VAMVATSIKOS, D.; CORNELL, C. A. Incremental dynamic analysis. **Earthquake engineering & structural dynamics**, v. 31, n. 3, p. 491–514, 2002.

VAMVATSIKOS, D.; CORNELL, C. A. Applied incremental dynamic analysis. **Earthquake spectra**, v. 20, n. 2, p. 523–553, 2004.

VANDERPLAATS, G. N. Structural optimization-past, present, and future. **AIAA journal**, v. 20, n. 7, p. 992–1000, 1982.

VARAEE, H.; SHISHEGARAN, A.; GHASEMI, M. R. The life-cycle cost analysis based on probabilistic optimization using a novel algorithm. **Journal of Building Engineering**, v. 43, p. 103032, 2021.

VETTER, C.; TAFLANIDIS, A. A. Global sensitivity analysis for stochastic ground motion modeling in seismic-risk assessment. **Soil Dynamics and Earthquake Engineering**, v. 38, p. 128–143, 2012.

WAKJIRA, T. G.; ALAM, M. S. Performance-based seismic design of ultra-high-performance concrete (uhpc) bridge columns with design example–powered by explainable machine learning model. **Engineering Structures**, v. 314, p. 118346, 2024.

WAN, L. *et al.* A new multiple stochastic kriging model for active learning surrogate-assisted reliability analysis. **Reliability Engineering & System Safety**, v. 260, p. 110966, 2025.

WANG, G. G.; SHAN, S. Review of metamodeling techniques in support of engineering design optimization. 2007.

WANG, X. *et al.* An efficient discrete optimization algorithm for performance-based design optimization of steel frames. **Advances in Structural Engineering**, v. 23, n. 3, p. 411–423, 2020.

WEN, Y.; ELLINGWOOD, B. R.; BRACCI, J. M. **Vulnerability function framework for consequence-based engineering**. Chicago: University of Illinois, 2004. (MAE Center Project DS-4 Report).

WEN, Y.; KANG, Y. Minimum building life-cycle cost design criteria. ii: Applications. **Journal of Structural Engineering**, v. 127, n. 3, p. 338–346, 2001.

WEN, Y.-K.; KANG, Y. Minimum building life-cycle cost design criteria. i: Methodology. **Journal of Structural Engineering**, v. 127, n. 3, p. 330–337, 2001.

WHITTAKER, A.; HAMBURGER, R.; MAHONEY, M. Performance-based engineering of buildings for extreme events. *In*: **AISC-SINY symposium on resisting blast and progressive collapse**. [*S.l.: s.n.*], 2003. p. 55–66.

WILLIAMS, C. K.; RASMUSSEN, C. E. **Gaussian processes for machine learning**. Cambridge: MIT Press, 2006. v. 2.

WU, C.; BURTON, H. V. Effects of probability model misspecification on the number of ground motions required for seismic performance assessment. **Earthquake Spectra**, v. 40, n. 4, p. 2888–2916, 2024.

WU, R.-Y.; PANTELIDES, C. P. Concentrated and distributed plasticity models for seismic repair of damaged rc bridge columns. **Journal of Composites for Construction**, v. 22, n. 5, p. 04018044, 2018.

XU, L.; SPENCE, S. M. Collapse reliability of wind-excited reinforced concrete structures by stratified sampling and nonlinear dynamic analysis. **Reliability Engineering & System Safety**, v. 250, p. 110244, 2024.

YANG, T. *et al.* Seismic performance evaluation of facilities: methodology and implementation. **Journal of Structural Engineering**, v. 135, n. 10, p. 1146–1154, 2009.

YANG, X.-S. **Nature-inspired metaheuristic algorithms**. [*S.l.: s.n.*]: Luniver press, 2010.

YAZDANI, H. *et al.* Probabilistic performance-based optimum seismic design of RC structures considering soil–structure interaction effects. **ASCE-ASME Journal of Risk and Uncertainty in Engineering Systems, Part A: Civil Engineering**, v. 3, n. 2, p. G4016004, 2017.

YI, P.; CHENG, G.; JIANG, L. A sequential approximate programming strategy for performance-measure-based probabilistic structural design optimization. **Structural Safety**, v. 30, n. 2, p. 91–109, 2008.

YI, S.-r.; TAFLANIDIS, A. A. Stochastic emulation with enhanced partial-and no-replication strategies for seismic response distribution estimation. **Earthquake Engineering & Structural Dynamics**, v. 53, n. 7, p. 2354–2381, 2024.

YI, S.-r.; TAFLANIDIS, A. A. Multi-output stochastic emulation with applications to seismic response correlation estimation. **Structural Safety**, p. 102578, 2025.

ZAREIAN, F.; LIGNOS, D.; KRAWINKLER, H. Evaluation of seismic collapse performance of steel special moment resisting frames using FEMA P695 (ATC-63) methodology. *In*: **Structures Congress 2010**. [*S.l.: s.n.*], 2010. p. 1275–1286.

ZHANG, C.; TIAN, Y. Simplified performance-based optimal seismic design of reinforced concrete frame buildings. **Engineering Structures**, v. 185, p. 15–25, 2019.

ZHANG, W. *et al.* Regional-scale seismic fragility, loss, and resilience assessment using physics-based simulated ground motions: An application to istanbul. **Earthquake Engineering & Structural Dynamics**.

ZHONG, K. *et al.* Surrogate modeling of structural seismic response using probabilistic learning on manifolds. **Earthquake Engineering & Structural Dynamics**, v. 52, n. 8, p. 2407–2428, 2023.

ZHU, X. **Surrogate modeling for stochastic simulators using statistical approaches**. 2023. Tese (Doutorado) — ETH Zurich, 2023.

ZHU, X.; BROCCARDO, M.; SUDRET, B. Seismic fragility analysis using stochastic polynomial chaos expansions. **Probabilistic Engineering Mechanics**, v. 72, p. 103413, 2023.

ZHU, X.; SUDRET, B. Emulation of stochastic simulators using generalized lambda models. **SIAM/ASA Journal on Uncertainty Quantification**, v. 9, n. 4, p. 1345–1380, 2021.

ZHU, X.; SUDRET, B. Stochastic polynomial chaos expansions to emulate stochastic simulators. **International Journal for Uncertainty Quantification**, v. 13, n. 2, 2023.

ZONA, A.; DALL'ASTA, A. Elastoplastic model for steel buckling-restrained braces. **Journal of Constructional Steel Research**, v. 68, n. 1, p. 118–125, 2012.

APPENDIX

APPENDIX A – ADAPTIVE KRIGING VALIDATION

In this Appendix, the adaptive Kriging approach is validated using univariate and multivariate functions. The selected functions are intended to challenge the method, as adaptive Kriging may encounter difficulties when dealing with highly nonlinear functions (Pires, 2021).

A.1 Univariate Functions

A.1.1 Function 1: $f(x) = x\sin(x)$

The first test of the Kriging metamodel considers the univariate function $f(x) = x\sin(x)$. Figure A.1a presents the target function and the results obtained with the Adaptive Kriging methodology, including both the initial and adaptive DoE points, along with the 95

Figure A.1 – Results for the adaptive Kriging for $f(x) = x\sin(x)$.

(a) Target function and Kriging prediction. **(b)** Scatter plot $Y_{kriging} \times Y$.

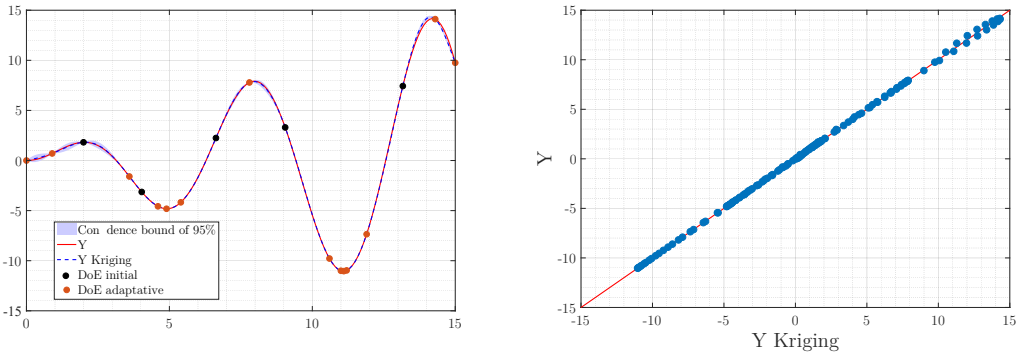

Source: Author.

The calculated RMSE is 0.0983, with a normalized value (NRMSE) of 0.39%. The coefficient of determination is $R^2 = 0.9998$. The initial DoE consisted of five support points, and the algorithm added 15 infill points to complete the metamodel. Figure A.2 illustrates iterations 1, 5, 10, and 15 of the algorithm, showing the expected improvement function at each stage.

Figure A.2 – Illustration of the adaptive Kriging at different iterations of the algorithm.

(a) Iteration 1 **(b)** Iteration 5

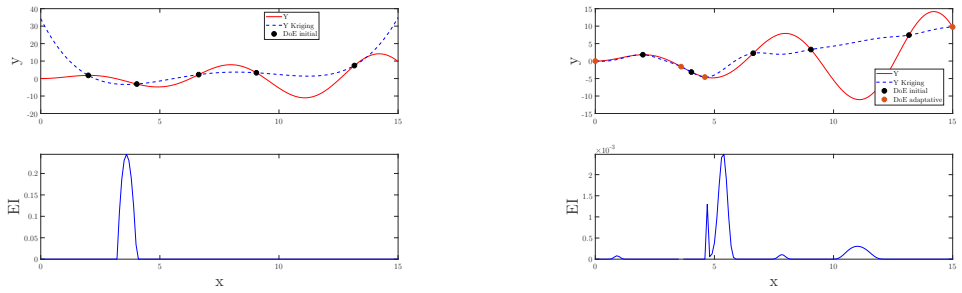

(c) Iteration 10 **(d)** Iteration 15

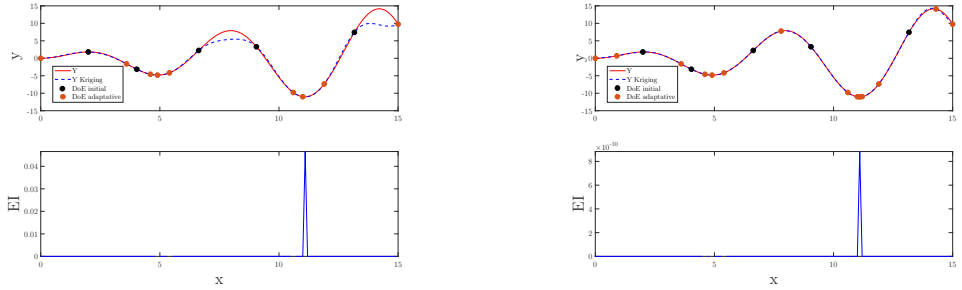

Source: Author.

A.1.2 Function 2: $f(x) = (6x - 2)^2 \sin(12x - 4)$

The second test of the Kriging metamodel considers the univariate function $f(x) = (6x - 2)^2 \sin(12x - 4)$. Figure A.3a presents the target function and the results obtained with the Adaptive Kriging methodology, including both the initial and adaptive DoE points, along with the 95% confidence interval. Figure A.3b shows the scatter plot with the target model values on the y-axis and the metamodel predictions on the x-axis.

The calculated RMSE is 0.1128, with a normalized value (NRMSE) of 0.51%. The coefficient of determination is $R^2 = 0.9994$. The initial DoE consisted of five support points, and the algorithm added 10 infill points to complete the metamodel. Figure A.4 illustrates iterations 1, 4, 7, and 10 of the algorithm, showing the expected improvement function at each stage.

A.2 Multivariate Functions

Multivariate functions are defined by n input variables and a single output value, expressed as $f(\mathbf{X})$, where $\mathbf{X} = x_1, x_2, \ldots, x_n$.

Figure A.3 – Results for the adaptive Kriging for $f(x) = (6x - 2)^2 \sin(12x - 4)$.

(a) Target function and Kriging prediction. **(b)** Scatter plot $Y_{kriging} \times Y$.

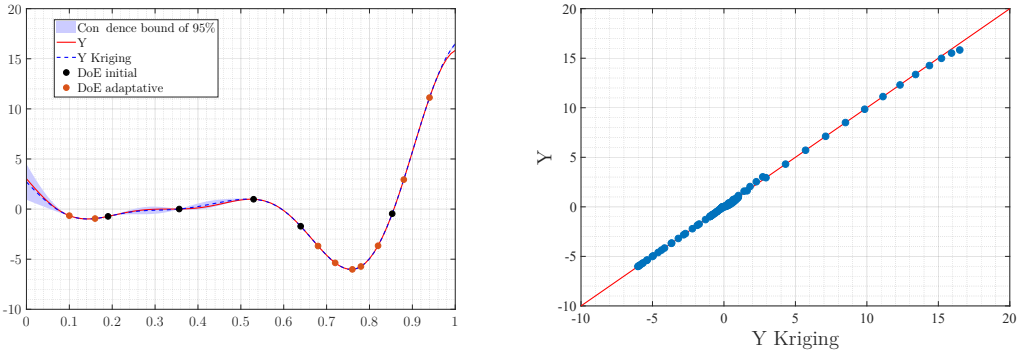

Source: Author.

Figure A.4 – Representation of the adaptive Kriging at different iterations of the algorithm.

(a) Iteration 1 **(b)** Iteration 4

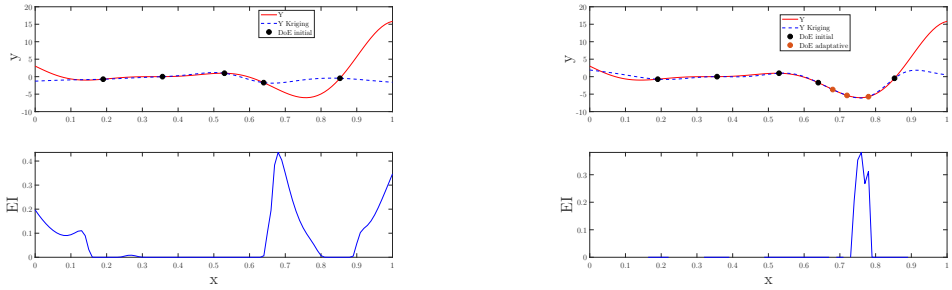

(c) Iteration 7 **(d)** Iteration 10

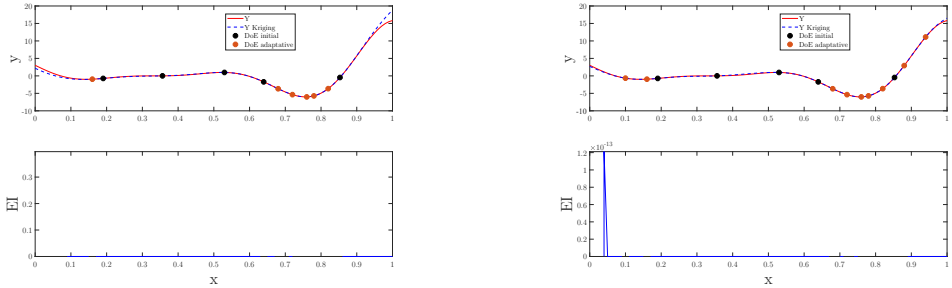

Source: Author.

A.2.1 Function 3: Ishigami Function

The first multivariate function evaluated is the Ishigami function (Ishigami; Homma, 1990), given in Equation A.1.

$$f(x_1, x_2, x_3) = \sin(x_1) + a\sin^2(x_2) + bx_3^4 \sin(x_1) \tag{A.1}$$

where a and b are scalar values adopted as $a = 7$ and $b = 0.1$, following Sudret (2015) and Pires (2021); x_1, x_2, and x_3 are uniformly distributed in the interval $[-\pi, \pi]$.

This is a highly nonlinear function widely used in the field of uncertainty quantification. Since it involves three input variables, it is not possible to present a figure with both the target function and the Kriging estimation; therefore, only the scatter plot is shown in Figure A.5.

Figure A.5 – Scatter plot $Y_{kriging} \times Y$.

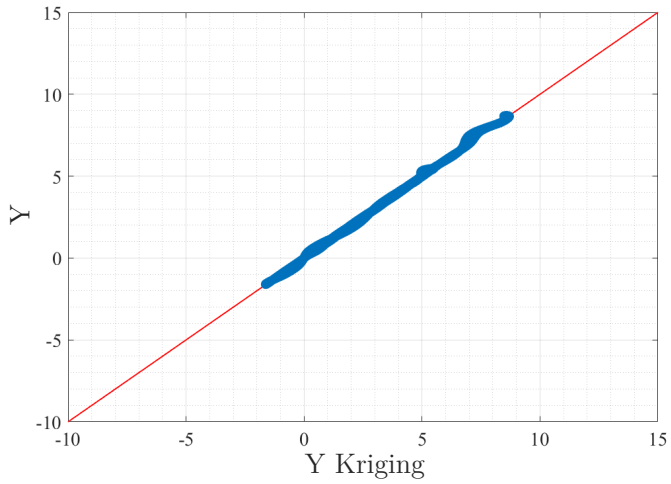

Source: Author.

The calculated RMSE is 0.1120, with a normalized value (NRMSE) of 1.08%. The coefficient of determination is $R^2 = 0.9986$. The initial DoE consisted of 20 support points, and the algorithm added 30 infill points to complete the metamodel.

To enable visualization in a 3D plot, variable x_3 was fixed at $x_3 = 1$, and the methodology was applied again. In this case, 40 support points were initially used and the convergence criterion was set to $R^2 = 0.9999$. The 3D plot is shown in Figure A.6a, while the corresponding scatter plot is presented in Figure A.6b. For this case, the calculated RMSE is 0.0228, with a normalized value (NRMSE) of 0.28%, and the coefficient of determination is $R^2 = 0.99992$. The initial DoE included 40 support points, and the algorithm added 16 infill points to complete the metamodel.

Figure A.6 – Results for the adaptive Kriging for Function 3 with $x_3 = 1$.

(a) Deterministic curve and Kriging prediction.

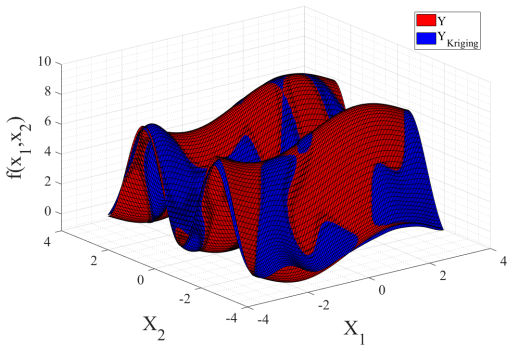

(b) Scatter plot $Y_{kriging} \times Y$.

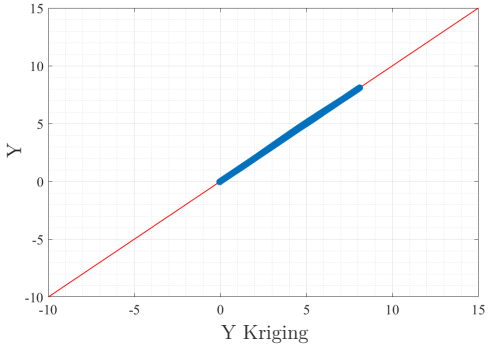

Source: Author.

APPENDIX B – COLUMN CALIBRATION WITHIN THE LUMPED PLASTICITY MODEL FRAMEWORK

The experimental results available at the Pacific Earthquake Engineering Research Center (PEER) are used to check whether the numerical model developed is giving satisfactory results. Herein, the calibration process is described considering the results from experiment number 5 from Tanaka (1990) for the Lumped Plasticity models.

The experiment consists of a cyclic load applied in a column with 1.65 meters height and a square cross-section with width and depth equal to 55 centimeters. The column design considered a concrete cover of 4 centimeters, 12 longitudinal reinforcement bars of 20 millimeter diameter disposed in a symmetric way corresponding to a longitudinal reinforcement ratio of 1.25%. Transverse reinforcement is composed of two stirrups of 12 millimeters diameter with 11 centimeters spacing, representing a transverse reinforcement ratio of 1.7% and 4 shear legs. The yield stress of longitudinal and transverse reinforcement are 511 MPa and 325 MPa, respectively, and the ultimate stress is 675 MPa for longitudinal and 429 MPa for transverse bars. A representation of the column and the design details of the cross-section is shown in Figure B.1.

Figure B.1 – Representation of the column and its cross-section (in millimeters).

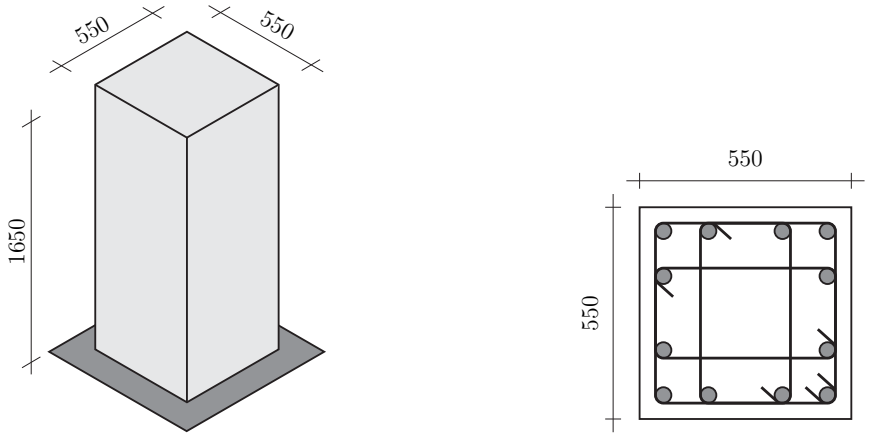

Source: Pereira (2021).

The numerical models are developed using OpenSees. Figure B.2 shows the comparison between the model with the experimental results.

Figure B.2 – Displacement history applied at column top.

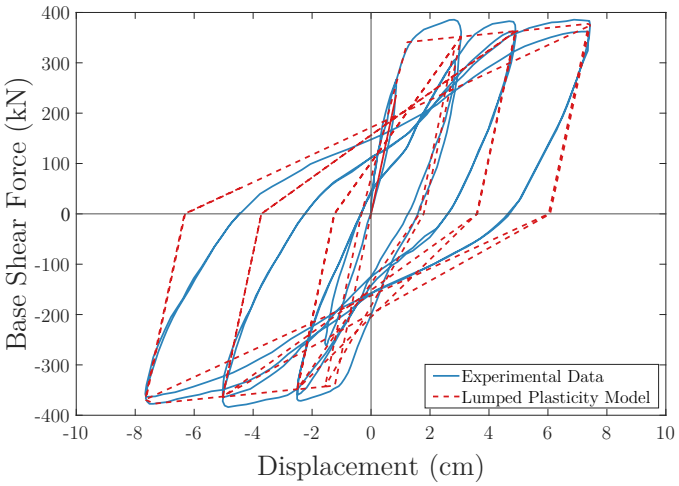

Source: Author.

ANNEX

ANNEX A – LUMPED PLASTICITY MODEL (LPM)

The Finite Element Model developed considering the Lumped Plasticity Model (LPM) uses OpenSees software and its own library to create beams and columns elements. Figure A.1 represents the model in a 2D frame.

Figure A.1 – Representation of the Finite Element Model for the Lumped Plasticity Model.

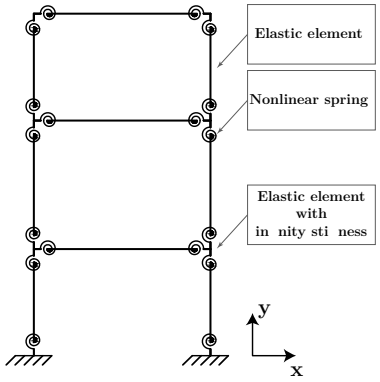

Source: Author.

For this, a non-linear spring model is used, developed by Ibarra, Medina and Krawinkler (2005) and described with details in the sequence. The material, named *uniaxialMaterial IMKPeakOriented* in OpenSees library, is applied to a zero-length element represented by the springs on Figure A.1. Joints are represented by an elastic element with the length of the joint and infinite stiffness. The rest of the element is also modeled with the *elasticBeamColumn* element with its area and Young's Modulus of the material. To account for the degradation of strength and stiffness associated with large deformations, suitable geometric transformations, and a leaning ($P-\Delta$) column are used in the analysis.

A.1 Plastic Hinge Model

The model is used to simulate the non-linear hysteretic response of reinforced concrete (RC) beams or columns under large deformations and is also developed to enable simulation of the non-linear dynamic response of RC frame buildings under earthquake ground motions. It consists of a monotonic backbone curve and hysteretic degradation rules to capture post-peak in-cycle softening which are associated with concrete crushing and reinforcing bar buckling at large cyclic deformations (Haselton *et al.*, 2016). Figure A.2 represents the monotonic curve by an idealized trilinear end moment (M) versus chord rotation (θ) response of an equivalent cantilever column.

Figure A.2 – Idealized trilinear end moment versus chord rotation.

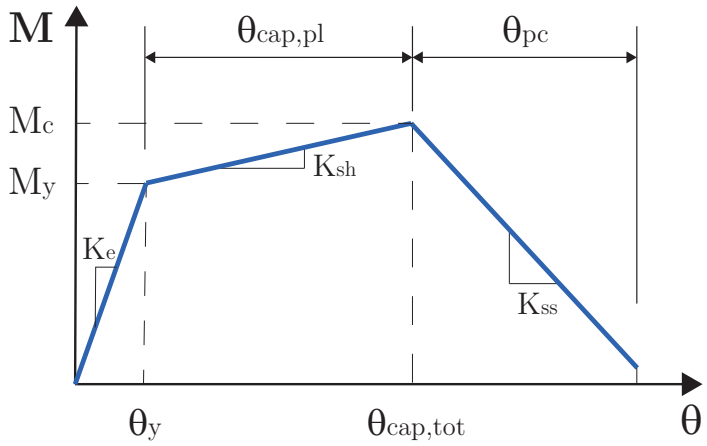

Source: Author.

The curve is defined considering five parameters: yield moment capacity M_y; initial elastic secant stiffness to yield point K_e; maximum moment capacity M_c; plastic chord rotation from yield to cap point $\theta_{cap,pl}$; post-capping plastic rotation capacity θ_{pc}. The flexural yield strength M_y generally is computed using a strain compatibility approach. It is assumed that sections remain plane and also an equivalent rectangular compressive stress distribution under ultimate loads with a concrete crushing strain of 0.003 (Haselton *et al.*, 2016). The equations for the model's parameters are presented in the following sections. Interested readers are referred to Haselton and Deierlein (2008) and Haselton *et al.* (2016) for more detailed information.

A.1.1 Effective Initial Stiffness (EI_y/EI_g and EI_{stf}/EI_g)

Two values of effective stiffness are defined: the secant stiffness to the yield point of the component (EI_y), represented by Equation A.1; and the secant stiffness to 40% of the yield force of the component (EI_{stf}), represented by Equation A.2. The values are expressed as a ratio of the gross cross-section stiffness (EI_g), and include all modes of deformation: flexure, shear and bond-slip.

$$\frac{EI_y}{EI_g} = 0.30 \left(0.1 + \frac{P}{A_g f'_c}\right)^{0.80} \left(\frac{L_s}{h}\right)^{0.72} \tag{A.1}$$

where $0.2 \leq EI_y/EI_g \leq 0.6$.

$$\frac{EI_{stf}}{EI_g} = 0.77 \left(0.1 + \frac{P}{A_g f'_c}\right)^{0.80} \left(\frac{L_s}{h}\right)^{0.43} \tag{A.2}$$

where $0.35 \leq EI_{stf}/EI_g \leq 0.8$.

P corresponds to the axial load; A_g is the gross concrete area; $f_c^{'}$ is the compressive strength of unconfined concrete; L_s is the shear span, corresponding to the distance between column end and point of inflection; h is the cross-section height. EI_{stf} is expected to be approximately 1.7 times stiffer than the secant stiffness to yield EI_y in a typical column. The choice between which stiffness is adequate depends on the deformation levels expected in the analysis. EI_{stf} is generally used for analysis at low deformation demands below yield, and the yield stiffness EI_y is intended for higher demands, where displacements are beyond yield and into the inelastic range. However, studies have shown that the value used for initial stiffness does not influence the response in a highly non-linear range and up to collapse (Haselton *et al.*, 2016).

A.1.2 Plastic rotation capacity ($\theta_{cap,pl}$)

Equation A.3 is proposed to determine the rotation capacity (measured in radians) between yield and the peak moment resistance.

$$\theta_{cap,pl} = 0.12\left(1+0.55a_{sl}\right)\left(0.16\right)^{\nu}\left(0.02+40\rho_{sh}\right)^{0.43}\times \left(0.54\right)^{0.01c_{unit}f_c^{'}}\left(0.66\right)^{0.1s_n}\left(2.27\right)^{10\rho} \tag{A.3}$$

where: a_{sl} is an indicator variable (0 or 1) to signify possibility of longitudinal reinforcing bar slip beyond the column end; $a_{sl} = 1$ if slip is possible (defined by Panagiotakos and Fardis (2001) and Fardis and Biskinis (2003)); ν is the axial load ratio, given by $\nu = P/\left(A_g f_c^{'}\right)$; $f_c^{'}$ is the compressive strength of unconfined concrete, based on standard cylinder test; ρ_{sh} is the transversal reinforcement ratio; ρ is the longitudinal reinforcement ratio; c_{unit} is an unit conversion variable that equals 1 when $f_c^{'}$ and f_y are in MPa and 6.9 for ksi; s_n is the reinforcing bar slenderness ratio, given by s/d_b (s corresponds to the spacing of transverse reinforcement measured along height of column and d_b is the longitudinal bar diameter). Since the experimental data used in the study are limited to columns with symmetrical arrangements of reinforcement, Equation A.3 is only applied to columns following this configuration.

A.1.3 Post-capping rotation capacity (θ_{pc})

Equation A.4 defines the post-capping rotation capacity.

$$\theta_{pc} = \left(0.76\right)\left(0.031\right)^{\nu}\left(0.02+40\rho_{sh}\right)^{1.02} \leq 0.10 \tag{A.4}$$

The parameters that influence deformation capacity are axial load ratio, transverse steel ratio, reinforcing bar buckling coefficient, stirrup spacing, concrete strength and longitudinal steel ratio. On the calibration process there are only 15 tests suitable for θ_{pc}, because only in them the post-capping slope was clear (Haselton *et al.*, 2016).

A.1.4 Post-yield hardening stiffness

The prediction of hardening stiffness has the axial load ratio and concrete strength as statistically significant parameters. Despite that, the inclusion of both did not improve the regression analysis, and it is recommended a constant value that is represented in Equation A.5 (Haselton; Deierlein, 2008), (FEMA, 2009), (Haselton *et al.*, 2016).

$$\frac{M_c}{M_y} = 1.13 \tag{A.5}$$

A.1.5 Cyclic energy dissipation capacity

Cyclic energy dissipation capacity can be quantified using two different expressions: $E_t = \gamma M_y \theta_y$ and $E_t = \lambda^{'} M_y \theta_{cap,pl}$ that are defined by the parameters γ and $\lambda^{'}$. The equations for each one of them are represented in A.6 and A.7, respectively.

$$\gamma = (170.7)\,(0.27)^{\nu}\,(0.10)^{s/d} \tag{A.6}$$

$$\lambda^{'} = (30)\,(0.3)^{\nu} \tag{A.7}$$

where: d is the depth of the column cross-section. The use of $\lambda^{'}$ is more interesting because the energy dissipation capacity E_t is more highly correlated with the associated plastic rotation capacity. Despite that, OpenSees uses the value of γ for the material developed by Ibarra, Medina and Krawinkler (2005), although it is referred to as λ in the software library.

ANNEX B – FIREFLY ALGORITHM

Firefly algorithm is a technique developed by Yang (2010), and it is based on the observation of the behavior of fireflies, which uses lights as a communication method. There are three rules for the algorithm (Luiz, 2020):

1. All fireflies are mutually attractive.
2. The degree of attraction is proportional to brightness, meaning that a less bright firefly will move toward a brighter one.
3. Brightness is associated with the objective function. If no difference in brightness exists between fireflies, they move randomly.

In a minimization problem, the brightest firefly corresponds to the smallest value of the objective function. Thus, the most relevant aspects of the algorithm are the variation of the light intensity I, which depends on the value of the objective function, and the formulation of the attractiveness β_{FR} between fireflies, which varies with the distance r_{ij} between fireflies i and j. Both light intensity and attractiveness decrease as the distance between fireflies increases. The light intensity is defined as:

$$I\left(r\right) = I_0 e^{-\gamma r^2} \tag{B.1}$$

where: I_0 is the original bright intensity, γ is a coefficient from the algorithm that represents bright absorption and r is the distance between the fireflies. Attractiveness can be defined as:

$$\beta_{FR}\left(r\right) = \beta_0 e^{-\gamma r^2} \tag{B.2}$$

where: β_0 is the original attraction of a firefly.

The movement of a firefly i toward a brighter and more attractive firefly j is defined as:

$$\vec{d}_{i+1} = \vec{d}_i + \beta_0 e^{-\gamma r_{ij}^2}\left(\vec{d}_j - \vec{d}_i\right) + \alpha\left(\text{rand} - \frac{1}{2}\right) \tag{B.3}$$

where: $\vec{d}_i$ and $\vec{d}_j$ are the coordinates of the fireflies i and j, α is a coefficient for randomness and $rand$ is a random number from an uniform distribution between $[0, 1]$. The random component of the movement introduces variations in the solution as the fireflies approach the optimum point. A gradual reduction of randomness improves solution quality, since excessive variation can hinder convergence (Yang, 2010; Luiz, 2020).

At each iteration, the brightest firefly I is identified, and all others move toward it, leading to convergence after a sufficient number of iterations. It is essential to have enough fireflies to adequately explore the entire design space, ensuring that the identified optimum corresponds to the global minimum rather than a local one (Ribeiro, 2020). Figure B.1 presents the flowchart of the Firefly algorithm.

Figure B.1 – Firefly algorithm.

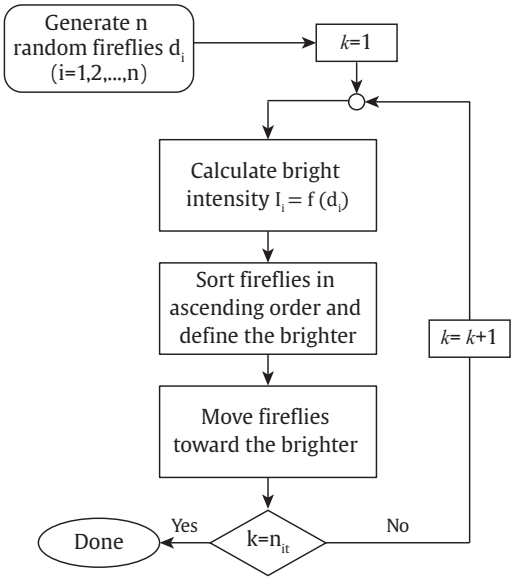

Source: Adapted from Luiz (2020).

PPG
SET

EESC • USP